MINISTERE DE LA CULTURE

Cahiers
du Centre Européen
de Géodynamique
et de Séismologie

Volume 31

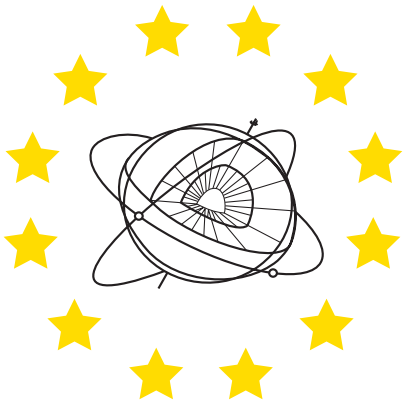

Proceedings of the ECGS & ESC/EAEE Joint Workshop:

Earthquake and Induced Multi-Risk Early Warning and Rapid Response

November 18-20, 2015
DoubleTree Hotel by Hilton
Luxembourg
(Grand-Duchy of Luxembourg)

Edited by Adrien Oth and Stefano Parolai

Luxembourg 2016

Proceedings of the ECGS & ESC/EAEE Joint Workshop:

EARTHQUAKE AND INDUCED MULTI-RISK EARLY WARNING AND RAPID RESPONSE

November 18-20, 2015

DoubleTree Hotel by Hilton
Luxembourg
Grand-Duchy of Luxembourg

Organized by
The European Center for Geodynamics and Seismology (ECGS)

In collaboration with

The European Seismological Commission (ESC)
The European Association for Earthquake Engineering (EAEE)

Supported by

Ministère de la Culture
Fonds National de la Recherche de Luxembourg (FNR)
The Council of Europe (EUR-OPA)
Musée National d'Histoire Naturelle (MNHN)
Seismological Society of America (SSA)
International Association of Seismology and Physics of the Earth's Interior (IASPEI)

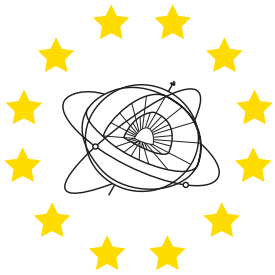

Edited by:

Adrien Oth and Stefano Parolai

Luxembourg - 2016

Workshop organized and Proceedings published with the support of

EUROPEAN SEISMOLOGICAL COMMISSION (ESC)
EUROPEAN ASSOCIATION FOR EARTHQUAKE ENGINEERING (EAEE)

MINISTERE DE LA CULTURE, LUXEMBOURG

FONDS NATIONAL DE LA RECHERCHE

Fonds National de la Recherche Luxembourg

ACCORD PARTIEL OUVERT

en matière de prévention, de protection et d'organisation des secours
contre les risques naturels et technologiques majeurs

du **CONSEIL DE L'EUROPE**

EUR-OPA
EUR-OPA MAJOR HAZARDS AGREEMENT
ACCORD EUR-OPA RISQUES MAJEURS

ISBN N° 978-99959-0-256-8

Centre Européen de Géodynamique et de Séismologie

Musée National d'Histoire Naturelle
Section Astrophysique et Géophysique, Luxembourg

ECGS & ESC/EAEE Joint Workshop
Earthquake and Induced Multi-Risk Early Warning and Rapid Response

Workshop Report by the Scientific Committee

Adrien Oth[1], Stefano Parolai[2], Carlo Cauzzi[3], Iunio Iervolino[4], Atilla Ansal[5], Maren Böse[3], Katsuichiro Goda[6], Thomas H. Heaton[7], Mitsuyuki Hoshiba[8] and Aldo Zollo[4]

[1] European Center for Geodynamics and Seismology, Luxembourg, adrien.oth@ecgs.lu
[2] GFZ German Research Centre for Geosciences, Germany
[3] ETH Zürich, Switzerland
[4] University of Naples Federico II, Italy
[5] Özyegin University, Istanbul, Turkey
[6] University of Bristol, United Kingdom
[7] California Institute of Technology, USA
[8] Japan Meteorological Agency (JMA), Japan

Introduction

A workshop on *Earthquake and Induced multi-risk early warning and rapid response* was convened in Luxemburg on 18-20 November 2015, in collaboration between the European Center for Geodynamics and Seismology (ECGS), the European Seismological Commission (ESC) and the European Association for Earthquake Engineering (EAEE). Sponsorship was received by the National Research Fund of Luxembourg, the EUR-OPA Major Hazards Agreement of the Council of Europe, the Luxembourg Ministry of Culture, the Luxembourg National Museum for Natural History, the Seismological Society of America and the International Association of Seismology and Physics of the Earth Interior. The main goal was to provide a platform to gather around one table scientists and engineers, including researchers and engineer practitioners, to discuss and look for solutions to the problems still encountered in the development and implementation of earthquake early warning and rapid response strategies. The workshop was attended by 64 participants from 20 countries, including researchers at universities, research centres and governmental organizations as well as representatives of commercial companies. The workshop programme and a list of participants are provided in the appendix to this report.

The workshop comprised four topical sessions, namely: (1) *Earthquake and early warning algorithms: state of the art and recent developments*; (2) *Tailor-made early warning for varying targets and socio economic context*; (3) *Multi-risk methodologies for early warning and rapid response*; and (4) *Real-time risk assessment and structural monitoring*. The programme comprised five keynote lectures by invited speakers aimed at giving a leading-edge, state-of-the-art overview on the topics. Strong emphasis was also put on discussion and exchange of ideas among participants. For this reason, the presentations were accompanied by poster sessions (all posters were hanging for the entire workshop duration) and debates on "hot" subjects such as the cost/benefit analysis for early warning systems and the usage and communication to end users of uncertainties, both from the researchers' and implementing engineers' perspectives. The final scientific programme was composed of five keynote lectures, twenty-one oral and twenty-three poster presentations.

This report attempts to summarize the main outcomes of the workshop providing first an overview of the workshop themes and then describing the range of opinions expressed during the discussion.

Background

In recent years, significant advances have been made in the development of earthquake early warning systems in various earthquake-prone regions around the world. In simple terms, these systems take advantage of the fact that information about the onset of a potentially damaging earthquake can be processed and transmitted faster via modern communication tools than the seismic waves, allowing to issue warnings on the order of seconds up to minutes in some cases before the damaging waves reach the target of interest to be protected. While some of these systems are at a very mature state, in particular in regions where excellent infrastructure is available (e.g., California, Japan), this is not the case in many economically developing countries. Some of these countries face an extraordinary level of seismic risk, yet large-scale seismic networks cannot be funded, and the principles used in such elaborate systems are not simply transportable to these situations. Significant research efforts are still underway to develop optimal systems for such cases, allowing for the extraction of a maximum of information from a minimum number of recordings.

Earthquake early warning does however not stop with the estimation of the ground shaking that the target may expect in the seconds/minutes to come. In many regions, the situation is highly complicated by the potential generation of earthquake-induced effects, such as tsunamis, gravitational mass movements (e.g., rockfall, landslides, avalanches) and liquefaction. The 2011 Tohoku earthquake and tsunami disaster in Japan is a tragic example of the importance to integrate early warning and risk mitigation procedures for ground shaking and these associated risks. In this endeavor, it is crucial to take into account the specific requirements of the end users in order to make early warning useful for society. For example, critical facilities such as nuclear power plants, large dams, chemical factories, public transportation systems etc. present highly specific requirements to early warning system design.

These non-trivial tasks require intense collaboration between scientists and engineers for designing the decision-making systems as well as their implementation. However, the interaction between these groups is not always easy, since the viewpoints on the problems encountered often differ significantly. In order to advance in the field, agreements need to be found between scientific investigation and engineering implementation, and the workshop was organized to provide a platform for exchange of ideas between the various communities involved in research and implementation. It aimed at contributing to improve the mutual understanding of the requirements and specifications that the different communities are subject to, consolidate conflicting views and foster the collaboration at the interface of fundamental research and engineering implementation.

Earthquake early warning algorithms: state-of-the-art and recent developments

During this session the most advanced solutions for earthquake early warning algorithms in the context of three design goals - maximum speed, maximum accuracy,

and maximum reliability - have been presented. In particular, the possibility of a rapid detection of the fault generating the earthquake and finite-source characterization was illustrated both using strong motion and GPS networks, as well as seismic arrays. The importance of the rapid detection of the source parameters for regional early warning systems was demonstrated, as well as the improvements in the capability in forecasting the ground motion at several sites by combining empirical data and numerical simulations. An overview of the performance of different software packages for regional early warning, and in particular the lessons learned from the eight years of operation of the early warning system run by the Japan Meteorological Agency (JMA), provided quantitative information about the effectiveness of EW systems, and their acceptance in the population.

Tailor made early warning for varying targets and socio-economic context

This session mainly focused on the development of early warning systems in developing countries, where both methodological and technical solutions have to be adapted to the lack in expertise and resources. The development of low-cost sensors, accompanied by innovative approaches for decentralized onsite as well as for risk-based early warning systems, and the particular interest of these approaches for local governmental agencies and civil protections were shown. Of crucial relevance to the discussion was the presentation on the cost-effectiveness of early warning system based on the example of a pubic early warning system in California, touching upon an often mentioned but largely unexplored issue.

Multi-risk methodologies for early warning and rapid response

During this session, innovative approaches for multi hazard early warning systems (including earthquake-induced phenomena) have been presented. The possibility of providing information on loss distribution in real time both at regional and local scale was illustrated. In particular, advanced procedures for integrating secondary earthquake hazard effects in already existing and robust methodologies developed for earthquakes only have been presented.

Real time risk assessment and structural monitoring

This session focused on the most advanced techniques for real-time assessment of risk in developing and developed countries. The necessity to develop and apply different approaches in these cases was highlighted. Of major relevance was the on-going attempt to move towards the application of performance-based earthquake engineering before, during and after a mainshock, therefore trying to satisfy one of the most crucial requests of public and private end-users, i.e. to carry out both monitoring and forecasting operations with a single tool. The potential of integrating semi-active structural control measures in real-time early warning systems was also illustrated (yet the convenience of such a strategy with respect to traditional passive control strategies still needs to be demonstrated), together with the possibility of using low-cost systems both to perform fully decentralized early warning operations as well as geotechnical and structural real-time building monitoring.

Main suggestions and highlights from the meeting

Based on the presentations at the meeting, the participants came to the following key conclusions and recommendations:

- The development of loss-based early warning systems for multi hazard applications represents a key element in future disaster risk reduction strategies.
- The detection and assessment of aftershocks following major earthquakes and in particular their effects is a major challenge for early warning and rapid response systems. The inclusion of these effects is however of key importance in order to exploit these systems.
- There is a continued need for basic research on earthquake ground motion generation, in particular regarding earthquake source characteristics, in order to ensure the robustness of current and future earthquake early warning algorithms and implementations.
- There is a need for improved communication of the uncertainties associated to rapid estimates of primary and secondary hazards, along with probabilities of occurrence of the expected shaking levels of induced phenomena. This is a critical for a completely informed input to decision making.
- There is a need to enhance the involvement of end-users of early warning systems in the development and testing of EEW methods and dissemination tools. The seismological community seems still much focused on hazard estimates, while public and private end-users would typically make decisions based on risk considerations.

A final important component of the workshop consisted in the support of young scientists (PhD students / post-docs) in order to give them the unique opportunity to meet and discuss with the key experts in the field in a quite familiar atmosphere and present their work outside the rush of big conferences. For that purpose, young scientists could apply for a set of travel grants covering travel and accommodation costs as well as the registration fees. Based on the evaluation of the scientific committee and the budgetary constraints, it was possible to fund as many as ten applications, ensuring that the young generation could actively participate in the workshop.

List of Travel Grantees

Marta Carranza	Universidad Complutense de Madrid, Spain
Simona Colombelli	University of Naples, Italy
Angga Vertika Diansari	Indonesian Agency of Meterology, Climatology and Geophysics, Indonesia
Admiral Musa Julius	Indonesian State College of Meterology, Climatology and Geophysics, Indonesia
Itzhak Lior	Tel Aviv University, Israel
Kyosuge Okamoto	Railway Technical Research Institute, Japan
Bojana Petrovic	GFZ German Research Centre for Geosciences, Germany
Mohammad Shavar	IIEES, Iran
Omar Ortiz Velazquez	University College of London, UK
Lucy Yin	California Institute of Technology, USA

ECGS & ESC/EAEE Joint Workshop 2015

EARTHQUAKE AND INDUCED MULTI-RISK EARLY WARNING AND RAPID RESPONSE

Scientific Program

TUESDAY NOVEMBER 17

16:00 – 18:00 Registration
18:00 – 21:00 Icebreaker

WEDNESDAY NOVEMBER 18

08:00 – 09:00 Registration

09:00 – 09:20 Welcome addresses

Morning session 1: Earthquake early warning algorithms: state-of-the-art & recent developments

09:20 – 10:00 Böse, M., Y. Behr, T. Heaton and J. Clinton **(Keynote)**

From Single-Station Prediction to Finite-Fault Detection: the Large Spectrum of EEW Algorithms and the Question of How to Combine Them

10:00 – 10:20 Picozzi, M., P. Brondi, A. Emolo, A. Zollo and M. Mucciarelli

An Attempt of Predicting the Macroseismic Intensity from Early Radiated Energy for On-site Earthquake Early Warning in Italy

10:20 – 10:40 Kodera, Y., Y. Yamada, S. Adachi, M. Morimoto, Y. Nishimae and M. Hoshiba

The Eight Years of Earthquake Early Warning Operation in the Japan Meteorological Agency

10:40 – 11:00 Coffee break

Morning session 2: Earthquake early warning algorithms: state-of-the-art & recent developments

11:00 – 11:20 Yin, L. and T. Heaton

Improvements of Earthquake Early Warning Using Prior Information

11:20 – 11:40 Noda, S., S. Yamamoto and W.L. Ellsworth **[cancelled]**

Rapid Estimation of Earthquake Magnitude from the Arrival Time of the Peak High-Frequency Amplitude

11:40 – 12:00 Okamoto, K., S. Tsuno and S. Yamamoto **[cancelled]**

Robust Epicenter Estimation Considering Local Heterogeneous Conditions for Single Station Method

12:00 – 14:00 Lunch

Afternoon session: Earthquake early warning algorithms: state-of-the-art & recent developments

14:00 – 14:20 Eisermann, A., A. Ziv and G.H. Wust-Bloch

Real-Time Back Azimuth for Earthquake Early Warning

14:20 – 14:40 Lior, I., A. Ziv and R. Madariaga

P-wave Attenuation with Implications for Earthquake Early Warning

14:40 – 15:00 Trampert, J., P. Kaeufl and A. Valentine **[cancelled]**

Rapid Probabilistic Source Inversion using Pattern Recognition

15:00 – 15:20 Colombelli, S., A. Zollo, G. Festa and M. Picozzi

A P-wave Based Methodology for the Rapid Source Characterization

Wednesday Poster Session

15:20 – 16:00 Poster introductions (1 slide / 1 min per poster)

16:00 – 17:00 Poster session and coffee

Debate

17:00 – 18:00 **How can we better prove the efficiency of currently implemented/planned EEW systems before the occurrence of the "big one" that they have to be designed for?**

THURSDAY NOVEMBER 19

Morning session 1: Earthquake early warning algorithms: state-of-the-art & recent developments

08:00 – 08:40 Hoshiba, M. **(Keynote)**

Numerical Shake Prediction for Earthquake Early Warning: Data Assimilation, Real-time Shake Mapping, and Simulation of Wave Propagation

08:40 – 09:00 A. Sato & K. Yomogida

Quick Estimation of Wavefield by a Neumann-type Extrapolation for a New Earthquake Early Warning System

09:00 – 09:20 Zollo, A., M. Picozzi, A. Emolo, S. Colombelli, L. Elia, G. Festa and C. Martino

Worldwide Applications Of Presto - Probabilistic And Evolutionary Early Warning System

09:20 – 09:40 Ziv, A.

Real-time Stress Drop Determination for Earthquake Early Warning

09:40 – 10:00 Carranza, M., E. Buforn, S. Colombelli, Y.-M. Wu and A. Zollo

Towards the Confirmation of the Differences on the Rupture Initiation of Earthquakes from the First Seconds of P-wave

10:00 – 10:10 Welcome address of Dr. Helena Burg, representative of the Luxembourg National Research Fund (FNR)

Thursday Poster Session 1

10:10 – 11:00 Poster session and coffee break

Morning session 2: Tailor-made early warning for varying targets and socio-economic contexts

11:00 – 11:20 Parolai, S., D. Bindi, M. Pittore, J. Stankiewicz, M. Pilz, A. Oth, T. Boxberger and K. Fleming **(Keynote)**

The Challenge of Earthquake Early Warning and Rapid Response in Developing Countries: the Example of the Kyrgyz Republic (Central Asia)

11:20 – 11:40 Stankiewicz, J., D. Bindi, A. Oth, M. Pittore and S. Parolai

The Use of Spectral Content to Improve Earthquake Early Warning Systems in Central Asia: Case Study of Bishkek, Kyrgyzstan

11:40 – 12:00 Woo, G.

The Cost-Effectiveness of a Public Californian Earthquake Early Warning System

12:00 – 12:20 Wust-Bloch, G.H., A. Ziv, A. Eisermann, J. Al-Dabbeek and A. Al-Zoubi

DeadSeaNet: Cross-border Array of Small-Aperture Arrays for EEWS

12:20 – 14:00 Lunch

Afternoon session: Multi-risk methodologies for early warning and rapid response

14:00 – 14:20 Cauzzi, C., J. Clinton, D. Fäh, P. Kästli, S. Wiemer, D.J. Wald, M. Hearne, C.B. Worden and E.M. Thompson

Secondary Earthquake Hazards in Swiss ShakeMaps

14:20 – 14:40 Goda, K.

Tsunami Warning and Hazard Prediction based on Inaccurate Earthquake Source Parameters

14:40 – 15:00 Ilhan, O., H. Khanbabazadeh, G. Tönük and A. Ansal

Early Warning for Rainfall Induced Landslides

15:00 – 15:20 Pilz, M., S. Parolai and T. Boxberger

A Multi-Parameter System for Real-time Monitoring of Landslide Activity

Thursday Poster Session 2

15:20 – 17:00 Poster session and coffee break

17:30 **Social program & conference dinner**

FRIDAY NOVEMBER 20

Morning session 1: Real-time risk assessment and structural monitoring

08:00 – 08:40 Wenzel, F. and J. Daniell **(Keynote) [cancelled]**

Earthquake Early Warning and Real-time Risk Reduction

08:40 – 09:20 Heaton, T. **(Keynote)**

Miscommunicating Predicted Shaking Intensity

09:20 – 09:40 Pittore, M., D. Bindi, J. Stankiewicz, A. Oth, M. Wieland, T. Boxberger and S. Parolai

From Early Warning to Rapid Response: Towards Efficient Earthquake Impact Forecasting

09:40 – 10:00 Shavar, M., G. Cua, M. Zare, E. Farzanegan and M. Mirzaei

Developing Of ShakeMap System for Iran Based On Strong Motion Data

10:00 – 10:20 Coffee break

Debate

10:20 – 11:00 **On the engineering use of real-time EEW methods & the associated uncertainties**

Morning session 2: Real-time risk assessment and structural monitoring

11:00 – 11:40 Iervolino, I. **(Keynote)**

Applying Performance-Based Earthquake Engineering before, during, and after a Mainshock

11:40 – 12:00 Velazquez Ortiz, O., P. Duffour and C. Galasso

Integrating Semi-active Structural Control and Earthquake Early Warning: Preliminary Results

12:00 – 12:20 Petrovic, B., S. Parolai, Ü. Dikmen, E. Şafak and B. Moldobekov

Interferometric Joint Analysis of Borehole and Building data

12:20 – 13:00 End of oral sessions / Closing remarks & discussion

13:00 – 14:00 Lunch

14:00 – Departure of participants

POSTERS

Earthquake early warning algorithms: state-of-the-art & recent developments

1. Zollo, A., M. Picozzi, S. Colombelli, L. Elia, A. Caruso and P. Brondi

   PRESTo On-Site 1.0: Concepts and Preliminary Analyses

2. Picozzi, M., A: Emolo, C. Martino, A. Zollo, S. Colombelli and the REAKT Working Group

   PRESTo^{Plus} and Sentinel an Earthquake Early Warning System for Schools: a Feasibility Study in Southern Italy

3. Caruso, A., S. Colombelli, A. Zollo, G. Festa and H. Kanamori

   A P-wave based, On-site Method for Earthquake Early Warning

4. Kuyuk, H.S., A. Pinar, R.M. Allen and M.O. Erdik

   Authorizing GRound shaking for Earthquake Early warning Systems, (AGREEs): Application to 2014 South Napa Earthquake

5. Hayashimoto, N., T. Nakamura and M. Hoshiba

   Stability of Ocean Bottom Seismograph Data Exposed to Strong Shaking: Efforts for Utilizing OBS for Earthquake Early Warning

6. Ogiso, M., N. Hayashimoto and M. Hoshiba

   Array Observation of Strong Motion for a Real-time Estimation of Current Wavefield

7. Montagner, J.-P., M. Barsuglia, K. Juhel, J.-P. Ampuero, E. Chassande-Mottin, J. Harms, B. Whiting, P. Bernard, E Clévédé and P. Lognonné

   Prompt Earthquake Detection based on Transient Gravity Signals

8. Moser, H.A. and G. Ruy

   Microsatellites to Support the Study of Potential Diagnostic Earthquake Precursors

9. Diansari, A.

   Acceleration of Release Energy (Accelerating Moment Release) of Earthquake Occurred as a Precursor in Bengkulu

Tailor-made early warning for varying targets and socio-economic contexts

10. Pinar, A., H.S. Kuyuk, M. Çomoğlu, M. Erdik and E. Şafak

    A Test Bed for Earthquake Early Warning Algorithms in Istanbul: The Virtual Seismologist, PRESTo and ElarmS-2

11. Pazos, A., M. López de Mesa, J. Gallego, C. Rioja, J.M. Davila, A. Morgado, W. Hanka, J. Saul, A. Strollo, A. Vera, A. Cibeira, R. Cabieces and ROA Seismic Group

    A Prototype of an EEWS for South Iberia: ALERT-SC3

12. Marumureanu, A., C. Ionescu, M. Craiu, L. Elia, S. Colombelli and A. Zollo

    Earthquake Early Warning in Romania – Recent Improvements

13. Savvaidis, A., K. Konstantinidou, B. Margaris, Ch. Papaioannou, N. Theodoulidis, P. Triantafyllidis and D. Kementzetzidou **[cancelled]**

    Real Time Shakemap Implementation using Strong Motion Data for the Broader Area of the Aegean Sea

14. Shahvar, M. and M. Poorveis

    Design of Early Warning System for Tehran Region

15. Ortega, R.

    The Future of Earthquake Early Warnings in Mexico: Towards an Integrated Seismological System in Real Time

16. Pittore, M., M. Wieland, M. Haas and S. Parolai

    CARAVAN: Near-real-time Earthquake Impact Forecasting for Central Asia

17. Jeon, Y., E.Y. Jo, D.K. Lee, S.M. Han and H.S. Lee

    The Application of EPGen System for Earthquake Early Warning in Korean Peninsula

Multi-risk methodologies for early warning and rapid response

18. Mendoza, L., A. Pazos and M. Becker

    GPS Capabilities for Tsunami Early-Warning: Expected Vertical Load in Coastal GPS receivers due to a Tsunami like the 1775 Lisbon Tsunami

19. Elia, G., C. Galasso, S. Latchman, S. Naqvi, P. Padmanabhan and A. Tsioulou

    Identifying Regions with High Liquefaction Potential Close to Large Populations in Europe

20. Picozzi, M., A. Manconi, V. Coviello and F. De Santis

    Landslide Induced Seismicity: Near real-time Detection and Characterization Using Regional Seismic Networks

21. Melbouci, B.

    Dynamic Behavior Analysis of Tigzirt Landslide

Real-time risk assessment and structural monitoring

22. T. Boxberger, D. Bindi, I. Iervolino, M. Pittore, E. Chioccarelli and S. Parolai

Applications of Wireless Sensing Units to Seismic Risk Assessment: Perspectives from the REAKT and SIBYL Projects

23. Diagourtas, D., L. Voumvourakis, L. Perlepes and A. Kostarids

Gsense: A Low Cost Real-Time Building Earthquake Damage Assessment System

24. Zembaty, Z., S. Kokot and P. Bobra

Investigations of the Application of Modern Rotation Rate Sensors in On-line Monitoring of Stiffness Variations of Structures

25. Musa Julius, A., B. Sunardi and A. Rudyanto

Time Lapse Storey Building Monitoring Based on Earthquake Response and Tremor Analysis

List of Participants

ANSAL Atilla
Ozyegin University
Civil Engineering
Nisantepe Mah. Orman Sk. No 34-36
Alemdag Cekmeköy
Istanbul 34794
Turkey
atilla.ansal@ozyegin.edu.tr

BARRIERE Julien
ECGS / MNHN
European Center for Geodynamics and Seismology
National Museum of Natural History
19, rue Josy Welter
Walferdange 7256
Luxembourg
julien.barriere@ecgs.lu

BINDI Dino
GFZ German Research Centre for Geosciences
Section 2.6, Seismic Hazard and Stress Field
Helmhotzstrasse 7
Potsdam 14467
Germany
bindi@gfz-potsdam.de

BIRO Talhan
GeoSIG Ltd
Sales
Wiesenstrasse 39
Schlieren 8952
Switzerland
tbiro@geosig.com

BONATZ Manfred
Member of ECGS Administrative Board
GeoObservatorium Odendorf
Wilkenstrasse 49
Swisttal 53913
Germany
geo.bonatz@t-online.de

BÖSE Maren
ETH Zürich
SED (Swiss Seismological Service)
Sonneggstr. 5
Zürich 8092
Switzerland
maren.boese@erdw.ethz.ch

BUFORN Elisa
Universitad Complutense de Madrid
Geophysics and Meteorology
Faculty of Physics
Madrid 28040
Spain
ebufornp@ucm.es

BURG Helena
Fonds National de la Recherche Luxembourg
Maison du Savoir
2, rue de l'Université
Esch-sur-Alzette 4365
Luxembourg
helena.burg@fnr.lu

BUTTINI Eric
Secretary of ECGS Administrative Board
European Center for Geodynamics and Seismology
National Museum of Natural History
25, rue Münster
Luxembourg 2160
Luxembourg
eric.buttini@ecgs.lu

CARRANZA Marta
Complutense University of Madrid
Geophysics and Meteorology
Calle Carracedo 27
3rd Door
Madrid 28024
Spain
macarran@ucm.es

CAUZZI Carlo
ETH Zürich
SED (Swiss Seismological Service)
Sonneggstr. 5
Zürich 8092
Switzerland
carlo.cauzzi@sed.ethz.ch

CELLI Gilles
ECGS / MNHN
European Center for Geodynamics and Seismology
National Museum of Natural History
19, rue Josy Welter
Walferdange 7256
Luxembourg
gilles.celli@ecgs.lu

COCCIA Stella
INERIS France
Ecole des Mines
Campus Artem
Nancy Cedex 54042
France
stella.coccia@ineris.fr

COLOMBELLI Simona
University of Naples Federico II
Department of Physics
Complesso Universitario Monte S. Angelo
Via Cinthia
Naples 80126
Italy
simona.colombelli@unina.it

d'OREYE Nicolas
ECGS / MNHN
European Center for Geodynamics and Seismology
National Museum of Natural History
19, rue Josy Welter
Walferdange 7256
Luxembourg
ndo@ecgs.lu

DIAGOURTAS Dimitris
SATWAYS, Ltd
Research & Development
3 Christou Lada Str.
Halandri - Attika 15233
Greece
d.diagourtas@satways.net

DIANSARI Angga Vertika
Indonesian Agency of Meteorology
Climatology and Geophysics
Jalan Pembangunan 156
Pasar-Ujung
Kepahinag Bengkulu 39172
Indonesia
anggav.bmkg@gmail.com

EISERMANN Andreas
Tel Aviv University
Earth Sciences
P.O. Box 39040
Tel Aviv 69978
Israel
eisermann@tau.ac.il

FABER Alain
Member of ECGS Administrative Board
National Museum of Natural History
25, rue Münster
Luxembourg 2160
Luxembourg
alain.faber@mnhn.lu

GALASSI Corine
ECGS
European Center for Geodynamics and Seismology
19, rue Josy Welter
Walferdange 7256
Luxembourg
corine.galassi@ecgs.lu

GEIRSSON Halldor
ECGS
European Center for Geodynamics and Seismology
19, rue Josy Welter
Walferdange 7256
Luxembourg
halldor.geirsson@ecgsl.lu

GODA Katsu
University of Bristol
Department of Civil Engineering
Queen's Building
University Walk
Bristol BS8 1TR
United Kingdom
katsu.goda@bristol.ac.uk

GOERENS Jean-Mathias
Member of ECGS Administrative Board
15, rue Raoul Follereau
Luxembourg 1529
Luxembourg
jmg@pt.lu

HAYASHIMOTO Naoki
JMA - Japan Meteorological Agency
Seismology and Tsunami Research Department
Nagamine 1-1
Tsukuba-city / Ibaraki 305-0052
Japan
hayashim@mri-jma.go.jp

HEATON Thomas
California Institute of Technology
Civil Engineering
MC104-44
1200 E California Blvd
Pasadena CA 91125
USA
heaton@caltech.edu

HICKS Stephen
Guralp Systems Limited
Midas House, Calleva Park
Aldermaston
Reading RG7 8EA
United Kingdom
shicks@guralp.com

HOSHIBA Mitsyuki
JMA - Japan Meteorological Agency
Seismology and Tsunami Research Department
Nagmine 1-1
Tsukuba-city / Ibaraki 305-0052
Japan
mhoshiba@mri-jma.go.jp

IERVOLINO Iunio
University of Naples Federico II
Dipartimento di Strutture per l'Ingegneria e l'Architettura
Via Claudio 21
Naples 80125
Italy
iunio.iervolino@unina.it

JEON Young Soo
Korea Meteorological Administration
National Institution of Meteorological Research
Global Environment System Research Division
33, Seohobuk-ro
Seogwipo-wi
Jeju-do 63568
Republic of Korea
ysjeon@korea.kr

JUHEL Kévin
Institut de Physique du Globe de Paris (IPGP)
Seismology
1, rue Jussieu
Paris 75005
Paris
juhel@ipgp.fr

JULIUS Admiral Musa
Indonesia State College of Meteorology
Climatology and Geophysics
Perhubungan 1 No 5
Pondok Betung - Pondok Aren
Tangerang Selatan. 15221
Indonesia
admiralmusajulius@yahoo.com

KODERA Yuki
JMA - Japan Meteorological Agency
Seismology and Volcanology Department
1-3-4 Otemachi
Chiyoda-ku
Tokyo 100-8122
Japan
y_kodera@met.kishou.go.jp

KUYUK Huseyin Serdar
Bogaziçi University
Kandilli Observatory and
Earthquake Engineering Institute
Cengelköy
Istanbul 34684
Turkey
serdarkuyuk@gmail.com

LIOR Itzhak
Tel Aviv University
Geosciences
P.O. Box 39040
Tel Aviv 69978
Israel
itzhaklior22@gmail.com

MARMUREANU Alexandru
National Institute for Earth Physics
Seismic Network
Calugareni 12
Magurele
Ilfov 077125
Romania
marmura@infp.ro

MELBOUCI Bachir
Mouloud Mammeri University of Tizi-Ouzou
Civil Engineering
B.P. no 17 R.P.
Tizi-Ouzou 15000
Algeria
melbouciba@hotmail.fr

MOSER Hubert Anton
LuxSpace
Mecanics and Propulsion
9, Rue Pierre Werner
Betzdorf 6832
Luxembourg
moser@luxspace.lu

NODA Shunta
Railway Technical Research Institute
U.S. Geological Survey
345 Middlefield Rd
MS - 977
Menlo Park CA 94025
USA
snoda@usgs.gov

OGISO Masashi
JMA - Japan Meteorological Agency
Seismology and Tsunami Research Department
Nagamine 1-1
Tsukuba-city / Ibaraki 305-0052
Japan
mogiso@mri-jma.go.jp

ONCESCU Lani
KINEMETRICS, Inc.
Open Systems and Services
222 Vista Ave
Pasadena CA 91107
USA
lani@kmi.com

ORTEGA Roberto
Centro de Investigaciòn Cientifica
y de Educacion Superior de Esenada
Miraflores 334
La Paz 23054
Mexico
ortega@cicese.mx

PAROLAI Stefano
GFZ German Research Centre for Geosciences
Section 7.1, Centre for Early Warning Systems
Telegrafenberg
Potsdam 14473
Germany
parolai@gfz-potsdam.de

PETROVIC Bojana
GFZ German Research Centre for Geosciences
Section 7.1, Centre for Early Warning Systems
Helmhotzstrasse 7
Potsdam 14467
Germany
petrovic@gfz-potsdam.de

PILZ Marco
ETH Zürich
SED (Swiss Seismological Service)
Sonneggstr. 5
Zürich 8092
Switzerland
pilz@gfz-potsdam.de

PITTORE Massimilliano
GFZ German Research Centre for Geosciences
Section 7.1, Centre for Early Warning Systems
Helmhotzstrasse 7
Potsdam 14467
Germany
pittore@gfz-potsdam.de

REISCH Bernard
Member of ECGS Administrative Board
Administration du Cadastre et de la Topographie
54, av. Gaston Diderich
Luxembourg 1420
Luxembourg
bernard.reisch@act.etat.lu

SMETS Benoît
ECGS
European Center for Geodynamics and Seismology
19, rue Josy Welter
Walferdange 7256
Luxembourg
benoit.smets@ecgs.lu

OTH Adrien
ECGS
European Center for Geodynamics and Seismology
19, rue Josy Welter
Walferdange 7256
Luxembourg
adrien.oth@ecgs.lu

PAZOS Antonio
Real Observatorio de la Armada
Geophysics
Plaza Las Marinas S/N
San Fernando - Cadiz 11100
Spain
pazos@roa.es

PICOZZI Matteo
University of Naples Federico II
Department of Physics
Complesso Universitario Monte S. Angelo
Via Cinthia
Naples 80126
Italy
matteo.picozzi@unina.it

PINAR Ali
Bogaziçi University
Kandilli Observatory and
Earthquake Research Institute
Cengelköy
Istanbul 34684
Turkey
pinara@boun.edu.tr

POURMOHAMMAD SHAHVAR M.
Road, Housing & Urban Development
Research Centre
Iran Strong Motion Network
Marvi Street, Farhangian phase 2
Sheikh Fazlollah Noori Highway
Tehran
Iran
mshahvar@gmail.com

SAVVAIDIS Alexandros
Institute of Engineering Seismology
and Earthquake Engineering
EPPO-ITSAK
P.O. Box 53
Finikas - Thessaloniki 55102
Greece
alexandros@itsak.gr

SPRIGGS Neil
Nanometrics
Co-CEO Global Operations
250 Herzberg Rd
Kanata
Ontario K2K 2A1
Canada
dianamartinez@nanometrics.ca

STANKIEWICZ Jacek
ECGS
European Center for Geodynamics and Seismology
19, rue Josy Welter
Walferdange 7256
Luxembourg
jacek@ecgs.lu

VELAZQUEZ Omar
University College London
Insititute for Risk and Disaster Reduction
Gower Street
London WCE1 6BT
United Kingdom
omar.ortiz.12@ucl.ac.uk

VOUMVOURAKIS Leuteris
SATWAYS, Ltd
Research & Development
3 Christou Lada Str.
Halandri - Attika 15233
Greece
l.voumvourakis@satways.net

WAGNER J. Frank
Member of ECGS Administrative Board
Trier University
Department of Geology
Behringstrasse
Campus II
Trier 54296
Germany
wagnerf@uni-trier.de

WOO Gordon
RMS - Risk Management Solutions, Inc
Peninsular House
30 Monument Street
London EC3R 8NB
United Kingdom
Gordon.Woo@rms.com

WUST-BLOCH Hillel
Tel Aviv University
Earth Sciences
P.O. Box 39040
Tel Aviv 69978
Israel
hillelw@tau.ac.il

ZEMBATY Zbigniew
Opole University of Technology
Faculty of Civil Engineering
Ul. Proszkowska 76
Opole 45-758
Poland
z.zembaty@po.opole.pl

ZIV Alon
Tel Aviv University
Geosciences
P.O. Box 39040
Tel Aviv 69978
Israel
zivalon@tau.ac.il

ZOLLO Aldo
University of Naples Federico II
Department of Physics
Complesso Universitario Monte S. Angelo
Via Cinthia
Naples 80126
Italy
aldo.zollo@unina.it

ARTICLES

From Single-Station Prediction To Finite-Fault Detection: The Large Spectrum of EEW Algorithms and The Question of How to Combine Them

Maren Böse[1], Yannik Behr[1], John Clinton[1], Thomas H. Heaton[2]

[1] ETH Zurich, Sonneggstrasse 5, 8092 Zurich, Switzerland, mboese@sed.ethz.ch
[2] Caltech, 1200 E. California Blvd., 91125 Pasadena, USA

Abstract

Earthquake early warning (EEW) systems shall fulfill three requirements: (1) maximum speed, (2) maximum accuracy, and (3) maximum reliability. These three design goals are interconnected through a trade-off between speed and accuracy, and the need to quantify respective uncertainties (i.e. reliability) in each single alert message. While maximum speed is most critical for EEW in small to moderate earthquakes (M<6.5), in which damaging shaking is restricted to areas close to the earthquake epicenter, reaching high accuracy in source and ground-motion estimates is most challenging in large earthquakes (M>6.5) due to magnitude saturation and finite-fault effects. The third objective, maximum reliability, which encompasses both high detection success and low false alert rates, is critical to EEW in earthquakes of all magnitudes. Building EEW systems, that combine various algorithms and that utilize both seismic and geodetic real-time data, are likely the best strategy to facilitate EEW for the entire range of earthquake magnitudes, including both small point- and large finite-source ruptures. Combined systems require consistent models, robust platforms, and central mediators. Building such combined systems will be one of the most challenging and important tasks for EEW research in upcoming years.

Introduction

Earthquake early warning (EEW) needs fast event detections and accurate shaking forecasts. In this paper we discuss the main challenges and possible solutions in the context of the three main design goals of EEW systems: (1) maximum speed, (2) maximum accuracy, and (3) maximum reliability (Figure 1).

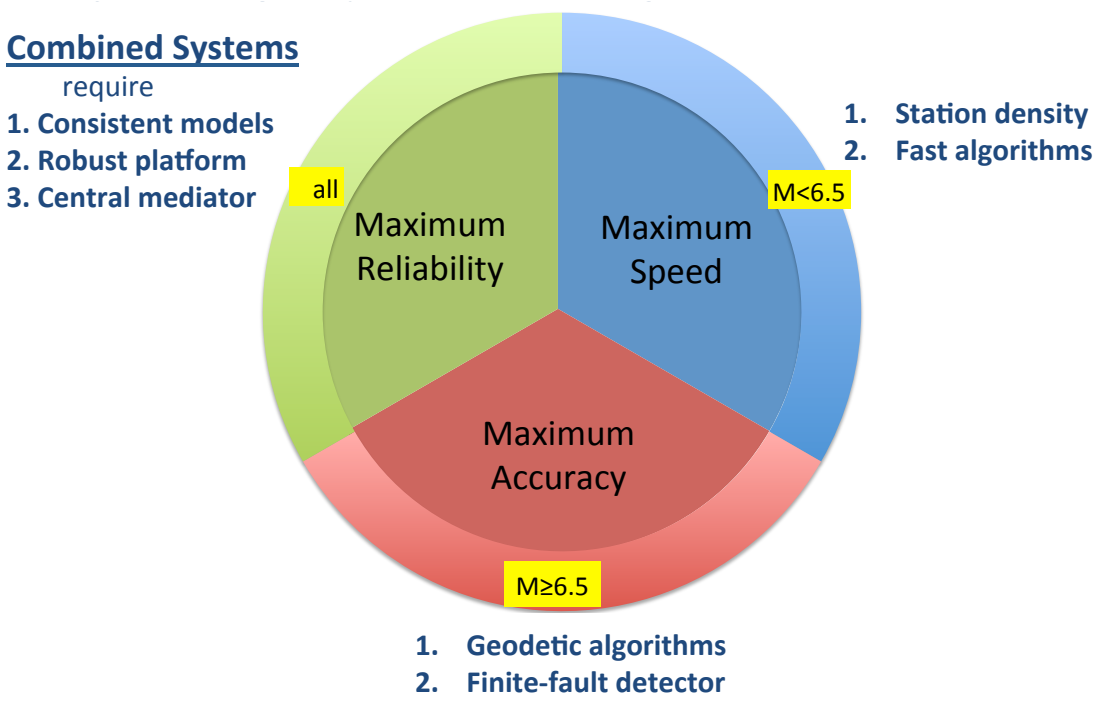

Figure 1. Earthquake early warning: objectives, challenges and solutions.

1. Maximum Speed

Strongest shaking in shallow crustal earthquakes typically occurs in areas close to the epicenter. The spatial extent of this zone can be estimated from empirical ground-motion prediction equations (GMPEs): for instance in magnitude M6 and M7 earthquakes, moderate to strong shaking with shaking intensities (MMI) of 5 and larger, generally occurs within epicentral distances of 20 km and 80 km, respectively. Assuming that strongest shaking initiates with the arrival of the S-wave (which propagates at a speed of ~3.6 km/s), and neglecting shaking complexities arising from rupture or site amplifications, a "useful" warning (with a sufficient lead time to act upon) needs to be issued within less than 7 seconds for M6 events, respective less than 22 seconds for M7 events (Figure 2).

The majority of presently operational and EEW demonstration systems are unable to provide timely warnings for events smaller than M6, and warnings for M6 to M6.5 events have very short lead times (e.g. Heaton, 1985). Fastest alerts in the Californian ShakeAlert Demonstration system (www.shakealert.org; Böse *et al.*, 2013a), for instance, are given within 4-5 seconds from event origin (e.g. 2014 M5.1 LaHabra: 4 seconds; 2014 M6.0 South Napa: 5.1 seconds). While fast alerts are of course important for earthquakes of all sizes, it appears to be the most critical design parameter for EEW systems targeting moderate-sized earthquakes in which damage areas are small and mostly close to the epicenter.

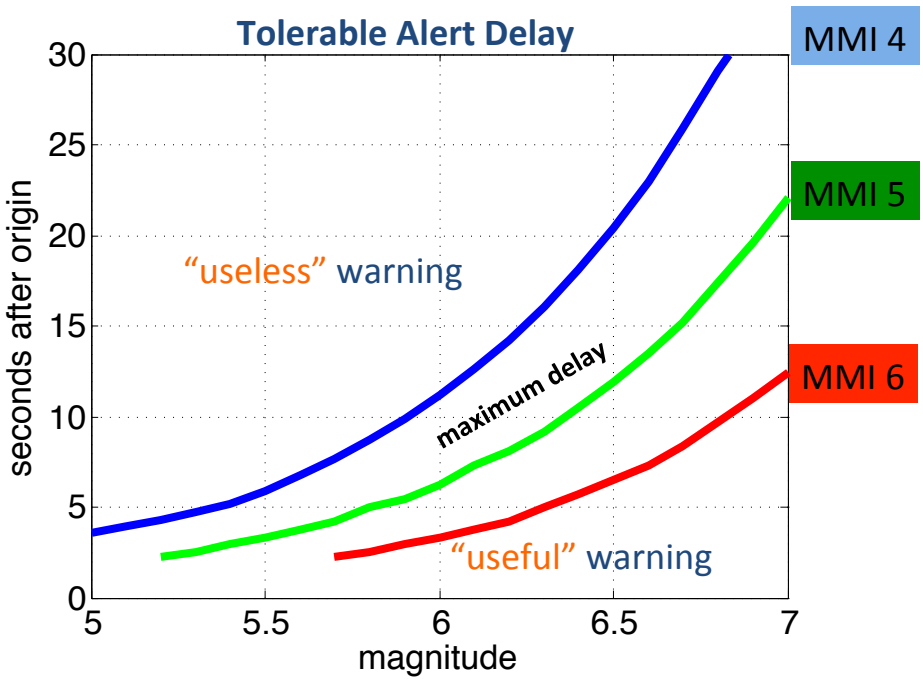

Figure 2. Maximum tolerable alert delay in EEW as a function of magnitude and seismic intensity (MMI): for MMI≥4 (light shaking), an alert needs to be issued within less than 11 seconds for M6; for MMI≥6 (strong shaking), the alert needs to be declared within less than 3 seconds for M6 and less than 12 seconds for M7. Tolerable delays are determined from GMPEs (here: Cua and Heaton, 2009) and peak value-to-MMI conversions after Worden et al., (2012) under the assumption that strongest shaking initiates with the arrival of the S-wave, which propagates at a speed of ~3.6 km/s.

Delays in EEW systems are caused by (1) the time required by the P-wave to reach the closest sensor, (2) datalogger and communication latencies, (3) and algorithm and processing delays (e.g. Behr *et al.*, 2015). EEW systems can become faster either by increasing sensor density and/or by usage of faster EEW algorithms. The so-called *no-warning-zone* of EEW systems, in which warnings arrive too late to be useful, generally decreases exponentially with increasing sensor density, because earthquakes can be more rapidly detected. Interestingly, there seems to be only little additional benefit (in terms of speed) when decreasing interstation spacing beyond 5 km, because other effects, such as processing delays, are becoming dominant (Kuyuk and Allen, 2013).

Still building a network of expensive high-quality sensors of even 10 to 20 km spacing only, is clearly unaffordable for most countries in the world. Various research groups have started to explore the feasibility of supplementing existing high-quality seismic networks with low-cost sensors, such as micro-electro-mechanical system (MEMS) accelerometers. Despite of their lower performance, these sensors are expected to produce information suitable for ShakeMaps, seismological research, and earthquake engineering (Evans *et al.*, 2014), mainly because they can be deployed in spatially much denser networks compared to expensive scientific instruments. Sensors with 70 mgal sensitivity at 1 Hz are available for ~US$100 only (Clayton *et al.*, 2011). Dedicated low-cost sensor networks for seismic real-time monitoring and EEW have been developed and tested, among others, in Japan (Home-seismometer,

Horiuchi *et al.*, 2009), Turkey (SOSEWIN, Fleming *et al*., 2009; Picozzi *et al.*, 2010), and Taiwan (Wu *et al.*, 2013). Other low-cost sensor networks harness the data from privately-owned accelerometers and/or infrastructure, including crowdsourcing projects like the Quake Catcher Network (QCN; Cochran *et al.*, 2009) or the Community Seismic Network (CSN; Clayton *et al.*, 2011). Other groups are currently exploring the use of accelerometers (Faulkner *et al.*, 2011; Finazzi and Fassò, 2015; MyShake, Kong *et al.*, 2016; Brooks *et al.*, 2016) and Global Navigation Satellite Systems (GNSS) receivers (Minson *et al.*, 2015; Brooks *et al.*, 2016) in dedicated or personal smartphones.

Also fast algorithms help reducing EEW delays (Figure 1). The most rapid algorithms derive quake information from single-station observations, typically from the initial few seconds of the faster traveling P-wave. Typical examples are the Tauc-Pd algorithm (Kanamori, 2005; Wu *et al.*, 2007; Böse *et al.*, 2009) or the recent Gutenberg algorithm (Meier *et al.*, 2015). In the case of larger earthquakes, these *onsite* algorithms can produce EEW magnitudes well before the rupture has terminated, raising the more general question of whether the temporal rupture evolution is predictable once an event has initiated (e.g. Colombelli *et al.*, 2014). Several recent studies indicate that the waveforms of moderate and large earthquakes are quite similar until the rupture has terminated, which indicates that during very early alerts, based on the very first seconds, earthquake magnitude can only be considered a lower bound (Rydelek and Horiuchi, 2006; Böse *et al.*, 2012b; Meier *et al.*, manuscript). Single-sensor based approaches, as a matter of principle, have also a higher risk of producing false alerts.

2. Maximum Accuracy

EEW computation usually comprises two separate processing steps. In the first step, point-source seismic source parameters, such as hypocenter location and magnitude, are estimated from the available real-time data. In the second step, GMPEs are used to predict shaking at the user site. While this concept works quite successfully for EEW in small to moderate earthquakes ($M<6.5$), magnitudes estimated from seismic data tend to saturate in large earthquakes. A well known event, where this issue was highlighted, was the 2011 M9.0 Tohoku earthquake, in which the JMA (Japanese Meteorological Agency) operated EEW system underestimated the event magnitude by almost a full unit (Hoshiba *et al.*, 2011). An additional complication arises from the fact that seismic shaking is controlled by site-to-rupture rather than hypocentral distances, implying that finite source-dimensions in large earthquakes cannot be neglected. While speed, as noted before, is most critical in moderate-sized earthquakes, accepting larger delays in order to obtain reasonably accurate source descriptions and shaking forecasts is the most challenging design goal for EEW targeting large earthquakes ($M\geq6.5$).

Magnitude saturation in large earthquakes can be avoided by usage of high-rate geodetic (GPS/GNSS) data that become world-wide increasingly available in real-time. Geodetic algorithms, such as BEFORES (Minson *et al.*, 2014), G-larmS (Grapenthin *et al.*, 2014), G-FAST (Crowell *et al.*, in press), or GPSlip (Böse *et al.*, 2013b; Yamada, 2007), allow real-time computation of seismic slip distributions along the rupturing fault and magnitudes to high accuracy. Finite-source dimensions, on the other hand, can be most reliably constrained from seismic data at high

frequencies, which are observed to preferentially radiate from the edges of the earthquake rupture (Yamada *et al.*, 2007). At the same time, high-frequency motions, such as peak ground acceleration (PGA), seem less affected by rupture directivity compared to long-period signals (Spudich and Chiou, 2008). These favorable characteristics of seismic high-frequency motions are exploited in the Finite-Fault Rupture Detector (FinDer*)* algorithm (Böse *et al.*, 2012a; Böse *et al.*, 2015a), which estimates the rupture centroid position, length, and orientation (along with their uncertainties) of an assumed line source. The algorithm uses tools developed for computer vision to match GMPE-based templates (pre-calculated for various rupture lengths and orientations), and maps or images of spatially distributed PGA values observed in a seismic network.

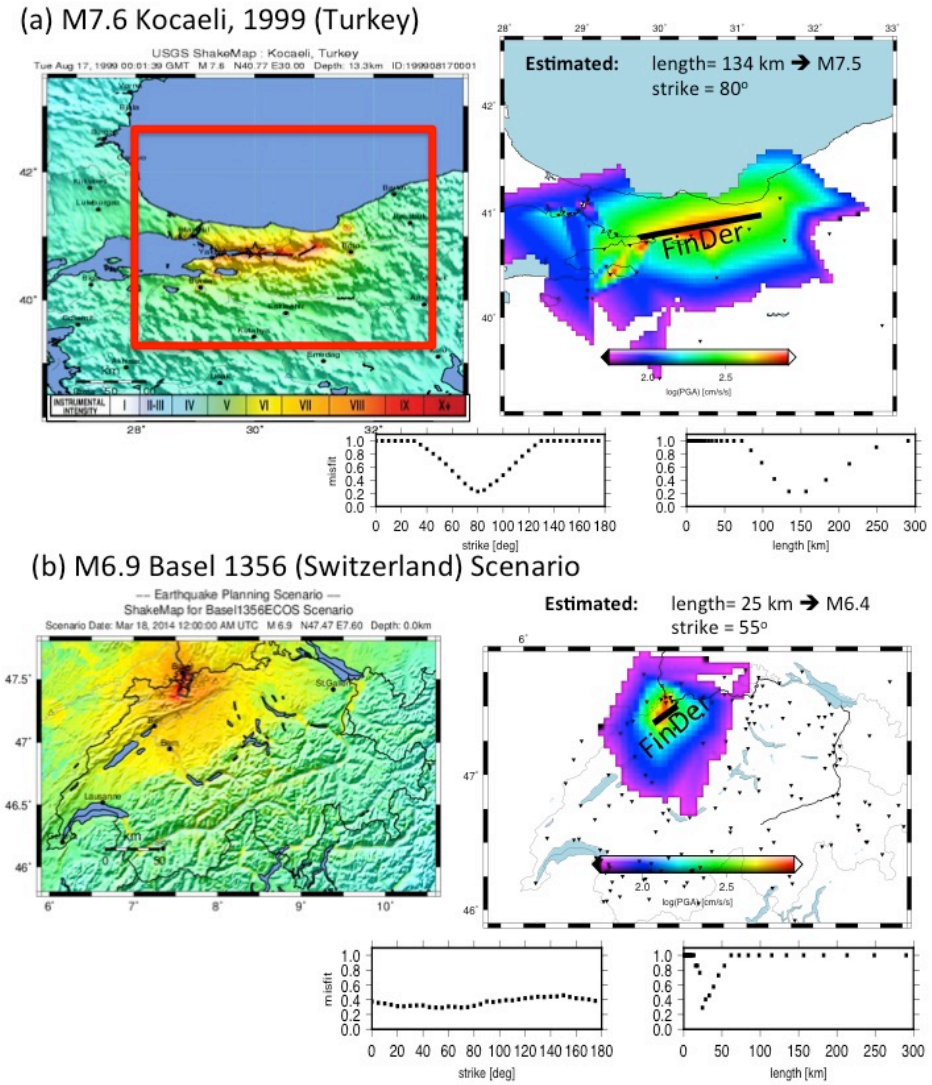

Figure 3. ShakeMaps (left, www.earthquake.usgs.gov/earthquakes/shakemap/) and FinDer estimated line-sources (right) for the (a) 1999 M7.6 Kocaeli (Turkey) and the (b) 1356 M6.9 Basel (Switzerland) scenario earthquakes. Though FinDer cannot reproduce the rupture of the Kocaeli earthquake along multiple fault segments, the results agree well with the observations during both events. Having real-time information on finite-fault dimensions is critically important to provide accurate shaking forecasts for EEW, because rupture-to-site distances can be taken into account.

Real-time and offline tests of FinDer (see Figure 3 for two examples), have demonstrated the successful estimation of finite-fault dimensions for various earthquake magnitudes, focal mechanisms, and network geometries. Since April 2015 FinDer is actively contributing to the Californian ShakeAlert Demonstration system and supplementing the previous three point-source algorithms Tauc-Pd Onsite (Wu *et al.*, 2007; Böse *et al.*, 2009), Virtual Seismologist (Cua *et al.*, 2009; Behr *et al.*, 2016b), and ElarmS (Allen, 2007; Kuyuk *et al.*, 2014) for improved performance in large earthquakes (Böse *et al.*, 2015a).

3. Maximum Reliability

Reliability is a critical design goal for EEW in earthquakes of all magnitudes. It refers to both high detection success (minimization of missed alerts) and low false alert rates. Many promising algorithms for EEW have been proposed during recent years, the majority of them targeting point-source events (M<6.5). These algorithms have been developed either for single sensor (e.g. Kanamori, 2005; Wu *et al.*, 2007; Böse *et al.*, 2012b; Meier *et al.*, 2015) or for sensor network applications (e.g. ElarmS: Allen, 2007; Kuyuk *et al.*, 2014; Virtual Seismologist: Cua *et al.*, 2009; Behr *et al.*, 2016b; PreSEIS: Böse *et al.*, 2008; or PRESTo; Satriano *et al.*, 2011). Also the number of algorithms targeting large finite-source events (M>6.5) is remarkably growing, including both seismic and geodetic approaches (Figure 4). EEW is also no longer restricted to high quality seismic real-time data from broadband and/or strong-motion sensors, but is increasingly exploiting additional data sources, such as from geodetic and gravity-sensitive sensors (Harms *et al.*, 2015). Various research groups have also started to explore the utilization of data from low-cost sensor networks (e.g. Clayton *et al.*, 2011; Cochran *et al.*, 2009; Kong *et al.*, 2016; Brooks *et al.*, 2016).

Commonly, EEW systems are not designed to meet the requirements of a particular class of events or magnitude range, but are supposed to perform well in all moderate to large earthquakes. The amount of data available to an EEW system is by definition limited and therefore extracting all possible information from the available data while reporting accurate uncertainties on the resulting source parameter estimates is a challenge. Probabilistic approaches seem well suited to meet the requirements and constraints of EEW. EEW systems that incorporate Bayesian statistics allow to additionally exploit available prior information, such as favoring hypocenters that lie on known faults or recent seismic activity, and constrain locations using null-information from the full network geometry (e.g. Cua, 2005). This prior information can improve parameter estimates and reduce uncertainties.

EEW algorithms as described above usually exploit different characteristics of seismic or geodetic data in order to infer some aspect of the seismic source, and each has its own strengths, weaknesses, and uncertainties. The most robust and reliable EEW system will likely combine multiple approaches in an evolutionary probabilistic manner in order to provide the best estimate of shaking at a particular time (Figure 4). But how should the parameter estimates from various approaches (models) - from single-station prediction to finite-fault detection - be combined to provide highest reliability with the fastest and most accurate warnings at any time from earthquake origin?

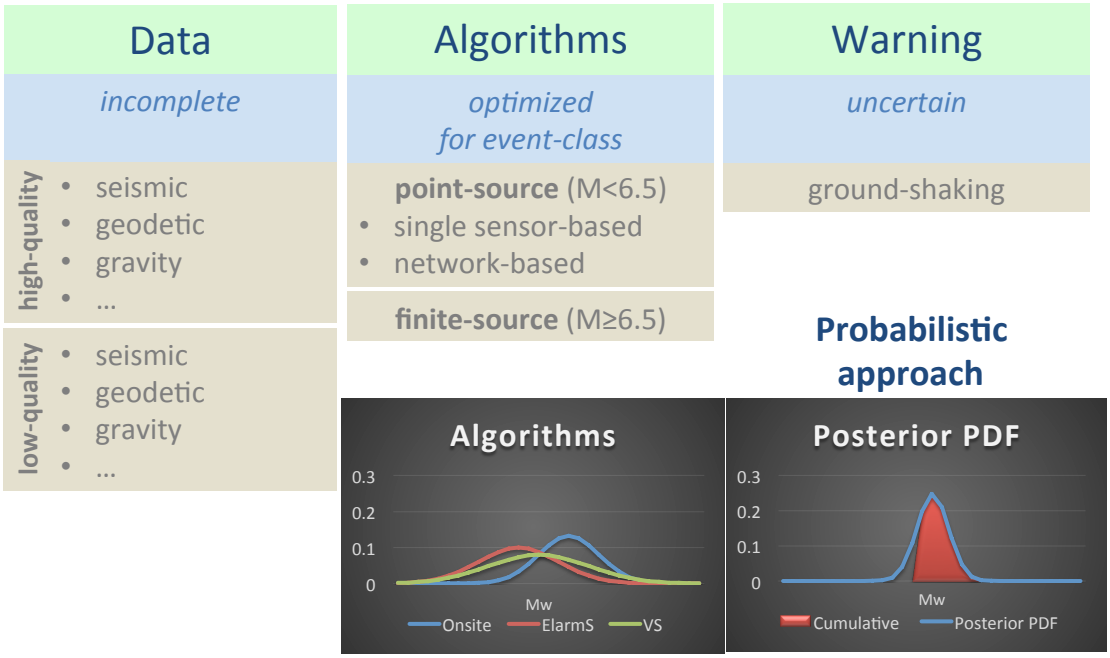

Figure 4. Combining various data sources and algorithms to provide shaking forecasts and early warnings for the entire range of earthquake magnitudes. Probabilistic approaches seem well suited to meet the requirements and constraints of EEW. The most robust and reliable EEW system will likely combine multiple approaches in an evolutionary probabilistic manner in order to provide the best estimate of shaking at any given time from earthquake nucleation.

Combining source parameter estimates from various algorithms requires a consistent interpretation of model parameters and uncertainties. Consistency among different models is typically lacking, because these models were often developed by different research groups using different constraints, targets, and datasets. A rare exception is FinDer2 (Böse *et al.*, 2015b) which extends the original FinDer algorithm by Böse *et al.* (2012, 2015a) to point-source events. FinDer2 supplements the original finite-fault template set of FinDer by templates of much smaller (point-source) dimensions, in which PGA distributions follow radial-symmetric rather than quasi-elliptical patterns. This extension enables FinDer2 to detect and process events of the entire magnitude range (M>2.5) with a consistent interpretation of model parameters and uncertainties. Moreover, FinDer2 guarantees a smooth transition from a small (point-source) to a large (finite-source) event without any abrupt changes (Figure 5).

Another example for model consistency and system reliability is the seismic-geodetic FinDer-BEFORES algorithm by Minson *et al.* (manuscript) that builds upon a Bayesian approach and that targets large earthquakes in particular. Seismic and geodetic data observe complementary parts of the earthquake. Combining the two datasets constraints rupture dimensions, slip, and magnitudes without saturation in large earthquakes. Combining the seismic FinDer (Böse *et al.*, 2012a) and geodetic BEFORES (Minson *et al.*, 2014) algorithms brings several advantages. First, BEFORES can build an optimized finite-fault mesh for slip inversion based on the FinDer estimated source dimensions. Second, since BEFORES is a Bayesian algorithm, it can use the FinDer estimated probability density function (PDF) for rupture strike as prior probability in order to determine probabilistic solutions for fault

geometry and spatial slip distributions (and thus magnitudes). The FinDer-BEFORES output thus maximizes the fit to both seismic and geodetic real-time observations without any additional computational cost, since both algorithms can run in parallel and only combine their separately derived estimates at the very end before releasing the final (combined) output. The Bayesian framework in FinDer-BEFORES can be arbitrarily extended to include other analyses of independent data (e.g. gravity, Harms *et al.*, 2015) without additional computational expense (Minson *et al.*, manuscript). The algorithm is expected to go live in California within the next couple of months.

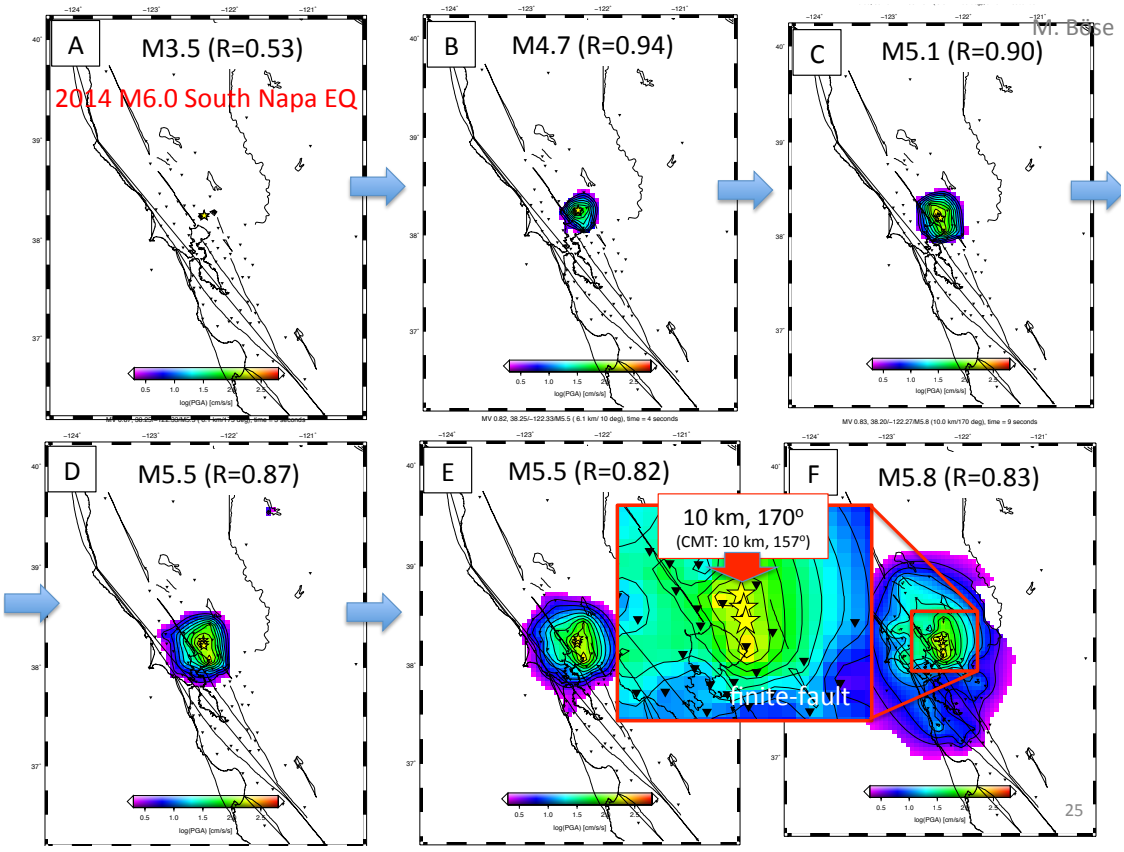

Figure 5. Demonstration of temporal evolution of FinDer2 estimated source parameters with a smooth transition from a point-source to a finite-fault solution using the example of the 2014 M6.0 South Napa, California, earthquake.

EEW systems that combine various algorithms or models will also benefit from robust processing platforms, as well as from the calibration and verification using consistent datasets (Figure 1). This strategy is employed by the new SeisComp3-based EEW system that is currently being developed at ETH Zurich (Behr *et al.*, 2016a). SeisComp3's modularity allows each EEW algorithm to run as a standalone program and to communicate with other modules through message groups for sending and receiving PDFs for each source parameter. In the beginning, the new system will include the two point-source algorithms Virtual Seismologist and Gutenberg Algorithms, as well as the point-source and finite-fault algorithm FinDer2. One of many advantages of system modularity, however, is that single modules can be easily removed and/or added. The planned ETH system will be calibrated and tested using a consistent large global dataset of locally recorded seismic events originally compiled by Meier (2015). The Virtual Seismologist in SeisComp3, VS(SC3), is already being

real-time operated in Switzerland, Iceland, Romania, Greece, Turkey, California, and New Zealand (Behr *et al.*, 2016b). Future real-time testing of the new system will be facilitated by the already existing SeisComp3 setup necessary to run VS(SC3).

Finally, EEW systems that combine various algorithms (and datasets) and exploit different features in the observed data, require some central mediator that outputs a single alert message by weighting the various (independent) estimates using some form of reality check (Figure 1). Minson *et al.* (pers. communication) propose to compare for each algorithm (and "No event") the predicted and observed waveform envelopes (Cua, 2005). Probabilities for each algorithm (and "No event") are computed depending on the respective agreement between predicted and observed motions (using the available waveform data up to the respective time when an estimate is given). A hyper-robust ground-motion PDF is computed from weighting the predictions from each of the algorithms (using the respective uncertainties/PDFs), which is then reported to the end-user.

Conclusions

Numerous algorithms for earthquake early warning (EEW) have been developed during the past two decades to provide fast and accurate warnings to end-users. The spectrum of these methods reaches from single-station prediction to finite-fault detection. To achieve maximum reliability of EEW systems, which encompasses both high detection success and low false alert rates, EEW systems should combine various algorithms and various data sources (in particular seismic and geodetic real-time data) to facilitate EEW for the entire magnitude range, including both small point-source and large finite-fault events. However, building such combined systems requires a consistent interpretation of model parameters and uncertainty estimates of the various algorithms, which we predict will be one of the most challenging and important tasks in EEW research in upcoming years.

References

Allen, R.M. (2007). The ElarmS earthquake early warning methodology and its application across California, In "Earthquake Early Warning Systems", P. Gasparini, G. Manfredi, J. Zschau (Eds), 21-44, Springer, ISBN-13 978-3-540-72240-3.

Behr, Y., J.F. Clinton, P. Kästli, C. Cauzzi, R. Racine, and M.-A. Meier (2015). Anatomy of an Earthquake Early Warning (EEW) alert: predicting time delays for an end-to-end EEW system, *Seismological Research Letters,* 86(3), 830-840, doi: 10.1785/0220140179.

Behr, Y., M. Böse, D. Smith, J. Clinton, and M.-A. Meier (2016a). Update on the Next Generation Earthquake Early Warning in SeisComP3, European Geosciences Union General Assembly 2016, 17-22 April, Vienna, EGU2016-13723.

Behr, Y., J.F. Clinton, C. Cauzzi, E. Hauksson, K. Jónsdóttir, C.G. Marius, A. Pinar, J. Salichon, and E. Sokos (2016b). The Virtual Seismologist in SeisComP3: A New Implementation Strategy for Earthquake Early Warning Algorithms, *Seismological Research Letters*, 87(2A), doi: 10.1785/0220150235.

Böse, M., F. Wenzel, and M. Erdik (2008). PreSEIS: A neural network based approach to earthquake early warning for finite faults, *Bulletin of the Seismological Society of America*, 98(1), 366–382, doi 10.1785/0120070002.

Böse, M., E. Hauksson, K. Solanki, H. Kanamori, and T.H. Heaton (2009). Real-Time Testing of the On-site Warning Algorithm in Southern California and Its Performance During the July 29 2008 Mw5.4 Chino Hills Earthquake, *Geophysical Research Letters*, 36, L00B03, doi:10.1029/2008GL036366.

Böse, M., T.H. Heaton, and E. Hauksson (2012a). Real-time Finite Fault Rupture Detector (FinDer) for Large Earthquakes, *Geophysical Journal International,* 191(2), 803-812, doi:10.1111/j.1365-246X.2012.05657.x.

Böse, M., T. Heaton and E. Hauksson (2012b). Rapid estimation of earthquake source and ground-motion parameters for earthquake early warning using data from single three-component broadband or strong-motion sensor, *Bulletin of the Seismological Society of America*, 102(2), 738-750, doi: 10.1785/0120110152.

Böse, M., R. Allen, H. Brown, G. Cua, M. Fischer, E. Hauksson, T. Heaton, M. Hellweg, M. Liukis, D. Neuhauser, P. Maechling and CISN EEW Group (2013a). CISN ShakeAlert – An Earthquake Early Warning Demonstration System for California, in: F. Wenzel and J. Zschau (eds.) *Early Warning for Geological Disasters - Scientific Methods and Current Practice*; ISBN: 978-3-642-12232-3, Springer Berlin Heidelberg New York.

Böse, M., T. Heaton, and K. Hudnut (2013b). Combining Real-Time Seismic and GPS Data for Earthquake Early Warning, AGU (American Geophysical Union) 2013 Fall Meeting, #G51B-05.

Böse, M., C. Felizardo, and T.H. Heaton (2015a). Finite-Fault Detector Algorithm (FinDer): Going Real Time in Californian ShakeAlert Warning System, *Seismological Research Letters,* 86(6), 1692-1704, doi:10.1785/0220150154.

Böse, M., D. Smith, and T. Heaton (2015b). Recent Improvements to the Finite-Fault Rupture Detector Algorithm: FinDer II, abstract #S33B-2757, AGU Fall Meeting, San Francisco, 14-18 December 2015.

Brooks, B.A., S.E. Minson, S. Barrientos, J.C. Baez, M. Böse, T.L. Ericksen, C. Guillemot, J.R. Murray, J.O. Langbein, C.L. Glennie, and C. Duncan (2016). Smartphone-Based Earthquake Early Warning in Chile, 2016 UNAVCO Science Workshop, March 29-31, Broomfield, Colorado.

Clayton, R.W., T. Heaton, M. Chandy, A. Krause, M. Kohler, J. Bunn, R. Guy, M. Olson, M. Faulkner, M.-H. Cheng, L. Strand, R. Chandy, D. Obenshain, A. Liu, and M. Aivazis (2011). Community Seismic Network, *Annals of Geophysics,* 54(6), doi: 10.4401/ag-5269.

Cochran, E.S., J.F. Lawrence, C. Christensen, and R.S. Jakka (2009). The Quake-Catcher Network: Citizen science expanding seismic horizons, *Seismological Research Letters,* 80, 26-30.

Colombelli, S., A. Zollo, G. Festa and M. Picozzi (2014). Evidence for a difference in rupture initiation between small and large earthquakes, *Nature Communications* 5, #3958, doi:10.1038/ncomms4958.

Crowell, B. W., D.A. Schmidt, P. Bodin, J.E. Vidale, J.S. Gomberg, R. Hartog, V. Kress, T.I. Melbourne, M. Santillan, and S.E. Minson (2016). Demonstration of the Cascadia G-FAST Geodetic Earthquake Early Warning System for the Nisqually, Washington Earthquake, *Seismological Research Letters*, in press.

Cua G (2005). Creating the Virtual Seismologist: developments in ground motion characterization and seismic early warning. PhD thesis, California Institute of Technology, Pasadena, California.

Cua, G.B., and T.H. Heaton (2009). Characterizing average properties of southern California ground motion amplitudes and envelopes, Earthquake Engineering Research Laboratory, Pasadena, CA. http://resolver.caltech.edu/CaltechEERL:EERL-2009-05.

Cua, G.B., M. Fischer, T.H. Heaton, and S. Wiemer (2009). Real-time Performance of the Virtual Seismologist Earthquake Early Warning Algorithm in Southern California, *Seismological Research Letters,* 80(5), 740–747, doi:10.1785/gssrl.80.5.740.

Evans, J., R. Allen, A. Chung, E. Cochran, R. Guy, M. Hellweg, and J. Lawrence (2014). Performance of several low-cost accelerometers, *Seismological Research Letters*, 85(1), 147–158, doi: 10.1785/0220130091.

Faulkner, M., M. Olson, R. Chandy, J. Krause, K. M. Chandy, and A. Krause (2011). The next big one: Detecting earthquakes and other rare events from community-based sensors, Proceedings of the 10th International Conference on Information Processing in Sensor Networks (IPSN), Chicago, 12 to 14 April 2011.

Finazzi, F., and A. Fassò (2015). A statistical approach to crowdsourced smartphone-based earthquake early warning systems, eprint arXiv:1512.01026, http://arxiv.org/abs/1512.01026.

Fleming, K., M. Picozzi, C. Milkereit, F. Kuehnlenz, B. Lichtblau, J. Fischer, C. Zulfikar, O. Oezel, J. Zschau, I. Veit, K. H. Jaeckel, M. Hoenig, J. Nachtigall, H. Woith, J. P. Redlich, K. Ahrens, I. Eveslage, S. Heglmeier, M. Erdik and N. Kafadar Seismic Early Warning for Europe (SAFER) Working Group Earthquake Data Information system for the Marmara Sea (EDIM) Working GroupsInternational (2009), The Self-Organizing Seismic Early Warning Information Network (SOSEWIN), *Seismological Research Letters,* 80(5), 755-771.

Grapenthin, R., I.A. Johanson, and R.M. Allen (2014). Operational real-time GPS-enhanced earthquake early warning, *J. Geophys. Res. Solid Earth*, 119, 7944–7965, doi:10.1002/2014JB011400.

Harms, J., J.-P. Ampuero, M. Barsuglia, E. Chassande-Mottin, J.-P. Montagner, S.N. Somala, and B. F. Whiting (2015). Transient gravity perturbations induced by earthquake rupture, *Geophysical Journal International*, 201(3), 1416-1425 doi:10.1093/gji/ggv090.

Heaton, T.H. (1985). A model for a seismic computerized alert network, *Science*, 228, 987-990.

Horiuchi, S., Y. Houriuchi, S. Yamamoto, H. Nakamura, C. Wu, P. Rydelek and M. Kachi (2009). Home seismometer for earthquake early warning, *Geophysical Research Letters*, 36, L00B04; doi: 10.1029/2008GL036572.

Hoshiba, M., K. Iwakiri, N. Hayashimoto, T. Shimoyama, K. Hirano, Y. Yamada, Y. Ishigaki, and H. Kikuta (2011). Outline of the 2011 off the Pacific coast of Tohoku Earthquake (Mw 9.0) - Earthquake Early Warning and observed seismic intensity, *Earth Planets Space,* 63, 547–551.

Kanamori, H. (2005). Real-time seismology and earthquake damage mitigation, *Annu Rev Earth Planet Sci,* 33, 195-214, doi:10.1146/annurev.earth.33.092203.122626.

Kong, Q., R.M. Allen, L. Schreier, and Y.-W. Kwon (2016). MyShake: A smartphone seismic network for earthquake early warning and beyond, *Sci. Adv.* 2, e1501055.

Kuyuk, H.S. and R.M. Allen (2013). A global approach to provide magnitude estimates for earthquake early warning alerts, *Geophysical Research Letters*, 40, 6329-6333 doi:10.1002/2013GL058580

Kuyuk, S., R.M. Allen, H. Brown, M. Hellweg, I. Henson, and D. Neuhauser (2014). Designing a Network-Based Earthquake Early Warning Algorithm for California: ElarmS-2, *Bulletin of the Seismological Society of America,* 104 (1), 162–173, doi: 10.1785/0120130146.

Meier, M.-A. (2015). Advancing Real-Time Seismic Risk Mitigation: Probabilistic Earthquake Early Warning and Physics Based Earthquake Triggering Models. PhD thesis, ETH-Zürich. http://doi.org/10.3929/ethz-a-010608242.

Meier, M.-A., T. Heaton, and J. Clinton (2015). The Gutenberg Algorithm: Evolutionary Bayesian Magnitude Estimates for Earthquake Early Warning with a Filter Bank, *Bulletin of the Seismological Society of America*, 105 (5), 2774-2786, doi: 10.1785/0120150098.

Meier, M.-A., T. Heaton, and J. Clinton. Evidence for universal earthquake initiation behavior, manuscript.

Minson, S. E., B. A. Brooks, C. L. Glennie, J. R. Murray, J. O. Langbein, S. E. Owen, T. H. Heaton, R. A. Iannucci, and D. L. Hauser (2015), Crowdsourced earthquake early warning, *Sci. Adv.*, 1(3), e1500036, doi:10.1126/sciadv.1500036.

Minson, S.E., M. Böse, T.H. Heaton, E. Hauksson, J.R. Murray, J.O. Langbein, D.E. Smith, and C. Felizardo. Joint seismic-geodetic real-time finite fault models for earthquake early warning, manuscript.

Minson, S.E., J.R. Murray, J.O. Langbein, and J.S. Gomberg (2014). Real-time inversion for finite-fault slip models and rupture geometry based on high-rate GPS data, *Journal of Geophysical Research: Solid Earth,* 119, 3201-3231, doi: 10.1002/2013JB010622.

Picozzi, M., C. Milkereit, S. Parolai, K.-H. Jaeckel, I. Veit, J. Fischer, and J. Zschau, (2010). GFZ Wireless Seismic Array (GFZ-WISE), a Wireless Mesh Network of Seismic Sensors: New Perspectives for Seismic Noise Array Investigations and Site Monitoring, *Sensors*, 10, 3280-3304; doi:10.3390/s100403280.

Rydelek, P., and S. Horiuchi (2006). Earth science: Is the earthquake rupture deterministic? *Nature,* 442, doi 10.1038/nature04963.

Satriano C., L. Elia, C. Martino, M. Lancieri, A. Zollo and G. Iannaccone (2011). PRESTo, the earthquake early warning system for Southern Italy: concepts, capabilities and future perspectives, *Soil Dynamics and Earthquake Engineering,* 31(2), 137–153, doi: 10.1016/j.soildyn.2010.06.008

Spudich, P. and B.S.J. Chiou (2008). Directivity in NGA Earthquake Ground Motions: Analysis Using Isochrone Theory, *Earthquake Spectra,* 24(1), 279-298, doi: http://dx.doi.org/10.1193/1.2928225.

Yamada, M. (2007). Early warning for earthquakes with large rupture dimension. Dissertation (Ph.D.), California Institute of Technology. http://resolver.caltech.edu/CaltechETD:etd-03152007-174624.

Yamada, M., T. Heaton, and J. Beck (2007). Real-time estimation of fault rupture extent using near-source versus far-source classification, *Bulletin of the Seismological Society of America*, 97 (6), 1890-1910.

Worden, C.B., D.J. Wald, and D.A. Rhoades (2012). Probabilistic Relationships between Ground-Motion Parameters and Modified Mercalli Intensity in California, *Bulletin of the Seismological Society of America,* 102(1), 204-221, doi: 10.1785/0120110156.

Wu, Y.-M., D.-Y. Chen, T.-L. Lin, C.-Y. Hsieh, T.-L. Chin, W.-Y. Chang, W.-S. Li, and S.-H. Ker (2013). A high-density seismic network for earthquake early warning in Taiwan based on low cost sensors, *Seismological Research Letters*, 84(6), 1048-1054.

Wu, Y.-M., H. Kanamori, R.M. Allen, and E. Hauksson (2007). Determination of earthquake early warning parameters, τc and Pd, for southern California, *Geophysical Journal International,* 170, 711–717, doi:10.1111/j.1365-246X. 3732007.03430.x

The Eight Years of Earthquake Early Warning Operation in the Japan Meteorological Agency

Yuki Kodera[1,*], Yasuyuki Yamada[1], Shimpei Adachi[1], Masahiko Morimoto[1], Yuji Nishimae[1] and Mitsuyuki Hoshiba[2]

[1] Earthquake and Tsunami Observation Division, Seismology and Volcanology Department, Japan Meteorological Agency, 1-3-4 Otemachi, Chiyoda-ku, Tokyo, Japan, y_kodera@met.kishou.go.jp
[2] Meteorological Research Institute, Japan Meteorological Agency, 1-1 Nagamine, Tsukuba, Ibaraki, Japan

Abstract

The Japan Meteorological Agency (JMA) began its Earthquake Early Warning service for the general public in October 2007. During the last years, the system has satisfactorily predicted ground motion for most earthquakes and has contributed to disaster mitigation for major earthquakes. However, the system under-predicted strong shaking for a huge earthquake with a large rupture zone such as the 2011 off the Pacific coast of Tohoku earthquake. Moreover, there were several cases of over-prediction when multiple simultaneous earthquakes occurred and noise trigger data was incorporated into the calculation of the hypocenter and magnitude estimations. To deal with these technical challenges in fundamental ways, JMA plans to introduce three new algorithms: the Integrated Particle Filter (IPF), Propagation of Local Undamped Motion (PLUM), and hybrid methods. It also intends to use large-scale seismometer networks to allow the system to more rapidly and accurately predict strong ground motion.

Introduction

It has been eight years since the Japan Meteorological Agency (JMA) launched its Earthquake Early Warning (EEW) service for the general public (Hoshiba *et al.*, 2008). Since then, the EEW system has processed various types of observational data, including the 2011 off the Pacific coast of Tohoku earthquake (the Tohoku earthquake) (Mw 9.0). The experiences over this long period of time have revealed that the system has often satisfactorily predicted strong ground motion and has contributed to earthquake disaster mitigation; however, several technical challenges have become obvious since the operation started.

The JMA EEW system predicts seismic intensities on a JMA scale. The JMA seismic intensity scale, or simply "JMA seismic intensity," is calculated from acceleration waveform and represented on a 10-degree scale (JMA, 1996). Details of the JMA

* Now at Meteorological Research Institute, Japan Meteorological Agency, 1-1 Nagamine, Tsukuba, Ibaraki, Japan, kodera@mri-jma.go.jp

seismic intensity are shown in Appendix. The EEW system reports predicted JMA seismic intensities on the basis of an area division that consists of 188 areas across Japan (JMA, 2014b) (Fig. 1, left). Each area has 2–100 prediction points. The system computes the intensities of all of the points (approximately 4,400 stations all over Japan as of 2016 (JMA, 2016a)), classifies them according to the divided areas, and provides users with the maximum prediction values for each area.

JMA reports the annual EEW scores to assess its prediction accuracy. The score is calculated on the basis of the percentage of the number of areas where the error of the predicted JMA seismic intensity was within one degree (Fig. 1, right). An annual score is computed from the total number of areas where the observed or predicted JMA seismic intensities are four or more in all earthquake events and EEW issuances in the target year. Figure 2 shows the scores from fiscal years 2007 to 2014 (JMA, 2015). (Note that the fiscal year begins in April and ends in March in Japan.) Over the eight years, the majority of the scores remain near 80%, which means that the system performed well in general. However, there are two major drops, which are evident in fiscal years 2010 and 2013. They correspond to unexpected events, such as the very active aftershocks of the Tohoku earthquake and a serious false alarm in 2013, which emphasized technical issues that needed to be solved.

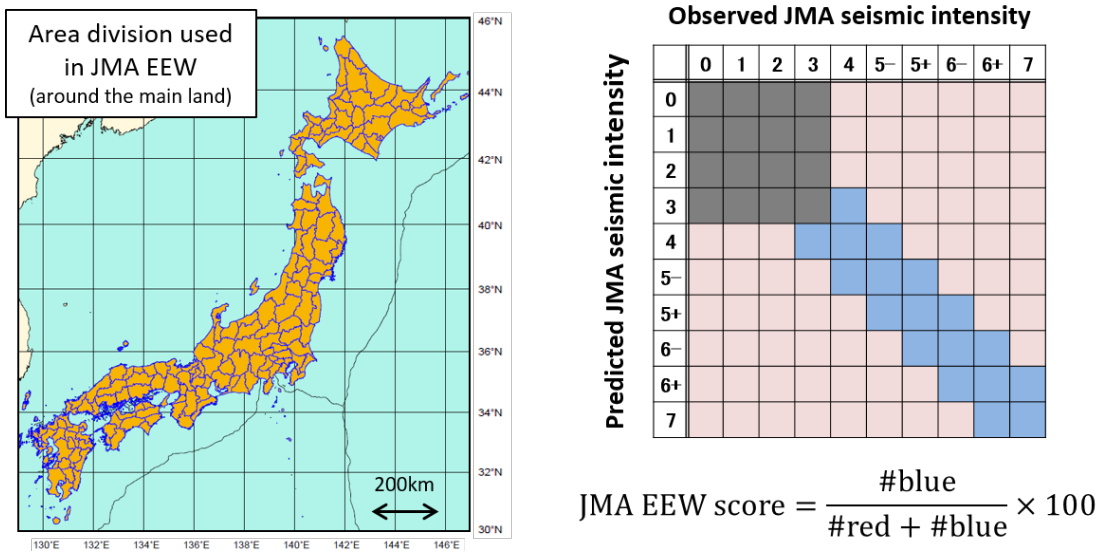

Figure 1. The area division that the JMA EEW system uses when it issues predicted JMA seismic intensities (left). The calculation method for the JMA EEW score (right). #blue (or #red) indicates the number of areas in blue (or red) cells in the table. Areas where the observed and predicted JMA seismic intensities are less than four were eliminated from the calculation.

Outline of the JMA EEW system

The JMA EEW system predicts JMA seismic intensities based on hypocenters and magnitudes estimated from several methods (e.g., Kamigaichi *et al.*, 2009; JMA, 2008a). The estimated hypocenters and magnitudes are updated repeatedly as the system receives additional observational data. Often, several to tens of EEW messages are issued for a single earthquake. Figure 3 is a typical example of an EEW announcement, issued for a M5.6 earthquake on September 16, 2014.

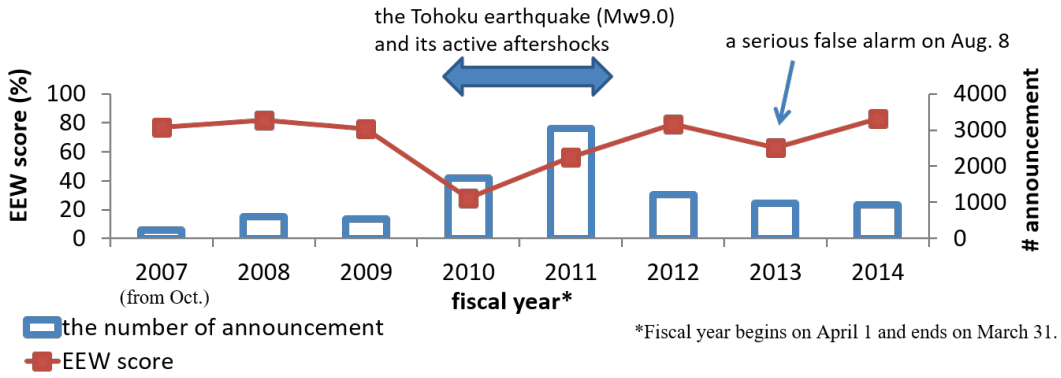

Figure 2. Time series of the JMA EEW scores and the number of EEW announcements from fiscal year 2007 to 2014 (modified after JMA (2015))

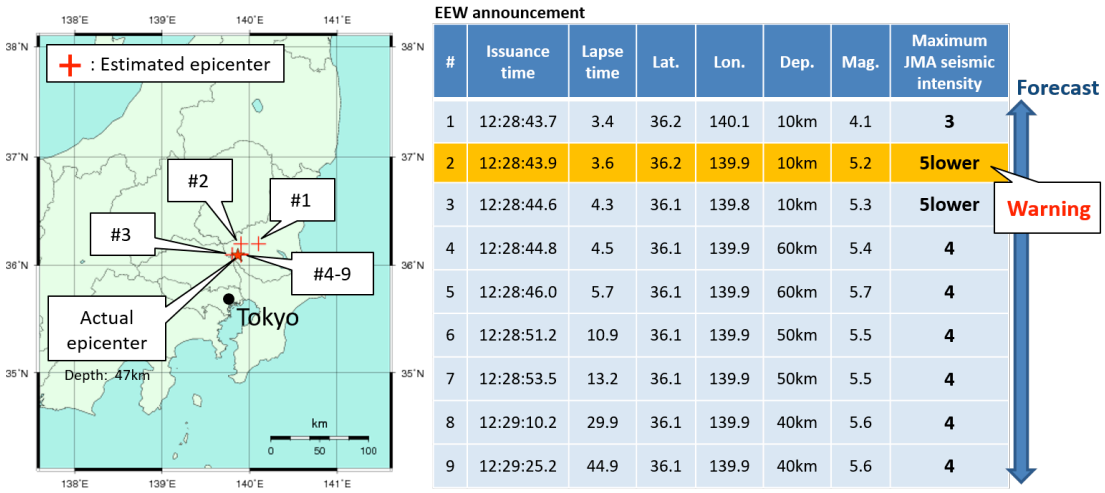

EEW announcement

#	Issuance time	Lapse time	Lat.	Lon.	Dep.	Mag.	Maximum JMA seismic intensity
1	12:28:43.7	3.4	36.2	140.1	10km	4.1	3
2	12:28:43.9	3.6	36.2	139.9	10km	5.2	5lower
3	12:28:44.6	4.3	36.1	139.8	10km	5.3	5lower
4	12:28:44.8	4.5	36.1	139.9	60km	5.4	4
5	12:28:46.0	5.7	36.1	139.9	60km	5.7	4
6	12:28:51.2	10.9	36.1	139.9	50km	5.5	4
7	12:28:53.5	13.2	36.1	139.9	50km	5.5	4
8	12:29:10.2	29.9	36.1	139.9	40km	5.6	4
9	12:29:25.2	44.9	36.1	139.9	40km	5.6	4

Forecast
Warning

Figure 3: EEW announcement of a M5.6 earthquake on September 16, 2014 (right) and locations of the estimated epicenters (left).

There are two types of JMA EEW messages: warnings and forecasts (e.g., Hoshiba, 2014). A warning is issued to the general public when at least two stations detect seismic signals and the maximum of the predicted JMA seismic intensities reaches 5-lower or more. A forecast is issued to specific users, many of whom intend to use the information in advanced ways. The conditions to issue a forecast are (1) the maximum of the predicted JMA seismic intensity is 3 or more, (2) its estimated magnitude is 3.5 or more, or (3) it has an acceleration amplitude of 100 cm/s^2 or more that is observed before the hypocenter is calculated. EEW forecast messages are issued many times for a single earthquake as the estimated hypocenter and magnitude and predicted seismic intensities are updated.

To estimate the hypocenter, the system uses several methods in parallel, which are classified into a main part and two sub parts. The main part, which includes the B-Δ method (Odaka *et al.*, 2003; Tsukada *et al.*, 2004), the territory method (Kamigaichi, 2004), and the grid search method using only P-wave arrivals, is aimed at rapid hypocenter determination using only the data from one to 10 stations. The main part uses observational data from 287 strong-motion seismometers (as of 2015) (JMA, 2016b). The two sub-parts primarily play supporting roles. One uses the grid search

method with "not-yet-arrived data" based on approximately 800 high-sensitivity seismometers (Hi-net of National Research Institute for Earth Science and Disaster Prevention (NIED) (Okada *et al.*, 2004)) (Horiuchi *et al.*, 2005). The other uses a conventional automatic hypocenter determination method using the P- and S-wave arrivals, and incorporates more than 1,000 seismometers, including the 287 strong-motion seismometers and the seismometers of Hi-net (JMA, 2008a; JMA, 2011). Because the two sub-parts have seismometer networks denser than that of the main part, they can provide more accurate hypocenter estimations. The system adopts their results if the accuracies of the hypocenter location meet certain high-level thresholds.

To estimate magnitude, the system uses P- and S-wave magnitudes (Kamigaichi, 2004). The P-wave magnitude is calculated using the maximum displacement within a time window from the P-arrival time to 70% of the S–P time, which enables the system to predict strong motion before the S wave hits and provides a long lead time. The S-wave magnitude is calculated using the entire waveform. Amplitude data is transmitted every second after a station is triggered and the estimation continues to be updated to the end of the event, which minimizes the under-estimation of the magnitude.

The JMA EEW system contributed to disaster mitigation during major earthquakes in the past eight years. In the case of the Tohoku earthquake, EEW users acquired positive lead times even in the locations closest to the epicenter when the system issued a warning for the Tohoku area (Fig. 4, left) (Hoshiba *et al.*, 2011). There were some reports that elevators stopped safely and factory operations that dealt with dangerous materials were interrupted due to the EEW announcement. At the construction site of a tall tower, called the Tokyo Skytree, at a height of 500 m, the announcement helped workers secure their safety (Abe, 2014). In the case of the M7.2 inland earthquake (the Iwate-Miyagi Nairiku earthquake) on June 14, 2008, while there were some areas where the warning was not issued before the S wave hit, the warning gave a 15 s lead time in Sendai city, which is the largest city near the epicenter (Fig. 4, right) (Kamigaichi *et al.*, 2009). In some kindergartens, children were led to safe spots in advance. At the Sendai airport, airplane traffic controllers who heard the announcement halted the landing of airplanes (JMA, 2008b).

Technical challenges during operation

During its eight-year operation, there were some cases when the EEW system did not appropriately predict strong motion. Most of these cases fall into two categories: (1) under-prediction for a huge earthquake and (2) false alarms with active aftershocks and noise data. The JMA immediately improved algorithms in tentative ways to reduce the risk of similar cases occurring. It also plans to introduce new algorithms to deal with these issues in fundamental ways.

(1) Under-prediction of a huge earthquake

In the Tohoku earthquake, the warning issued for the Tohoku area was successful, as mentioned above. However, most of the predicted JMA seismic intensities were lower than the actual intensities, especially in the Kanto region, even in the final EEW (Fig. 5) (Hoshiba *et al.*, 2011; JMA, 2012). One of the primary causes of this under-prediction was the occurrence of magnitude saturation. The estimated magnitude,

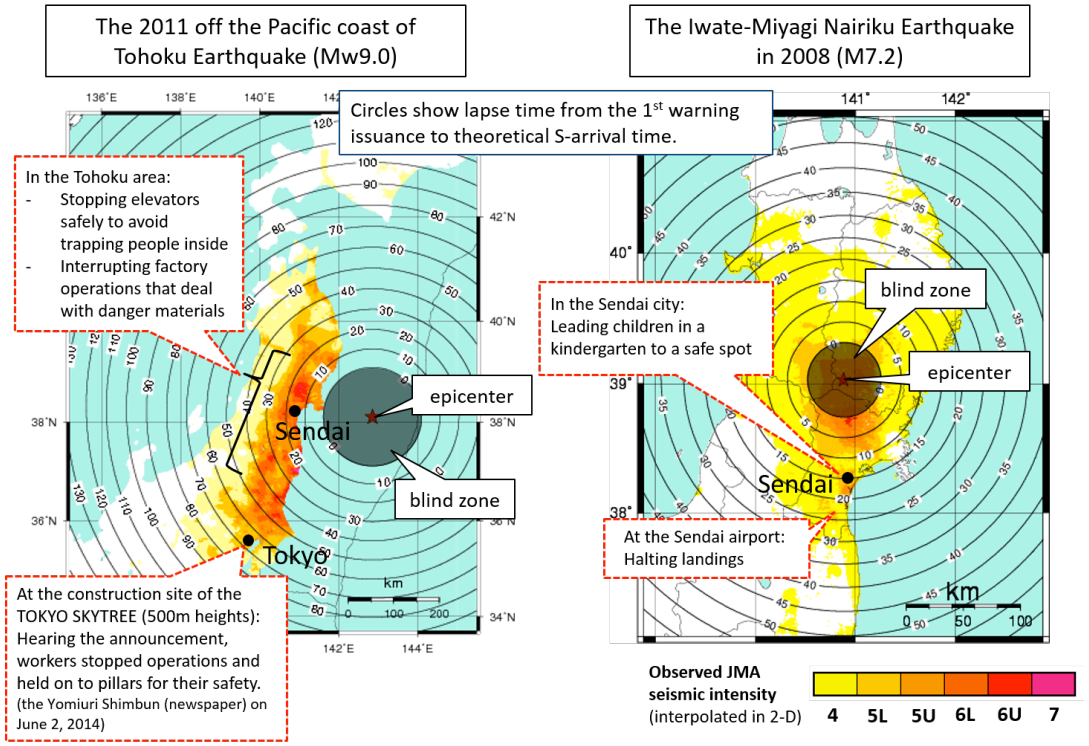

Figure 4: Lapse times from warnings and reports about utilization of EEW announcements (left: the 2011 off the Pacific coast of Tohoku earthquake (Mw9.0), right: the Iwate-Miyagi Nairiku earthquake on June 14th, 2008 (M7.2))

calculated from the displacement data near the epicenter, did not exceed M8.1. The other cause was the complexity of the source process. The rupture zone was too large for a point-source model to represent it adequately.

To minimize the effect of magnitude saturation, JMA upgraded the S-wave magnitude equation, adjusting terms and coefficients (JMA, 2012). The new equation estimates a magnitude of 8.5 for the Tohoku earthquake and leads to an appropriate prediction for the areas near the hypocenter. For the large extension of the rupture zone, JMA plans to introduce a new method, called the Propagation of Local Undamped Motion (PLUM) method, which can predict the JMA seismic intensity without the hypocenter and magnitude estimations.

(2) False alarms with active aftershocks and noise data

Just after the Tohoku earthquake, highly active aftershocks occurred and the system issued many false alarms (Hoshiba *et al.*, 2011; JMA, 2012). In the case of the multiple simultaneous earthquakes on May 28, 2011, it misinterpreted two small earthquakes whose magnitudes were 3.6 and 1.5 as a single large earthquake whose magnitude was 5.8 (Fig. 6). Observational data from the M3.6 and M1.5 earthquakes were classified into the same trigger group, and the estimated magnitude was calculated from the displacement data of the M3.6 earthquake with a hypocenter location near the M1.5 earthquake.

EEW announcement

#	Lapse time	Lat.	Lon.	Dep.	Mag.	Maximum JMA seismic intensity
1	5.4	38.2	142.7	10km	4.3	1
2	6.5	38.2	142.7	10km	5.9	3
3	7.5	38.2	142.7	10km	6.8	4
4	8.6	38.2	142.7	10km	7.2	5L
5	9.6	38.2	142.7	10km	6.3	4
6	10.7	38.2	142.7	10km	6.6	4
7	11.0	38.2	142.7	10km	6.6	4
8	15.9	38.1	142.9	10km	7.2	4
9	22.2	38.1	142.9	10km	7.6	5L
10	30.0	38.1	142.9	10km	7.7	5L
11	45.0	38.1	142.9	10km	7.7	5L
12	65.1	38.1	142.9	10km	7.9	5U
13	85.0	38.1	142.9	10km	8.0	5U
14	105.0	38.1	142.9	10km	8.1	6L
15	116.8	38.1	142.9	10km	8.1	6L

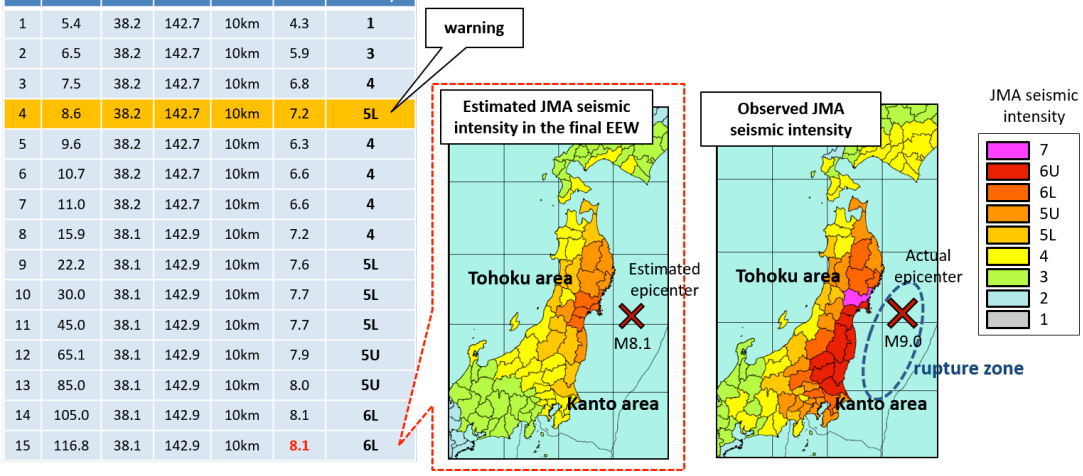

Figure 5: The EEW announcement of the Tohoku earthquake (left) and a comparison of the estimated JMA seismic intensities in the final EEW (center) and the actual observed intensities (right).

On August 8, 2013, the system issued a serious false alarm for a wide range of areas (Fig. 7) (JMA, 2014a). The estimated magnitude was 7.8, whereas the actual magnitude was 2.3, which did not generate perceptive ground motion. The primary cause of this false alarm was noise data derived from a device failure of one of the ocean-bottom seismometers (OBSs) in the Tonankai area. Its trigger time was close to that of the trigger data from the M2.3 earthquake and was therefore classified into the same group. The displacement amplitude of the noise data, which was more than 10,000 μm, resulted in the over-estimation of the magnitude.

As a tentative measure, JMA revised the parameters related to earthquake identification logic. The distance limitation classifying two trigger data into the same group was changed from 350 km to 150 km (JMA, 2012). In addition, as an essential measure, JMA plans to introduce a new method, called Integrated Particle Filter (IPF) method, which uses Bayesian estimation and can distinguish multiple simultaneous earthquakes and noise data.

Plans for improvement

To address the technical challenges, JMA develops three new methods: the (1) IPF, (2) PLUM, and (3) Hybrid methods. JMA also intends to incorporate new seismometer networks to allow the system to provide EEW announcements more rapidly and accurately.

(1) The IPF method

The IPF method (Tamaribuchi et al., 2014; JMA, 2014a; JMA, 2014c) is a hypocenter determination method that uses a Bayesian estimation framework and is expected to minimize false alarms with active aftershocks and noise data. In the IPF method, a set of estimated parameters of the hypocenter location θ^* is calculated from the maximum a posteriori estimation (e.g., Bishop, 2006):

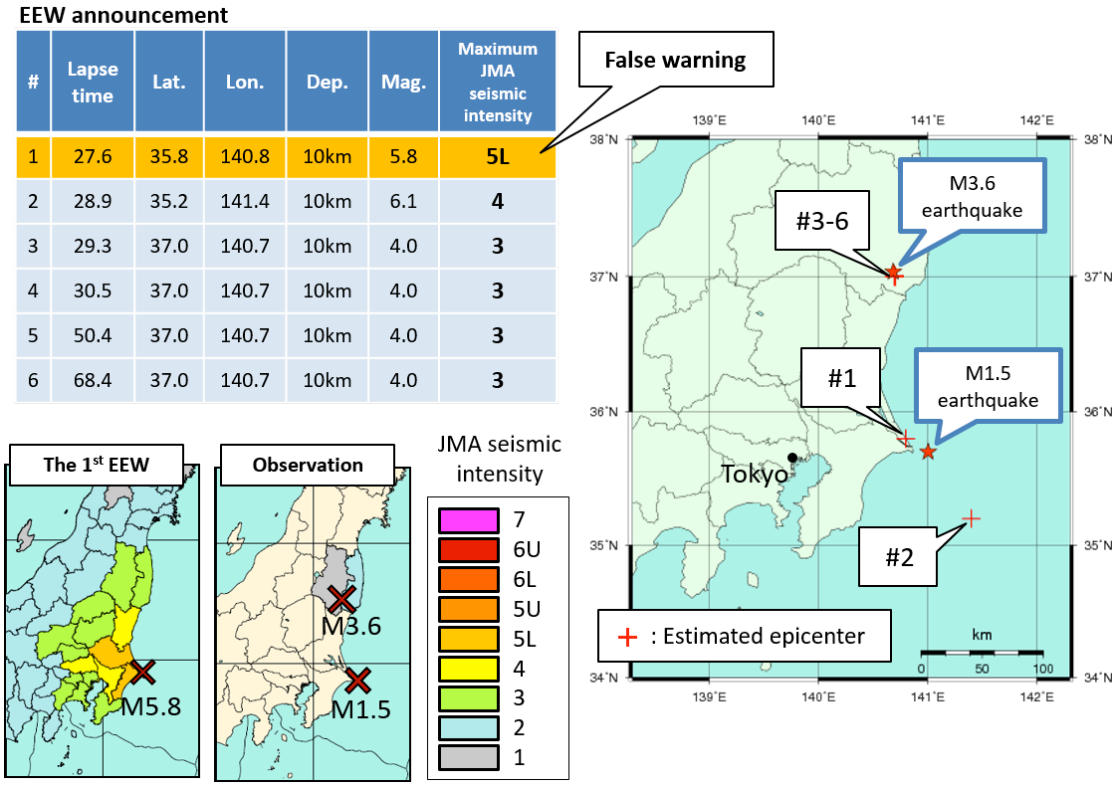

#	Lapse time	Lat.	Lon.	Dep.	Mag.	Maximum JMA seismic intensity
1	27.6	35.8	140.8	10km	5.8	5L
2	28.9	35.2	141.4	10km	6.1	4
3	29.3	37.0	140.7	10km	4.0	3
4	30.5	37.0	140.7	10km	4.0	3
5	50.4	37.0	140.7	10km	4.0	3
6	68.4	37.0	140.7	10km	4.0	3

Figure 6: The EEW announcement of multiple simultaneous earthquakes on May 28, 2011 (upper left), the comparison of the estimated JMA seismic intensities in the final EEW and actual observed intensities (lower left), and the locations of the estimated and actual epicenters (right).

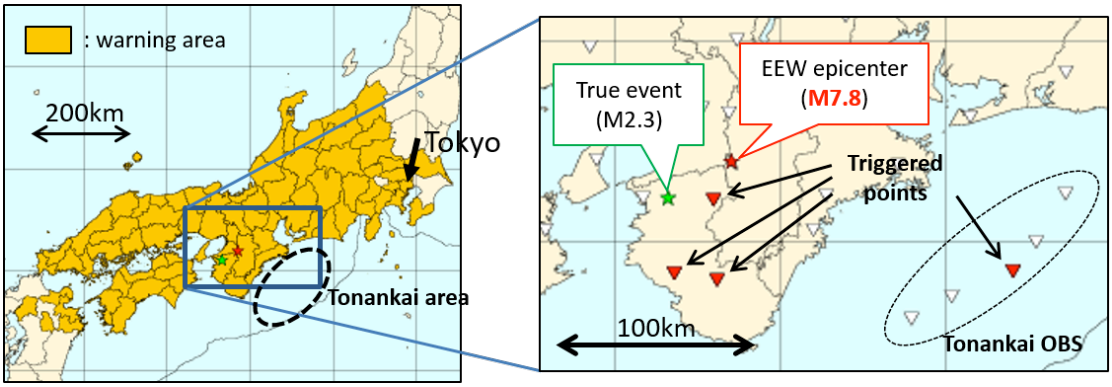

Figure 7: Warning areas for the false alarm on August 8, 2013 (left), and the distribution of observation stations that were triggered and sent auto-picking data (right).

$$\theta^* = \arg\max_{\theta} p(\theta|\boldsymbol{D}) = \arg\max_{\theta} p(\boldsymbol{D}|\theta)\, p(\theta), \qquad (1)$$

where θ is a set of parameters of the hypocenter location and $\boldsymbol{D}$ is a set of observations of characteristic features. The probabilistic distributions of $p(\boldsymbol{D}|\theta)$ and $p(\theta)$ are empirically assumed on basis of past observational data and seismic activity. The distribution of $p(\boldsymbol{D}|\theta)\, p(\theta)$ is calculated using the particle filter method, which gives a numerical solution for θ^*. $\boldsymbol{D}$ contains the distance and direction of hypocenter

(obtained from the B-Δ method and principal component analysis), travel time, and magnitude, and $p(\theta)$ includes the area constraint (calculated from the Voronoi cells) and past seismicity. The use of various types of observational data leads to robust hypocenter determination.

The IPF method has a better algorithm for classifying trigger data than the conventional method. In the present approach, when new trigger data is compared with an existing estimated hypocenter, only the residual of the travel time is used for classification. In the IPF method, residual of the amplitude is used as well as the travel time, which helps distinguish multiple simultaneous earthquakes and noise data robustly.

(2) The PLUM method

The PLUM method (JMA, 2014a; JMA, 2014c) is a simplified version of "numerical shake prediction" (Hoshiba and Aoki, 2015) and is expected to address the under-prediction of a huge earthquake.

The input data of the PLUM method is the real-time seismic intensity (Kunugi *et al.*, 2008). Currently, JMA seismic intensities are sent once, or a few times, from seismic intensity meters that are triggered by earthquake signals. JMA plans to collect real-time seismic intensities every second from its nationwide seismic intensity network even when earthquakes are not occurring.

The PLUM method predicts seismic intensity directly from real-time observed intensities with no need to estimate the hypocenter and magnitude. The basic assumption is that strong motion can propagate 30 km without attenuation. A prediction value is obtained by taking the maximum value of the real-time seismic intensities within 30 km from a target point after taking into account site amplification factors at the observation and prediction points. Figure 8 shows an example of a calculation using the PLUM method. In this case, the prediction value at the target point is 4.5.

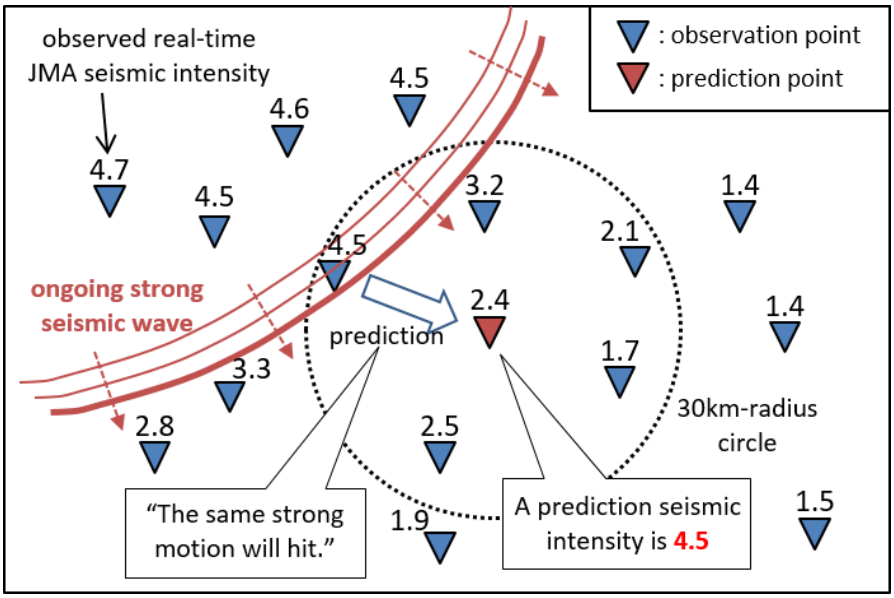

Figure 8: A schematic illustration of a calculation using the PLUM method (modified after JMA, 2014c).

(3) The Hybrid method

JMA plans to use the IPF and PLUM methods concurrently with the Hybrid method to optimize the performance of the EEW system (JMA, 2014a; JMA, 2014c). The two methods have a complementary relationship, and an appropriate combination can generate a method that derives advantages from both. The IPF method can give a long lead time when it determines the appropriate hypocenter and magnitude with the observational data of a few stations; however, it risks under-predicting strong ground motion when a huge earthquake with a large rupture zone occurs. Conversely, the PLUM method has no difficulty with huge earthquakes; however, it does not provide a long lead time because it cannot predict strong ground motion until the corresponding seismic wave is within 30 km from a target point.

JMA proposes the following calculation process for the Hybrid method. (A) If a hypocenter and magnitude estimated by the IPF method are consistent with real-time displacement data of observation stations near the hypocenter, a prediction for each area is given by the maximum of the IPF and PLUM predictions. (B) If the hypocenter and magnitude of the IPF method are inconsistent, a prediction is given only by the PLUM method.

The consistency judgement aims to reduce the risk of issuing false alarms when the IPF method estimates the wrong hypocenter and magnitude. Currently, JMA takes the following steps to perform a judgement: (a) it calculates the "station magnitude" of the station closest to the estimated hypocenter, which is given by the displacement data of the station and the estimated hypocenter location, and (b) it compares the station magnitude and the estimated magnitude and rejects the result of the IPF method if the estimated magnitude is 2.0 or more greater than the station magnitude.

(4) The use of new seismometer networks

Since the EEW operation started, JMA has continued to incorporate various types of new seismometers into the main part of the hypocenter estimation (Table. 1). From 2009 to 2011, the system incorporated a total of 12 strong motion seismometers located on islands and five OBSs in the Tonankai area to improve the rapidity and accuracy of the determination of earthquakes in oceanic areas (JMA, 2009; JMA, 2010; JMA, 2011). In 2015, 50 new strong motion seismometers established near the Pacific coast were added to the system (JMA, 2016b). In addition, the system started using two OBSs in DONET1 of the Japan Agency for Marine-Earth Science and Technology (JAMSTEC) (JAMSTEC, 2011) and 15 deep borehole seismometers in KiK-net of NIED (Okada *et al.*, 2004; Iwakiri *et al.*, 2012) (JMA, 2016b). The two OBSs are anticipated to contribute to the rapid detection of the Nankai Trough earthquake, which is a M9-class earthquake expected to occur along the fault of the Nankai Trough in the future (e.g., Cabinet Office, Government of Japan, 2012). The deep borehole seismometers, located at approximately 500 to 3000 m depths near the Tokyo metropolitan area, are anticipated to shorten the time between the occurrence of an inland earthquake and the detection of the signal.

In addition, JMA has plans to use four additional large-scale seismometer networks after checking their data quality (Fig. 9) (JMA, 2012; JMA, 2014a; JMA, 2016b). S-net

	2007	2008	2009	2010	2011	2012	2013	2014	2015
Strong motion seismometer network, JMA	203	→	205	→	215	→	→	→	265
Ocean-bottom seismometer network, JMA			5	→	→	→	→	→	→
A part of KiK-net, NIED (deep borehole seismometers)									15
DONET1, JAMSTEC (ocean-bottom seismometers)									2

Table 1: History of the number of seismometers used for the main part of the JMA EEW system.

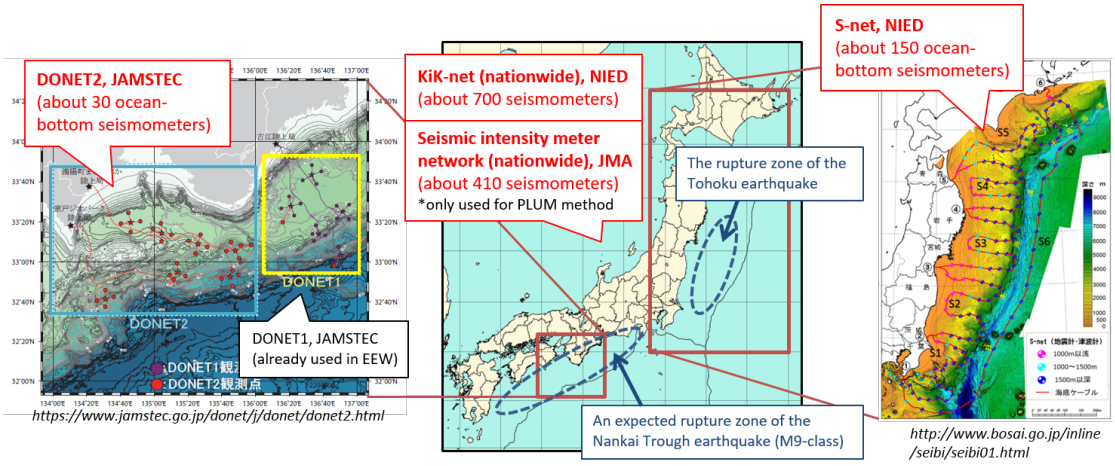

Figure 9: Relationship between S-net, DONET2, KiK-net, and the seismic intensity meter network and the detailed distributions of S-net (right) and DONET2 (left).

of NIED (NIED, 2012) is an OBS network that includes 150 OBSs located near the rupture zone of the Tohoku earthquake, which will improve the system's detection capability for earthquakes near the Japan Trench. DONET2 of JAMSTEC (e.g., JAMSTEC, 2015) is a OBS network that includes approximately 30 OBSs located near DONET1, which will enhance the rapidity of detecting the Nankai Trough earthquake with DONET1. To get a denser inland network, the system will incorporate the rest of KiK-net, which includes approximately 700 strong motion seismometers (Okada *et al.*, 2004). The seismic intensity meter network of JMA, which includes approximately 410 stations, will also be used to collect additional real-time seismic intensity data for the PLUM method.

Summary

JMA has operated its EEW system for the general public since October 2007. The EEW system predicts JMA seismic intensities based on hypocenter and magnitude estimations using several methods. During the past eight years, the system has performed well in general and has contributed to disaster mitigation for major earthquakes such as the Tohoku earthquake. The IPF, PLUM, and Hybrid methods will be introduced to address under-prediction for huge earthquakes and false alarms with

active aftershocks and noise data. The system is also scheduled to incorporate large-scale OBS and inland seismometer networks to enhance its rapidity and accuracy.

Acknowledgments

We would like to thank Professor Dr. Friedemann Wenzel for his helpful comments on the manuscript. The JMA EEW system is based on joint research with JMA and the Railway Technical Research Institute and technological achievements by the National Research Institute for Earth Science and Disaster Prevention. Seismic intensity and waveform data were obtained from the JMA network, K-NET of NIED and local governments and municipals. The figures were drawn with the Generic Mapping Tools (Wessel and Smith, 1995). This work was partially supported by JSPS KAKENHI Grant Number 25282114.

Appendix

The JMA seismic intensity is calculated from "JMA instrumental seismic intensity," which is computed using the following equation:

$$I_{\mathrm{inst}} = 2.0 \log_{10} a_{\mathrm{c}} + 0.94, \tag{2}$$

where I_{inst} is a JMA instrumental intensity, and a_{c} is a value that satisfies

$$\int_{\Delta t} \mu(a(t) \geq a_{\mathrm{c}})\, \mathrm{d}t = 0.3 \text{ sec.}$$
$$\mu(A) \equiv \begin{cases} 1 \text{ if } A \text{ is true} \\ 0 \text{ if } A \text{ is false} \end{cases} \tag{3}$$

Here, $a(t)$ is a time series of the amplitude of the three-component acceleration, which is band-pass filtered near 0.5 Hz, and Δt is the length of the time window (ordinarily set to 60 s). The JMA seismic intensity is obtained by converting I_{inst} into a discrete value according to the 10-degree scale. Figure 10 illustrates the relationship between a_{c}, I_{inst}, and the JMA seismic intensity and a rough comparison with the modified Mercalli intensity scale.

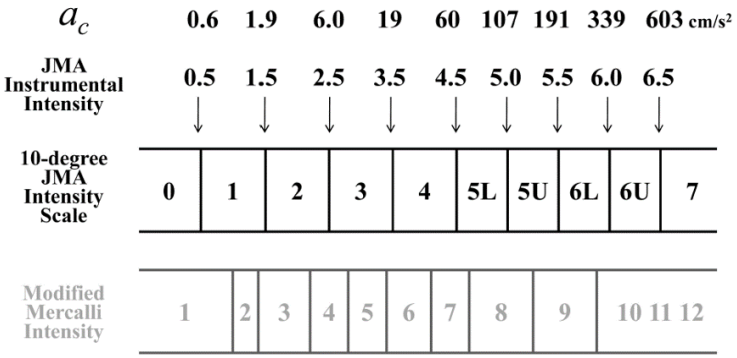

Figure 10: Relationship between a_{c} in Eq. (2), the JMA instrumental intensity, and the JMA seismic intensity and an approximate comparison with the modified Mercalli intensity scale (from Hoshiba et al. (2010)).

References

Abe, K. (2014). Instantaneous prediction of shaking and tsunami (in Japanese), Yomiuri Shimbun, morning newspaper (Osaka version) on 2 June, p.1.

Bishop, C. M. (2006). *Pattern Recognition and Machine Learning,* Springer, Berlin, Germany, 738 pp.

Cabinet Office, Government of Japan (2012). The second report of the committee of huge earthquake model of the Nankai trough (on strong motion fault model) (in Japanese), available at http://www.bousai.go.jp/jishin/nankai/model/pdf /20120829_2nd_report05.pdf (last accessed April 2016).

Horiuchi, S., H. Negishi, K. Abe, A. Kamimura, and Y. Fujinawa (2005). An Automatic Processing System for Broadcasting Earthquake Alarms, *Bull. Seismol. Soc. Am.* **95,** 708–718, doi: 10.1785/0120030133.

Hoshiba, M., O. Kamigaichi, M. Saito, S. Tsukada, and N. Hamada (2008). Earthquake early warning starts nationwide in Japan, *Eos Trans. AGU* **89,** 73–74, doi: 10.1029/2008EO080001.

Hoshiba, M., K. Ohtake, K. Iwakiri, T. Aketagawa, H. Nakamura, and S. Yamamoto (2010). How precisely can we anticipate seismic intensities? A study of uncertainty of anticipated seismic intensities for the Earthquake Early Warning method in Japan, *Earth Planets Space* **62,** 611–620, doi:10.5047/eps.2010.07.013.

Hoshiba, M., K. Iwakiri, N. Hayashimoto, T. Shimoyama, K. Hirano, Y. Yamada, Y. Ishigaki, and H. Kikuta (2011). Outline of the 2011 off the Pacific coast of Tohoku Earthquake (Mw 9.0) Earthquake Early Warning and observed seismic intensity, *Earth Planets Space* **63,** 547–551, doi: 10.5047/eps.2011.05.031.

Hoshiba, M. (2014). Review of the Nationwide Earthquake Early Warning in Japan during Its First Five Years, in *Earthquake Hazard, Risk, and Disasters,* J. F. Shroder (Series Editor) and M. Wyss (Volume Editor), Elsevier, Amsterdam, Netherlands, 505–529, doi:10.1016/B978-0-12-394848-9.00019-5.

Hoshiba, M. and S. Aoki (2015). Numerical Shake Prediction for Earthquake Early Warning: Data Assimilation, Real-time Shake Mapping, and Simulation of Wave Propagation, *Bull. Seismol. Soc. Am.* **105,** 1324-1338, doi: 10.1785/0120140280.

Iwakiri, K., M. Hoshiba, K. Ohtake, and T. Shimoyama (2012). Application of Strong Motion Data Observed in and around Southern Kanto to the Earthquake Early Warning System, *Quarterly Journal of Seismology* **75,** 37–59.

Japan Agency for Marine-Earth Science and Technology (2011). DONET, an Ocean-Floor Observatory Network for Earthquakes and Tsunamis (Press Release), available at http://www.jamstec.go.jp/e/about/press_release/20110826_2/ (last accessed April 2016).

Japan Agency for Marine-Earth Science and Technology (2015). Twenty-eight observatories of DONET2 are working now; just three observatories remain to be installed, available at http://www.jamstec.go.jp/ceat/e/topics/20151222.html (last accessed April 2016).

Japan Meteorological Agency (1996). *Seismic Intensity* (in Japanese), Gyosei, Tokyo, Japan, 238 pp.

Japan Meteorological Agency (2008a). The technical reference on outline and processing method of the Earthquake Early Warning (in Japanese), available at

http://www.data.jma.go.jp/svd/eew/data/nc/katsuyou/reference.pdf (last accessed April 2016).

Japan Meteorological Agency (2008b). On the actual state of utilization of the Earthquake Early Warning for the Iwate-Miyagi Nairiku earthquake in 2008 (Press Release) (in Japanese), available at http://www.jma.go.jp/jma/press/0808/11b/0811eewchousakekka2.pdf (last accessed April 2016).

Japan Meteorological Agency (2009). The first technical panel in the committee of evaluation and improvement of the Earthquake Early Warning (document) (in Japanese), available at http://www.data.jma.go.jp/svd/eqev/data/study-panel/eew-hyoka/t01/shiryou.pdf (last accessed April 2016).

Japan Meteorological Agency (2010). The second technical panel in the committee of evaluation and improvement of the Earthquake Early Warning (document) (in Japanese), available at http://www.data.jma.go.jp/svd/eqev/data/study-panel/eew-hyoka/t02/shiryou.pdf (last accessed April 2016).

Japan Meteorological Agency (2011). The third technical panel in the committee of evaluation and improvement of the Earthquake Early Warning (document No.1) (in Japanese), available at http://www.data.jma.go.jp/svd/eqev/data/study-panel/eew-hyoka/t03/shiryou1.pdf (last accessed April 2016).

Japan Meteorological Agency (2012). The forth technical panel in the committee of evaluation and improvement of the Earthquake Early Warning (document No.1) (in Japanese), available at http://www.data.jma.go.jp/svd/eqev/data/study-panel/eew-hyoka/t04/20121001_siryou1.pdf (last accessed April 2016).

Japan Meteorological Agency (2014a). The fifth technical panel in the committee of evaluation and improvement of the Earthquake Early Warning (document) (in Japanese), available at http://www.data.jma.go.jp/svd/eqev/data/study-panel/eew-hyoka/t05/20140304_siryou.pdf (last accessed April 2016).

Japan Meteorological Agency (2014b). Area names used in Earthquake Information and Earthquake Early Warning (as of April 8th, 2014) (in Japanese), available at http://www.data.jma.go.jp/svd/eqev/data/joho/shindo-name.html (last accessed April 2016).

Japan Meteorological Agency (2014c). On future technical improvements of the Earthquake Early Warning (attached document) (Press Release) (in Japanese), available at http://www.jma.go.jp/jma/press/1407/14a/EEW_kaizen_tech_20140714.pdf (last accessed April 2016).

Japan Meteorological Agency (2015). the JMA report of meteorological service evaluation in fiscal 2015 (document No.2) (in Japanese), available at http://www.jma.go.jp/jma/kishou/hyouka/hyouka-report/27report/27shiryo2.pdf (last accessed April 2016).

Japan Meteorological Agency (2016a). Seismic intensity observation stations (nationwide) (in Japanese), available at http://www.data.jma.go.jp/svd/eqev/data/intens-st/index.html (last accessed May 2016).

Japan Meteorological Agency (2016b). The sixth technical panel in the committee of evaluation and improvement of the Earthquake Early Warning (document No.2) (in Japanese), available at http://www.data.jma.go.jp/svd/eqev/data/study-panel/eew-hyoka/t06/20160224_siryou2.pdf (last accessed April 2016).

Kamigaichi, O. (2004). JMA Earthquake Early Warning, *Journal of Japan Association for Earthquake Engineering* **4,** 134–137.

Kamigaichi, O., M. Saito, K. Doi, T. Matsumori, S. Tsukada, K. Takeda, T. Shimoyama, K. Nakamura, M. Kiyomoto, and Y. Watanabe (2009). Earthquake Early Warning in Japan: Warning the General Public and Future Prospects, *Seismological Research Letters* **80,** 717–726, doi: 10.1785/gssrl.80.5.717.

Kunugi, T., S. Aoi, H. Nakamura, H. Fujiwara, and N. Morikawa (2008). A Real-Time Processing of Seismic Intensity, *Zisin 2* **60,** 243−252 (in Japanese).

National Research Institute for Earth Science and Disaster Prevention (2012). Starting the construction project of seafloor observation network for earthquakes and tsunamis along the Japan trench (Press Release) (in Japanese), available at http://www.bosai.go.jp/press/2011/pdf/20120329_01.pdf (last accessed April 2016).

Odaka, T., K. Ashiya, S. Tsukada, S. Sato, K. Ohtake, and D. Nozaka (2003). A New Method of Quickly Estimating Epicentral Distance and Magnitude from a Single Seismic Record, *Bull. Seismol. Soc. Am.* **93,** 526 − 532.

Okada, Y., K. Kasahara, S. Hori, K. Obara, S. Sekiguchi, H. Fujiwara, and A. Yamamoto (2004). Recent progress of seismic observation networks in Japan Hi-net, F-net, K-NET and KiK-net, *Earth Planets Space* **56,** xv–xxviii.

Tamaribuchi, K., M. Yamada, and S. Wu (2014). A new approach to Identify Multiple Concurrent Events for Improvement of Earthquake Early Warning, *Zisin 2* **67,** 41 − 55 (in Japanese).

Tsukada, S., T. Odaka, K. Ashiya, K. Ohtake, and D. Nozaka (2004). Analysis of the Envelope Wave form of the Initial Part of P-waves and its Application to Quickly Estimating the Epicentral Distance and Magnitude, *Zisin 2* **56,** 351–361 (in Japanese).

Wessel, P. and W. H. F. Smith (1995). New version of the Generic Mapping Tools released, *Eos Trans. AGU* **76,** 329.

ALERTES: An Earthquake Early Warning System for the Ibero-Maghrebian region

E. Buforn[1], A. Pazos[2], A. Roca[3], M. Carranza[1], J. M. Dávila[2], A. Udías[1], A. Zollo[4], M. López[2] and the ALERTES team

[1] Universidad Complutense de Madrid, Madrid, Spain, ebufornp@ucm.es
[2] Real Observatorio de la Armada, San Fernando , Spain
[3] Institut Cartogràfic i Geològic de Catalunya, Barcelona, Spain
[4] University of Naples Federico II, Naples, Italy

Abstract

This paper presents the main results obtained in the ALERTES project aimed to develop an EEWS for the Ibero-Maghrebian region. The occurrence of large and destructive earthquakes, in this region, such as those of Lisbon 1755 or Boumerdes (Algeria) 2003, justifies the development of an EEWS. We have checked empirical correlations to homogenize the different magnitude scales used. Specific correlations between τ_c, P_d and M_w have been developed. The study of the blind zone for SW Iberia shows the feasibility of an EEWS for the region. Results obtained from a prototype of EEWS developed for the region and the PRESTo software show the utility of an EEWS for the region.

Introduction

The Ibero-Maghrebian Region (IMR), including southern Iberian Peninsula and northern Morocco and Algeria, is located at the plate boundary between Eurasia-Africa. The occurrence of large earthquakes in the region is a consequence of the collision between these two plates. Some of these earthquakes have caused severe damage and generated devastating tsunamis (Lisbon 1755, Imax=X; Saint Vincent Cape, 1969 Mw=7.8; Boumerdes 2003, Mw=6.8; Figure 1). The 20th century has been seismically very anomalous in the IMR, with a deficit of large earthquakes (Buforn et al., 2015). However, some of the moderate magnitude events (5.0<Mw<6.5) occurred in this region have produced severe damage (Al-Hoceima, 2004; Lorca, 2011) or caused social unrest (Alboran, 2016). In order to mitigate the damage generated by earthquakes in the region in 2011 a feasibility study has been launched to asses the potential of an Earthquake Early Warning System (EEWS) in the region: the ALERTES (2011-2013) and the ALERTES-RIM (2014-2016) projects.

These projects are coordinated by the Universidad Complutense de Madrid (UCM) with the participation of Real Instituto y Observatorio de la Armada de San Fernando, Cádiz (ROA) and the Institut Geologic de Cataluña (IGC). Researchers from other institutions such, as the Instituto Geográfico Nacional (IGN, Madrid, Spain) University Federico II (Naples, Italy), Instituto Portugués do Mar et Atmósfera (IPMA, Portugal), University of Evora (Portugal), GFZ (Potsdam, Germany), Institut

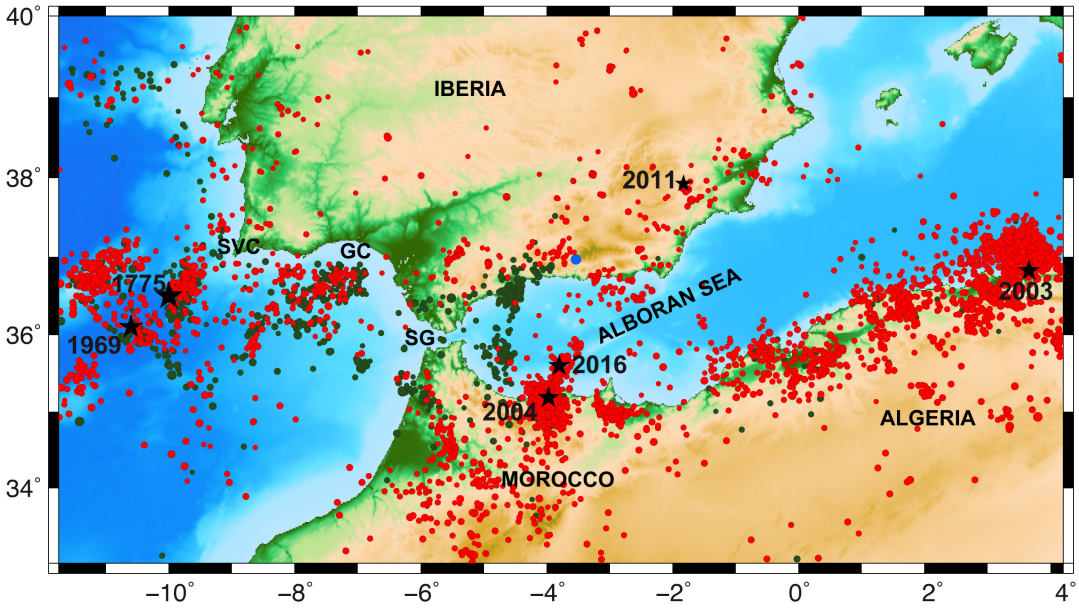

Figure 1. Distribution of epicenters (M>3.0) for the period 2001-2016 taken from the Instituto Geográfico Nacional Data Base. In red shallow earthquakes (h<40 km), in green intermediate depth events (40<h<150 km), in blue very deep events (h≈650km). Stars correspond to large or damaging earthquakes occurred in the Ibero-Maghrebian region. SVC= Saint Vincent Cape, GC= Gulf of Cadiz, SG= Strait of Gibraltar

Scientifique Mohamed V (Morocco), Instituto Técnico Superior (Lisbon, Portugal), etc participated together with the Spanish groups.

The basic hypothesis on which EEWS's are based is that the initial portion of P waves contains sufficient information on the final size of an earthquake (Wu and Kanamori, 2005a). Several parameters obtained from the early portion of P wave (2-4 seconds) are then used as Earthquakes Early Warning (EEW) parameters (Allen and Kanamori, 2003; Kanamori, 2005; Wu and Zhao, 2006; Festa *et al*., 2008). The analysis of the relation between these EEW parameters and the magnitude of earthquakes allows to obtain empirical correlations between them. These empirical correlations are used in the EEWS for a rapid estimation of the final size of an earthquake and therefore of its potential damage (Kanamori, 2005; Wu and Kanamori, 2005b; Zollo *et al*, 2006, 2013).

First the ALERTES project was focused on the feasibility of an EEWS for the SW of Iberia, mainly on the region of Saint Vincent Cape and Gulf of Cadiz where the 1755 and 1969 large earthquakes occurred. Second the EEWS has been extended to the whole region, from Saint Vincent Cape to Algeria. In this study we report specific correlations between the EEW parameters for the IMR, a re-assesment of the blind zone spatial extent and a prototype developed for IMR.

Database

We have used real time data recorded by broad-band velocity stations of three different networks installed in the region (Figure 2): IGN seismic network (Spain, black triangles), IPMA network (Portugal, blue triangles) and Western Mediterranean

network (ROA/UCM, Spain, red triangles). The data base corresponds to earthquakes which occurred in the period 2001-2016, with magnitude M_w larger than 3.1 and focus at shallow depth (less than 40km). For this period the number of strong motion records available is very small due to the lack of large earthquakes in the region.

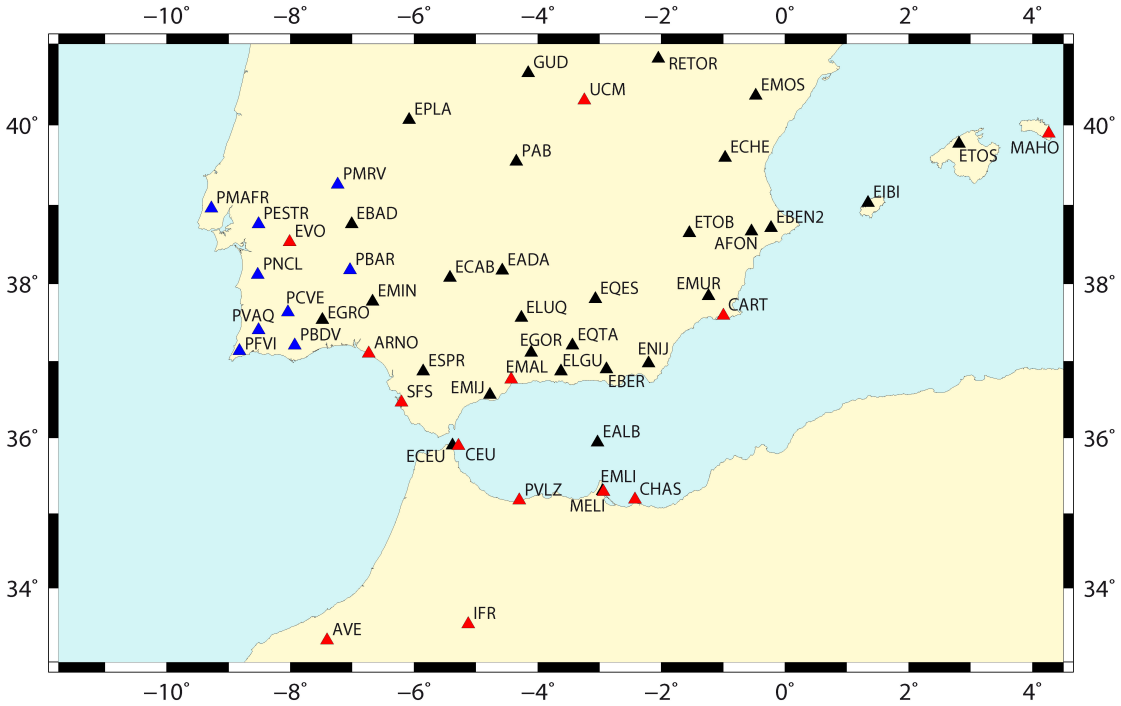

Figure 2. Distribution of stations used in the ALERTES project. In blue stations from Instituto Portugues do Mar et Atmósfera (Portugal), black from Instituto Geográfico Nacional (Spain) and red from Western Mediterranean network (WM).

In order to address the poor azimuthal coverage for off-shore earthquakes 6 broad band OBS instruments (FOMAR network, ROA and UCM) have been deployed. The first survey was located near the Strait of Gibraltar (January-November 2014) and the second west of Saint Vincent Cape from September 2015 to April 2016.

A problem with our data base is the non-homogeneity of magnitudes for earthquakes in the IMR. The IGN uses three different magnitude scales: the local magnitude M_{bLg}, (based on Lg waves amplitudes), the body wave magnitude m_b(V-C) and the moment magnitude M_w (http://www.ign.es/ign/head/sismoTipoMagnitud.do). The IPMA uses a local magnitude different from that of IGN. Consequently, the first step has been to homogenize the magnitudes of the data base using empirical correlations between the different scales developed by the IGN (Cabañas *et al*, 2015). We have converted to M_w magnitude all the different magnitudes of earthquakes in our data base. In order to check these correlations, we have selected earthquakes occurred in the region with moment magnitude (M_w) estimated by different authors and methods. We have plotted these values (M_w) versus the converted catalogue magnitude (M_c^* equivalent to the moment magnitude M_w) using the following empirical correlations (Figure 3).

$$M_c^* = 1.213 m_{b(v-c)} - 1.528$$
$$M_c^* = 0.836 m_{bLg(L)} + 0.676$$

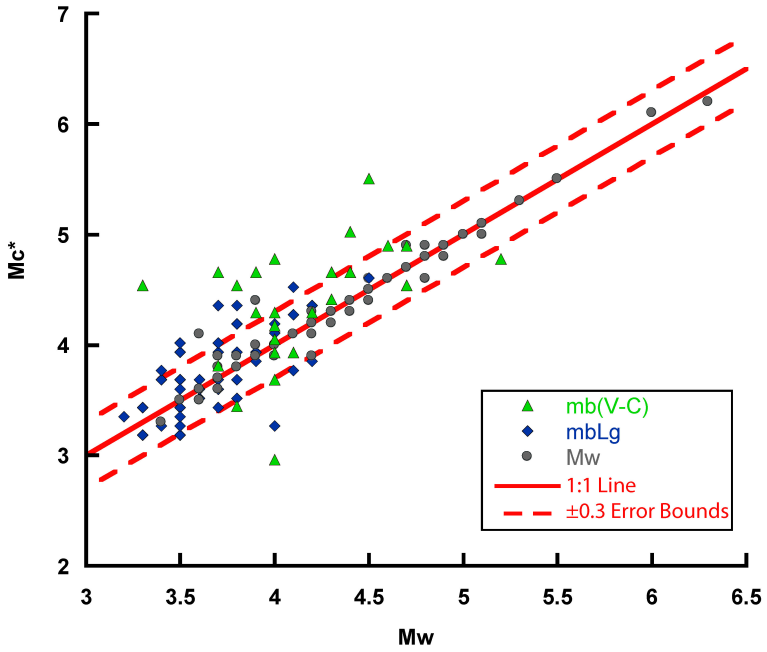

Figure 3. Magnitude M_c^* versus M_w. Symbols correspond to the different magnitudes used by the IGN. Continuous line slope 1, dashed lines are the ±0.3 error bounds

We observe that most earthquakes are around the solid line (slope=1) within the error bounds (dashed lines). The worst agreement is for the m_b(V-C) converted magnitudes (green triangles in Figure 3). Details of the study may be found in Carranza *et al.*, (2015).

Empirical correlations for IMR

In the ALERTES project we have mainly used the predominant period τ_c and the peak ground displacement P_d as EEW parameters (Carranza *et al.*, 2013). The τ_c (Wu and Kanamori, 2005a) is defined as:

$$\tau_c = 2\pi\sqrt{\int_0^{\tau_0} u^2(t)dt / \int_0^{\tau_0} v^2(t)dt},$$

where *u(t)* and *v(t)* are the displacement and the velocity measured over a time window of τ_0 seconds (normally 3 seconds) starting at the first P arrival. The P_d is defined as the peak ground displacement of P wave at the τ_0 window corrected to a reference distance (Wu and Zhao, 2006; Wu *et al.*, 2007; Lancieri and Zollo, 2008; Zollo *et al.,* 2009).

From our data base, we have selected data from those earthquakes where the signal-noise ratio is greater than 5 (Carranza *et al.*, 2015). Using these data, we have developed specific correlations between τ_c, P_d and M_w for IMR (Figure 4). To obtain the predominant period we have used the vertical component, integrated to obtain displacement and applied a high pass Butterworth filter with corner at 0.075 Hz to remove the low frequencies introduced by the integration. For P_d we have used the same type of processing and reference distance of 10 km. For both parameters we use a time window of 3 seconds. A problem in our correlations is the lack of observations for large earthquakes. The largest shock occurred in this area is the 2003 Boumerdes

earthquake (M_w=6.8). This earthquake has been used to test the correlations obtained, concluding that a larger time window is necessary (Carranza *et al.,* 2015).

Linear regression lines were obtained by averaging τ_c and P_d in bins of ΔMw = 0.3 and weighted each bin by the standard deviation of each bin (short vertical red lines). The regression line (solid red line in Figures 4a and 4b) has a slope of 0.30 for the predominant period and 1.00 for the peak of ground displacement (Carranza *et al*., 2013, 2015). To obtain the correlation between P_d and magnitude M_w we have first corrected for the attenuation using the expression

$$\log P_d = -4.6(\pm 0.2) + 1.02(\pm 0.03) M_w - 1.70(\pm 0.08) \log R,$$

where R is the reference distance.

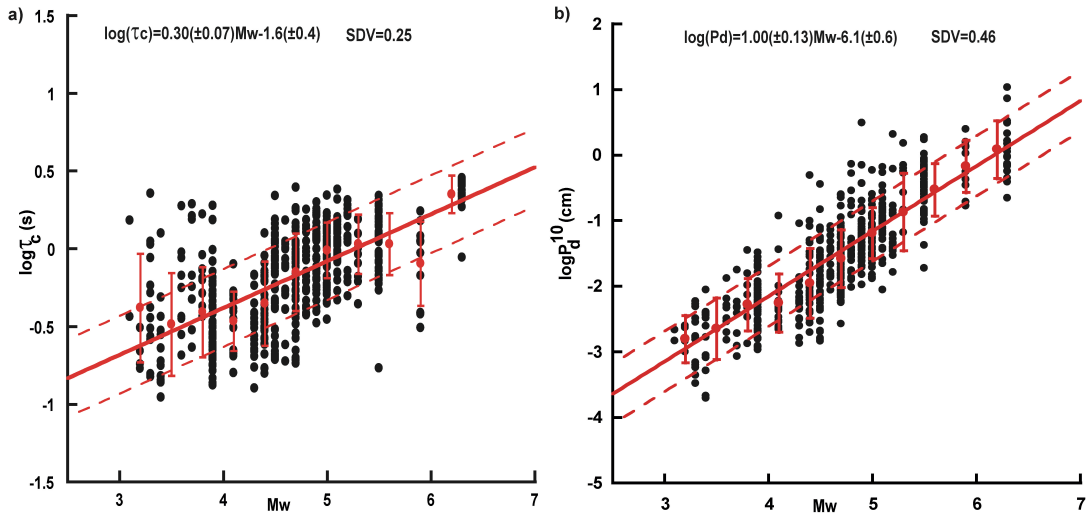

Figure 4. τ_c versus M_w (top) and P_d versus M_w bottom. The reduced distance is 10km. Red circles are the average values for each bin ($\Delta M = 0.3$) with their standard deviations. Red continuous line is the best fit for the means and dashed lines the $\pm 1\sigma$ standard deviation bounds.

Assessing the blind zone

An important problem in an EEWS is the blind zone, that is, the area around the epicenter where no warning can be provided (Kanamori, 2005; Allen *et a*l., 2009). In order to check the extension of the blind zone for SW Iberia we have carried out several simulations using different epicenter locations. In figure 5 we show an example for two earthquakes occurred close to the 1755 earthquake, the 12-02-2007, M_w=6.1 and 17-12-2009, M_w=5.5 (named events SV1 and SV2 respectively), with well constrained hypocentral parameters (Pro *et al*., 2013) and low noise level. We have used two different software packages: SeisComP3 (Hanka *et al*., 2010) and Earthworm (U. S. Geological Survey, 2005), both with a specific configuration for this zone. In addition we have used the PRESTo software (Satriano *et al*., 2010) to validate these results. We have used the empirical correlations obtained by Carranza *et al*. (2013) for a rapid estimation of the magnitude and the same Earth model. Several simulations have been carried out with a minimum of six-stations association, before to declare an event. Details of this study may be found in Pazos *et al*. (2015).

In figure 5 we show a comparison between the results obtained using Earthworm (A), SeisComp3 (B) and PRESTo (C) software. The epicenter estimated by these different systems is indicated by a star and the blind zone is shown as a circle. In figure 5D we have plotted the blind zone estimated by these three software using the epicenter determined by the Instituto Geográfico Nacional (IGN).

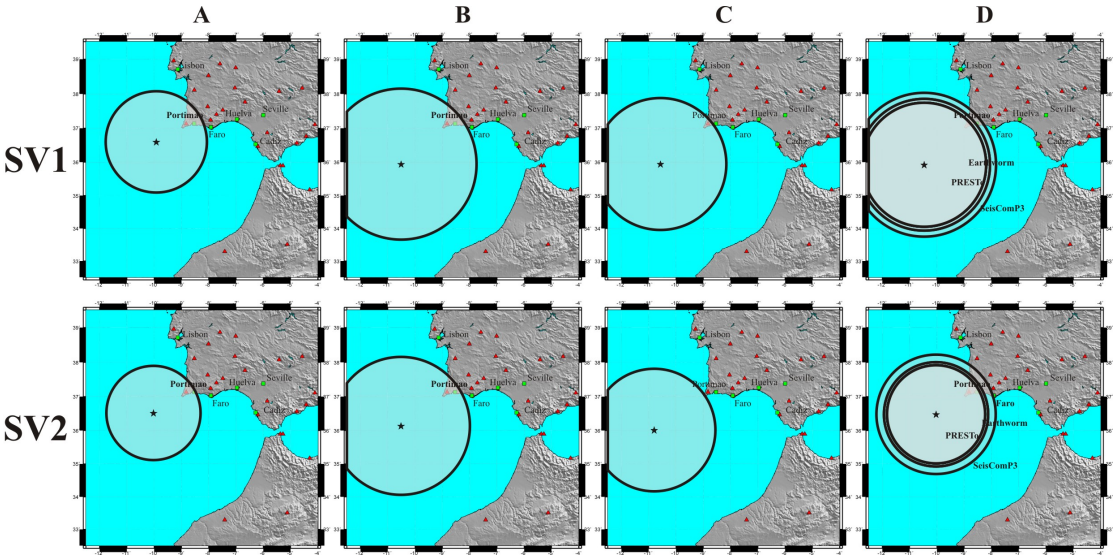

Figure 5.- Blind zone for SV1 and SV2 earthquakes occurred close to the 1755 event. Stars are the epicenter located by Earthworm (A), SeisComP3 (B), PRESTO (C), and by these software using the IGN epicentre (modified from Pazos et al., 2015)

From figure 5 we observe that in all cases the epicenter estimated is very similar, and thus an EEWS can be considered to be feasible for SW Iberia. For an earthquake with epicenter close of that of 1755 only the region of Saint Vincent Cape is inside of the blind zone, while for other more distant sites, such as Cadiz, Seville or Lisbon a warning would be possible. Estimated lead times, defined as the time elapsed between the alert notification and the S-wave arrival to a site, are for example, 5-15s for Faro, 30-40s for Huelva and Lisbon, 40-50s for Cadiz and 55-65s for Seville (Carranza *et al*., 2013; Pazos *et al*., 2015.

New developments

Pazos *et al.,* (2015), recommended that new magnitude modules should be developed and incorporated for Earthworm and SeisComP3. For this reason a prototype called ALERTES-SC3 has been developed in the framework of the ALERTES and ALERTES-RIM projects. This is a specific software developed for the Ibero-Maghrebian region and it is based on the SeisComP3, but adding a new module (López Mesa *et al*., 2015) and using the specific correlations developed by Carranza *et al*., (2013). The structure is shown in figure 6. In green the modules from the original SeisComP3, in yellow the modified modules and the new SCALERTES modulus. This prototype is currently under test at ROA.

In figure 7 we show some examples of results obtained by this prototype for the Saint Vincent Cape region. In black are the epicenters estimated by the ALERTES-C3

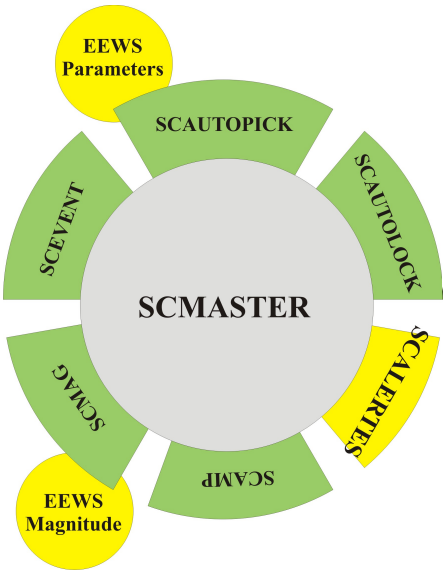

Figure 6. Scheme of the ALERTES-CS3 prototype. In yellow new modules developed.

prototype using 6 picks and in red the epicenters located by the IGN. Triangles correspond to stations used by the prototype. We observe a good agreement between the ALERTES-SC3 epicenters and those determined by IGN. This prototype needs to be improved and will be extended to the whole Ibero-Maghrebian region in the next years.

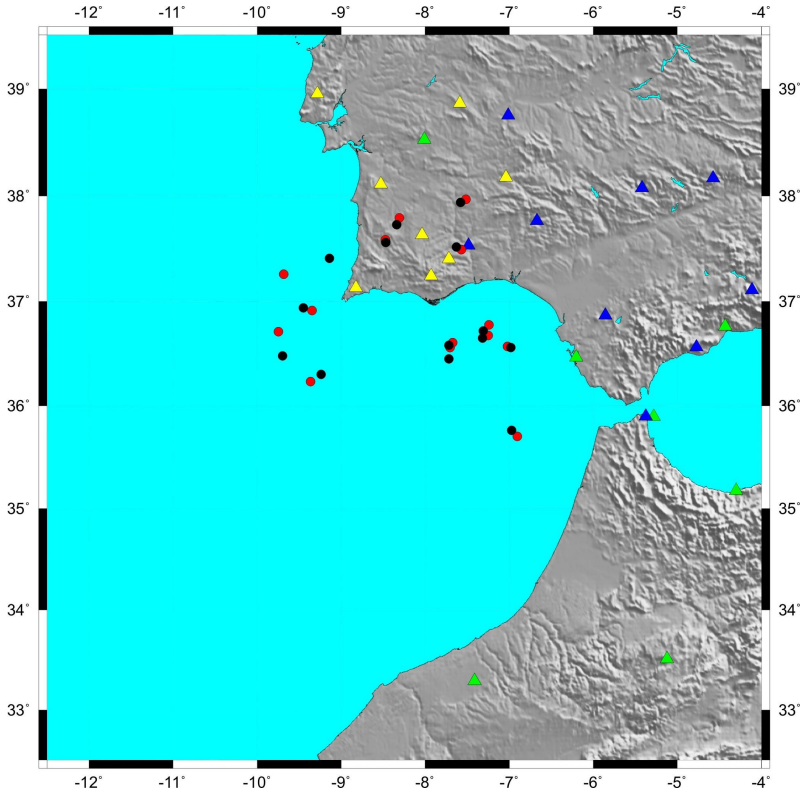

Figure 7. Testing the ALERTES-SC3 prototype. Red circles are the epicenters estimated by IGN and black circles by the ALERTES-SC3. Blue triangles stations from IGN network, yellow IPMA network and green WM network.

In addition to this prototype, the PRESTo software has been installed at the UCM. The method has been adapted to the IMR using the Earth model for the region and the empirical correlations developed by Carranza *et al.*, (2013). An example of its application is shown in figure 8. It corresponds to the Mw = 6.4 South Alboran Sea earthquake of 25 January 2016. The system is configured to give the alert with 5 stations detecting the earthquake. The alert was issued 23s after the occurrence of the earthquake. This time may decrease if PVLZ and MELI stations would have been working, but unfortunately for this earthquake they were not operative. The lead time is 8s for Malaga city and 16s for Almeria. The city of Melilla, however, is in the blind zone. The estimated Mw is 6.7 using the first 5 stations, but the final magnitude, using 21 stations is 6.4, in agreement with the final value estimated by other agencies. The difference in the location of the epicenter in comparison with those of IGN or CSEM is less than 10 km and in the estimated origin time less than 1s.

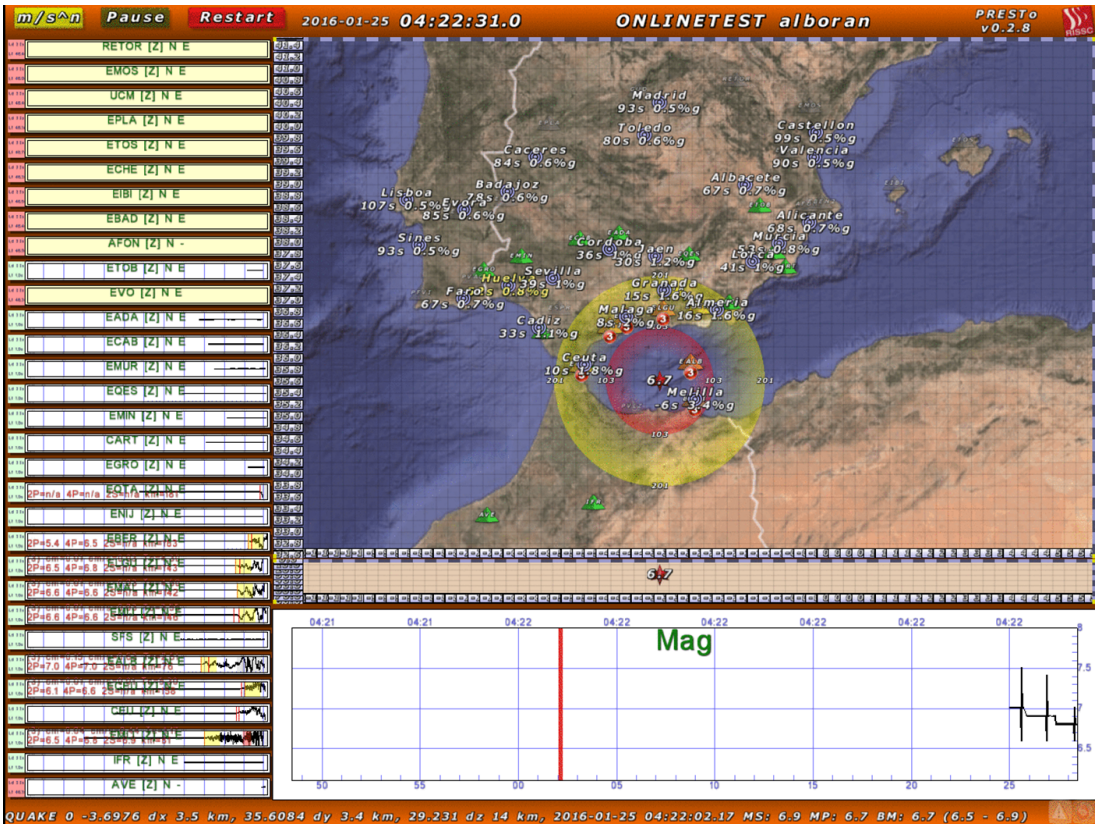

Figure 8. Example of the PRESTo for the 25 January 2016 South Alboran Sea earthquake (Mw=6.4)

Conclusions

From 2011 an EEWS has been developed for the Ibero-Magrebian region. As a first step, in order to homogenize the different scales of magnitude used by the IGN for earthquakes in the region, empirical correlations were developed between the magnitudes. Results presented here show that they are a good approximation to solve this problem and their application allows the conversion to Mw magnitudes of those given by other scales used for earthquakes in this region.

We have obtained specific correlations for the IMR for a rapid estimation of the Mw magnitude for earthquakes using the alert-parameters τ_c and P_d. The study of the

blind zone for SW of Iberia shows that for an earthquake with epicenter similar to that of 1755, it is possible to issue an alert, with lead-times between 5 and 60s for localities of SW Iberia.

An EEWS prototype, called ALERTES-SC3, based on SeisComP3 is under testing. Preliminary results show a good agreement between the epicenters estimated by the prototype and those determined by IGN using standard methods. Also an adaptation of the PRESTo software has been developed and tested showing good results for earthquakes in SE Iberia. The ALERTES projects show that an EEWS is feasible for the Ibero-Maghrebian region.

Acknowledgements

This work has been partially supported by the MINECO (Spain) projects CGL2010-19803-C3 and CGL2013-45724-C3-R, Universidad Complutense de Madrid- CEI project INNOCAMPUS and the Spanish Navy. Authors want to thank their support to the institutions participants in the ALERTES and ALERTES-RIM projects, namely: Instituto Geográfico Nacional (Spain), University of Extremadura (Spain), Instituto Portugues do Mar et Atmosfera (Portugal), University Federico II, Naples (Italy), University of Evora (Portugal), University of Cadiz (Spain), GFZ (Potsdam, Germany), Institut Scientifique Mohamed V (Rabat, Morocco), Instituto Técnico Superior (Lisbon, Portugal).

References

Allen, R.M. and H. Kanamori (2003). The potential for earthquake early warning in southern California. *Science* 300, 786–789

Buforn, E., M. Bezzeghoud, A. Udías and C. Pro (2004). Seismic sources on the Iberia-African plate boundary and their tectonic implications. *Pure Appl. Geophys.*, 161, 623-646

Buforn, E., A. Udías and C. Pro (2015). Large earthquakes at the Ibero-Maghrebian region. Basis for an EEWS. *Pure Appl. Geophys*. doi 10.1007/s00024-014-0954-0

Cabañas. L., A. Rivas-Medina, J. M. Martínez Solares, J. M. Gaspar-Escribano, B. Benito, R. Antón and S. Ruíz-Barajas (2015). Relationships between Mw and other earthquake size parameters in the Spanish IGN Catalogue. *Pure Appl. Geophys*. 172

Carranza, M., E. Buforn, S. Collombelli and A. Zollo (2013). Earthquake early warning for southern Iberia: A P wave threshold-based approach. *Geophys. Res. Lett*. 40, 45-88-4593

Carranza, M., E. Buforn and A. Zollo. (2015). Testing the Earthquake Early Warning parameter correlations in the southern Iberia Peninsula. *Pure Appl. Geophys*. 172, 2435-2448

Festa, G., A. Zollo and M. Lancieri (2008). Earthquake magnitude estimation from early radiated energy. *Geophys. Res. Lett.,* 35, L22307.

Hanka, W., J. Saul, B. Weber, J. Becker, P. Harjadi, Fauzi, and GITEWS Seismology Group (2010). Real-time earthquake monitoring for tsunami warning in the Indian Ocean and beyond. *Nat. Hazards Earth Syst. Sci*. 10, 2611–2622.

Kanamori, H. (2005). Real-time seismology and earthquake damage mitigation. *Ann. Rev. Earth Planet Sci.,* 33, 195–214

Lancieri, M. and A. Zollo (2008). A Bayesian approach to the real-time estimation of magnitude from the early P and S wave displacement peaks. *J. Geophys. Res.,*113, B12302

López Mesa, M., A. Pazos, J. Martín Dávila, J. Gallego, C. Rioja, A. Morgado-Estévez (2015). Boletín ROA 03/15. Ministerio de Defensa, NIPO 083-15-311-7

Pazos, A., N. Romeu, L. Lozano, Y. Colom, M. López Mesa, X. Goula, J. A. Jara, J. V. Cantavella, A. Zollo. W. Hanka and F. Carrilho (2015). A regional approach for Earthquake Early Warning in south west Iberia: a feasibility study. *Bull. Seism. Soc. Am*. 105,. 560–567, doi: 10.1785/0120140101

Pro, C., E. Buforn, M. Bezzeghoud and A. Udías (2013). The earthquakes of 29 July 2003, 12 February 2007, and 17 December 2009 in the region of Cape Saint Vincent (SW Iberia) and their relation with the 1755 Lisbon earthquake. *Tectonophysics* 583, 16-27, dx.doi.org/10.1016/j.tecto.2012.10.010

Satriano, C., L. Elia, C. Martino, M. Lancieri, and A. Zollo (2010). PRESTo, the earthquake early warning system for Southern Italy: Concepts, capabilities and future perspectives. *Soil. Dynam. Earthq. Eng*., 31,137–153,

doi :10.1016/j.soildyn.2010.06.008

U.S. Geological Survey (2005). Earthworm Documentation v6.2, http://folkworm.ceri.memphis.edu/ew-doc/index.html

Wu, Y-M. and H. Kanamori (2005a). Experiment on an onsite early warning method for the Taiwan early warning system. *Bull. Seism. Soc. Am.,* 95, 347-353

Wu, Y-M. and H. Kanamori (2005b). Rapid assessment of damage potential of earthquakes in Taiwan from the beginning of P-waves. *Bull. Seism. Soc. Am.,*95, 3, 1181-11.

Wu, Y-M. and L. Zhao (2006). Magnitude estimation using the first three seconds of P-wave amplitude in earthquake early warning. *Geophys. Res. Lett*., 33, L16312

Wu, Y-M., H. Kanamori, R.M. Allen and E. Acusón (2007). Determination of earthquake early warning parameters, τc and Pd, for southern California. *Geophys. J. Int.,*170 711-717

Zollo, A., M. Lancieri and S. Nielsen (2006). Earthquake magnitude estimation from peak amplitudes of very early seismic signals on strong motion records. *Geophys. Res. Lett.* 33, L23312

Zollo, A., G. Iannaccone, V. Convertito, L. Elia, I. Iervolino, M. Lancieri, A. Lomax, C. Martino, C. Satriano,E. Weber and P. Gasparini (2009). The earthquake early warning system in Southern Italy. *Encyclopedia of Complexity and System Science,* 5, 2395-2421

Zollo, A, O. Amoroso, M. Lancieri, Y-M. Wu and H. Kanamori (2010). A threshold-based earthquake early warning using dense accelerometer networks. *Geophys. J. Int.,* 183 963-974

Zollo, A., S. Colombelli, L. Elia, A. Emolo, G. Festa, G. Iannaccone, C. Martino and P. Gasparini (2013). An integrated regional and on-site Earthquake Early Warning System for Southern Italy: Concepts, methodologies and performances. In: Wenzel and Zschau (eds.) *Early Warning for Geological Disasters, Scientific Concepts and Current Practice*, Springer, Berlin, 117–136.

Stability of Ocean Bottom Seismograph data exposed to strong shaking: Efforts for utilizing OBS for Earthquake Early Warning

Naoki Hayashimoto[1,*], Takeshi Nakamura[2,†] Mitsuyuki Hoshiba[1]

[1] Meteorological Research Institute, Japan Meteorological Agency, 1-1 Nagamine, Tsukuba 305-0052, Japan, hayashim@mri-jma.go.jp
[2] Japan Agency for Marine-Science and Technology, 3173-25, Showa-machi, Kanazawa-ku, Yokohama 236-0001, Japan

Abstract

We investigated in-line cable type ocean-bottom seismograph (OBS) data exposed to strong shaking to evaluate its usability for Earthquake Early Warning (EEW) system operated by Japan Meteorological Agency (JMA). We analysed acceleration waveforms of the Off-Kushiro OBS. We found that the change of acceleration offset caused by inclination of OBS increases with increasing input acceleration (PGA) at strong ground motions of over 100 cm/s^2. Since displacement waveforms used in magnitude estimation of JMA EEW are obtained from integration of acceleration waveforms by using the recursive filter, acceleration offset change during earthquake may cause overestimation of the EEW magnitude. To estimate more stable magnitudes from OBS data, we propose an alternative estimation method by using the maximum amplitude of vertical component displacement waveform.

Introduction

Megathrust earthquakes sometimes occur in subduction areas around the Japanese archipelago like the 2011 off the Pacific coast of Tohoku earthquake (Mw 9.0). The installation of ocean-bottom seismograph (OBS) systems will have an important role in monitoring earthquakes. In recent years, huge-scale OBS networks, such as S-net (deployed by NIED: National Research Institute for Earth Science and Disaster Resilience) and DONET (deployed by JAMSTEC: Japan Agency for Marine-Earth Science and Technology) are now under construction in Japan to make use of those data for real-time monitoring, and it is expected that those OBS systems are able to contribute to rapid EEW issuance. However, since OBSs are installed on unconsolidated marine sediments, we should note the differences between the installation environment of OBSs and those of land stations. The quality check of

* At present: Japan Meteorological Agency, 1-3-4 Otemachi, Chiyoda-ku, Tokyo 100-8122, Japan
† At present: National Research Institute for Earth Science and Disaster Resilience, 3-1 Tennodai, Tsukuba 305-0006, Japan

OBS data and the evaluation of stability for waveform analyses at strong motion are one of the important issues in the data processing for EEW because of the worse condition for the coupling of seismometer to the seafloor compared with that to the free surface in land areas. Duennebier and Sutton (1995) suggested that the discontinuity of shear-wave across the seafloor boundary results in torques that cause package rotation of pop-up type OBS in response to horizontal relative motion between the water and the sea-floor. At the 2003 Tokachi-oki earthquake (JMA catalogue magnitude M_{jma} 8.0), Yamamoto *et al*. (2004) suggested that one seismometer enclosed within a cable line in the Long-Term Deep Sea Floor Observatory off Kushiro-Tokachi deployed in the Kuril Trench (operated by JAMSTEC, hereafter we call this system as the "Off-Kushiro OBS") was rotated about 5 degree by the strong motion. The seismometer observed anomalous signals of long-period components that are possibly associated with this rotation. In the current JMA EEW system, since hypocenter and magnitude are promptly determined by using real-time data from several stations near the epicenter (Kamigaichi *et al*. (2008), Hoshiba *et al*. (2008)), OBS data with such anomalous signals might cause inaccurate EEW information. In this study, we investigate the characteristic features of OBS data exposed to strong ground motion at the Off-Kushiro OBS as a representative of in-line cable type OBS, and estimate the influence of the signals to the EEW magnitude estimation. We also investigate H/V and H/H spectral ratio from S-wave portion to investigate the coupling between the OBS and seafloor. Finally, we propose a new approach to improve the EEW magnitude estimation using OBS data.

Data and Methods

We analyze acceleration waveforms observed at Off-Kushiro OBSs in Figure 1a. The OBS system which is the in-line cable system composed of three seismic stations

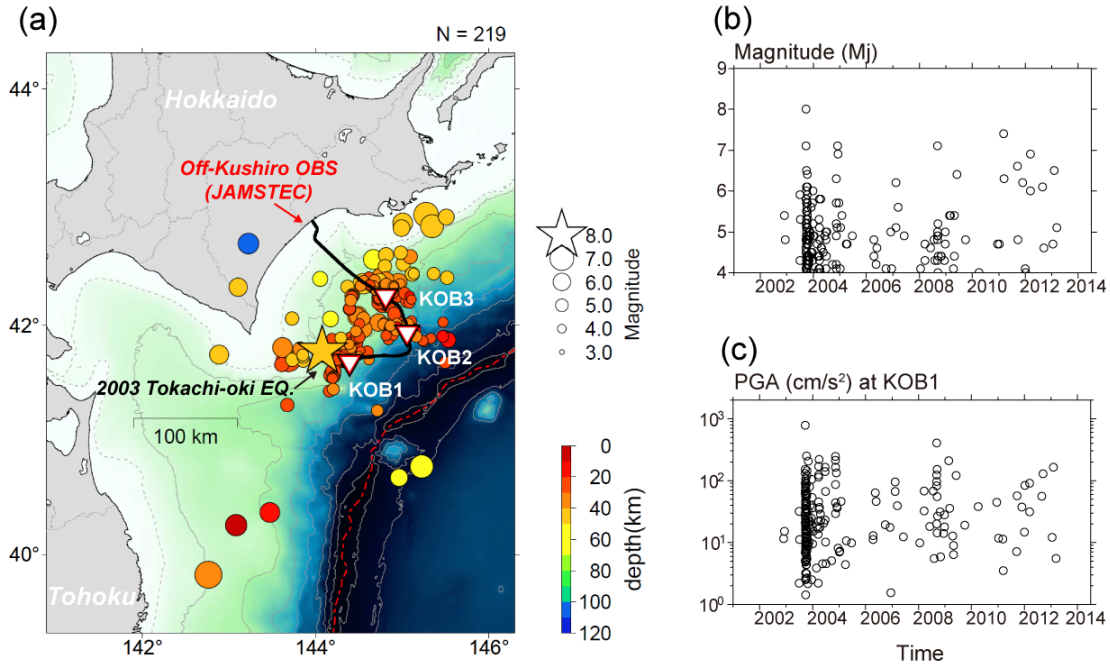

Figure 1: (a) Location map of station and earthquake epicenter used in offset analysis. Black line indicates the cable line of Off-Kushiro OBS. White inverted triangles on the cable line indicate the location of OBSs. (b) Time series of earthquake magnitude (M_{jma}). (c) Time series of PGA recorded at the KOB1 station.

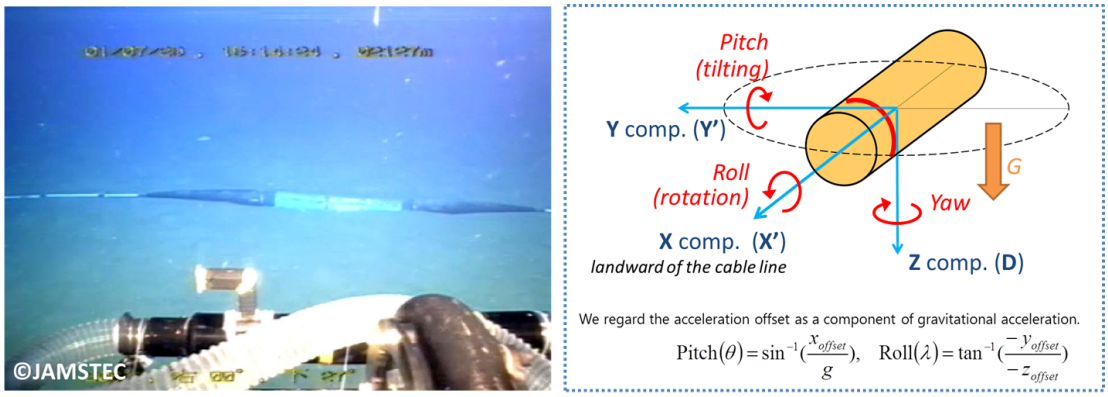

Figure 2: (left) Picture of installation situation of In-line cable type OBS. After the picture was taken by ROV, Off-Kushiro OBSs were buried under the surface of seafloor in June and July 2002. (right) A schematic illustration of an acceleration seismometer enclosed within a cylindrical pressure housing and the direction of the three components in the seismometer.

(KOB1, KOB2 and KOB3) has recorded a lot of strong ground motion data such as the 2003 Tokachi-oki earthquake (Fig. 1b, c). In this system, three-component acceleration sensors (JA-5III made by Japan Aero Electronics Corporation, Hirata *et al*. (2002)) are equipped in the cylindrical pressure housing (length: 169.5cm, diameter: 26.5 cm, Fig. 2) and are able to record ground motion up to DC component. Since one component is oriented in the direction along the cable line, the component records motions parallel to the line on a nearly horizontal plane (X in Fig. 2). The other two components (Y and Z in Fig. 2) are not aligned in the vertical and horizontal direction. Since gimbal units are not installed in this system, we need to correct the inclination of each component from gravitational acceleration offset for the further analyses of waveforms in the horizontal and vertical component. We analyze waveform data that are those at earthquakes with the predicted peak ground acceleration (PGA) of more than 10 cm/s^2 at Off-Kushiro OBS by using the following empirical attenuation relationship (Fukushima and Tanaka (1992)):

$$\log_{10} A = 0.51 \cdot M_{jma} - \log_{10}\left(R + 0.006 \cdot 10^{0.51 M_{jma}}\right) - 0.0033 \cdot R + 0.59, \qquad (1)$$

where A and R is PGA (in cm/s^2) and the epicentral distance (in km), respectively.
Fig. 3 shows a flow of the processing to obtain waveform data of the horizontal and vertical component at KOB1 station at the 2003 Tokachi-oki earthquake (M_{jma} 8.0). Firstly, we estimate the time-series variation of attitude angle of OBS housing from gravitational acceleration offsets. By applying cascaded median-filter (Kinoshita (2008), 2s and 50s are used in this study) for the original acceleration records, we estimate acceleration offset change during earthquakes (Fig. 3b). We regard the acceleration offset as a component of gravitational acceleration, and estimate roll-angle and pitch-angle of OBS cylindrical housing by estimating Euler's angle rotation (Fig. 3c). Secondary, we convert 3-component waveforms (X, Y, Z) to vertical and two horizontal component waveforms (X', Y', UD) by correcting roll-angle and pitch-angle from estimated attitude angle of OBS before the arrival of seismic waves (Fig. 3e). We then convert to displacement waveform by using recursive filter which provides equivalent characteristics to the displacement seismometer having an eigenperiod of 6 s and damping factor h=0.5 (Fig. 3f). We also estimate H/V and H/H spectral ratio from Fourier spectra of S-wave portion (Fig. 3d).

Acceleration offsets caused by OBS Inclination

Fig. 3c indicates the attitude angle change of KOB1 station at the 2003 Tokachi-oki earthquake. The roll-angle of KOB1 changed -5.2 degrees during the earthquake, which is consistent with the previous study of Yamamoto *et al*. (2004). Fig. 4a shows a comparison between PGA and attitude angle changes at KOB3 station at all earthquakes shown in Fig. 1a. Fig. 4b indicates a relationship between PGA and acceleration offset changes. It should be noted that the acceleration offset caused by slight inclination of OBS increases with increasing input acceleration (PGA). At strong ground motions of over 100 cm/s^2, the roll angle variations are clearly larger than the pitch angle variations, and the acceleration offsets on the horizontal component Y' (perpendicular to the cable line) are significantly larger than those on the other horizontal X' (along the cable line) and the vertical UD component (Fig. 4b).

Magnitude of JMA EEW is mainly determined from the maximum amplitude of three-component vector summation of displacement waveform. We obtain the displacement waveform integrated from acceleration waveform using the recursive filter. In this conversion process, the acceleration offset can remain as an offset to the displacement waveform. Thus, for acceleration offset data, the EEW magnitude might be overestimated because the offsets lead to the displacement waveforms with large displacement offsets (Fig. 3f) and Fig. 4c).

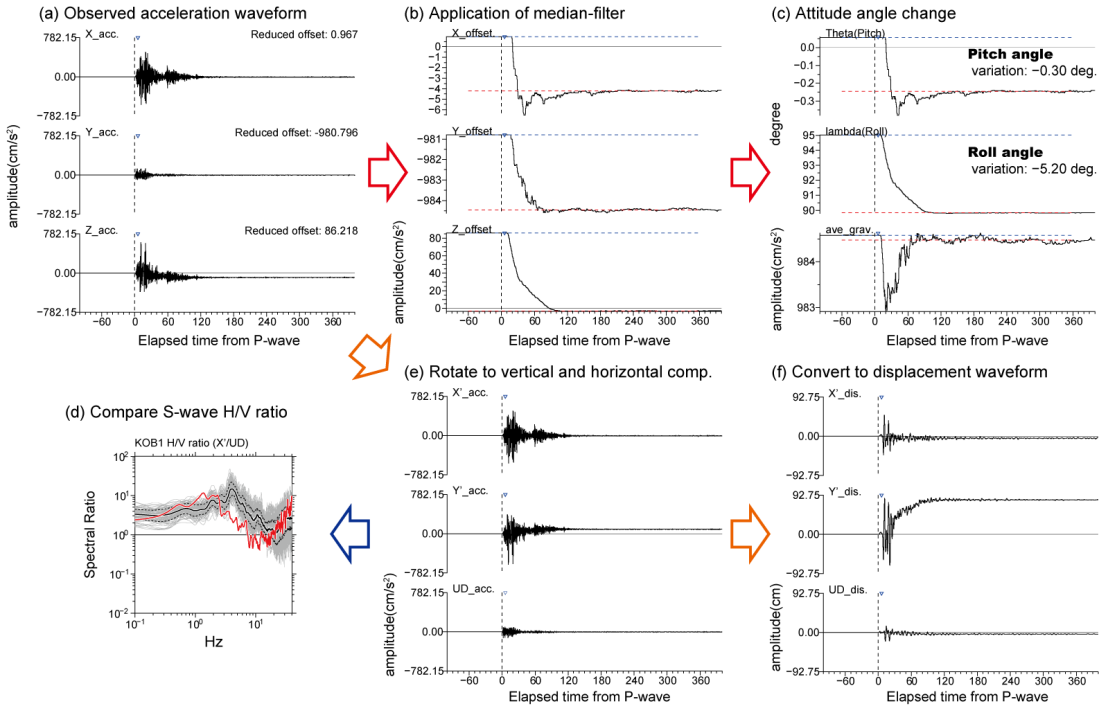

Figure 3: Examples of waveforms and processing results at KOB1 station during the 2003 Tokachi-oki earthquake (M_{jma} 8.0).

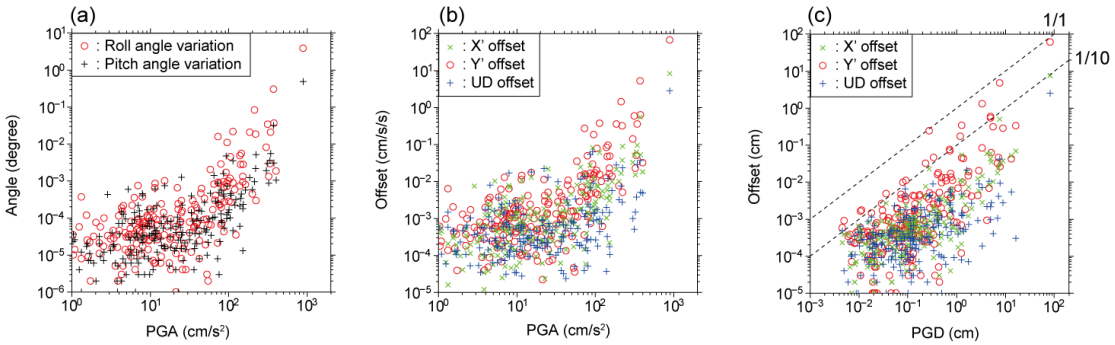

Figure 4: Correlation diagram of (a) angle variation and (b) acceleration offsets as a function of PGA, and (c) displacement offsets as a function of PGD at KOB3 station.

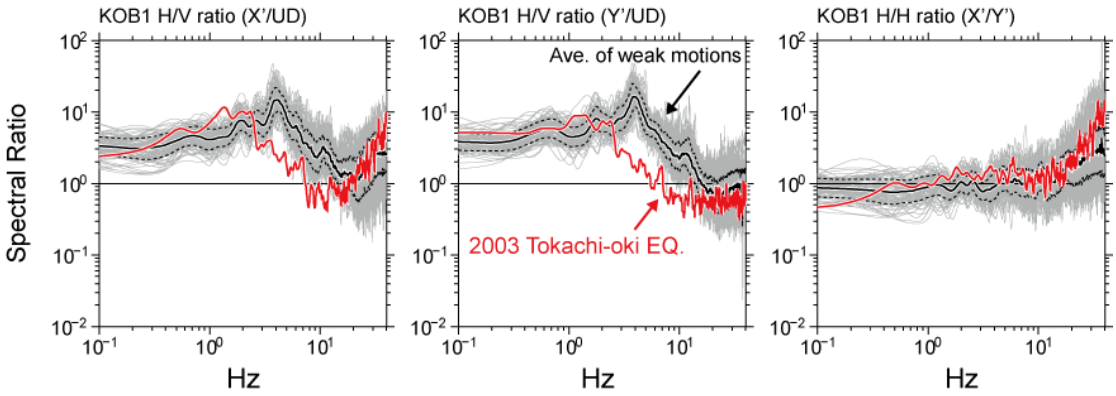

Figure 5: Comparison of H/V (X'/V and Y'/V) and H/H (X'/Y') spectral ratio at each component. Red line indicates the ratio of the 2003 Tokachi-oki earthquake (M_{jma} 8.0). Gray lines indicate ratios of weak motions. Black line indicates average of ratios of weak motions.

Characteristics of S-wave H/V and H/H spectral ratio

Fig. 5 indicates S-wave H/V (X'/UD and Y'/UD) and H/H (X'/Y') spectral ratio at KOB1. The S-wave H/V spectral ratio of the 2003 Tokachi-oki earthquake (M_{jma} 8.0) is different from that of weak motions in following two characteristics; 1) the dominant peak shifts lower frequency, and 2) the amplification at high frequency decreases. There are typical features of nonlinear site response, which is similar with land stations (e.g. Wen *et al*. (2006)). We also estimate DNL (Degree of nonlinear site response, Noguchi and Sasatani (2008, 2011)) value of S-wave H/V ratio. The DNL value is summation of differences between the ratio for strong motion and that for weak motion,

$$DNL = \sum \left| \log\left(R_{strong}(f) / R_{weak}(f)\right) \right| \Delta f \,. \qquad (2)$$

Figure 6 shows a relation between DNL and PGA. We found that the DNL values increase with observed PGA. When PGA is up to 200cm/s^2, the DNL values are significantly larger than that of weak motions.

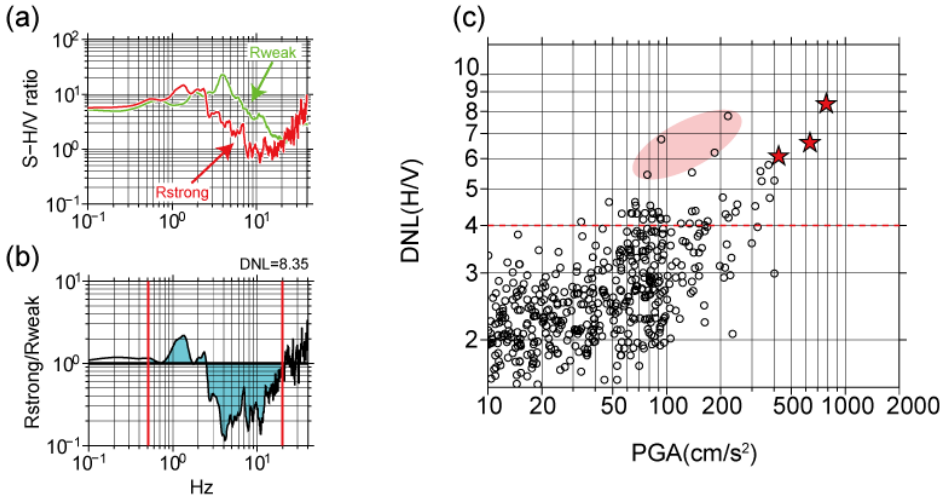

Figure 6: (a) Examples of DNL estimation. The frequency range of DNL summation is set from 0.5 to 20 Hz. Weak ground motions of less than 50cm/s^2 are used for averaged weak motion H/V ratio. (b) The ratio of H/V spectral ratio of the 2003 Tokachi-oki earthquake to that of average of weak motion. (c) Relation between DNL (H/V) and observed PGA. Red stars indicate the DNL of main shock of the 2003 Tokachi-oki earthquake, and pink hatch indicates that of aftershocks of M8.0 earthquake. The DNL values are clearly larger when PGA is up to 200 cm/s^2. Red broken line indicates the DNL value 4 as an index of occurrence of non-linear soil response (Noguchi and Sasatani (2011)).

Other interesting features are also found in almost all H/H spectral ratios. Amplitude of Y' component is smaller than that of X' component for frequency range over 10 Hz. These results may indicate that roll-angle is able to rotate easier than pitch-angle, thus Y' component easily lacks coupling between cylindrical housing and seafloor in high frequency range. Therefore, we have to keep in mind about the difference of response characteristics when we analyze a particle motion of waveform over 10 Hz at in-line cable type OBS.

Influence on magnitude estimation

Magnitude of JMA EEW is mainly determined from the maximum amplitudes of 3-component vector summation of displacement waveforms. As described previously, EEW magnitude might be overestimated when acceleration offset appears in an acceleration waveform, because acceleration offsets lead to the displacement waveforms with large displacement offsets as shown in Fig. 4. To evaluate the influence of strong motion on the magnitude estimation, we estimate a S-wave EEW magnitude (*M*eewS) using Off-Kushiro OBS and K-NET land station data. The waveforms of the peak ground displacement (PGD) of larger than 100 micro-meters are used in the magnitude estimation (Fig. 7). We first apply S-wave magnitude formula to adjacent K-NET stations data, and then apply the same formula for Off-Kushiro OBS data. We adopted two-step stratified method (Joyner and Boore (1981)) to estimate magnitude formula,

$$a \times M = \log(A) + b \times \log(R) + c \times R + d \times D + e, \qquad (3)$$

where A is the maximum displacement of the three-component vector amplitude measured in 10 micro-meter, R and D are the hypocentral distance and the focal depth in km, respectively. Coefficients a, b, c, and d are determined from regression analysis; a is the magnitude coefficient, b and c are the coefficient of geometrical attenuation and viscous attenuation, respectively, d which is usually estimated to be a negative value is the correction factor of source depth in the attenuation relation specialized for intra-plate earthquakes. e is the residual term of the predicted value $a \times M$.

Fig. 8a and 8b-1 show a comparison of *M*eewS and M_{jma} at K-NET and that of Off-Kushiro OBS, respectively. We found that *M*eewS of Off-Kushiro OBS overestimate by 0.30 in average. These overestimations may be due to amplification by marine sediment. Another remarkable characteristic is found in the correlation diagram between PGA and magnitude residuals (*M*eewS-M_{jma}) (Fig. 8b-2), indicating that the magnitude residual increases with increasing PGA. We conclude that these overestimations at large PGA values occur as the result of the remaining offset changes on displacement waveforms.

In order to improve the estimation errors, we proposed an alternative magnitude estimation for EEW by using the maximum amplitude of the vertical component displacement waveform. Figs. 9a and 9b-1 show a comparison of vertical component magnitude (M_UD) and M_{jma} at K-NET and that of Off-Kushiro OBS, respectively. We found that the magnitude overestimation due to the inclination of OBS can be reduced by using the vertical component (Fig. 9b). We also found that the variance of the estimated magnitude at each station becomes smaller by using the vertical component. These improvements can be confirmed not only OBS network but also land station data. By using this estimation, we would be able to reduce the effect of the difference of site amplification factor and to estimate more stably magnitude even without using empirical station corrections.

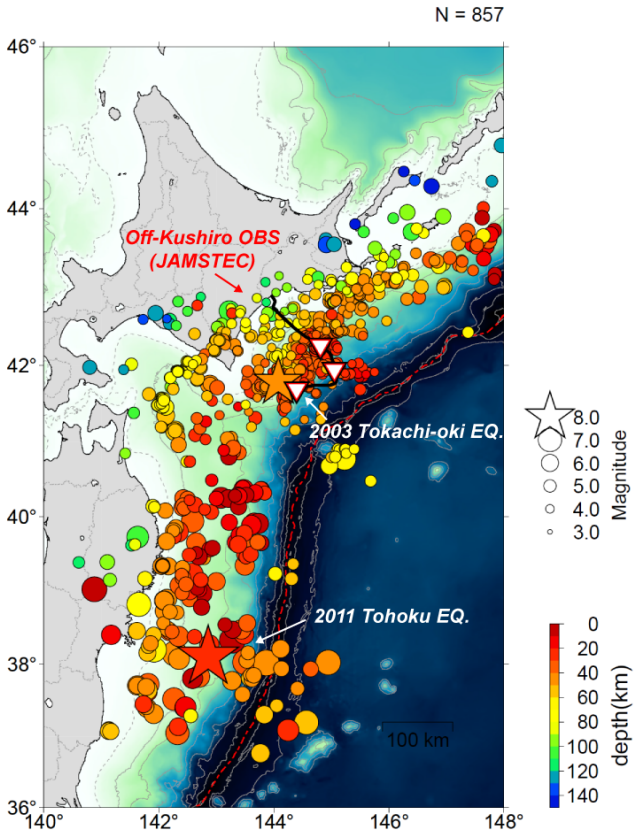

Figure 7: Hypocenter distribution map used in magnitude estimation.

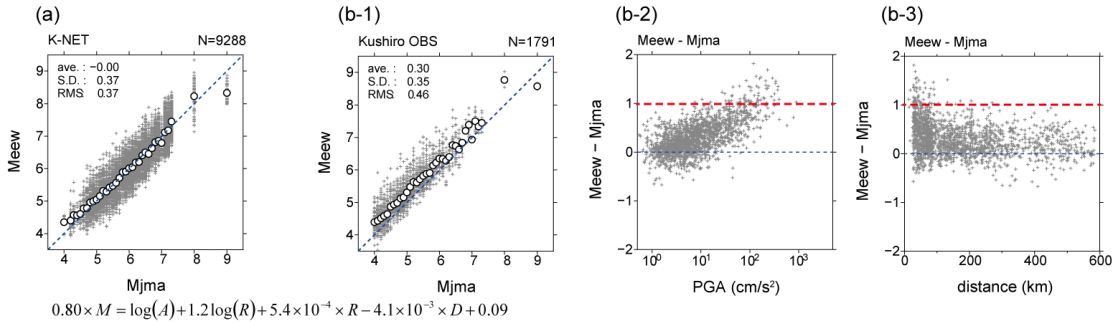

Figure 8: (a) Comparison of 3-component S-wave magnitude in this study (MeewS) at K-NET station with M_{jma}. (b-1) Comparison of MeewS at Off-Kushiro OBS with M_{jma}. (b-2) Correlation between magnitude residual (MeewS - M_{jma}) and PGA. (b-3) Correlation between magnitude residual and distance.

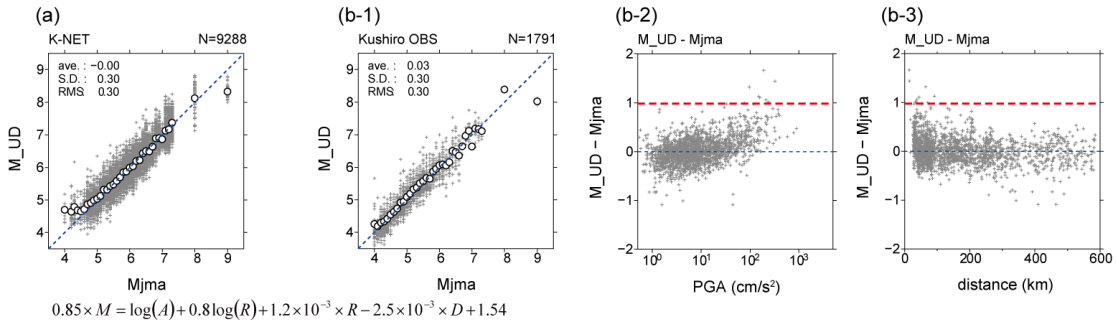

Figure 9: (a) Comparison of UD-component S-wave magnitude in this study (M_UD) at K-NET station with M_{jma}. (b-1) Comparison of M_UD at Off-Kushiro OBS with M_{jma}. (b-2) Correlation between magnitude residual (M_UD - M_{jma}) and PGA. (b-3) Correlation between magnitude residual and distance.

Conclusion and Future works

We investigated anomalous OBS waveform data of an inline-cable system at strong ground motions to evaluate feasibilities of the use of data for Earthquake Early Warning (EEW). We found that the attitude angle change of OBS housing can cause overestimation of EEW magnitude. We propose an alternative approach of the magnitude estimation using the vertical displacement component to improve such overestimation. By applying this approach, we can not only reduce the overestimation due to the inclination of OBS, but also suppress a strong variance of the estimated magnitude caused by the difference of site amplification factor among stations. Since the effect of site amplification factor on the vertical component is small, we may be able to apply this approach for OBS data without station corrections. For utilizing huge-scale OBS network data such as DONET and S-net to EEW, our future work is further developments of our approach that are applicable to waveform data at earthquakes occurred in the whole Japan.

Acknowledgements

We thank the anonymous reviewer for the helpful comments. The strong ground motion acceleration waveform data used in this study were obtained from the database of Off-Kushiro OBS of the Japan Agency Marine-Earth Science and Technology (JAMSTEC) and K-NET of the National Research Institute for Earth Science and Disaster (NIED). The ROV pictures of OBS were obtained from JAMSTEC E-library of Deep-sea Images (J-EDI). This work was supported in part by JSPS KAKENHI Grant Number 25282114.

References

Duennebier, F. K. and G. H. Sutton (1995). Fidelity of Ocean Bottom Seismic Observations, Mar. Geophys. Res. **17**, 535-555.

Fukushima, Y. and T. Tanaka (1992). Revised attenuation relation of peak horizontal acceleration by using a new data base. Programme and Abstracts, SSJ 2, 116. (in Japanese).

Hirata, K., M. Aoyagi, H. Mikada, K. Kawaguchi, Y. Kaiho, R. Iwase, S. Morita, I. Fujisawa, H. Sugioka, K. Mitsuzawa, K. Suyehiro, H. Kinoshita, and N. Fujiwara (2002). Real-time geophysical measurements on the deep seafloor using submarine cable in the southern Kurile subduction zone, IEEE J. Oceanic Eng., 27, 170-181, 2002.

Hoshiba, M., O. Kamigaichi, M. Saito, S. Tsukada, and N. Hamada (2008). Earthquake early warning starts nationwide in Japan, Eos Trans. AGU, **89**, 73–74, 2008.

Joyner, W. B. and D. M. Boore (1981). Peak horizontal acceleration and velocity from strong-motion records including records from the 1979 Imperial Valley, Calfornia, Earthquake, Bull. Seismol. Soc. Am., **71**, 2011-2038.

Kamigaichi, O., M. Saito, K. Doi, T. Matsumori, S. Tsukada, K. Takeda, T. Shimoyama, K. Nakamura, M. Kiyomoto, and Y. Watanabe (2008). Earthquake Early Warning in Japan: Warning the general public and future prospects, Seismol. Res. Lett., **80**, 717–726, 2009.

Kinoshita, S. (2008). Tilt measurement using broadband velocity seismograms, Bull. Seismol. Soc. Am. **98**, 1887-1897, 2008.

Noguchi, S. and T. Sasatani (2008). Quantification of Degree of Nonlinear Site Response. The 14th World Conference on Earthquake Engineering, October 12-17, 2008, Beijing, China.

Noguchi, S. and T. Sasatani (2011). Nonlinear Soil Response and Its Effects on Strong Ground Motions during the 2003 Miyagi-Oki Intraslab Earthquake, Zisin2, 63, 165-187 (In Japanese).

Wen, K. L., T. M. Chang, C. M. Lin, and H. J. Chiang (2006). Identification of Nonlinear Site Response Using the H/V Spectral Ratio Method. Terr. Atmos. Ocean. Sci. 17:3, 533-546.

Yamamoto, Y., H. Takenaka, K. Hirata, T. Watanabe (2004). Estimation of Broadband Ground Motion at Ocean-bottom Strong-motion Stations for the 2003 Tokachi-oki Earthquake, AGU Fall Meeting 2004, S34A-08.

Preliminary Feasibility Study of an Earthquake Early Warning System for Tehran Region

M. Shahvar[1], M. Poorveis[2], M. Mojarab[2], N. Norouzi[2] and Z. Asadi[2]

[1] Road, Housing & Urban Development Research Centre (BHRC), Tehran, Iran, mshahvar@gmail.com
[2] OZP Consulting Engineers, Tehran, Iran

Abstract

A feasibility study of Early Warning System application in Tehran is the main aim of present the investigation. First, a sensitivity analysis of various parameters such as warning time and blind zone, regardless of tectonics condition, has been performed. Subsequently, warning times were calculated based on probability density approach, for more than 5000 earthquake scenarios, initial dense network and other parameters. The main output of present study indicated that the warning time for all possible earthquakes is variable from approximately -5 to 33 seconds. In addition, based on probabilistic studies, there are also more than 10 seconds of warning time for about 60 percent of the events in a radius of 300 km of Tehran.

Introduction

There are numerous faults around Tehran within a radius of approximately 150 to 200 kilometers, like: North of Tehran, North and South of Rey, Kahrizak, Taleghan, Abyek, Mosha, Firuzkuh, Astaneh, Parchin, Pishva, Robat Karim, Eshtehard, Ipak, Kashachal, North of Qazvin, Khazar, North of Alborz, Indes and Qom (Figure 1).

The aim of an earthquake early warning system is to provide a fast and reliable estimation of the earthquake before the strong ground motion reaches the target site. A "regional" EEWS is based on a network of stations located in the source area, while the target sites to be protected are situated far away. The most common examples of regional systems are ElarmS Method (Allen, 2007) and ElarmS2 (Kuyuk et al., 2014), Virtual Seismologist (Cua and Heaton, 2007; Behr et al., 2015) and PRESTo (Satriano et al., 2011) are instances of the current regional method.

On the other hand, the "on-site" system consists of a single station (or an array of sensors) located at the target site. In this configuration, the purpose is to estimate the expected strongest shaking produced by S- or surface waves, directly from the initial portion of the recorded P-wave signal. Among on-site methodologies, the most relevant are those proposed by Wu and Kanamori (2005), Böse et al. (2009) and recently, Meier et al. (2015).

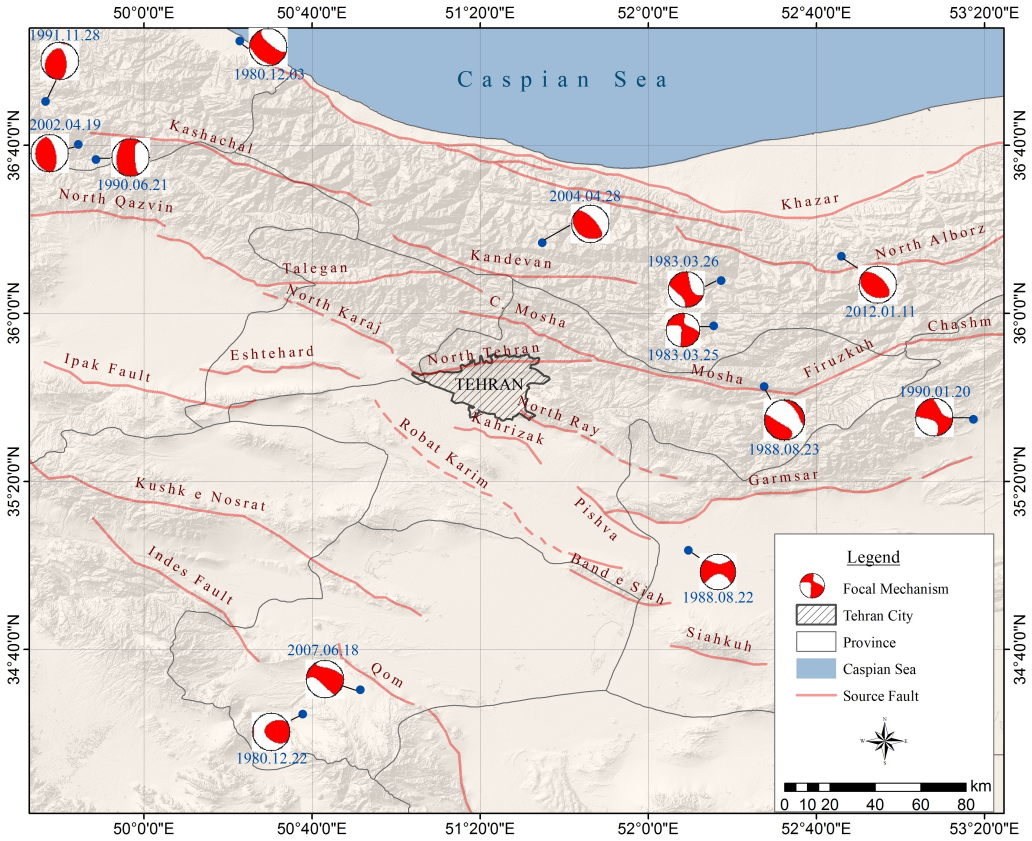

Figure 1. Main faults in the area of study. The major, past events are shown by their focal mechanism.

The feasibility of EEWS in Tehran

In this section, analysis, evaluation and feasibility study of the status of an early warning system in Tehran will be presented. Here, we seek to answer the following question: is it possible to install a warning system in Tehran, according to Tehran's tectonic conditions with a dense seismic network fundamentally? In the following, the feasibility of an EWS is evaluated by computing the theoretical warning times as done by Allen (2006), and assuming a theoretical network and the selected method parameters. Total delays of warning system including delays due to the volume of data, faxing, processing and decision-making of warning algorithm for issuing warnings assumed 4 seconds based on Brown et al. (2011) and Allen et al. (2009) studies and experience of ElarmS2 algorithm (Kuyuk et al., 2014) in California. 4 stations are assumed as the minimum number of required stations for recording the P-wave, position and magnitude calculations. Also, the P-wave velocity model in crust is selected based on the studies of Ashtari et al. (2005) and the depth of scenario earthquakes considered as 8 km.

Probable scenarios

To determine the possible scenarios, all of the major and active faults in the region, which are shown in Figure 1, are considered as the location of probable scenarios. Probability of occurrence for a magnitude M ≥ 6.4 on these faults determined for 30-

year range by using the Poisson distribution and the location of each scenario on a fault is considered as a distance of approximately one kilometer and with equal probability. Also, for background earthquake, magnitude of 6 is considered in the range of 110 km wide (35.2 to 36.2 degrees North) and 150 km long (50.7 to 52.2 degrees East) and with distance of 5 km of each other. In total, 59 scenarios and 5900 events were considered for the region (Figure 2).

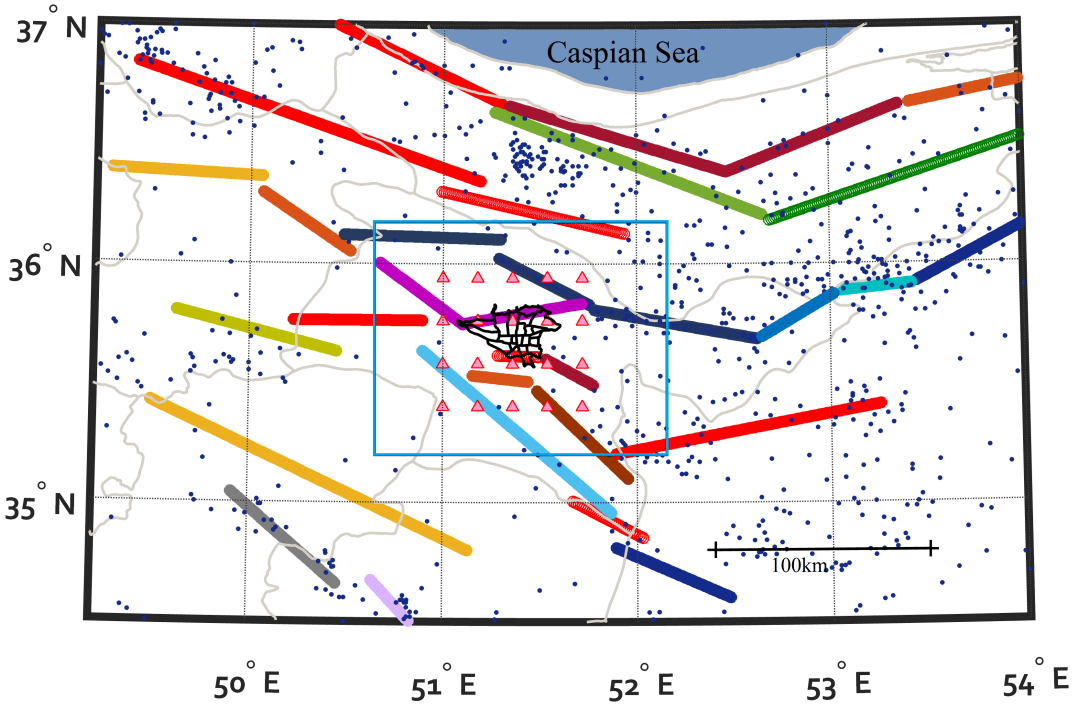

Figure 2. Map of the study region showing the fault segments with broad coloured lines. The location of M > 3 earthquakes are shown as small dots. The area of Tehran is shown with black lines in center of figure. The rectangular shows the area of background earthquake scenarios and the triangles show theoretical network distribution.

Warning time probability density

In this section, the warning time, time difference between the S arrival at the target and estimating of earthquake parameters, calculated for all of events for center of Tehran. To calculate the warning time, a minimum of 4 triggered stations has been considered and a delay time of 4 seconds has been included to account for data latency and earthquake parameters calculation. Computed probability density function of warning time for Tehran are shown in Figure 3 to 5. Also, the earthquakes which have warning times smaller or greater than zero, 10 and 20 seconds have been estimated and graph of results are as follows. By modeling of scenarios, empirical ground motion prediction equations (Akkar and Bommer, 2010; Campell and Bozorgnia, 2008; Abrahamson and Silva, 2008) are used to predict the expected peak ground motion parameters in the target site, and the mean intensity of earthquakes were estimated based on the MMI~PGV and MMI~PGA conversion equation developed for Iran by Shahvar (2013), Wald et al. (1999), and Worden et al. (2012).

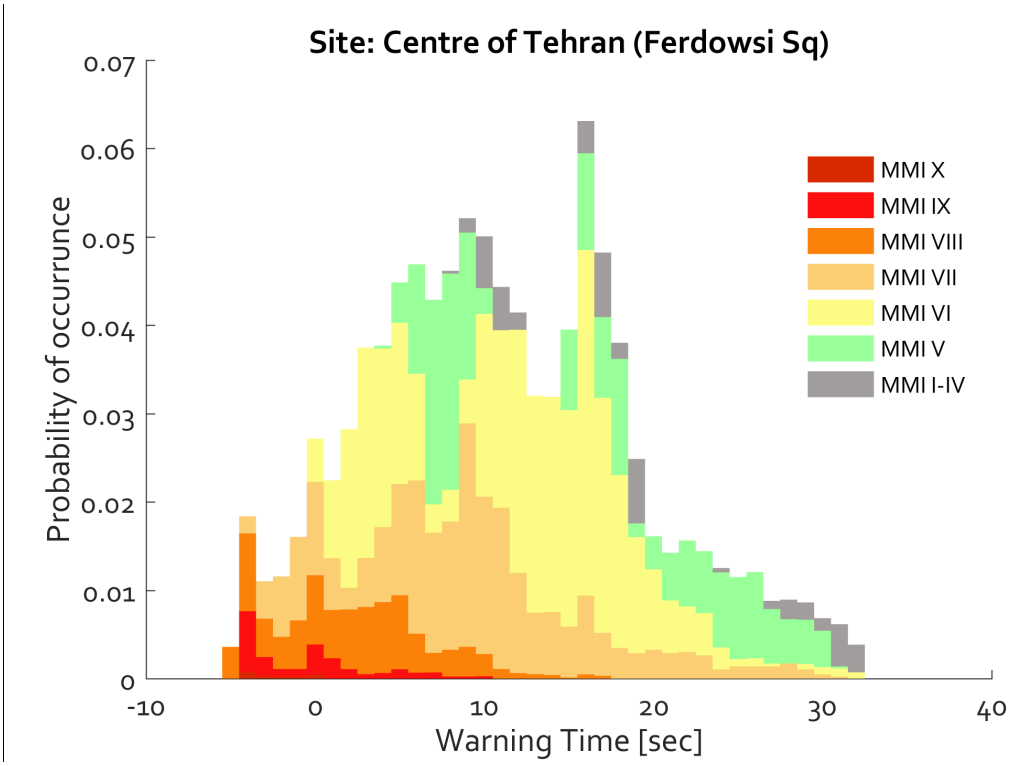

Figure 3. Graph of the probability density function of warning time for center of Tehran based on Allen (2006). The time interval for the horizontal axis (warning time) is one second and colors represents the amount of modified Mercalli intensity which intensities smaller than 5 is shown in gray. Warning time for all probable earthquakes are from - 5 seconds to 33 seconds, where negative warning times mean impossibility of warning. The vertical axis represents the probability of occurrence of one or more earthquakes for a period of 30 years and for a specified warning time.

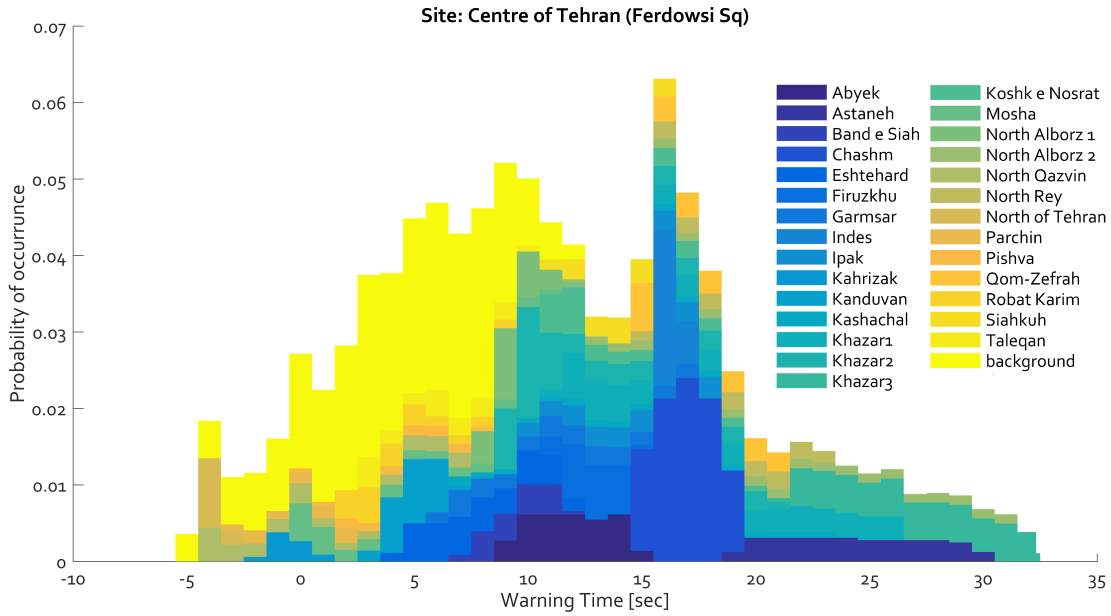

Figure 4. Histogram of warning time for center of Tehran based on their probability of occurrence (top) and frequency (next page). The color indicates the scenarios sources that are shown in Figure 1 and 2.

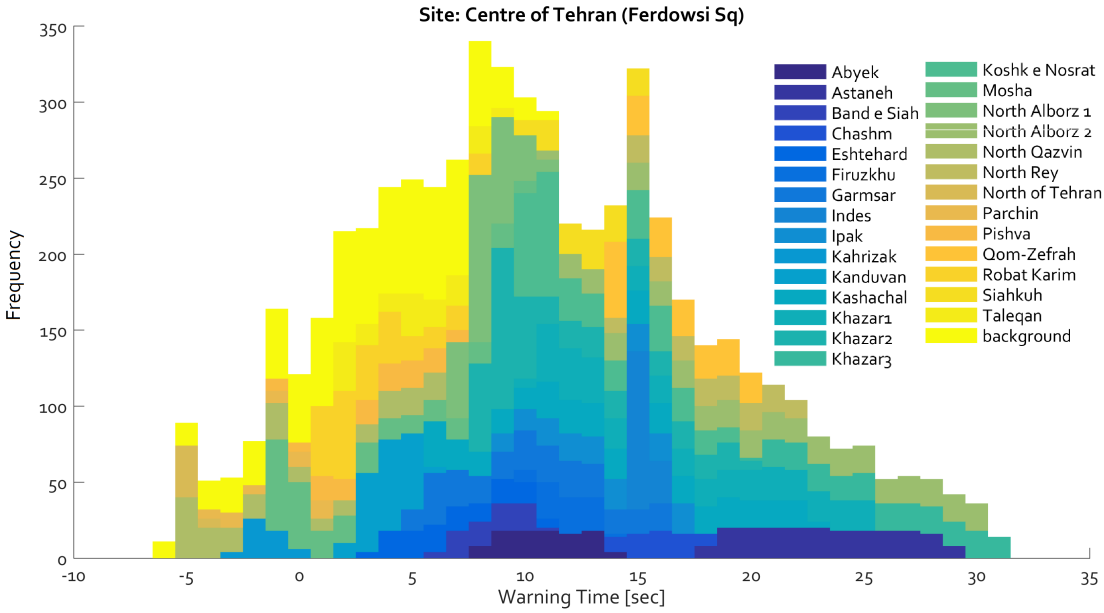

Figure 4 (continued).

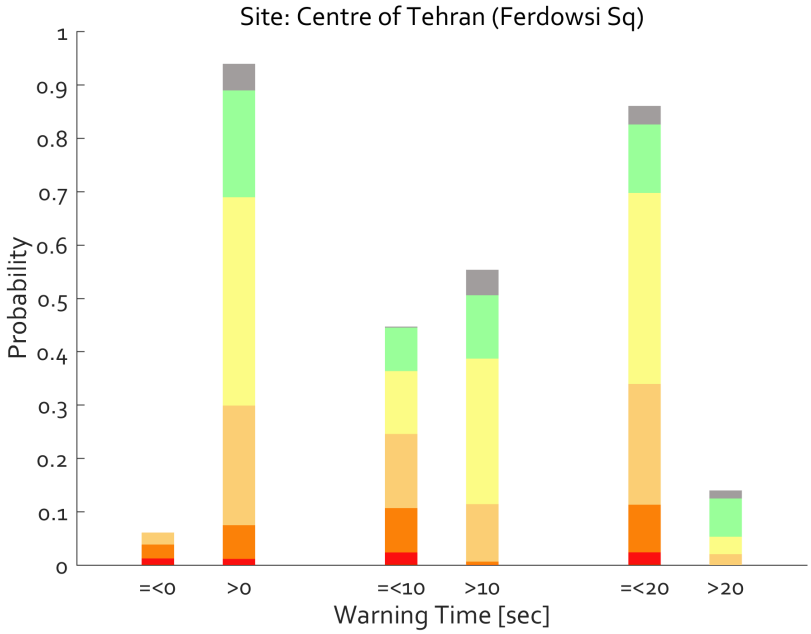

Figure 5. Probability of occurrence of one or more earthquakes for 30 years with warning time less than or equal to or greater than zero, 10 and 20 seconds for center of Tehran. Colors represent the modified Mercalli intensity (same as in Figure 3).

As shown in Figures 3 to 5, most of earthquakes with intensity over IX, have maximum warning time of about 10 seconds. This is because of the fact that intensity is directly proportional to the distance and almost all events with the intensity over IX will be occur near site. Also, we reproduce these results for other sites in Tehran (South, east, West, and north) and see slight changes in the probability of occurrence which is because selected sites are in the metropolitan area and they are close to each other.

Conclusions

In the last two decades, the subject of earthquake early warning has been raised in the world and is still a subject of many researches. A few countries, such as Japan and Mexico have implemented such systems and are in operation and some other countries like United States, Italy, Switzerland and Turkey are currently conducting studies in this field.

According to the analyses have been done for hypothetical earthquake sources and hypothetical seismic station, the main results can be summarized as follow:

- Warning time for all possible earthquakes and dense station network is variable from approximately -5 to 33 seconds for Tehran.
- According to the probabilistic calculations, in the case of having a dense network, almost for all sites, for over 90% of events with intensity of higher than five, warning time is greater than zero.
- According to warning time greater than zero, it is possible to design a regional early warning network to cover some of the earthquakes.
- With regard to the number of faults in Tehran and around the city and considering the blind radius is an inevitable part of early warning systems, in the case of occurring any earthquake on these faults, there is not warning possibility for parts of the city. A valid option for an early warning system in Tehran region could be based on the on-site approach, i.e., by installing single stations in vital areas or in the general populated centers like subways. The efficiency of these types of systems will be increases and warning system errors in area will be reduced in the case of existing a highly reliable regional warning system.
- Based on probabilistic studies, for a number of destructive events, there are also more than 10 seconds warning time (About 60 percent of the events, have warning time of about more than 10 seconds and there is also some high-intensity earthquake among them).
- In view of economic location and political situation in Tehran and the risk of earthquake, an early warning system is essential and is a sign of progress in the country and the world.

Acknowledgment

This work was supported by Tehran Urban Planning and Research Center. We would also like to thank Simona Colombelli for her helpful comments and suggestions.

References

Abrahamson, N. A., and W. J. Silva (2008). Summary of the Abrahamson & Silva NGA Ground-Motion Relations, Earthquake Spectra 24, 67–97.

Akkar, S. and Bommer, J.J., 2010. "Empirical Equations for the Prediction of PGA, PGV and Spectral Accelerations in Europe, the Mediterranean Region and the Middle East. Seismological Research Letters March/April 2010v. 81 no. 2 p. 195-206

Allen, R.M., 2006, "Probabilistic warning times for earthquake ground shaking in the San Francisco Bay Area", Seismological Research Letters, Vol. 77 (3), 371-376.

Allen, R.M., 2007, "The ElarmS earthquake early warning methodology and application across California", In Earthquake Early Warning Systems, In "Earthquake Early Warning Systems", P. Gasparini, G. Manfredi, J. Zschau (Eds), p. 21-44, Springer, ISBN-13 978-3-540-72240-3.

Allen, R.M., Gasparini, P., Kamigaichi, O., Bose, M., 2009, "The Status of Earthquake Early Warning around the World: An Introductory Overview", Seismological Research Letters Vol. 80, No. 5, doi: 10.1785/gssrl.80.5.682.

Ashtari, M., Hatsfeld, D., Kamalian, N., 2005, "Microseismicity in the region of Tehran", Tectonophysics, Vol. 395, 193-208.

Behr, Y., Clinton, J., Kastli, P., Cauzzi, C., Racine, R., & Meier, M.A., 2015, "Anatomy of an Earthquake Early Warning (EEW) Alert: Predicting Time Delays for an End-to-End EEW System", Seismological Research Letters, Vol. 86, No. 3, 830–40, doi: 10.1785/0220140179.

Bose, M., Hauksson, E., Solanki, K., Kanamori, H., Wu, Y. M., Heaton, T. H., 2009, "A new trigger criterion for improved real- time performance of onsite earthquake early warning in Southern California", Bulletin of the Seismological Society of America, Vol. 99 (2A), 897-905.

Brown, H.M., Allen, R.M., Hellweg, M., Khainovski, O., Neuhauser, D., Souf, A., 2011, "Development of the ElarmS methodology for earthquake early warning: Realtime application in California and offline testing in Japan", Soil Dynam. Earthq. Eng. Vol. 31, 188-200, doi: 10.1016/j.soildyn.2010.03.008

Campbell, K. W., and Y. Bozorgnia (2008). NGA Ground Motion Model for the Geometric Mean Horizontal Component of PGA, PGV, PGD and 5% Damped Linear Elastic Response Spectra for Periods Ranging from 0.01 to 10 s, Earthquake Spectra 24, 139–171.

Cua, G., Heaton, T., 2007, "The Virtual Seismologist (VS) method: a Bayesian approach to earthquake early warning", In: Gasparini P, Manfredi G, Zschau J, editors, Earthquake early warning systems. Berlin: Springer, 97–132, doi: 10.1007/978-3-540-72241-0-7.

Kuyuk, H. S., Allen, R. M., Brown, H., Hellweg, M., Henson, I., Neuhauser, D., 2014, "Designing a network- based earthquake early warning algorithm for California: ElarmS-2", Bulletin of the Seismological Society of America, Vol. 104, No. 1, 162–173, doi: 10.1785/0120130146.

Meier, M. A., Heaton, T., Clinton, J., 2015, "The Gutenberg Algorithm: Evolutionary Bayesian Magnitude Estimates for Earthquake Early Warning with a Filter Bank", Bulletin of the Seismological Society of America, Vol. 105 (5), 2774-2786.

Satriano, C., Elia, L., Martino, C., Lancieri, M., Zollo, A., & Iannaccone, G., 2011, "PRESTo, the earthquake early warning system for Southern Italy: concepts, capabilities and future perspectives", Soil Dynamics and Earthquake Engineering, Vol. 31 (2), 137-153.

Shahvar M. (2013). ShakeMaps implementation for Iran. PhD thesis, IIEES, Iran.

Worden CB, Wald DJ, Allen TI, Lin K, Garcia D, Cua G (2010) A Revised Ground-Motion and Intensity Interpolation Scheme for ShakeMap. Bull Seismol Soc Am 100(6), 3083-3096

Wald, D. J., V. Quitoriano, T. H. Heaton, and H. Kanamori (1999b). Relationship between peak ground acceleration, peak ground velocity, and Modified Mercalli Intensity for earthquakes in California, Earthquake Spectra 15, 557–564.

Quick Estimation of Wavefield by Neumann-type Extrapolation for a New Earthquake Early Warning System

Asuka Sato[1,2] and Kiyoshi Yomogida[1]

[1] Earth and Planetary Dynamics, Hokkaido University, North 10 West 8, Kita-ku, Sapporo 060-0810, Japan, yomo@mail.sci.hokudai.ac.jp
[2] Now at Geospatial Information Authority, 1 Kitasato, Tsukuba 305-0811, Japan

Abstract

We propose a new approach based on the extrapolation of the early observed waveforms alone without estimating its epicenter information. The idea is similar to the migration method in exploration seismology with Green's functions, but we use not only the information of wavefield (i.e., a boundary integral formulation of the Dirichlet type) but also the apparent velocity and direction of propagation (the Neumann type) on an early stage. Since the complete 3-D wave propagation is extremely complex, particularly in and around Japan whose structure is highly heterogeneous, we considered a phenomenological or empirical 2-D Green's function, that is, a wavefront of P wave propagates on the surface with certain values of apparent velocity and direction. The velocity and direction may vary significantly depending on, for example, a focal depth and a region of propagation, so that we examined those of P wave propagating in various situations in Japan. For example, the apparent velocity in Nagano prefecture in central Japan is less than 6 km/s for shallow events, probably due to its high mountains or thick crust of low velocity. While the velocity for shallow events is large in Hokkaido, it is slow for deep events, compared with other regions. In order to estimate apparent velocity and propagation direction of P wave, we attempted *f-k* array analysis with data at adjacent five or six stations as an observational array. Using the seismograms band-passed by 0.3-5 Hz, both P-wave velocity and its direction could be estimated precisely as long as the current station density of Hi-net in Japan, within less than 10 seconds of each origin time. In summary, our proposed extrapolation approach can robustly estimate the arrival time and amplitude of P wave only from the P-wave waveforms observed at several stations, which will be complimentary to the currently operating warning systems.

Introduction

The earthquake early warning system operated by Japan Meteorological Agency is one of the warning systems to inform the expected arrival time and intensity of shaking at a given location immediately after the occurrence of an earthquake in and

around Japan (e.g., Kamigaichi et al., 2009). When an earthquake is detected at two or more stations and more than five intensity on the Japanese intensity scale is also predicted, a warning is announced with the forecasted arrival time at a station further than the points where ground motions are already recorded. Its test operation started in 2004, and operations for the public in Japan started on 1 October 2007. It determines the location and size of an earthquake by arrival times and amplitudes of P wave at a few stations close to its epicenter, then arrival times of S wave and seismic intensity are estimated at points away from the estimated epicenter in advance. Despite of various kinds of improvement introduced every year, there are still some cases in which actual announced warnings were false or missed, particularly there were many cases related to the main shock and aftershocks of the Tohoku-Oki earthquake of M 9.0 in 2011 (e.g., Hoshiba and Iwakiri, 2011).

Since its operation started, this system has been found not to work properly in the following cases: (a) a large event whose finite fault area cannot be neglected, say, M larger than 8, (b) a deep event whose wavefront propagates in a different manner from shallow ones, particularly with very high apparent velocity on the surface, (c) more than one earthquakes occur nearly simultaneously. In case (a), the assumption of an epicenter as a point is violated, while an earthquake is located incorrectly to be shallow and close to the observed stations in most cases of (b). In case (c), epicenters cannot be estimated properly without the knowledge of the number of simultaneous events on an early stage of their occurrence.

In order to overcome these troubled cases as well as to enhance the accuracy of warnings, we may need to introduce a completely different approach from the present one that estimates an earthquake epicenter at first. That is, we like to develop a new system without the information of an epicenter. Hoshiba (2013) introduced an idea of wavefield extrapolation in an early warning system, based on the Kirchhoff integral formulation. Hoshiba and Aoki (2015) then expressed an expanding wavefield in terms of radiative transfer theory, because high-frequency waves are suffered by strong scattering originated from small-scale heterogeneities in the crust. Their approach adopted a constant velocity for Green's functions to estimate the arrival time and intensity at a given point. Moreover, they did not consider deep earthquakes. In addition, they estimated arrivals and amplitudes of S wave from S-wave observations, which may not be practical in early warning systems, because we need to predict them from P-wave observations on an early stage.

In this study, we shall discuss how we can fill gaps between the above simple application of wavefield extrapolation and practical utilization in early warning systems. Because it is possible to obtain the velocity and direction of wave propagations on the surface in the process of an earthquake early warning system, we may be able to estimate the future wavefield by using not only the waveforms observed early but also their spatial derivatives, based on the representation theorem with Green's functions. We shall also consider the use of Green's functions with the velocity depending on a region and a focal depth. A new earthquake early warning system with our proposed approach should be able to deal with a variety of cases, including two or more earthquakes nearly at a same time, a deep earthquake not far from stations, and a large earthquake with large spatial extent of its fault area.

Estimation of wavefield in a future time from the observations in the present by extrapolation

The goal of this study is the accurate and stable estimation of wavefield at a time of the future from a set of the waveforms observed in the present. In a practical point of view for the improvement of early warning systems, it may be sufficient to estimate not an entire waveform but the arrival time and overall amplitude of a specific seismic phase such as P and S waves. One fundamental formulation in seismology is the representation theorem with Green's functions (e.g., Aki and Richards, 2009). This theorem has been also widely used in exploration seismology in terms of the imaging of a reflector or scatterer from an array of many waveforms observed on the surface. In this study, we shall apply this formulation to the improvement of early warning systems.

Hoshiba (2013) proposed an approach to estimate future wavefield by the integral theorem of Kirchhoff from the observed waveforms that have already arrived at stations close to an epicenter. As shown in Figure 1a, the point that we like to predict its ground motion represented by $U(\mathbf{r},t)$ while we suppose to have observed the wavefields $U(\mathbf{r}_0,t_0)$ over a surface S. The wavefield $U(\mathbf{r},t)$ at the point $\mathbf{r}$ is expressed by the following integral theorem named the Kirchhoff migration (e.g., Shearer, 2009):

$$U(\mathbf{r},t) \approx \int_S \frac{1}{v(\mathbf{r}_0)} \dot{G}(|\mathbf{r}-\mathbf{r}_0|, t-t_0) * U(\mathbf{r}_0,t_0) dS(\mathbf{r}_0), \quad (1)$$

where $v(\mathbf{r})$ is the velocity, G is the Green's function, and the asterisk and the dot represent the convolution and the time derivative, respectively. Equation (1) has been used extensively in exploration seismology in terms of seismic "migration". It uses the waveforms $U(\mathbf{r}_0,t_0)$ observed on a given surface S. Without a sufficient density of stations on S, however, equation (1) does not provide us with reliable or accurate estimation of the extrapolated wavefield $U(\mathbf{r},t)$. In addition, the Green's function G in equation (1) corresponds to a three-dimensional P or S wave propagating mainly in a shallow part of the crust. This means that a direct application of equation (1) requires very complicated Green's functions. Since present early warning systems use P waves of relatively high frequency (> 1Hz), it may be far from practical to introduce any satisfactory 3-D Green's functions.

In order to overcome the above two major difficult points in the use of equation (1) in the wavefield extrapolation for an early warning system, we shall adopt (a) a new integral theorem different from a Kirchhoff type and (b) a kind of empirical Green's functions that express a wavefront propagating on the surface, that is, a two-dimensional scalar Green's function, in this study. Because we can measure the apparent velocity and direction of the P-wave propagation on the surface on a preparation stage of an early warning system, we (a) propose a new formulation for the extrapolation of wavefield with the normal derivative of U or $\partial U/\partial n$ as our observed or input data, and (b) introduce an "empirical Green's function" to express the propagation on the surface in a two dimensional manner (Figure 1b):

$$U(\mathbf{r},t) \approx \int_S G(|\mathbf{r}-\mathbf{r}_0|, t-t_0) * \frac{\partial U(\mathbf{r}_0,t_0)}{\partial n} dS(\mathbf{r}_0). \quad (2)$$

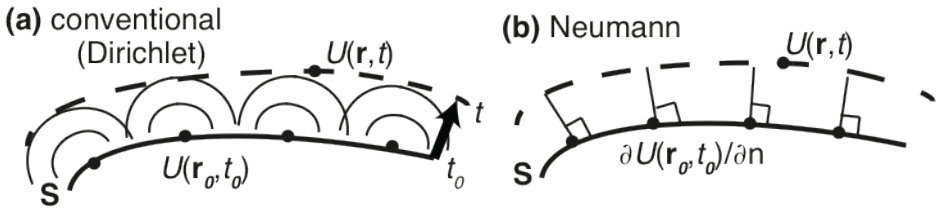

Figure 1: Extrapolation of wavefield by the integral theorems of (a) Kirchhoff migration or a Dirichlet type with input wavefields over the surface S and (b) a Neumann type with their normal derivatives.

Compared with equation (1), we may not need a dense coverage of our observations or data over *S*, in order to obtain stable and relatively reliable wavefield extrapolation. That is, the additional information of apparent velocity and propagation direction should enable us to estimate wavefield in the future only with a relatively small number of seismic stations.

Figure 2 shows a numerical example to represent the effect of apparent velocity and direction. Synthetic seismograms were computed at stations on the surface for a uniform medium with one heterogeneous body. An isotropic source is located near the surface in the left, so that the waves scattered by the heterogeneous body would be focused by the extrapolation of the synthetic seismograms. The first two results were obtained by a conventional Kirchhoff-type formulation or equation (1). The body was clearly focused (i.e., an accurate result of the extrapolation) if stations are distributed uniformly and densely (Figure 2a) while the resulted image was elongated towards the directions of sparse station distributions (Figure 2b). When we extrapolated the synthetic seismograms only in a finite range of directions from each station to the body based on equation (2), as shown in Figure 2c, the image of the body became less degraded than the case of Figure 2b. That is, the use of the direction of each observed record should enhance the accuracy of our wavefield extrapolation even with sparse or non-uniform distribution of stations. For heterogeneous media of complex velocity structures, the information of the measured velocity at each station should be also effective.

Since two-dimensional propagations on the surface are considered, as mentioned above, we shall express the Green's function in equation (2) only by the apparent velocity and propagation direction of P wave. Even for such rather simple 2-D empirical Green's functions, we have to take care of strong lateral or regional variations, for example, if we apply it to early warnings in Japan. In addition, we have to measure the velocity and direction of wave propagation, which will be used as the input data $\partial U/\partial n$ in equation (2), quickly and accurately with a limited number of stations. We shall test *f-k* spectral analysis with Hi-net data of Japan, whether we can estimate them or not, to meet our present purpose.

Data

In this study, the seismic waveform data recorded by Hi-net stations of Japan are used. The Hi-net stations are installed throughout the Japanese islands with about 20 km intervals, consisting of high sensitivity seismographs of underground borehole

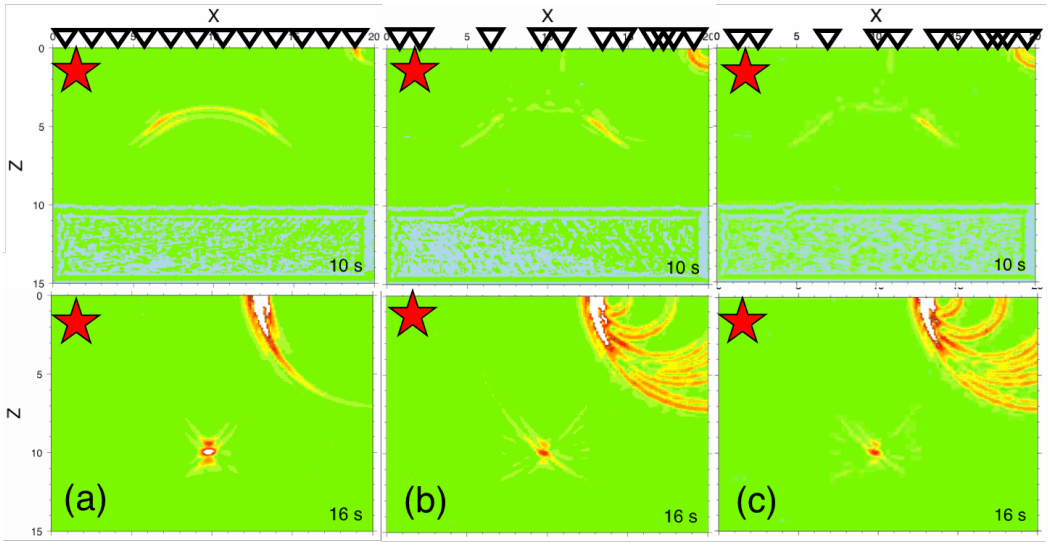

Figure 2: Numerical experiments for the estimation of wavefronts. The medium is uniform (1km/s in the non-dimensional manner) with one heterogeneous body, and the source is located near the surface in the left (red star) while stations are located on the surface (triangles). The wavefronts at two different timings (10 and 16 seconds) were estimated by the extrapolation of synthetic seismograms of (a) one hundred uniformly distributed, (b) twenty unevenly distributed, and (c) same as (b) except for the extrapolation only to a limited range of incident angles to each station. The waves scattered by the heterogeneous body would be focused or imaged at 16 seconds.

type with 24-hour continuous operation (Obara, 2002). The Hi-net system has been operated since 1995 by the Natural Research Institute for Earth Science and Disaster Prevention (NIED) whose waveforms can be downloaded on the Internet (http://www.hinet.bosai.go.jp). Three-component velocity seismograms are stored in the Hi-net system. Without any special notices, we shall use vertical waveform data after bandpass filtering in a frequency range of 0.1 to 5 Hz in the following discussions.

Figure 3 shows a plot of vertical-component seismograms in the order of epicentral distances for an earthquake on 2 December 2010 in the Ishikari district of central Hokkaido of M4.1 and 10 km in depth. As shown in this plot, we measured the gradient of P-wave arrival times as a function of epicenter distances around 300 to 400 km, as its apparent velocity of P wave. Figure 3 also shows a plot of seismograms for a deep earthquake on 21 May 2013 beneath northern Hokkaido of M4.8 and 210 km in depth. Its apparent velocity is much faster than that of the previous example. We may also need to pay attention to the arrival times of S wave (the secondary arrival phase in each record), whose interval time from the arrival time of P wave is much shorter than those of the previous shallow earthquake.

Regional variations of P-wave apparent velocity

In this chapter, we shall summarize a variety of P-wave propagations in and around Japan, utilizing the waveform data recorded at dense seismic stations of the Hi-net on the Japanese islands. As shown in Figure 3, as an example, we measured apparent

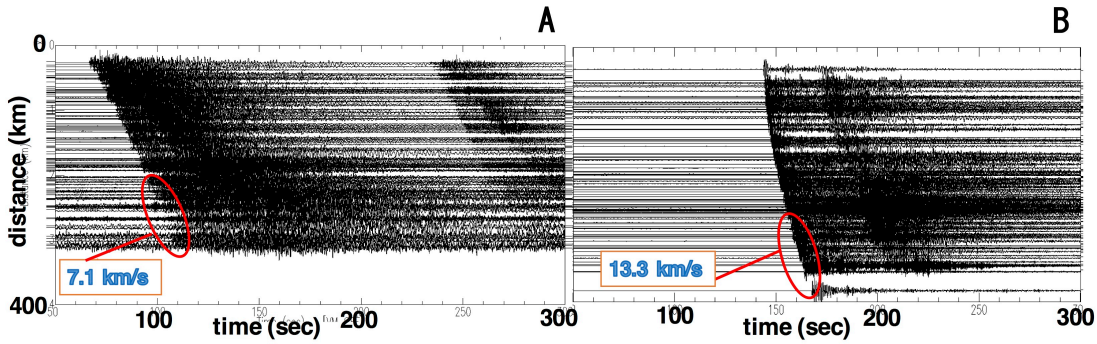

Figure 3: Vertical-component seismograms ordered by epicentral distances for (A) shallow (10 km) and (B) deep (210 km) earthquakes in Hokkaido, Japan, showing how to measure their apparent velocities of P wave.

velocities of P wave propagating across Japan for a variety of events in order to examine their variations such as region and focal depth. We measured the gradient of P-wave arrival times with respect to epicentral distance as its apparent velocity.

The apparent velocity on the surface, different from actual propagation velocity, is related to the incident angle, so that it should depend on both focal depth and epicentral distance. Figure 3 indeed shows the gradient of arrival times varying in epicentral distance. Figure 4 shows the apparent velocity of P wave as a function of distance for earthquakes of four focal depths in Hokkaido, Japan. For earthquakes deeper than 50 km, the apparent velocity becomes very large in an epicentral distance less than 100 km, due to its nearly vertical incidence. On the other hand, it becomes nearly constant in the distance further than 200 km. We shall use apparent velocities in the epicentral range from 250 to 400 km in the following discussions. In the case that an earthquake is deeper than 50 km and a distance is less than 100 km, we cannot define a single value of apparent velocity, varying with anomalously large values, more than 10 km/s. The detection of such an anomalous value may be introduced to the present warning system, so that we can distinguish it from shallow or distant earthquakes.

In Figure 5, we summarize our measurements in the form of apparent velocity as a function of focal depths in four different regions. We fit a quadratic polynomial to the result of each region by the least squares method, except for a linear line to the events in Hokkaido because its quadratic fit is virtually identical. In all the regions, the deeper an earthquake is located, the faster a value of apparent velocity becomes, due to the difference in incident angles to stations. Nevertheless, the relationship between apparent velocity and focal depth is significantly different from region to region within the Japanese islands of a scale less than 1000 km. The gradients of this relation are large for Ibaraki and Nagano prefectures compared to those for Hokkaido and the Kinki region, that is, their apparent velocities are systematically larger. For shallow earthquakes (shallower than 10 km), for example, it is 7.1 km/s in Hokkaido but only 5.5 km/s in Nagano prefecture in central Japan, slower by 20 %.

Three-dimensional P-wave velocity maps of the Japanese islands were estimated by many tomographic studies, using local earthquakes in and around Japan. For example, the result of Matsubara et al. (2008) showed P-wave velocity in central Japan (Nagano

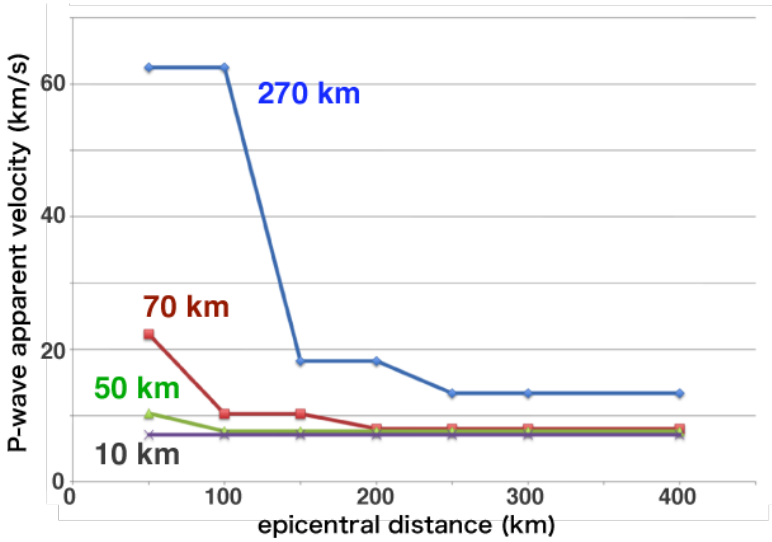

Figure 4: P-wave apparent velocities as functions of epicentral distance for earthquakes in Hokkaido, Japan with four focal depths.

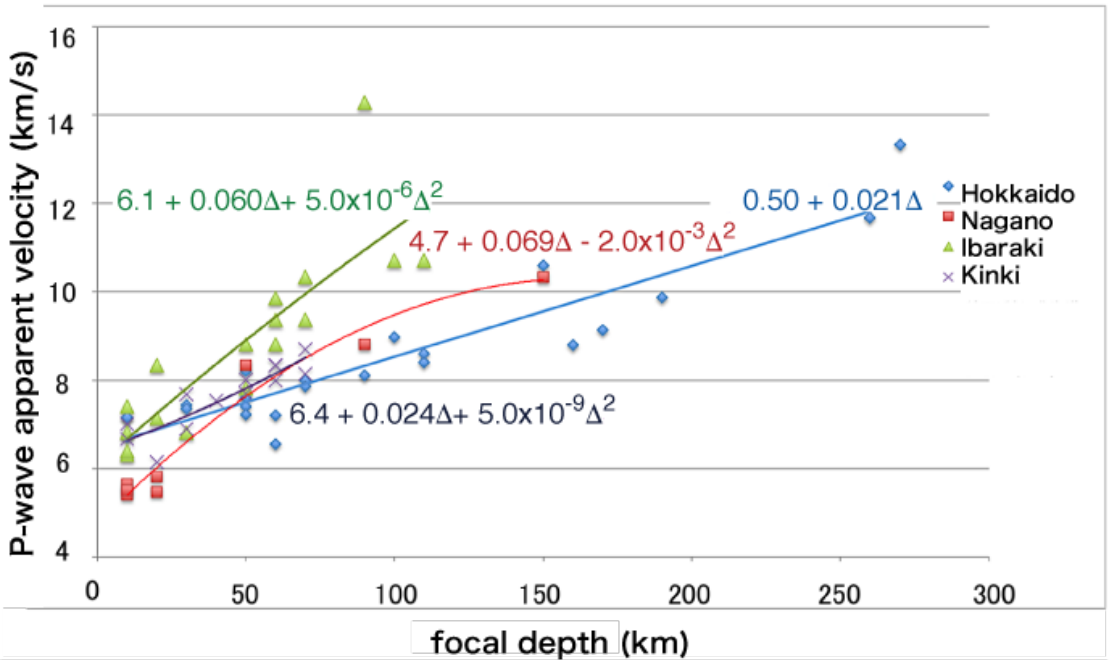

Figure 5: P-wave apparent velocities as functions of focal depth in four regions of Japan (Hokkaido, Nagano, Ibaraki and Kinki) fitted by quadratic polynomials. Epicentral distances from 250 to 400 km were selected.

prefecture) is slower than the average by about 10 % in the lower crust (30 km in depth). High mountains in this region should be linked with a thick crust of low velocities. The overall spatial pattern of those tomographic maps agrees with our present results, but the magnitude of variations in this study is much larger than theirs, probably because tomographic approaches tend to smooth out large and abrupt variations in velocity. The results of apparent velocity in this study should be related mainly to shallow velocity structures of the upper crust. In the practical application to early warning systems, therefore, we may need to classify regions by direct measurements of apparent velocities, as we did in this study, rather than any

references of conventional tomographic studies of P wave. The classification of regions could be done in detail to enhance the precision of our empirical Green's function. For the practical application to a warning system, however, it may be sufficient if we can estimate the arrival time of each point with the accuracy of several seconds. In the case of Japan where regional variations in velocity may be one of the largest regions in the world, each region to be classified seems to be of several hundreds kilometers in scale, as shown in Figure 5.

Abnormal seismic intensity: Effect of subducting slabs

In subduction zones such as Japan, it is well known that a subducting slab of low temperature or high velocity, compared with its surrounding mantle, leads to abnormal characters of seismic wave propagation and amplitude distribution of ground shakings related to the attenuation of high-frequency waves (Utsu, 1966). The apparent velocity in Japan thus turns to be highly anisotropic for deep events whose propagations have been characterized as a zone of "abnormal seismic intensity": ground motions of high frequency are amplified in specific zones on the surface while very weak in other regions. Such observations have been widely recognized in Japan if a deep event occurs under the Sea of Okhotsk or under the Sea of Japan. This phenomenon has to be taken into consideration in our extrapolation approach because the pattern of seismic wave propagation does not show a simple circular form in such a case.

As an example, we checked seismic wave propagations in Japan for three earthquakes in the west of Japan beneath Vladivostok, Russia: (1) on 18 February 2010 of M 6.9 and 590 km in depth, (2) on 5 April 2013 of M6.3 and 593 km, and (3) on 29 July 2013 of M 5.7 and 476 km. Figure 6 shows the wavefronts represented by isochrone contours for Event (2) from the arrival time of P wave at each observation point, together with the wavefronts for a large deep earthquake of M7.3 and 590 km in depth in the Sea of Okhotsuk on 14 August 2012. The apparent velocity is slow in the Souya district in the north of Hokkaido Island while fast in the Tokachi district in the south for both examples of Figure 6. The average apparent velocity is 7.5 km/s in Souya versus 13 km/s in Tokachi. The Pacific plate is subducting beneath the Hokkaido island from its southeastern coast in the direction of northwest. The upper boundary of the plate is about 300 km deep in Souya while about 50 km in Tokachi. The fast apparent velocity in Tokachi may be related to the slab of high velocity while the slow in Souya is linked to the mantle wedge of very low velocity over the plate. We also found that there are significant small-scale variations in apparent velocity within Hokkaido Island.

In addition, we compared the propagations of P wave for shallow earthquakes, for example, an event on 19 April 2013 in Kuril Islands of M7.0 and 10 km in depth, having not occurred in a deep part of the subducting Pacific plate. For such shallow earthquakes, we cannot find any abnormal propagations with systematic difference in apparent velocity within Hokkaido. Waves propagate only in shallow parts in this case, so that the effect of the slab in the mantle can be negligible.

Furthermore, we investigated the difference in apparent velocity depending on propagation directions. In other words, there may be apparent anisotropy in P-wave

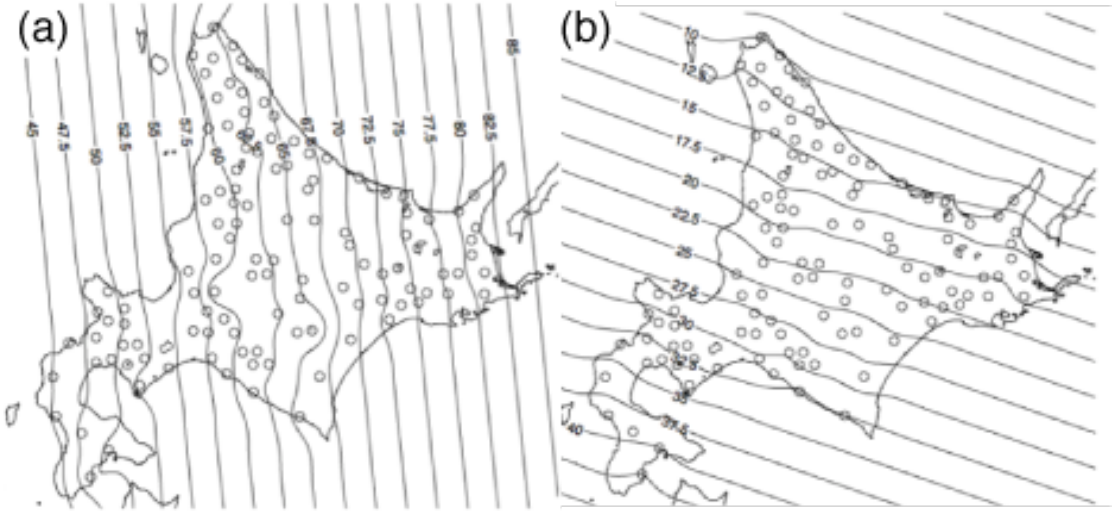

Figure 6: P-wave wavefronts in Hokkaido for deep earthquakes (a) on 5 April 2013 of M6.3 and 593 km in depth in the west (beneath Vladiostock) and (b) on 14 August 2012 of M7.3 and 590 km in the northeast (beneath the Sea of Okhotsuk). The numbers of wavefronts are measured in seconds after each origin time.

propagation. Figure 6 shows different apparent velocities for two deep earthquakes in the Pacific plate by the direction of wave propagation. The apparent velocity is clearly anisotropic on the surface, that is, 11.1 km/s from west to east, while 14.0 km/s from northeast to southwest. This anisotropic character may be caused by a complex structure within the Pacific plate as well as its complex geometry.

Measurement of local apparent velocity and direction

In the proposed extrapolation method of seismic wavefield for an earthquake early warning system, we need to measure not only the velocity but also the direction of P-wave propagation promptly with a limited number of seismogram records. In this chapter, we shall apply the frequency-wavenumber (*f-k*) spectral analysis to the Hi-net data of Japan with a group of adjacent stations as a small array.

The *f-k* spectral analysis has been applied to seismology in order to utilize a dense seismic network as an array effectively. The waveforms or seismograms recorded at stations whose locations are not distant may resemble each other. If each waveform is shifted in time properly, the resulted ensemble of waveforms may express a plane wave propagating on the surface with a specific apparent velocity v and direction θ. This property is expressed by a wavenumber vector (k_x, k_y) where $|k| = \omega/v$, $\tan\theta = k_y/k_x$ and ω is the angular velocity. In order to estimate the wavenumber vector, we calculate the following quantity as a beam power in the form of a function of k_x and k_y by summing all the recorded waveforms $u(x,y,t)$:

$$P(k_x,k_y,\omega) = \iiint \left\langle u(x,y,t)u(x+x',y+y',t+t') \right\rangle \exp(i\omega t' - ik_x x' - ik_y y')dx'dy'dt' , \qquad (3)$$

where $\left\langle u(x,y,t)u(x+x',y+y',t+t') \right\rangle$ represents the auto-correlation of all the recorded waveforms. In the present analysis, we shall use the slowness vector instead of the

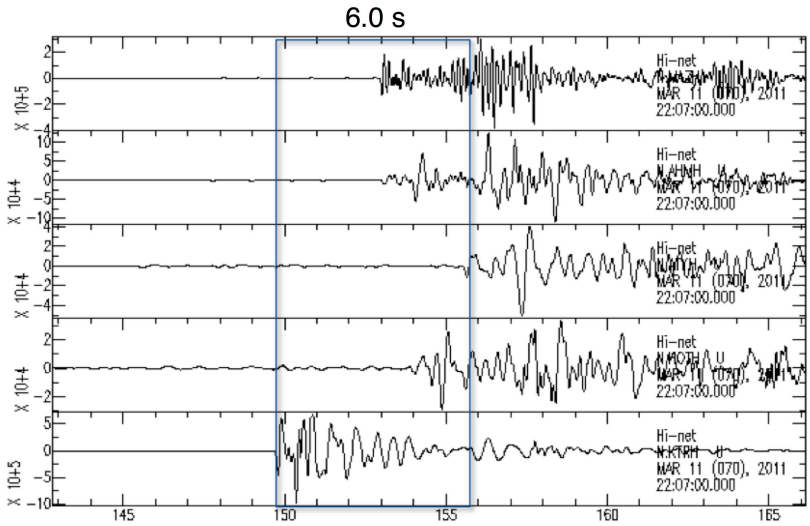

Figure 7: Example of a group of seismograms (array C) bandpass filtered from 0.3 to 5 Hz for an event in the Hida district of Gifu prefecture, central Japan, with a time window for the f-k analysis to estimate the propagating direction and velocity of P wave.

wavenumber vectors: $s_x=\cos\theta/v$ and $s_y=\sin\theta/v$. In the two-dimensional wavenumber or slowness domain (k_x, k_y) or (s_x, s_y), we identify the maximum spectral peak of the beam power of equation (3) that corresponds to the arrival of a specific phase (P wave in this study) into the array of stations (Osada et al., 2006; Havskov, 2010).

As mentioned earlier, the spatial derivative of wavefronts, $\partial U/\partial n$, in Figure 1b can be estimated by this analysis, which should improve the accuracy of an earthquake early warning system in the process of wavefield extrapolation. With the Hi-net data of Japan with their station interval of about 20 km, we grouped four to six adjacent stations as an array for the *f-k* analysis of P wave observed on an early stage of its propagation, that is, near its epicenter. In this study, we conducted *f-k* analysis of Hi-net seismograms for an earthquake on 11 March 2011 in the Hida district of Gihu prefecture of M 3.4 and 3 km in depth. Figure 7 shows an example of a group of seismograms (array C) in the frequency range from 0.3 to 5 Hz for our *f-k* analysis. We apply a time window of 6.0 seconds to seismograms, staring at the earliest P-wave arrival time of all the stations.

Figure 8 shows the plot of beam powers in the slowness domain (s_x, s_y) for array C with the map of its epicenter and their stations, using the seismograms of Figure 7. The location of the spectral peak gives the direction of the incident P wave on the surface so that it should point out the direction of the epicenter from the center of the array. The location of the peak in Figure 7 is in the southwest (240 degrees clockwise from the north), and its actual direction of the epicenter is indeed in the southwest (249 degrees), as viewed from the array or the group of the used stations. That is, the direction of the epicenter was successfully estimated in this example. The apparent velocity of P wave can be also estimated by the location of the peak in this plot with its slowness as the distance from the origin. The velocity was estimated to be 6.8 km/s in this example.

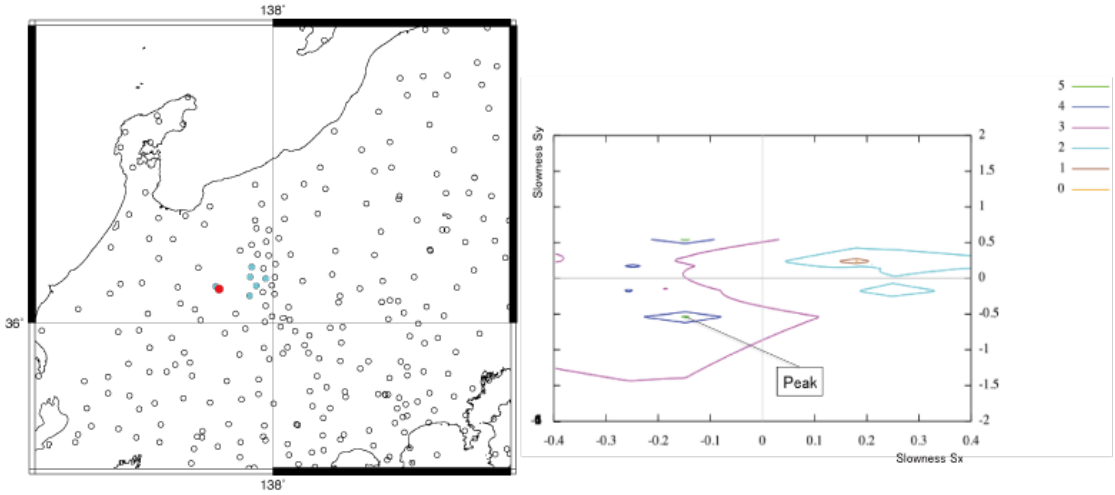

Figure 8: Locations of stations of Figure 7 (array C) in blue and the epicenter of an event in red in the left, and contours of their f-k power spectra of frequency from 0.3 to 5 Hz in the slowness domain in the right.

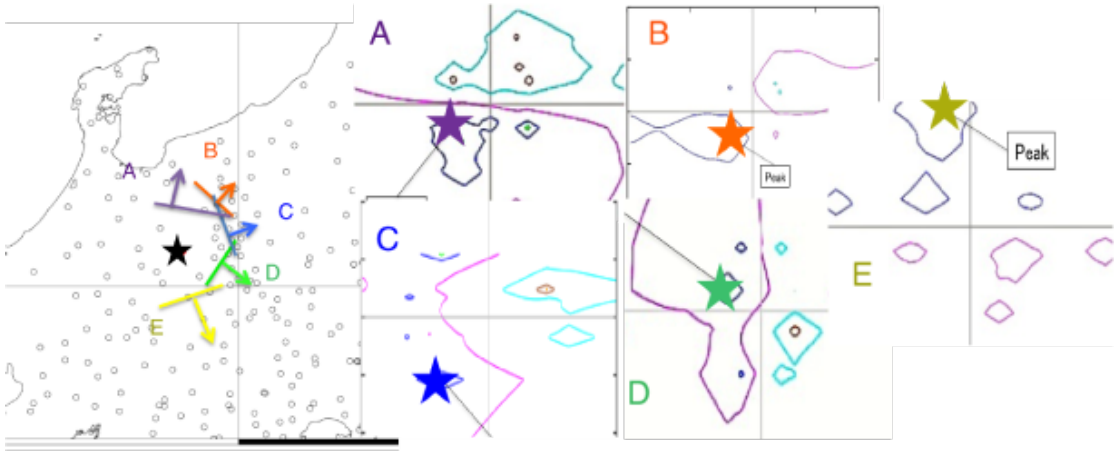

Figure 9: f-k power spectra of five different groups (arrays A-E) of stations for an event of Figure 8 with their estimated directions of P-wave propagation from peaks of their f-k spectra. The epicenter (the star) in the right figure can be retrieved by combining all the estimated directions.

Changing groups of neighboring stations, we set up different arrays from array C. Figure 9 shows the results of five different arrays, arrays A to E (array C is same as Figure 8). The location of the peak is varied for each array, that is, the estimated directions and velocities were slightly different from each other. All the above five results combined, the propagation of seismic wave can be imaged as a circular wavefront. The center of the circle agrees with the epicenter well. For our purpose, however, it is essential that the analysis with the combination of these five patterns in Figure 8 was conducted by the time window of only about 6 seconds after the earliest P-wave arrival of each array, as shown in Figure 7. The present *f-k* analysis can be applied to our proposed new warning system, that is, we can obtain not only the timing but also the direction of the propagating wavefield for our Neumann-type extrapolation approach (Figure 1b).

Table 1: Azimuths and apparent velocities measured with each array of Figure 9. θ is the azimuth in degree clockwise from the north, and v is the apparent velocity in km/s in frequency from 0.3 to 5 Hz. θ' and v' are those for frequency from 0.1 to 1 Hz. ϕ is the actual azimuth from the center of each array to the epicenter.

	θ (deg.)	v (km/s)	θ' (deg.)	v' (km/s)	ϕ (deg.)
array A	246	6.4	230	6.1	210
array B	229	4.1	265	5.1	241
array C	240	6.8	249	5.2	249
array D	296	6.4	289	5.2	305
array E	343	5.1	344	4.5	332

The *f-k* analysis assumes coherent plane-wave arrival at each seismic array. Since the epicentral distances in the present example were less than 100 km, the actual wavefront incident to each array should be slightly curved. In addition, the double-couple radiation pattern may yield the P waves of opposite polarities recorded at stations of one array. These factors would degrade the accuracy and stability of the estimation of direction and velocity. In the present example, the range of take-off angles from the source region was less than 30 degrees for each array, and the actual curved wavefront could be well approximated to be planar. That is, the observed curvature of wavefront did not affect our measurement significantly. If a node of the radiation pattern were included in the azimuthal range that covered a specific array, our measurement might not work well. In the present example, however, this appears not to have taken place because clear peaks in the slowness or wavenumber domain were identified. In summary, we may be able to apply our approach to array observations not far from a source region, that is, to early warning systems in practice.

Next, we conducted another *f-k* analysis using exactly the same observational groups and the same earthquake but in a lower frequency range from 0.1 to 1 Hz. Table 1 summarizes the directions and velocities estimated by each array. θ and v are the directions and velocities in the previous frequency range from 0.3 to 5 Hz (Figure 8) while θ' and v' in the low frequency range from 0.1 to 1 Hz, respectively. ϕ represents the actual azimuth from the center of each array to the epicenter. Compared with the results in frequency from 0.3 to 5 Hz with those from 0.1 to 1 Hz, we may be able to estimate the directions of wave propagation (the direction of the epicenter from each array in this case) with sufficient accuracy in each frequency range. In the estimation of apparent velocity, the results in the low frequency are slightly accurate, considering the apparent velocity of shallow earthquakes of Nagano prefecture to be 5.5 km/s, as shown in the previous chapter (Figure 5). It does not, however, mean that the values estimated at low frequency are much better than those of high frequency in every situation. The optimal frequency range of each array in *f-k* spectral analysis should be estimated with actual data a priori. As far as we use waveforms in the frequency range from 0.1 to 5 Hz at Hi-net stations, it is possible to obtain the apparent velocity and direction of propagation accurately enough to meet the present purpose of a new warning system.

Conclusions and future perspectives

In the present earthquake early warning system of Japan, it does not occasionally work properly in the following cases: (1) more than one earthquakes occur nearly

simultaneously, (2) a deep event whose wavefront propagates in a different manner from shallow ones, (3) a large event whose finite fault area cannot be neglected (M > 8). We proposed a new approach to extrapolate the wavefield observed near its epicenter on an early stage of its occurrence without determining the epicenter location and magnitude. Although we refer to the technique proposed by Hoshiba (2013), our approach estimates the wavefield in the future at remote points by using not only the observed waveforms but also their spatial derivatives, based on the representation theorem with Green's functions (Neumann type). The spatial derivatives correspond to the apparent velocity and direction of seismic waves. By using this additional information, we can predict the arrival time and amplitude of the wavefield accurately even with a small number of observation points.

In order to investigate whether we can estimate Green's functions that are sufficient to the above approach with actual data or not, we measured apparent velocities of P wave for various earthquakes in and around Japan with the Hi-net data. There are large variations in apparent velocity from region to region even in Japan of scale of several hundreds kilometers. The deeper an earthquake occurs, the faster its apparent velocity becomes. As a function of focal depths, we may classify regions for different apparent velocities, which appears to be sufficient for a new warning system as a prior information of the Green's function to be used. In Japan with subducting plates just beneath it, abnormal propagation patterns should be cared for deep earthquakes. We calculated the apparent velocities for deep earthquakes that cause an abnormal seismic intensity pattern in Hokkaido, identifying small-scale variations and anisotropy of apparent velocity.

Next, we proposed *f-k* spectral analysis to estimate the apparent velocity and direction of P-wave propagation. By the analysis of a shallow earthquake in central Japan, we could determine the direction of P-wave propagation accurately in not much later than 6 seconds after its origin time at stations near its epicenter in the frequency range from 0.1 to 5 Hz. This confirmed the actual applicability of our approach with not only arrival times but direction/velocity of wave propagation to a new warning system. High frequency seismic waveforms are, however, affected by the site effect of each station, as small-scale heterogeneities or complex near-surface structures just beneath the station. In order to correct such site effects, we may need site correction terms by taking the spectral ratio of waveforms at stations to an adjust reference station in advance for further tunings of accurate estimation by *f-k* spectral analysis.

Another possible improvement may be possible by not the direct use of the Green's function in equation (2) but the introduction of a function smoothed over space. One example is the Gaussian beam method (Červeny and Pšenčík, 2010). Equation (2) means the extrapolation from the specific direction of each observed point. The direction corresponds to the spectral peak in the *f-k* spectral analysis, as shown in Figures 8 and 9. Since we are going to make a wavefield $U(\mathbf{r}, t)$ or $\partial U/\partial n$ from input data only at a few points over the obseration surface S, however, this process will often give unstable results. Each peak in the wavenumber or slowness domain of Figure 9 has a finite extent. The width of this extent may give the accuracy in our measurement of propagating direction but also it indicates the smoothing effect of the wavefield to be extrapolated. The Gaussian beam with a certain width introduces such a smoothing effect originated from finite frequency or wavelengths of actual data. If

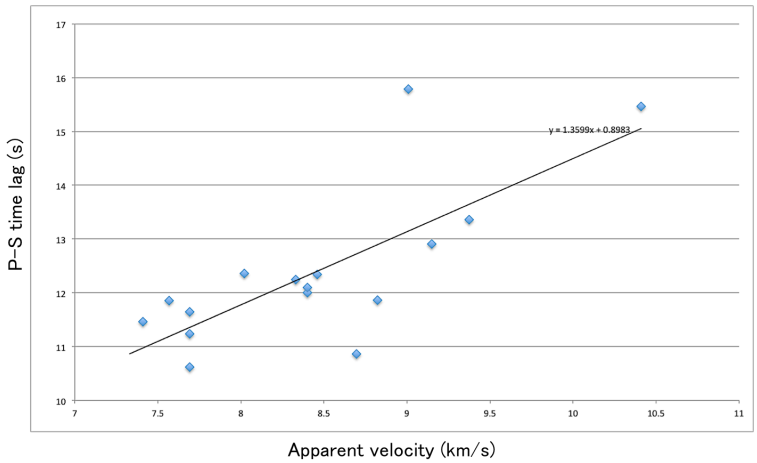

Figure 10: Apparent velocity of P wave versus P-S time lag diagram for earthquakes of shallower than 70 km in depth in the southwest region off Nemuro Peninsula, Hokkaido, Japan.

we replace Green's functions for extrapolation in equation (2) by Gaussian beams with the width of each measured *f-k* spectral peak, the estimated wavefield should be more stable than in a case with the use of the single value of each propagating direction.

In our approach based on the wavefield extrapolation, we have considered P waves for both input and output data. In a similar manner, adopting radiative transfer theory, Hoshiba and Aoki (2015) estimated S-wave arrival times from the S-wave data observed early. While a useful warning system estimates S-wave arrival times from P-wave observations on an early stage or near the epicenter of an earthquake, any warning systems based on the information of wave propagations alone cannot directly predict the wavefield of S wave from P-wave data in principle. We therefore need to introduce any additional empirical relations to estimate the propagation of S wave from the input data of P wave. As the first step, we propose the use of empirical relations of P-S time lag as a function of apparent velocity. We preliminary examined them for earthquakes in Hokkaido. Such an attempts with various types and locations of earthquakes did not give any satisfactory results. Once we limited earthquakes in a small regional and of similar focal depths, however, we could obtain a relatively good empirical relation. Figure 10 shows an example only with earthquakes shallower than 70 km in the southwest off the coast of the Nemuro peninsula where the Pacific plate is subducting. A relatively good linear relation was obtained between apparent velocity of P wave and P-S time lag in this case. That is, we show the possibility to estimate the arrival times of S wave only with P-wave seismograms, if its apparent velocity is measured, by the proposed wavefield extrapolation with this type of empirical relations. Such an effort may lend us to a truly practical level of our approach with wavefield extrapolation in the future.

Acknowledgments

We used seismic data of the Hi-net stations operated by National Research Institute for Earth and Disaster Prevention of Japan. We appreciate useful comments of a reviewer on the original manuscript. Some figures were drawn by software tools of SAC (Tull, 1986) and GMT (Wessel and Smith, 1998).

References

Aki, K., and Richards, P.G. (2009). *Quantitative Seismology, 2nd ed.*, University Science Books, pp. 699.

Červený, V., and Pšenčík, I. (2010). Gaussian beams in inhomogeneous anisotropic layered structures, *Geophys. J. Int.*, **180**, 798-812, doi:10.1111/j.1365-246X.2009.0442.x.

Havskov, J., and Ottenmoeller, L. (2010). *Routine Data Processing in Earthquake Seismology: With Sample Data, Exercises and Software*, Springer Verlag, pp. 347.

Hoshiba, M. (2013). Real-time prediction of ground motion by Kirchhoff-Fresnel boundary integral equation method: Extended front detection method for earthquake early warning, *J. Geophys. Res.*, **118**, 1038–1050, doi: 10.1002/jgrb.50119.

Hoshiba, M., and Aoki, S. (2015). Numerical shake prediction for earthquake early warning: Data assimilation, real-time shake mapping, and simulation of wave propagation, *Bull. Seismol. Soc. Amer.*, **105**, doi: 10.1785/0120140280.

Hoshiba, M., and Iwakiri, K. (2011). Initial 30 seconds of the 2011 off the Pacific coast of Tohoku earthquake (M_W9.0) –amplitude and t_c for magnitude estimation for earthquake early warning, *Earth Planets Space*, **63**, 553–557.

Kamigaichi, O., Saito, M., Doi, K., Matsumori, T., Tsukada, S., Takeda, K., Shimoyama, T., Nakamura, K., Kiyomoto, M., and Watanabe, Y. (2009). Earthquake Early Warning in Japan – Warning the general public and future prospects, *Seism. Res. Lett.*, **80**, 717–726.

Matsubara, M., Obara, K., and Kasahara, K. (2008). Three-dimensional P- and S-wave velocity structures beneath the Japan Islands obtained by high-density seismic stations by seismic tomography, *Tectonophys.*, **454**, 86-103.

Obara, K. (2002). Hi-net: High sensitivity seismograph network, Japan, in *Methods and Applications of Signal Processing in Seismic Network Operations*, ed. by Takanami, T. and Kitagawa, G., Springer Verlag, 79-88.

Osada, K., Yoshizawa, K., and Yomogida, K. (2006). Upper boundary of the Pacific plate subducting beneath Hokkaido, Japan, estimated from ScSp phase, *Phys. Erath Planet. Inter.*, **183**, 63-72.

Shearer, P.M. (2009). *Introduction to Seismology*, *2nd ed.*, Cambridge Univ. Press, pp. 396.

Tull, J.E. (1986). SAC: Assigned processing system for research seismology, *IEEE Symposium Circuits Systems*, **2**, 441-443.

Utsu, T. (1966). Regional differences in absorption of seismic waves in the upper mantle as inferred from abnormal distribution of seismic intensities, *J. Fac. Sci. Hokkaido Univ. Ser. 7*, **4**, 359-374.

Wessel, P., and Smith, W.H.F. (1998). New improved version of the Generic Mapping Tools released, *EOS Trans. AGU*, **79**, 579.

Array Observation of Strong Ground Motion for Real Time Estimation of Current Wavefield

Masashi Ogiso, Naoki Hayashimoto, Mitsuyuki Hoshiba

Meteorological Research Institute, Japan Meteorological Agency, 1-1 Nagamine, Tsukuba, Japan, mogiso@mri-jma.go.jp

Abstract

When we aim to predict ground motion in real time without any hypocentral information, estimates of current wavefield is important, similar to numerical weather prediction. In addition to seismic amplitude distribution, propagation direction and speed of wavefield can be used for estimating current wavefield. Seismic array observation enables us to estimate slowness vector of the wavefield at the observation site. In order to utilize this feature to real time estimation of current wavefield, we have deployed a seismic array network using six accelerometers. By using an ingenious grid search method, we were able to estimate slowness vector within 1 s, which is required for real time calculation. Estimated backazimuth was affected by the subsurface structure beneath the array even for the case of local earthquake. Simple correction methods, static correction and dipping layer correction, worked well to remove the influence of subsurface structure with little influence on the calculation time.

Introduction

The 2011 off the Pacific coast of Tohoku Earthquake (M_w 9.0) revealed two fundamental issues in the earthquake early warning (EEW) system of the Japan Meteorological Agency (JMA): one is underestimation of strong ground motion area due to the large extent of focal area and the other is false alarms after a few tens of days according to the simultaneous occurrence of multiple aftershocks (Hoshiba et al., 2011). To deal with these issues, we aim to construct a ground motion prediction method without estimating any hypocentral parameters (Hoshiba, 2013). Hoshiba and Aoki (2015) successfully implemented this idea to the actual cases of the 2011 Tohoku Earthquake and the 2004 Mid-Niigata Prefecture Earthquake (M_w 6.7), and they named the method "Numerical Shake Prediction" from an analogy to the numerical weather prediction in meteorology. There are two key techniques in their method. One is the accurate estimation of current wavefield and the other is the real time ground motion simulation from the estimated current wavefield as the initial condition. In Hoshiba and Aoki (2015), they used amplitude distribution in the dense seismic network for the estimation of current wavefield. However, there should be more parameters which can be used for estimating current wavefield. Array observation is a powerful tool for the observation of propagation direction and apparent velocity of the wavefield (e.g. Rost and Thomas, 2002). Propagation direction and apparent velocity of the wavefield may help an accurate estimation of current wavefield. To utilize an array observation to

estimate the current wavefield, i.e. not only initial P-wave of earthquakes but also strong ground motion and their coda part, we have constructed a small-aperture array and we investigate how to utilize array observation for the EEW system. In this paper, we describe the details of the array network, the method to calculate slowness vector in real time, and the features of estimated backazimuth.

Configuration of the array network

At this time, the array network consists of six seismometers, located on the premises of Meteorological Research Institute (Fig. 1a). Array response function is shown in Fig. 1(b). Stations 204, 205, 206 and 208 are located linearly in NE-SW direction. Due to such the array configuration, array response function has relatively sharp in NE-SW direction. Resolution is better for the earthquakes occurred in NE-SW direction than those of NW-SE direction. We use CV-374 strong motion seismometer (Tokyo Sokushin Co.) for array observation. This seismometer is accelerometer with a full-scale range of ±2g. We selected each site considering the use of pre-existing power and line of communication as well as the expanse of array network. As a result, two seismometers are installed on the free surface: stations 204 is on the concrete pier and 208 is buried on the ground. Other four stations are fastened to the concrete floor of each building (Fig. 2). Aperture of the array is about 300 m. To detect arrival time differences between seismometers in such a small-aperture array, we select 500 Hz as the sampling frequency. Seismograms are recorded continuously in the WIN format (Urabe, 1994) on each seismometer. Although the seismometer has an ability to send a waveform data in every 1 s packet, we have not yet constructed the on-line array analysis system, and our results described below are based on the off-line analysis using waveform files.

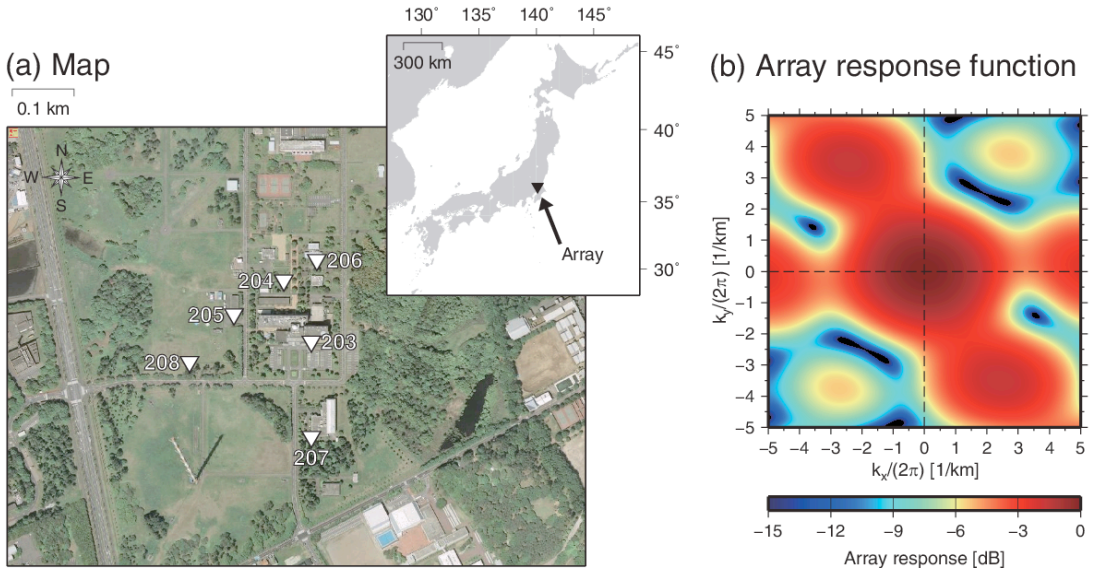

Figure 1: (a) Station distribution of the array network. (b) Array response function of the array.

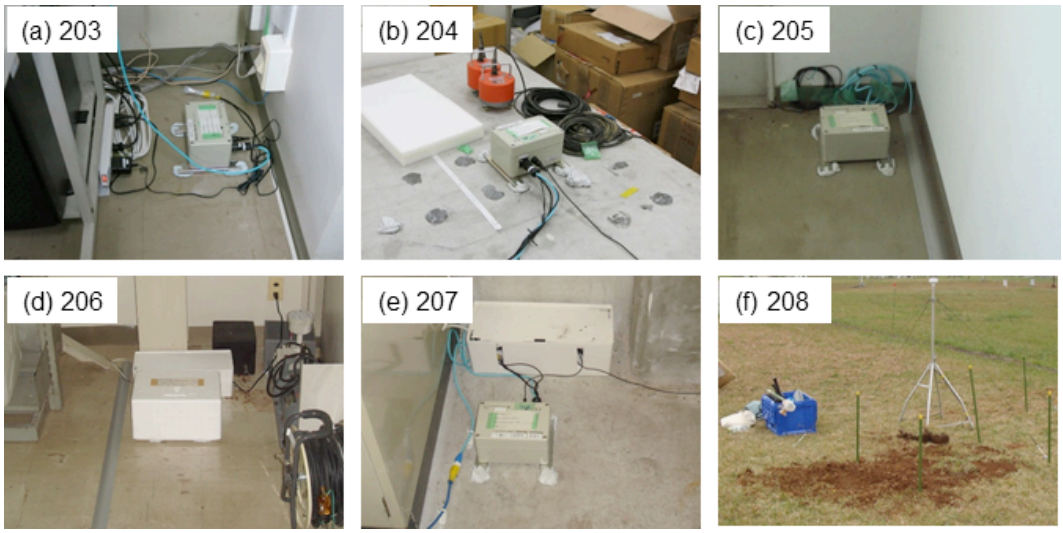

Figure 2: Installation status of each seismometer of the array. Station (b) 204 is on the concrete pier and (f) 208 is buried on the ground. Other stations are fastened to the floor of each building.

Method of estimating backazimuth and apparent velocity

In this study, we focus on the propagation direction and apparent velocity of coherent waves rather than amplitude. Hence, we adopt semblance method (Neidell and Taner, 1971) to estimate backazimuth and apparent velocity. Since semblance is defined in the time domain, it avoids a transformation in the frequency domain. Hence, calculation load will be small compared with other methods defined in the frequency domain.

Semblance $S(s_x, s_y)$ at certain slowness vector (s_x, s_y) is defined by the following equation:

$$S(s_x, s_y) = \frac{1}{N} \frac{\sum_{k=1}^{M} \left[\sum_{i=1}^{N} u_i \{ t_k + (s_x \cdot x_i + s_y \cdot y_i) \} \right]^2}{\sum_{k=1}^{M} \sum_{i=1}^{N} u_i^2 (t_k)}, \quad (1)$$

where $u_i(t_k)$ is the amplitude of waveform on station i at time t_k, (x_i, y_i) is the station location vector of station i, M is the number of data points corresponds to the time window for semblance calculation, and N is the number of stations, respectively. Backazimuth and apparent velocity is calculated from the slowness vector where the semblance is maximum.

Usually grid search method is used to find the maximum semblance value defined in eq. (1). Grid search is a simple and robust algorithm, however, it is time-consuming to apply in real time. To balance the advantages of grid search and less computation time, we adopt oct-tree search algorithm (Lomax et al., 2009). We defined an evaluation function $D(s_x, s_y)$ as follows:

$$D(s_x, s_y) = \alpha \cdot S(s_x, s_y) \cdot (ds)^2, \quad (2)$$

where α is an coefficient which determines whether global or local search precedes and ds is the size of grid, respectively. Fig. 3 is the schematic illustration of how oct-tree search works in this study. At first, we conduct a grid search in a large grid size (Fig. 3a). In initial sampling (Fig. 3a), coefficient α is set to be 1. Next, we calculate

evaluation function (eq. 2) in each grid, and find the grid where $D(s_x, s_y)$ is maximum. Then, we divide the grid where the evaluation function is maximum by 2 in both x and y direction (Fig. 3b) and calculate $S(s_x, s_y)$ and $D(s_x, s_y)$ in each new grid with a coefficient $\alpha \neq 1$. As we successively conduct the same procedure with α larger than 1 (Fig. 3c-e), finally we get a semblance distribution shown in Fig. 3f. Semblance calculation is terminated when the number of grids exceeds the pre-defined value. Comparing the assumed semblance distribution (Fig. 3a) and those by calculation (Fig. 3f), the grid size is finer in the high semblance area than the low semblance area. Coefficient α determines whether global or local search precedes. Because the value range of semblance is $1/N \leq S(s_x, s_y) \leq 1$, evaluation function at the greater semblance area may easily become lower than the minimum value of semblance when we divide the grid by 4. When we use small α, the grid with low semblance in initial sampling may divide in the early stage of the search, which means the global search . If we take an array response function into consideration to set a grid size in the initial search, we may not have to search an area around a low semblance value. In such a case we set the coefficient α large to search relatively narrow region around high semblance. Grid search may result in multiple maxima. Such the situation should reflect current wavefield correctly. Semblance values would be used as the proxy of reliability so that we should make use of estimated slowness vectors with their semblance values.

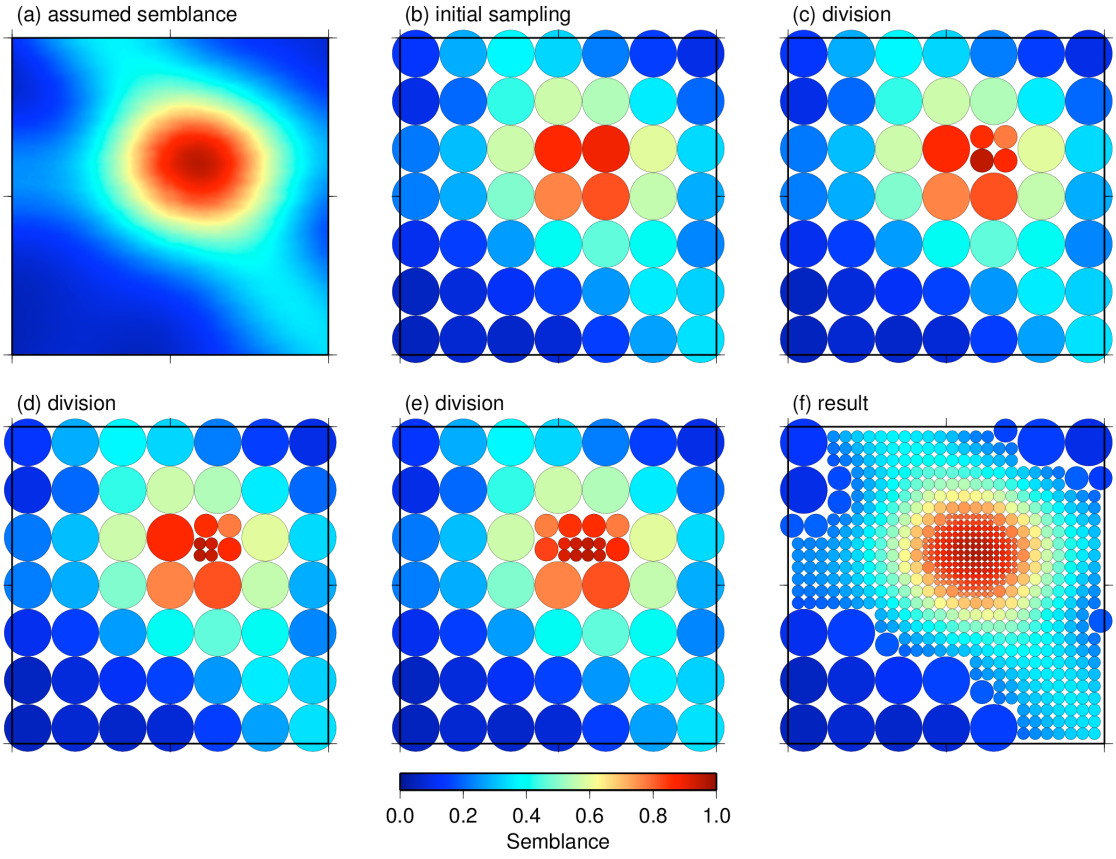

Figure 3: A schematic illustration of oct-tree search algorithm in this study.

At this time, the analysis program works for an offline waveform data. Flow chart of analysis is shown in Fig. 4. We utilize "shmdump" command of WIN system (Urabe, 1994) which dumps waveform data in each 1 s block from the file or shared memory to the standard output. Making use of this command, we are able to change the off-line system to on-line easy like the GRiD MT, on-line real time moment tensor monitoring system (Tsuruoka et al., 2009).

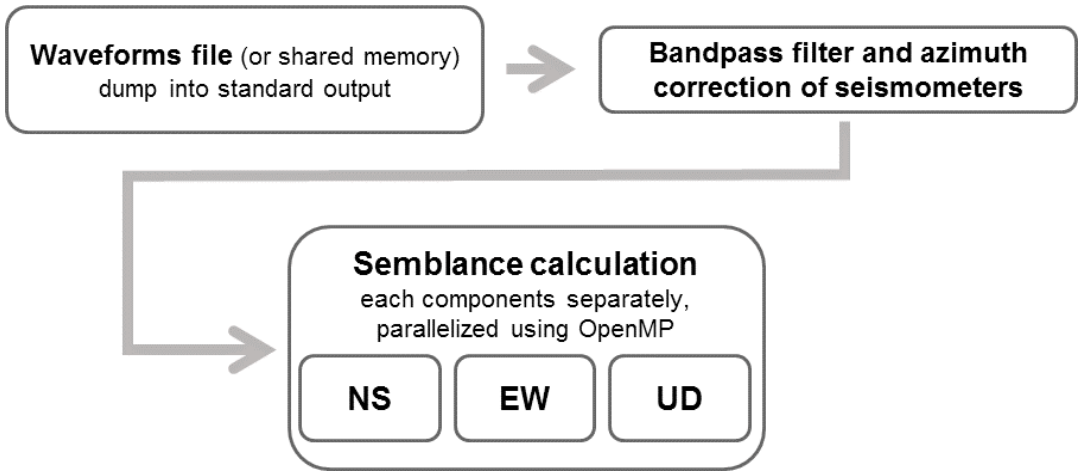

Figure 4: Flowchart of the calculation procedure.

Our analysis programs are written in C. We calculate backazimuth and apparent velocity in each three component separately, parallelized using OpenMP. We adopted the frequency range of 2-4 Hz for array analysis in this study. Lower limit of the frequency is determined by the array shape. From the array response function (Fig. 1b), slowness resolution for body waves would be worse under 1 Hz. We conducted some trial analyses and concluded phase characteristics for higher than 4 Hz were not stable and could not be used for the analysis. We set the search range of slowness vector as $-2.5 \le s_x, s_y \le 2.5$(s/km). Initial sampling grids are equally spaced in both x and y direction and the number of grids is 1600. We terminate the oct-tree search when the number of grids exceeds 4000. Coefficient α is set to be 10. Using recent personal computer (CPU: Core i7-4770 3.4GHz) and standard C compiler (gcc 4.4.5) in Linux OS, computation time is 0.8 s for semblance calculation using 500 sample/s data, 4 s time window and 6 stations. Recent telemetry system usually sends its waveform data to the data center every 1 s so that we are able to complete the calculation of backazimuth and apparent velocity before the arrival of the next 1 s data block. Note that time window of 4 s is the maximum length to calculate within 1 s for our programs. Short time window would avoid contamination of multiple phase arrivals and lead to stable estimation of backazimuthes and apparent velocities (e.g. Eisermann et al., 2015). Calculation time will also be reduced with short time window. We will compare the analysis results with various time windows in the future.

Evaluation of estimated backazimuth and apparent velocity

Fig. 5a shows a result of array analysis for the M_w 6.3 earthquake occurred in Nagano Prefecture on 22 November, 2014 using the frequency range of 2-4 Hz and 4 s time

window shifted by every 1 s. Epicenter and array site are shown in Fig. 5b. We could see that semblance of UD component and horizontal component (EW in this case) became high immediately after the P wave arrival. Semblance value of UD component decayed gradually as the time passed, while those of EW component kept relatively high until S wave arrived. When the time window corresponded to the S coda waves, semblance of each component were almost the same as the time before P wave arrival. Apparent velocity had large variations especially in the time around direct P-wave arrival. If the apparent velocity is fast, small perturbation of slowness vector (e.g. one grid difference in the grid search) leads to large perturbation in apparent velocity. We do not discuss apparent velocity in this study because of its large variation, and we only point out the necessity of improvement in the grid search algorithm especially for fast apparent velocity. One obvious characteristic was that the backazimuth estimated from horizontal component was not consistent with those inferred from the JMA earthquake catalogue. To check whether this feature was common in the array or not, we conducted array analysis for other 102 earthquakes occurred from November 2014 to July 2015 and compared backazimuth and apparent velocity with those of the JMA earthquake catalogue. Fig. 6 shows the backazimuth and apparent velocity residuals referred for the catalogue values. For P-wave results (Fig. 6a), we picked up the backazimuth and apparent velocity values when the highest semblance value was derived in UD component around the arrival time of P-wave, and either NS or EW component with highest semblance in horizontal components around the arrival time of S-wave for S-wave results (Fig. 6b). We found that backazimuth residuals had clear azimuthal dependency in both P and S waves while apparent velocity residuals had no obvious characteristics.

To investigate the causes of backazimuth residuals with azimuthal dependency, we analyzed the particle motion of initial P wave of adjacent strong motion station, IBR011 (K-NET Tsukuba, Fig. 7). We analyzed the direction of principal component of particle motion ellipse of initial P waves for 155 earthquakes in a similar manner to Matsumura (1981) and compared them with catalogue values (Fig. 8). We also plot the backazimuth residual distribution of initial P wave calculated by UD component of the array in Fig. 8(a). Note that some of the backazimuthes estimated from particle motion have large differences from catalogue values. Because low velocity layer exists under IBR011, amplitude of initial P-wave on horizontal component is quite small. Hence, estimated backazimuth shows opposite direction from that of catalogue. Nevertheless, qualitative characteristics of residual distribution were similar to each other, that is, positive residuals in the northeastern side of observation site while negative residuals in the southwestern side of the site. This feature suggests that backazimuth residuals with azimuthal dependency reflects the subsurface structure beneath the observation site rather than the site condition of each sensor in the array. The array is located on the large plain and there is a mountain (Mt. Tsukuba) in the north of the array (Fig. 7). It is expected that the seismic basement under the array have some ups and downs corresponding to the mountain. Existence of dipping layer boundary under an array causes backazimuth residuals with azimuthal dependency, and large velocity contrast between two layers emphasizes this effect (e.g. Niazi, 1966). We attributed the feature of residuals in the array to the dipping seismic basement.

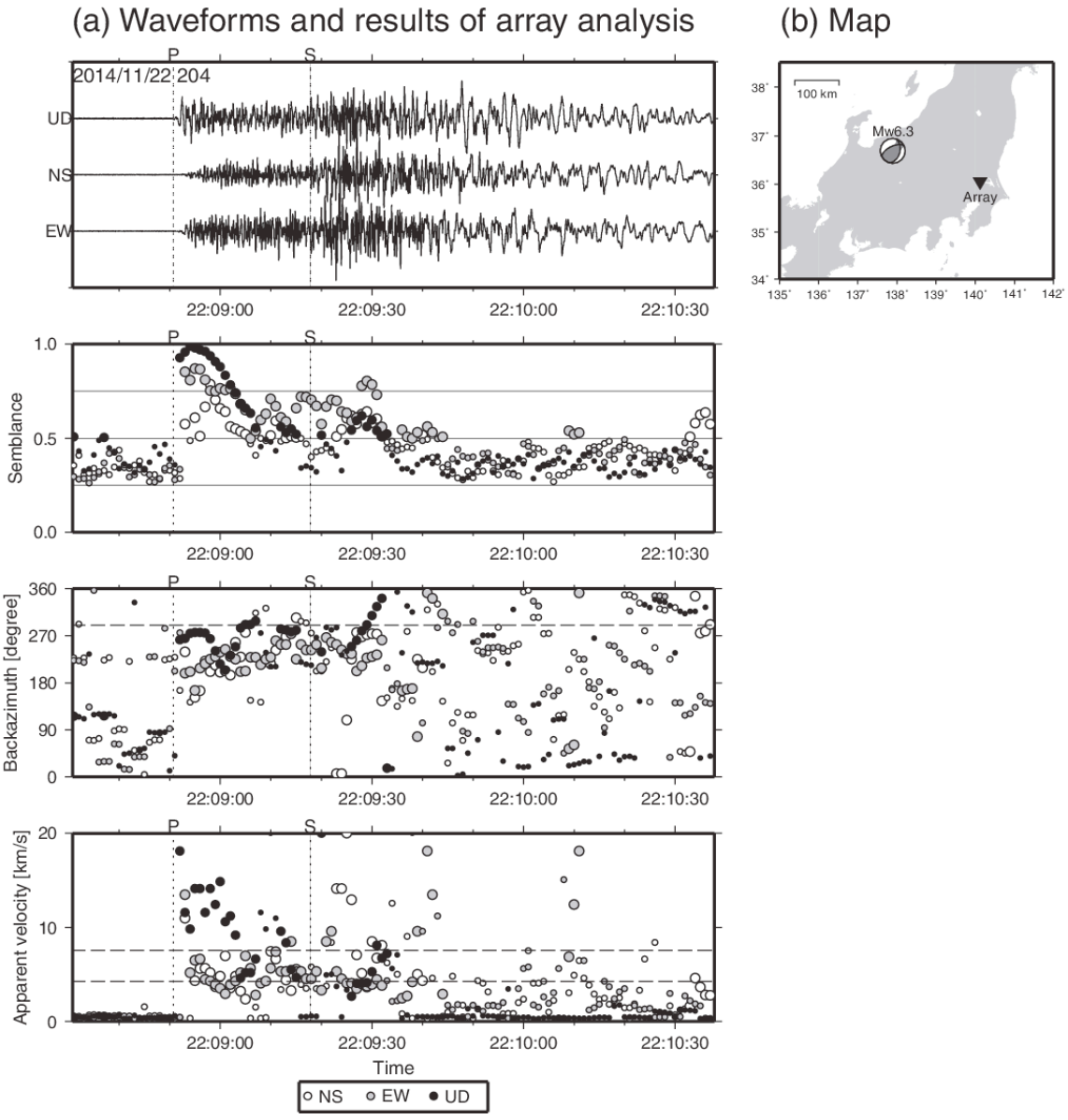

Figure 5: (a) Recorded waveforms at station 204 and calculated semblance, backazimuth and apparent velocity for the Nagano Prefecture earthquake (M_w 6.3, 22 November, 2014). (b) Map of epicenter and array site.

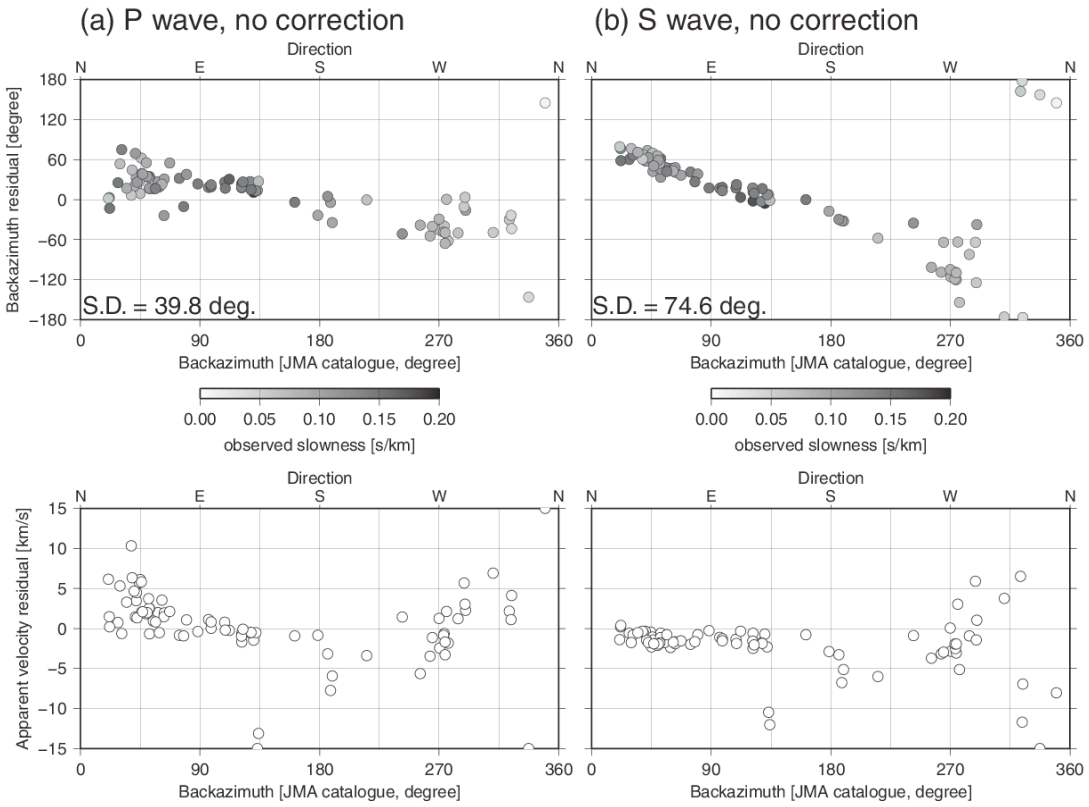

Figure 6: Backazimuth and apparent velocity residuals referred for the JMA earthquake catalog. Horizontal axis is the theoretical backazimuth of the earthquake catalogue, and (a) residuals around P-wave arrivals calculated from vertical component and (b) around S-wave arrivals calculated from horizontal component of the array.

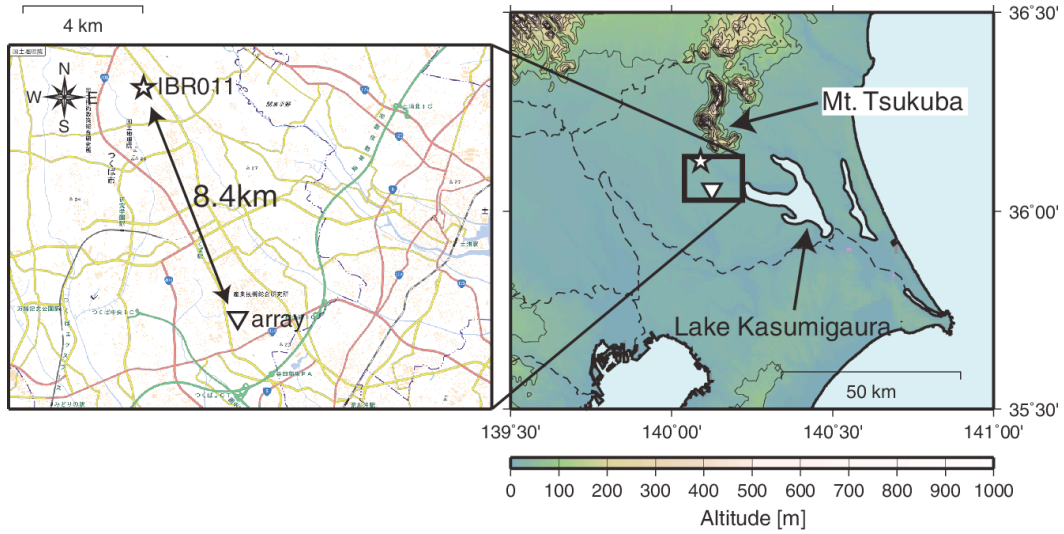

Figure 7: Location map of the array and seismic station IBR011 (K-NET Tsukuba).

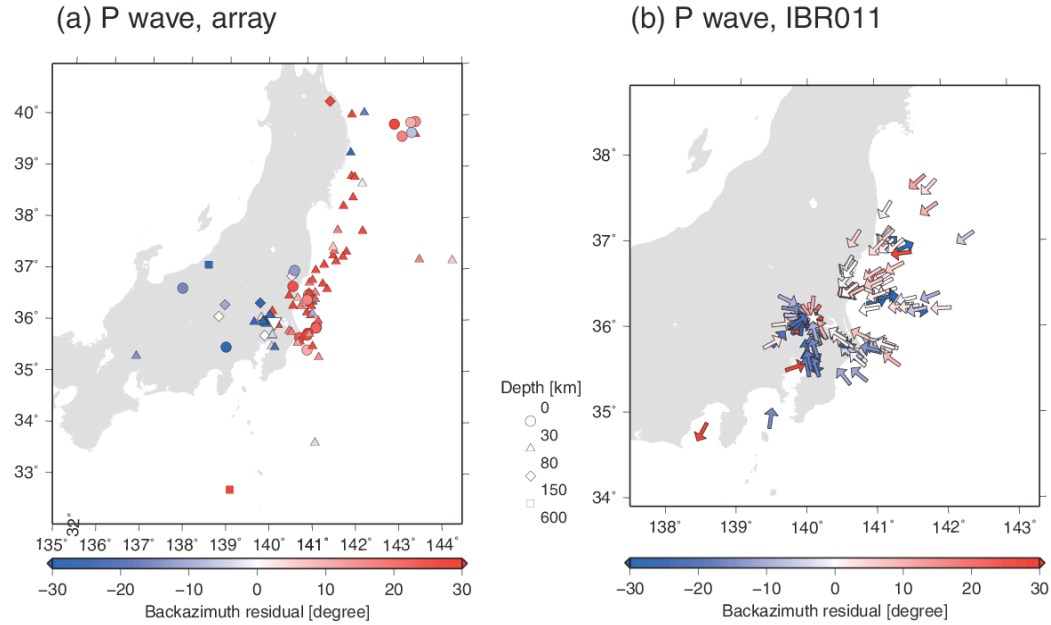

Figure 8: Regional distribution of backazimuth residuals derived by P-wave analysis of (a) the array and (b) IBR011. In (a), array is drawn in inverted triangle. Earthquakes are drawn in different symbols corresponds to the hypocentral depth. In (b), star denotes the location of IBR011. Direction of each arrow corresponds to the direction of major axis of particle motion.

Correction of backazimuth residuals

Considering our purpose of array observation described in the Introduction section, these backazimuth residuals should be corrected, because at this time it is difficult to simulate wave propagation with the fine subsurface structure which causes backazimuth residuals discussed before. In this section, we compare two correction methods. One is static correction of travel times. If the dipping layer exists, it causes travel time differences in each station of the array in addition to original time differences correspond to the slowness vector of incident waves. To correct the time differences caused by the dipping layer, we compared the observed travel time differences between reference station 204 and the others and theoretical ones, and calculated correction values for each stations. These correction values are applied when calculating semblance value (eq. 1). The other is dipping layer correction. At first, we estimated the direction and degree of dipping layer using the equations in Niazi (1966) and grid search method. Referring to the Cho et al., (2006), P-wave velocity and S-wave velocity of sediment and basement layer were assumed to be V_P=2.00km/s, V_S=0.50km/s for sediment and V_P=4.80km/s, V_S=2.84km/s for basement. After conducting grid search to minimize the backazimuth and apparent velocity residuals, strike and dip were estimated as 69 degree and 9 degree, respectively. Using equations on Maki et al., (1987) or Hao and Zheng (2010) and these velocities, strike and dip, we were able to remove the effect of dipping layer in both backazimuth and apparent velocity from the original results (Fig. 5). Note that computation time was less affected by the applying both two correction methods.

Fig. 9 shows the results that two correction methods were applied for the earthquake occurred in Nagano Prefecture on 22 November, 2014. Comparing Fig. 5 with Fig. 9,

both two correction methods worked well to correct backazimuth. Fig. 10 shows the corrected results of backazimuth and apparent velocity estimated for S waves of other 102 earthquakes. Azimuthal dependency found in Fig. 6b was reduced by the correction as shown in Fig. 10a and b.

Conclusions and future perspectives

We have conducted small-aperture hi-sampling strong motion array observation. Utilizing the effective grid search, we were able to calculate slowness vector within 1 s, which meant that we were able to evaluate slowness vector in almost real time. Comparing a backazimuth estimated from the array and that from earthquake catalogue, residuals showed clear azimuthal dependency, which should be caused by the dipping boundary between sediment and seismic basement. Considering the current situation of real time wave propagation simulation, these backazimuth residuals should be corrected and both dipping layer correction and static travel time correction worked well. Note that dipping layer correction (Maki et al., 1987; Hao and Zhang, 2010) are based on the snell's law so that we have to check that the estimated apparent velocity satisfies a ray theory when we would like to apply the correction.

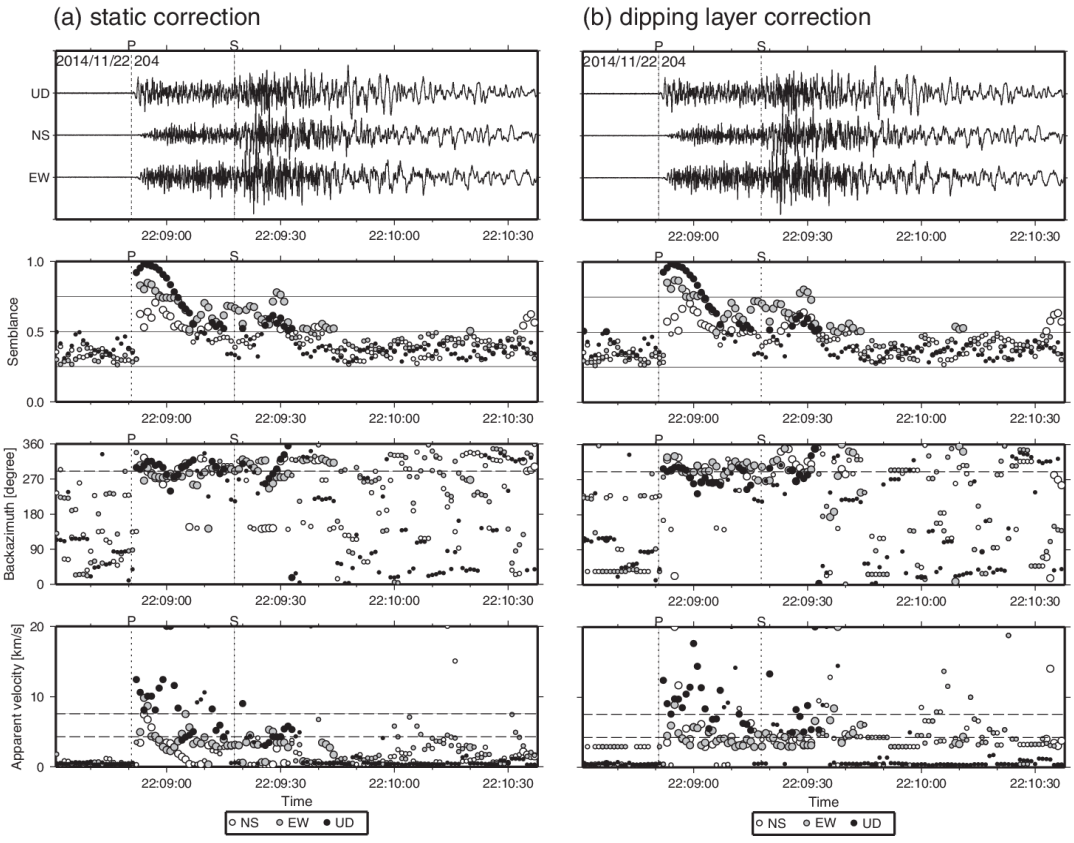

Figure 9: Same as Fig. 5a but for (a) after static correction and (b) after dipping layer correction.

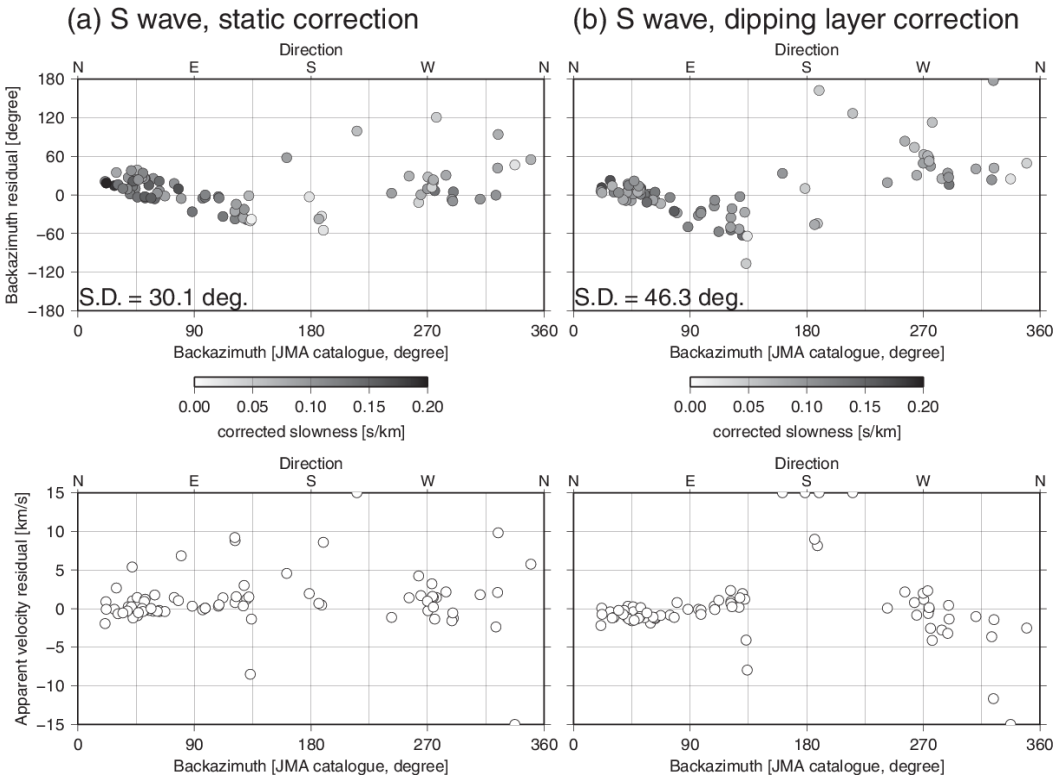

Figure 10: Same as Fig. 6b but for (a) after static correction and (b) after dipping layer correction.

We are able to obtain more observation parameters of the current wavefield in addition to the amplitude distribution through array observation. Similar to the case of numerical weather prediction, increment of observation data should lead to more accurate estimation of current wavefield. Generally, observation data include some errors. Data assimilation technique may be suitable for combining observation data and result of wave propagation simulation to estimate current wavefield (e.g. Hoshiba and Aoki, 2015). We will further estimate two essential parameters for data assimilation: observation error in the array analysis and background error in the wave propagation simulation.

Acknowledgments

We thank Gilles Hillel Wust-Bloch for his constructive comments. We used K-NET waveforms operated by the National Research Institute for Earth Science and Disaster Prevention, Japan. We used aerial photographs and digital topographic map produced by the Geospatial Information Authority of Japan. Part of this study was supported by the Earthquake Research Institute, the University of Tokyo cooperative research program and KAKENHI Grant Number 25282114 from the Japan Society for the Promotion of Science.

References

Cho, I., Tada, T. and Shinozaki, Y. (2006). New methods of microtremor exploration: the centerless circular array method and the two-radius method. Proceedings of the Third International Symposium on the Effects of Surface Geology on Seismic Motion.

Eisermann, A. S., Ziv, A. and Wust-Bloch G.H. (2015). Real-Time Back Azimuth for Earthquake Early Warning. Bull. Seismo. Soc. Am., **105**, 2275-2285. doi: 10.1785/0120140298.

Hao, C. and Zheng, Z. (2010). P-Wave Back-Azimuth and Slowness Anomalies Observed by an IMS Seismic Array LZDM. Bull. Seismo. Soc. Am., **100**, 657-669. doi: 10.1785/0120090059.

Hoshiba, M., Iwakiri, K., Hayashimoto, N, Shimoyama, T., Hirano, K., Yamada, Y., Ishigaki, Y. and Kikuta, H. (2011). Outline of the 2011 Off the Pacific coast of Tohoku earthquake (Mw 9.0)—Earthquake early warning and observed seismic intensity. Earth Planets Space, **63**, 547–551, doi: 10.5047/eps.2011.05.031.

Hoshiba, M. (2013). Real-time prediction of ground motion by Kirchhoff-Fresnel boundary integral equation method: Extended front detection method for earthquake early warning. J. Geophys. Res., **118**, 1038–1050, doi: 10.1002/jgrb.50119.

Hoshiba, M. and Aoki, S. (2015). Numerical Shake Prediction for Earthquake Early Warning: Data assimilation, Real-Time Shake Mapping, and Simulation of Wave Propagation. Bull. Seismo. Soc. Am., **105**, 1324-1338. doi: 10.1785/0120140280.

Lomax, A., Michelini, A. and Curtis, A. (2009). Eathquake Location, Direct, Global-Search Methods, in Encyclopedia of Complexity and System Science, Part 5, Meyers, R. A. (ed.), 2449-2473, Springer, New York. doi: 10.1007/978-0-387-30440-3.

Maki, T., Kashiwabara, S., Osada, Y., Nishiwaki, M., Kakishita, T. and Nagare, S. (1987). Determination of Apparent Velocities and Azimuths of Distant Earthquakes by the Matsushiro Seismic Array System — Effects of Dipping Structure of the Crust and Near-surface—, Technical Reports of the Matsushiro Seismological Observatory, JMA, **8**, 1-21. (In Japanese)

Matsumura, S. (1981). Three-dimensional expression of seismic particle motions by the trajectory ellipsoid and its application to the seismic data observed in the Kanto district, Japan. J. Phys. Earth, **29**, 221-239.

Niazi, M. (1966). Corrections to apparent azimuths and travel-time gradients for a dipping mohorovičić discontinuity, Bull. Seismo. Soc. Am., **56**, 491-509.

Tsuruoka, H., Kawakatsu, H. and Urabe, T. (2009). GRiD MT (grid-based real-time determination of moment tensors) monitoring the long-period seismic wavefiled, Phys. Earth. Planet. Int., **175**, 8-16.

Urabe, T. (1994). A common format for multi-channel earthquake waveform data. Program and Abstracts. Seism. Soc. Jpn. 2, P24.

DeadSeaNet: Cross-border array of mini-arrays for EEWS

G. H. Wust-Bloch[1], A. Ziv[1], A. S. Eisermann[1] and A. Al-Zoubi[2]

[1] Department of Earth Sciences,Tel Aviv University, Tel Aviv, Israel, hillel@seismo.tau.ac.il
[2] Department of Engineering, Surveying and Geomatics, Al-Balqa' Applied University, Al-Salt, Jordan

Abstract

DeadSeaNet is a unique seismic research network that consists of an array made up of sparse, small-aperture arrays. Deployed across three borders over the Dead Sea Fault zone, it monitors local microseismicity in realtime and is jointly operated by a group of Israeli, Palestinian and Jordanian earthquake seismologists. Because DeadSeaNet covers the earthquake source area closest to each of the Israeli, Palestinian and Jordanian capital cities, respectively, in addition to eight million inhabitants of the Dead Sea region, it is now being utilized to develop and test new array-based EEWS algorithms.

The mini-arrays comprise a wide range of sensors: short-period, broadband, accelerometers and MEMS. Their layout varies from basic tripartite (6 channels) to random multipartite (12 channels). Intra- and inter-array aperture ranges between 45 m - 350 m and 1,700 m - 13,500 m, respectively. Waveforms are sampled at 500 Hz and streamed by ADSL to the central DeadSeaNet server. Customized realtime data acquisition and data transfer software reduces total latency below 0.1 sec, making DeadSeaNet one of the fastest, realtime, earthquake monitoring platforms available today.

In-house, cross-correlation based algorithms allow for automated event detection in low SNR conditions and backazimuth (particle motion and mini-array) estimations. Initial results show that mini-array computed backazimuths provide independent control on location ambiguities while being less sensitive to velocity models and random system latency. Off-line analyses of local earthquakes indicate that DeadSeaNet mini-arrays can significantly speed up and improve the robustness of source parameter evaluation for EEWS.

Introduction

Israel, Jordan and Palestine are located at the edge of a tectonic plate boundary that has produced devastating earthquakes. Because this tectonic boundary is presently locked, seismic energy increases steadily, thus constantly increasing the seismic hazard for eight million Israeli, Palestinians and Jordanians residing in the region. The potential hazard posed by earthquakes is further compounded in the Dead Sea region due to rapid population growth, a high concentration of governmental institutions and substandard seismic monitoring. It is thus vital to develop an advanced, realtime earthquake-monitoring infrastructure in the Dead Sea region. DeadSeaNet is a unique seismic research network, consisting of an array of sparse arrays, deployed across borders on top of the active Dead Sea fault zone. Using advanced array-based waveform analysis techniques, DeadSeaNet is used to develop and test innovative EEWS locations schemes that are both, very fast and robust.

Earthquake hazard in the Dead Sea region

Earthquake activity in Israel, Jordan and Palestine is associated primarily with the Dead Sea Transform (DST). The DST is an active N-S trending left-lateral transform (Ben-Avraham and Ginzburg, 1990; Ben-Avaham et al., 2012) (Figure 1). Recent GPS analyses (Sadeh et al., 2012) indicate that the majority of DST segments between the Gulf of Eilat and the Sea of Galilee are presently locked down to a depth of about 10-15 kilometers (Al-Tarazi et al., 2011; Sadeh et al., 2012). Since current slip rates along the DST ranges between 5-3.8 mm/yr (Sadeh et al., 2012), elastic strain along these segments is currently accumulating. Despite modest slip rates and a moderate to low seismicity rate, the DST is known to have caused extensive damage and losses of life over the past millennia (Ben-Menahem et al., 1991; Hamiel et al., 2009; Marco et al., 2005; Marco and Klinger, 2014). Today, the DST is the main source for earthquake hazard for eight million Israeli, Palestinian and Jordanians living within the Dead Sea region. The cites of Jericho, Jerusalem, Amman and Nablus, suffered heavily during the Mb 6.3 Jericho earthquake of 11 July, 1927 (Shapira et al, 1993). The Mw 7.2 Nuweiba earthquake of November 22, 1995, surprisingly, caused significant shaking to structures in Jericho even though the epicenter was located over 300 km to the south (Wust-Bloch, 2002). Even the weaker (ML 4.7) 2004 Kalia Earthquake generated panic and widespread non-structural damage within the Dead Sea region (Hofstetter et al., 2008).

The DST consists of an extremely deep (>15 km) pull-apart basin (Al-Zoubi et al., 2002; Ben Abraham et al., 2010), which has the ability to trap seismic loads (Gottschämmer et al., 2002; Gottschämmer et al., 2005) or function as a wave-guide, resulting in selective destruction of ancient structures (Wust-Bloch, 2002). The Israel Seismic Network (ISN) and Jordan Seismic Observatory (JSO) operate modern monitoring facilities on either side of the DST (Hofstetter et al., 2014), but joint realtime earthquake monitoring is not yet available. Because Israel decided to implement a nationwide EEWS, the ISN is in the process of being thoroughly upgraded (Allen et al., 2012; Hamiel et al., 2013). The complex internal structure of the Dead Sea basin is an important source of inaccuracy for hypocentral locations (Aldersons et al., 2003; Aldersons and Ben-Avaham, 2014; Oth et al., 2007) and thus

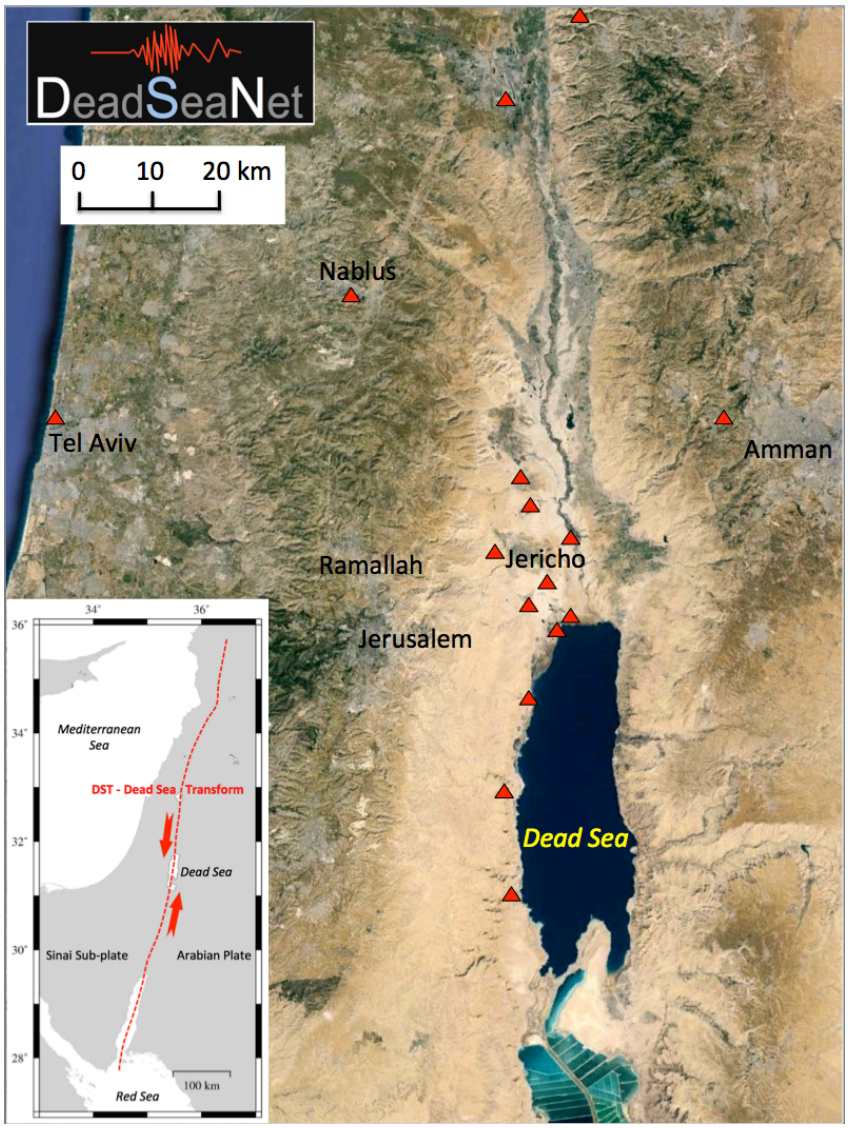

Figure 1. Map of the Dead Sea region with location of DeadSeaNet mini-arrays (red triangles). The active Dead Sea Transform (DST) and boundaries of regional tectonic plates are shown in red dashed lines (sketch to the left).

has the potential to generate location ambiguities with disastrous implications. This is further complicated by the lack of a reliable seismic velocity model for the Dead Sea basin, a low sensor density and substandard azimuthal coverage of the ISN and JSO in relation to the DST (both are deployed at the edge of the DST). Reducing the earthquake exposure of eight million people and their infrastructure in the Dead Sea region requires the deployment of an advanced EEWS with realtime, transborder monitoring capacities. DeadSeaNet, which is deployed across borders on top of the DST, presently monitors local microseismicity in the northern Dead Sea region in realtime (Wust-Bloch et al., in prep.). Because DeadSeaNet is deployed in the earthquake source region, nearest to Jericho, Jerusalem, Ramallah, Amman and Nablus, it has the ability to locate an event rapidly and reliably, which in turn is crucial in reducing the blind zone and providing life-saving alerts for several million Israelis, Palestinians and Jordanians.

DeadSeaNet – A transborder array of mini-arrays

Portable, sparse, small-aperture arrays were initially developed for temporary deployment in order to characterize natural source processes (Wust-Bloch and Joswig, 2006; Joswig, 2008; Sick et al., 2013) and to carry out forensic seismology investigations (Sick et al., 2012). Together with advanced signal processing techniques (Joswig, 2008; Sick et al., 2015), low-energy spiky energy bursts generated by sinkhole or cavity collapse (Wust-Bloch 2010; Wust-Bloch and Tsesarsky, 2013) or by landslides (Walter and Joswig, 2008; Walter et al., 2012; Sick et al., 2013) could be picked up in background noise. This approach was also tested for temporarily local microseimic moitoring (Ben-Avraham et al., 2014; Vouillamoz et al, in press; Wust-Bloch et al., in prep.).

DeadSeaNet is the first attempt to deploy a permanent array consisting of many mini-arrays over an active fault, and to stream data in true realtime to a remote server. To optimize backazimuth accuracy, the basic 6-channel configuration of mini-arrays has been extended to 12 channels, and the dynamic range is being maximized by including broadband velocity-meters and high-resolution accelerometers. DeadSeaNet integrates 16 mini-arrays (see list of mini-arrays) concentrated within the Dead Sea region (Figure 1) and is jointly operated by a group of Israeli, Palestinian and Jordanian scientists.

DeadSeaNet mini-arrays integrate four components: sensors, data acquisition, control and communication systems. The sensor interface is modular (Figure 2), whereas the three others are standard for every mini-array.

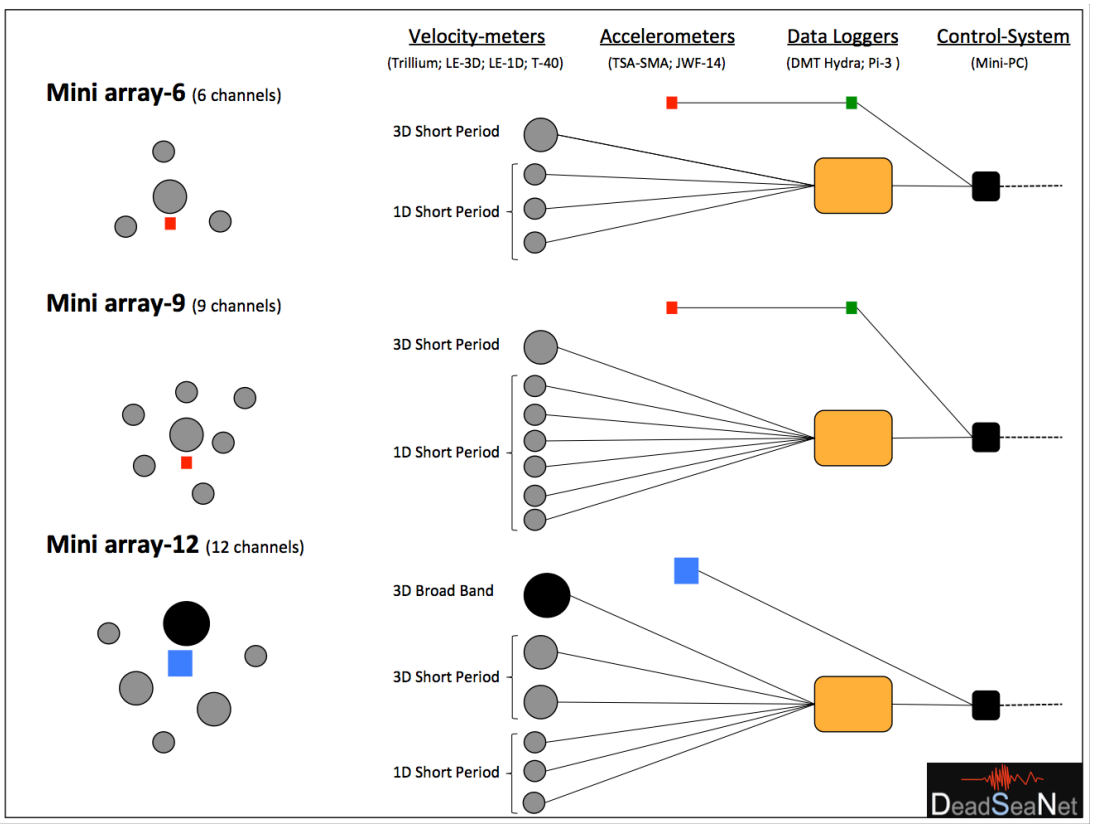

Figure 2. DeadSeaNet: Scheme showing sensors and layout of three types of mini-arrays (6, 9 and 12 channels) deployed.

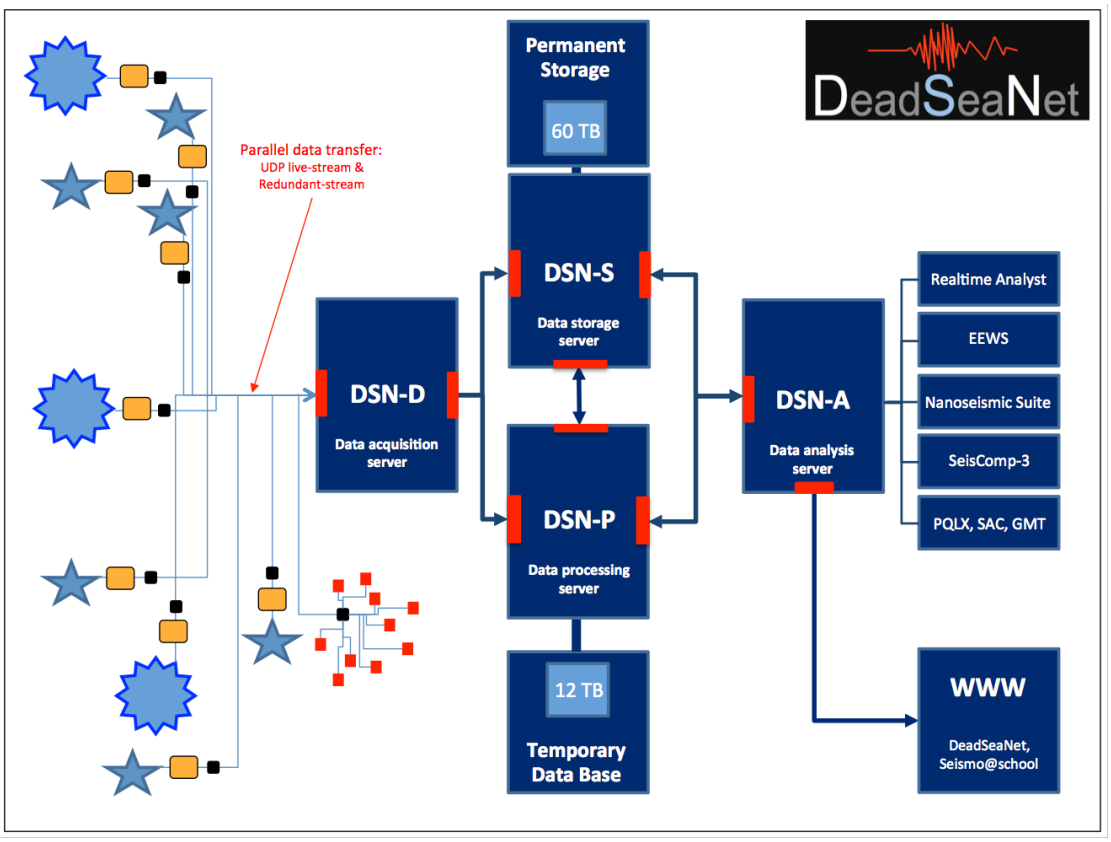

Figure 3. DeadSeaNet: Scheme showing the interactions between the different mini-arrays and the four DeadSeaNet servers: DSN-D, DSN-S, DSN-P and DSN-A.

The sensors used by DeadSeaNet include: 3D Broadband (0.008-100 Hz) velocity-meters (Trillium compact and Guralp T-40); 3D and 1D short-period (1-80 Hz) velocity-meters (Lennartz LE-3D and LE-1D); 3D 24-bit (0.1-40 Hz) high performance accelerometers (EQMet TSA-SMA) and 3D 14-bit MEMS (0.1-11 Hz) (JoyWarrior JWF-14). Mini-array geometry starts with a tripartite layout (3x 1D sensors) around a central (1x 3D sensor) sensor, with a total of six channels (Mini array-6), and extends to random multipartite (3x 3D sensors and 3x 1D sensors) layout (Figure 2), with 9 - 12 channels (Mini array-12). To optimize the dynamic range, each mini-array is being equipped with either one high-performance accelerometer or one MEMS collocated with the central 3D sensor. In addition, MEMS-based mini-arrays are being deployed in schools and connected to a Mini-PC, supplying further realtime data to DeadSeaNet (Figure 3).

Within the Dead Sea basin, intra- and inter-array aperture ranges between 45 m - 350 m and 1,700 m - 13,500 m, respectively (Figure 1). The geometry of mini-arrays is random: it attempts to maximize sensor spacing while accounting for anthropogenic and logistical constraints as well as maximal cable length (± 250m). Velocity-meters are installed at a minimal depth of 200 cm on a concrete base in a cased shallow borehole or in vaults. The housing is designed to improve SNR (Night-time peak-to-peak ground noise amplitudes of ± 150 nm s^{-1} for 0.3-10 Hz), limit the effects of thermal spikes (>50° C in summer), humidity and salt on the instruments, and prevent vandalism. Every mini-array is directly connected to ADSL lines and is powered either by a local electric outlet or by solar panels. The data from all velocity-meters is acquired at 500Hz by 24-bit dataloggers (DMT Summit M Hydra) with 6 – 12

channels. The data is pulled from one long-term internal ringbuffer and stored as sg2 files (size: 1-86400 sec). Additionally, realtime raw data is pulled from an internal short-term ringbuffer. Single-board computers record data acquired as *.mseed* by the MEMS accelerometers, whereas the seedlink server installed on the standalone TSA-SMA accelerometers is directly connected to the control system (Figure 2). One NUC-type Mini-PC functions as control systems for each mini-array. Open VPN tunnels provide direct safe connection to the DeadSeaNet server. The Mini-PCs enable remote access and full system operation, mainly monitoring State Of Health (SOH) functions in realtime, supervising data transfer, supporting and controlling communication. Data transfer and storage occurs through two redundant modes: realtime and safe. To guarantee true, realtime data transfer, data is grabbed instantaneously from the small ringbuffer of the datalogger and forwarded to the DeadSeaNet server as encrypted UDP packages, bypassing packaging and reading of the smallest data packages presently available (1 sec). A customized code installed in the DeadSeaNet server checks for data quality and completeness, and when flagged, sends requests to the mini-PC for missing or incomplete data strings. The total latency of DeadSeaNet data transfer from datalogger to server ranges between 0.02 - 0.1 sec. After temporary archiving one-second *.sg2* files on site, the safe data mode transfers them in near-realtime to the server. As the safe mode operates in FIFO (First In - First Out), it guarantees complete data but may lag behind in time when bandwidth is low. In contrast, the life-mode provides true realtime data operating in LIFO (Last In - First Out) mode but may have gaps.

The DeadSeaNet operates four independent servers (Figure 3): DSN-D, DSN-P, DSN-S and DSN-A. DSN-D is the front-end server that manages communication and data acquisition with the Mini-PCs controlling each mini-array. DSN-D simultaneously forwards the data to two redundant data servers: DSN-P and DSN-S. DSN-S is the data storage server, where the data is permanently archived in a 60 TB RAID-1 storage. DSN-S operates a seedlink server for data retrieval by external clients. DSN-P is the central data processing server and the general control system that handles all data traffic between DSN-D, DSN-S and DSN-A. DSN-P operates a 12 TB ringbuffer, where the most recent data is processed and evaluated: automatic detection, location, source parameter estimation, SOH data. DSN-A is the data analysis server that runs and benchmarks different data analysis software in parallel: our in-house Realtime Analyst, existing EEWS algorithms, NanoseismicSuite, SeisComp-3. DSN-A also handles Web-based earthquake education and preparedness activities that DeadSeaNet is leading (seismo@school) and provides public access to realtime waveform visualization (www.deadseanet.net).

DeadSeaNet – Using mini-array data for EEWS

A low seismicity rate and the presence of a deep sedimentary basin in the Dead Sea region are significant challenges for EEWS calibration. The low seismicity rate means that relatively few and weak events ($M_L > 5$) are available to calibrate detection thresholds and benchmark location accuracy. Solving these issues bears a strong impact on reducing the blind zone for Jerusalem, Ramallah and Amman, when considering a possible repeat of the 1927 Jericho earthquake.

Given the lack of an adequate velocity model for the Dead Sea basin and the complexity of the substructure, avoiding location errors requires the use of

independent data sets and location schemes. Adding backazimuth estimations to standard location modules significantly raises the confidence level of locations and integrating them to NYAD (Not Yet Arrived Data) at an earlier stage, brings vital time gains (Eisermann et al., 2015; Eisermann et al, in prep.).

It was recently shown that robust backazimuth estimations can already be retrieved by advanced particle motion analysis on the first 0.2 seconds of data recorded by 3D sensors (Eiserman et al., 2015). Mini-array backazimuth are estimated on a growing window (P-peak until SNR $\geq$ 10) of (1-10 Hz) filtered traces. Robust backazimuth estimations, whose accuracy increases as a function of available vertical traces (4-7), are recovered within 0.1 sec and tested by jackknifing (Wust-Bloch and Joswig, 2006, Joswig, 2008). Figure 4 shows that the accuracy of mini-array backazimuth (white <10° error; blue >10° error) is a function of the number of sensors and the incidence angle. The more traces (max 7) used to compute backazimuth, the less sensitive solutions become to sensor geometry. The larger the aperture, the more accurate the backazimuth estimates will be for steep incident angles. The benefit of integrating realtime backazimuth estimations for EEWS is illustrated with a scenario earthquake recorded by DeadSeaNet (Figure 5).

Three mini-arrays located along the western Dead Sea shore triggered, from south to north: Ein Gedi (ENGD); Ovnat (OVNT) and Kalia Beach (KALI). In the first case, we consider a standard scenario (Figure 5, left), whereby each mini-array functions only as a normal single station within a network. After three detections (1st at OVNT; 2nd at ENGD and 3rd at KALI), we have three dependent constraints (three Equal Different Time (EDT) surfaces whose thickness displays p-phase picking uncertainty) intersecting and providing two ambiguous potential locations, about 35 km apart. At least a fourth trigger is needed to solve the ambiguity. In the second case (Figure 5, right), we use all the traces recorded by each mini-array of DeadSeaNet. The first

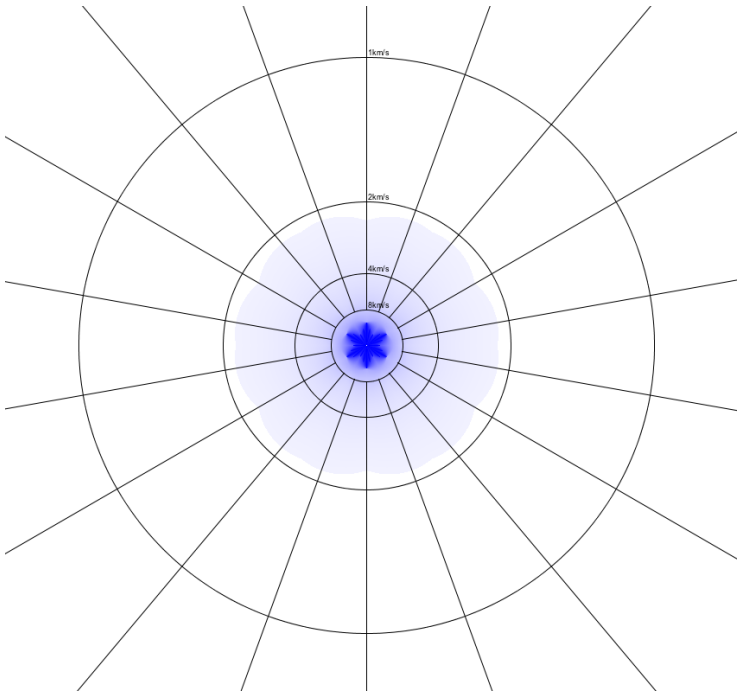

Figure 4. Sensitivity analysis showing the resolution of mini array-6 based back-azimuth as a function of incident angle (white <10° error*; blue: >10°* error*).*

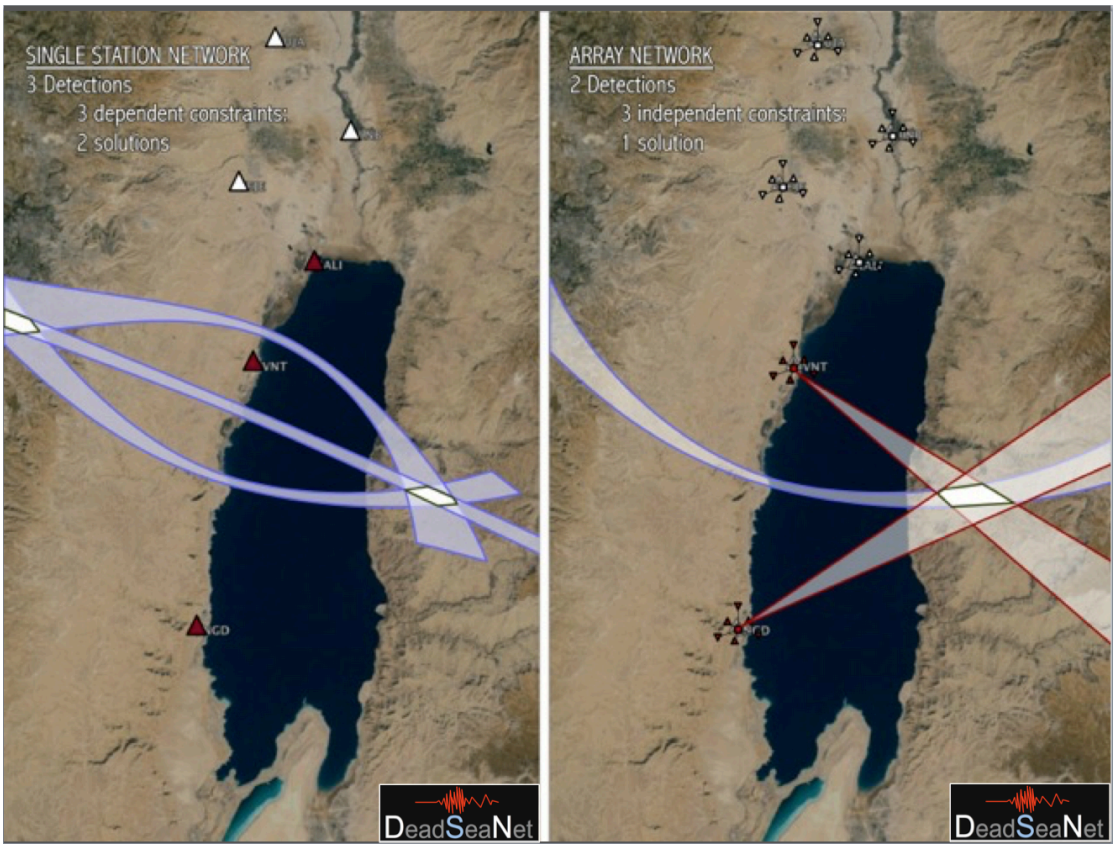

Figure 5: Comparative location scenario for EEWS using standard network analysis (left) and array mode analysis (right). Location with data from three standard stations uses three dependent constraints (3 Equal Different Time (EDT) surfaces) and cannot solve the ambiguity. Location with data from two mini-arrays uses three independent constraints (2 backazimuths and 1 EDT) and delivers one unique solution.

detection occurs at OVNT and after 0.1 sec an initial backazimuth points SE towards the source. The epicentral distance is not yet constrained. The second detection occurs at ENGD: the EDT crosses the initial backazimuth, thus providing a coarse location. After an additional 0.1 sec, the second NE backazimuth intersects both the first backazimuth and the EDT. This epicentral location is obtained with only two detections by mini-arrays, and since it is based on three independent constraints, it is already robust. In many instances, mini-array data can provide faster and more robust location estimates. Mini-arrays are particularly beneficial to EEWS when sensors are sparse, aligned, and when sources are located outside or at the edge of networks.

Furthermore, integrating mini-arrays in EEWS can play a critical role in avoiding false alarms, mainly supporting the discrimination between earthquakes and anthropogenic sources. A realtime screening module checks waveform amplitudes and cross-correlation coefficients on the vertical traces (4-7) of each mini-array. First, waveform amplitudes are compared (Figure 6).

If amplitude variations exceed 50% on one or more horizontal traces within a mini-array, it indicates that the source is confined within or very near the mini-array at distances that are shorter than the minimal depth of shallow earthquakes. In that case,

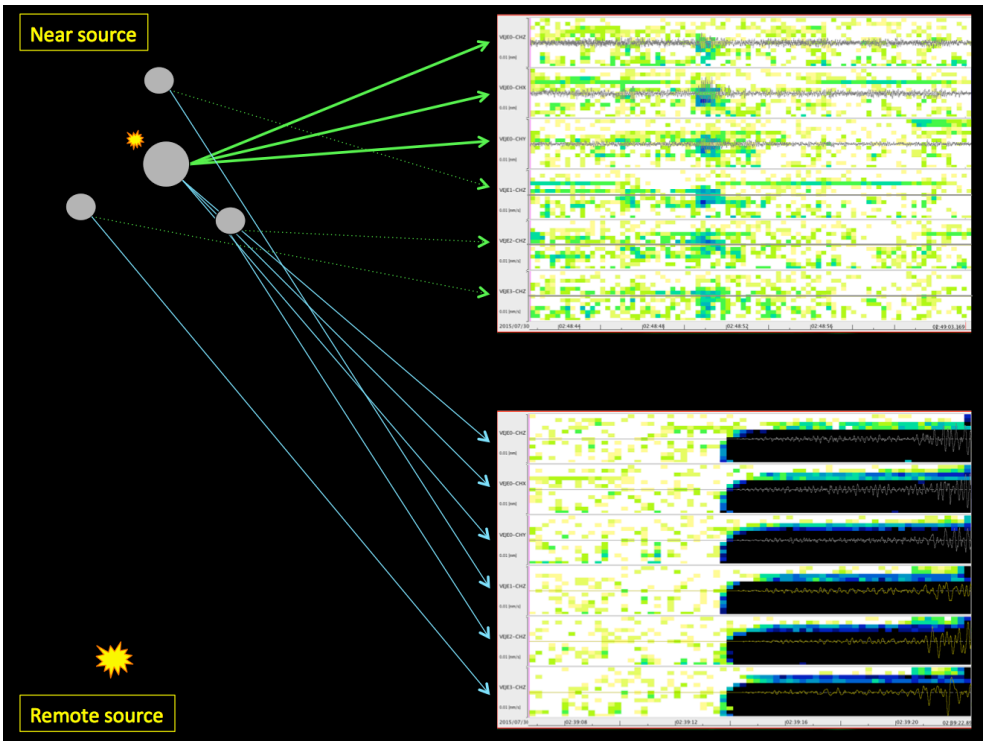

Figure 6: Lowering false alerts for EEWS: Comparing waveform amplitudes on mini-array traces to discriminate between near and remote sources. Background sonograms display frequency distribution (high frequencies on top) of signal energy (darker colors show higher energy) and gray traces show common-scale standard waveforms

the event is flagged and can be attributed it to a nearby non-seismic source. Low to minimal amplitude variations relate to a remote source. Second, the backazimuth is estimated by cross-correlating all vertical traces of each mini-array (Figure 7).

Several scenarios can be flagged down as anthropogenic sources: a) an anomalously low (≥ 500 m/sec) backazimuth velocity (Figure 7, top); b) a lack of consistency between backazimuth velocity estimations for P-phase and for S-phase (Figure 7, bottom); c) Backazimuth estimations for P-phase showing high angular dispersion (≥ 10°); d) Backazimuth estimations for P-phase and for S-phase with high angular misfit (≥ 20°). b and d are not yet implemented as they requires a reliable realtime s-phase identification.

DeadSeaNet – Benefits of mini-arrays for EEWS

Initial results show that integrating DeadSeaNet mini-array data can be extremely beneficial in speeding up and increasing the robustness of locations for EEWS. These benefits are even more substantial when any of the following conditions are met: the network density is low; the network does not cover the seismogenic zones; SNR conditions are substandard; the subsurface is complex; and logistics and vandalism/tampering are issues of concern.

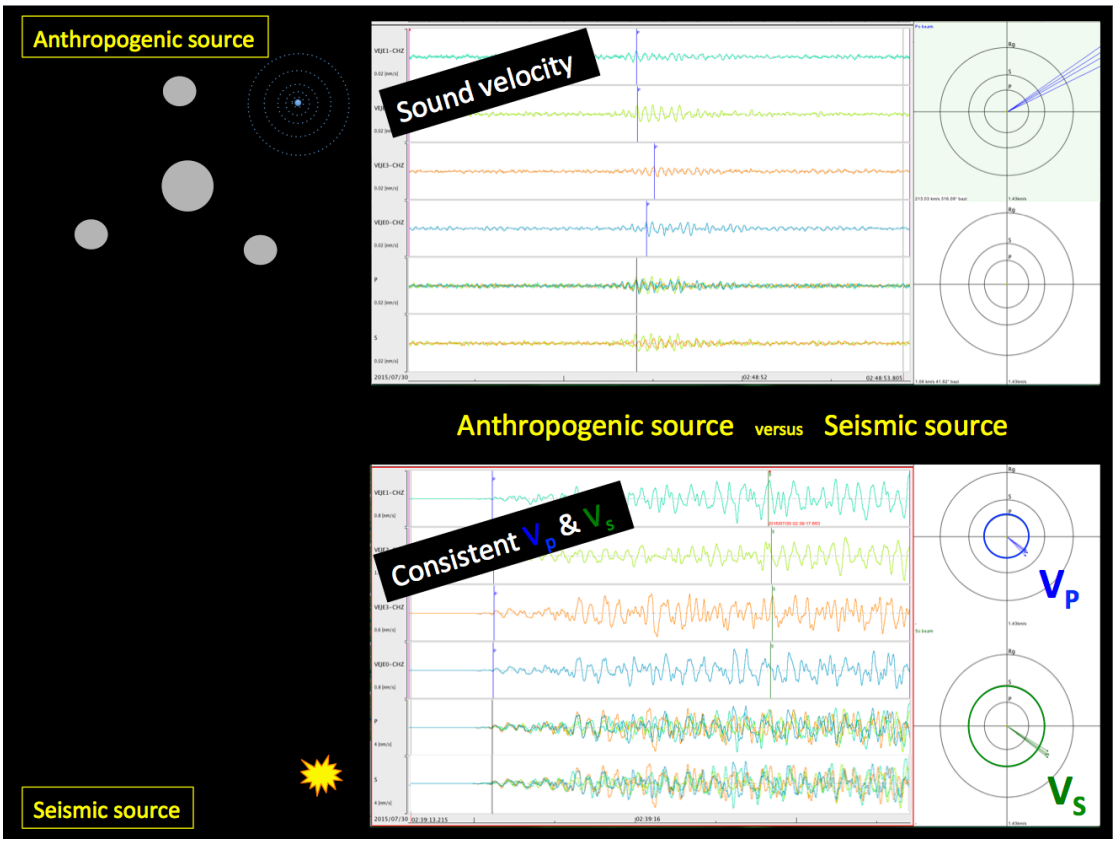

Figure 7: Lowering false alerts for EEWS: Comparing mini-array backazimuth estimations to discriminate between anthropogenic and seismic sources.

References

Aldersons, F., Z. Ben-Avraham, A. Hofstetter, E. Kissling and T. Al-Yazjeen (2003). Lower-crust strength under the Dead Sea basinfrom local earthquake data and rheological modeling, Earth Planet. Sci. Lett. 214, 129-142.

Aldersons, F. and Z. Ben-Avraham (2014). The Seismogenic Thickness in the Dead Sea Area. In: Garfunkel, Z., Ben-Avraham, Z., Kagan, E. (Eds.) The Dead Sea Transform: Reviews. Modern Approaches in Solid Earth Sciences. Volume 6. Springer, Dordrecht. pp. 53-89.

Allen, R.M., G. Baer, J. Clinton, Y. Hamiel, R. Hofstetter, V. Pinsky, A. Ziv and A. Zollo, (2012). Earthquake early warning for Israel: Recommended implementation strategy, Geol. Surv. Rep., GSI/26/2012.

Al Tarazi, E., Abu Rajab, J., Gomez, F., Cochran, W., Jaafar, R., and Ferry, M. (2011). GPS measurements of near-field deformation along the southern Dead Sea Fault System. Geochemistry, Geophysics, Geosystems, 12, 1-12.

Al-Zoubi, A., H. Shulman and Z. Ben-Avraham (2002). Seismic reflection profiles across the southern Dead Sea basin, Tectonophys., 346, 61-69.

Ben-Avraham, Z. and A. Ginzburg (1990). Displaced terranes and crustal evolution of the Levant and the eastern Mediterranean, Tectonics, 9, 613-622.

Ben-Avraham Z., V. Lyakhovsky and G. Schubert (2010). Drop-down formation of deep basins along the Dead Sea and other strike-slip fault systems, Geophys. J. Int., 181, 185-197.

Ben-Avraham, Z., M. Lazar, Z. Garfunkel, M. Reshef, A. Ginzburg, Y. Rotstein, U. Frieslander, Y. Bartov and H. Shulman (2012). Structural styles along the Dead Sea Fault, in: Regional Geology and Tectonics: Phanerozoic Passive Margins, Cratonic Basins and Global Tectonic Maps, Roberts D.G. and A.W. Bally editors, Volume 1c, 617-633, Elsevier B.V.

Ben-Avraham, Z., Rosenthal, M., Tibor, G., Navon, H., Wust-Bloch, H., Hofstetter, R., and Rybakov, M. (2014). Structure and Tectonic Development of the Kinneret Basin. In Lake Kinneret (pp. 19-38). Springer Netherlands.

Ben-Menahem, A. (1991). Four thousand years of seismicity along the Dead Sea Rift. Journal of Geophysical Research: Solid Earth, 96(B12), 20195-20216.

Eisermann, A. S., Ziv, A. and Wust-Bloch, G. H. (2015). Real-time Back Azimuth for Earthquake Early Warning. Bull. Seis. Soc. Am., 105/4, 939-950.

Eisermann, A. S., Wust-Bloch, G. H. and Ziv, A. (in prep.). NYAS (Not-Yet-Arrived S-phase) for realtime hypocentral determination scheme.

Gottschämmer, E., Wenzel, F., Wust-Bloch, H., and Ben-Avraham, Z. (2002). Earthquake modeling in the Dead Sea basin. Geophysical Research Letters, (12) 1-29.

Gottschämmer, E., Wenzel, F., Wust-Bloch, H., and Ben-Avraham, Z. (2005). Finite-Difference Simulations of the 1927 Jericho Earthquake. In Perspectives in Modern Seismology (pp. 31-45). Springer Berlin Heidelberg.

Hamiel, Y., Amit, R., Begin, Z. B., Marco, S., Katz, O., Salamon, A., and Porat, N. (2009). The seismicity along the Dead Sea Fault during the last 60,000 years. Bulletin of the Seismological Society of America, 99/3, 2020-2026.

Hamiel, Y., G. Baer, R.M. Allen, J. Clinton, R. Hofstetter, V. Pinsky, A. Ziv and

A. Zollo, (2013). Earthquake early warning for Israel: Recommended implementation

strategy, EGU General Assembly Conference Abstracts 15, EGU2013-4358.

Hofstetter, R., Gitterman, Y., Pinsky, V., Kraeva, N., & Feldman, L. (2008). Seismological observations of the northern Dead Sea basin earthquake on 11 February 2004 and its associated activity. Isr. J. Earth Sci, 57, 101-124.

Hofstetter, A. Dorbath C. and Dorbath, L. (2014). Instrumental data on seismic activity along the Dead Sea Transform. (eds. Garfunkel, Z, Ben-Avraham, Z., and Kagan E.) Dead Sea Transform Fault System: Reviews, Springer, 263-278.

Joswig, M. (2008). Nanoseismic Monitoring fills the gap between micro- seismic networks and passive seismic, First Break, 26, 121-128.

Marco, S., Rockwell, T.K., Heimann, A., Frieslander, U. and Agnon, A. (2005). Late Holocene slip of the Dead Sea Transform revealed in 3D palaeoseismic trenches on the Jordan Gorge segment. Earth Planet. Sci. Lett., 234(1-2), 189-205

Marco, S. and Klinger, Y. (2014). Review of On-Fault Palaeoseismic Studies Along the Dead Sea Fault, in Garfunkel, Z., Ben-Avraham, Z., and Kagan, E. J., eds., Dead Sea Transform Fault System: Reviews, Volume 6: Dordrecht, Springer, p. 183-205.

Oth, A., Wenzel, F., Wust-Bloch, H., Gottschämmer, E., and Ben-Avraham, Z. (2007). Parameterization of a composite attenuation relation for the Dead Sea

area based on 3-D modeling of elastic wave propagation. Pure and Applied Geophysics, 164/1, 23-37.

Sadeh, M., Hamiel, Y., Ziv, A., Bock, Y., Fang, P., and S. Wdowinski (2012). Crustal deformation along the Dead Sea Transform and the Carmel Fault inferred from 12 years of GPS measurements. Journal of Geophysical Research: Solid Earth, 117, 1-14.

Shapira, A., Avni, R., and Nur, A. (1993). A new estimate for the epicenter of the Jericho earthquake of 11 July 1927. Isr. J. Earth Sci, 42/2, 93-96.

Sick, B., Guggenmos, M. and Joswig M. (2015). Chances and limits of single-station seismic event clustering by unsupervised pattern recognition, Geophysical Journal International, 201/3, 1801-1813

Sick, B., Walter, M., and Joswig, M. (2013). Near-surface fracture and impact discovery from landslides and sinkholes by sonogram screening, First Break, 31, 95-101.

Sick, B., Walter, M., and Joswig, M. (2012). Visual Event Screening of Continuous Seismic Data by Supersonograms. Recent Advances in Nuclear Explosion Monitoring Vol. 2 - Pure and Applied Geophysics, 171, 549-559.

Vouillamoz, N., Wust-Bloch, G. H. Abednego, M. and Mosar, J. (in press). Optimizing Event Detection and Location in Low-Seismicity Zones: Case Study from Western Switzerland, Bull. Seis. Soc. Am., in press.

Walter, M. and Joswig, M. (2008). Seismic monitoring of fracture processes generated by a creeping landslide in the Vorarlberg Alps, First Break, 26, 131-135.

M. Walter, U. Schwaderer, and Joswig, M. (2012). Seismic monitoring of precursory fracture signals from a destructive rockfall in the Vorarlberg Alps, Austria. Nat. Hazards Earth Syst. Sci., 12, 3545-3555.

Wust-Bloch, G. H. (2002). The active Dead Sea Rift fault zone: a seismic wave-guide. EGU Stephan Mueller Spec. Public. Ser, 2, 11-20.

Wust-Bloch, H. G. (2010). Characterizing and locating very weak ($-2.2 \geq M_L \geq -3.4$) induced seismicity in unstable sandstone cliffs by nanoseismic monitoring. Pure and applied geophysics, 167(1-2), 153-167.

Wust-Bloch, G. H., and Joswig, M. (2006). Pre-collapse identification of sinkholes in unconsolidated media at Dead Sea area by 'nanoseismic monitoring'(graphical jackknife location of weak sources by few, low-SNR records). Geophysical Journal International, 167/3, 1220-1232.

Wust-Bloch, G. H., and Tsesarsky, M. (2013). Structure Health Monitoring in Natural Environments: Pre-failure Event Location and Full-waveform Characterization by Nanoseismic Monitoring JEEG, 18/4, 219–232.

Wust-Bloch, G. H., Ziv, A., Eisermann, A. S., Al-Dabbeek, J. and Al-Zoubi, A. (in prep.). DeadSeaNet: Active fault mapping the Jericho Valley with an array of mini-arrays.

List and coordinates of DeadSeaNet mini-arrays

Name	Location	Lat	Long	Height	Channels
ALBA	Al-Balqa	32.022437	35.717697	+924	6
ALMG	Almog	31.788917	35.463725	-276	6
ALNB	Allenby	31.866853	35.532279	-371	15
AUJA	Auja	31.951844	35.463785	-229	9
BETA	Beit Arava	31.811161	35.474272	-284	12
ECOP	Shahabil	32.522221	35.620792	-151	6
ENGD	Ein Gedi	31.452535	35.385000	-295	6
HILT	Hilton	31.773789	35.510205	-392	6
KALI	Kalia Beach	31.762940	35.501505	-397	9
MASR	Nablus	32.209189	35.263885	+839	9
MITZ	Mitzpe Shalem	31.569343	35.403031	-301	6
NAAM	Na’ama	31.907709	35.468115	-191	6
OVNT	Ovnat	31.675041	35.441697	-381	8
SDEE	Sde Eliahu	32.434504	35.514496	-192	9
TAUA	Tel Aviv	32.112138	35.806190	+ 44	6
VEJE	Vered Jericho	31.826259	35.427199	-120	6

The Cost-Effectiveness of a West Coast Earthquake Early Warning System

Gordon Woo[1], Maurizio Gobbato[2], Nilesh Shome[2]

[1] RMS, 30, Monument Street, London EC3R 8NB, UK, Gordon.Woo@rms.com
[2] RMS, 7575 Gateway Blvd, Newark, CA 94560, USA

Abstract

The RMS catastrophe earthquake model has been used to assess the cost-effectiveness of a West Coast earthquake early warning system. Taking a thirty year time frame, there is a reasonable expectation that the safety investment would be warranted by the number of lives saved and the reduced fire loss following earthquake. Significant additional early warning benefits also accrue to a number of corporate stakeholders. Given the balance between societal and corporate benefits, it would be equitable if the private sector supported this investment in public safety.

Introduction

The concept of an earthquake early warning system for California dates back to the Hayward Fault earthquake of October 21, 1868. An astute physician, Dr. J.D. Cooper, figured out that telegraph cables could transmit an earthquake warning. This was a remarkably prescient observation, for earthquake science barely existed in 1868, and the telegraph had only reached California fifteen years before. Furthermore, with 30 fatalities, the death rate was only about 1:10,000, so this was far from being a humanitarian disaster.

A warning system would never have actually been viable before the modern digital era. But progressively the seismological challenges in issuing reliable and timely earthquake warnings in California have been resolved, so that a public earthquake early warning system (EEWS) could at last become operational 150 years after Dr. Cooper's vision. But how cost-effective would such a system be? This is an important question, not just in California but elsewhere in seismic zones around the world lacking EEWS. The relative cost-effectiveness of retrofitting seismically vulnerable buildings and implementing EEWS matters when policy-makers have to decide on seismic safety resource allocation. Indeed, progress in EEWS acceptance is slowed by concerns that this initiative would detract to a greater or lesser extent from engineering efforts to mitigate earthquake risk to vulnerable buildings.

With its headquarters in Newark, close to the southern end of the Hayward Fault, RMS not only has the earthquake risk management expertise to address this question, it is itself a potential safety beneficiary of such a system. A magnitude 7.0 rupture of the Hayward Fault starting at the northern end is a plausible scenario for a recurrence

of the 1868 event. If an EEWS were operational, RMS staff would have up to ten seconds to find an office desk to duck under, cover and hold.

There is a strong political consensus in California for a public EEWS. This was re-affirmed soon after the South Napa earthquake of August 24, 2014 at a Berkeley symposium on earthquake early warning. In the previous year, the California State Legislature had passed an earthquake early warning system bill. The installation of a public EEWS for California and the Pacific Northwest would cost $38 million, and the annual running costs would be $16.1 million. The task of bringing a public warning system the last mile to the stakeholders is facilitated by the near-universal ownership of cell phones. Indeed, the mass use of cell phones as tremor sensors holds the promise of shrinking the earthquake early warning blind zone. Given the widespread availability of electronic public alert devices, the incremental cost of ensuring public access to earthquake warnings should be comparatively small.

Investment to avoid accidental death

Public safety has its own socio-economic and geographical context. What is affordable in one region may be extravagant in another. California has the highest GDP of any state in America, and has a population of almost 40 million. In some affluent zip codes, the price of a modest mansion would pay the annual cost of EEWS operation. California is earthquake country. Seismic motion is the only natural hazard to which all Californians are exposed, and earthquake safety is a state priority.

In the 21st century, Dr. Cooper's successors in medicine have carried California to the international forefront of clinical treatment and research into healthy aging. In California, the psychology of wellbeing has been pioneered, and life expectancy is amongst the highest in the United States. To improve life expectancy further, there is a strong willingness to invest to reduce the incidence of accidental death.

Almost half of U.S. home fires start in the kitchen. Mitigation of this fire following earthquake risk is one of the potential EEWS benefits: warning time may allow some ignition sources to be controlled. There are several thousand house fire deaths each year in the United States. As of 2011, residential fire sprinklers have been required in all new one-and two-family dwellings and townhouses in California. The cost-effectiveness of such a home safety measure was earlier demonstrated in a report produced for the U.S. Fire Administration [1]. For deciding on U.S. investment to reduce fatality risk, this study used the median figure of $7.94 million in 2005 dollars. This amounts to $10 million in 2015 dollars, and is the figure adopted here.

The equivalent figure for terrorism is much greater [2]. Since 9/11, the investment by the Department of Homeland Security to reduce U.S. terrorism fatalities is counted in billions of dollars. This includes resilience measures in California that have dual function in reducing risk from both terrorism and earthquakes. In as much as the earthquake risk exceeds the terrorism risk in California, this implies a substantial value accorded to earthquake safety. For a public EEWS, the potential to save a significant number of lives is crucial if it is to be cost-effective. This potential is not self-evident, and cannot be assessed quantitatively without an elaborate computer model of earthquake casualties, having a fine geographical resolution with state-wide California exposure information on the population at risk.

Detailed earthquake casualty risk analysis is required, taking due account of three factors that curtail the safety benefits of EEWS. First, there is a blind zone around the earthquake epicenter within which warning time is eroded by the time for the nearest station to record a seismic signal, and the time delay in data processing and telemetry. Secondly, there is already a high standard of earthquake construction and retrofit in California which reduces the extent of future earthquake damage: citizens of California are safer indoors now than in the 20th century. Thirdly, those who find themselves trapped in collapsed buildings are unlikely to have been helped by any early warning.

Duck, cover, and hold

Earthquake engineers recommend for those indoors when an earthquake is perceived the Duck-Cover-Hold strategy: move no more than a few steps to a safe place, such as under a sturdy table, then drop down onto hands and knees to avoid falling; cover your head and neck under the table or with your arms and hands; and then hold on.

A century of U.S. experience has shown that taking shelter under sturdy furniture during earthquakes is far more effective at protecting lives than running outside. The outsides of buildings pose many additional hazards that may fall on people trying to run outside. Many of the 120 fatalities from the March 1933 Long Beach earthquake occurred when people ran outside of buildings only to be killed by falling debris from collapsing walls. Seventy years later, in the San Simeon earthquake of December 2003, two people died attempting to exit a collapsing unreinforced masonry building. Those who remained in the same building were subsequently rescued.

It may not be possible to execute the Duck-Cover-Hold strategy. At the precise moment of ground shaking, an occupant of a building may be on a staircase, in a corridor or hallway, in a bathroom or other room with no large sturdy table to crawl under - or simply in the wrong room at the wrong time, e.g. room with a fragile table top, store room, library, garage, wine cellar etc. Two people were crushed when buried under books, model trains and other collectibles during the 1994 Northridge earthquake [3]. Contemporary photographic records of overturned bookcases and detached air conditioning ducts confirm the sound sense of seeking a safe shelter during the 1989 Loma Prieta earthquake.

Especially for older people, the risk of falling would be high if they tried to reach their safe place whilst the ground is moving. In the Loma Prieta earthquake, more than half of hospitalizations in Santa Cruz County were attributable to falls. Of these, the elderly were the most frequent fall victims [4]. During the Northridge earthquake, those over 60 had six times the risk of a more serious earthquake-related injury, and those who fell had five times the risk compared with those struck or cut by objects [5]. The population of California is ageing. The California Department of Finance projects that in 25 years' time there would be ten million people aged 65 and over. On average, one in three U.S. adults aged 65 and older falls each year [6]. Of those who fall, 20% to 30% suffer moderate to severe injuries that make it hard for them to get around or live independently, and increase their risk of early death. Even if the proximate cause of death may be respiratory failure, in reality a bad fall may be the original cause.

Better shelter with EEWS

Particularly the elderly, and others with mobility restrictions, need time to find shelter in an earthquake. The time challenge in reaching a preferred safe place is eased by an earthquake early warning. In the Loma Prieta earthquake, 60% of those injured during the period of shaking were trying to evacuate or move to a safer place in the building. The additional EEWS seconds might be used to find a safer place than one that just happens to be closer. A safer place could be a sturdier, larger table. Where there are multiple occupants of an apartment or home, several tables in different rooms may be needed. A safer place might also be in a room where the damage consequences of a ceiling collapse are lower. Extra time also helps to avoid back strain in getting under a table, which was a problem faced by about 10% in the Loma Prieta earthquake [7].

Assuming a future projected California EEWS inter-station distance of 20km, warning times at varying epicentral distances have been estimated [8]. The area close to the epicenter is called the blind zone, where no early warning is achievable. However, as the distance increases from 25km to 50km, 75km and 100km, the warning times lengthen progressively from 1 to 8, 15, and 22 seconds. One second would only allow an occupant time to find a safe place a few steps away. But Japanese tests have shown that even a single second of warning may have a human stabilizing effect. In 8 seconds, a safe place could be found in the same room; in 15 seconds, a safe place could be found in an adjacent room; in 22 seconds a safer place could be found further away on the same floor level. These timings should be adequate for most people, even those with some mobility impairment. With increasing number of seconds of earthquake warning, proportionately more occupants should manage to find their preferred safe place without falling and injuring themselves.

By enabling more people to find shelter, EEWS should be effective at preventing some critical injuries and deaths that might be categorized as avoidable, given the prevailing seismic building codes. Such deaths include those resulting from falls, blows, cuts and impacts from falling and overturning objects, as well as from some trauma injuries. The EEWS payoff depends on reducing the number of severe trauma injuries, categorized in the 1994 Northridge earthquake as blunt force, crushing and piercing trauma [9].

For collapsed buildings, securing even the optimum shelter inside is assumed to be of no avail since occupants would be crushed or asphyxiated. EEWS mitigation of earthquake fatalities comes from those buildings that have not collapsed, but are severely or moderately damaged, so there is a prospect of rescue or recovery. For earthquakes of magnitude 7 and higher, there may be a substantial number of such buildings beyond the EEWS blind zone in regions which are exposed to substantial levels of ground shaking of Intensity VIII or more. However, for lesser magnitude 6 events, there would be far fewer such buildings beyond the blind zone, and so less opportunity for EEWS to save lives.

Fault rupture hazard scenarios

The standard time period for long-term earthquake fault rupture forecasting is thirty years. This has an economics link with the typical duration of a home mortgage, and is also a suitable time frame to consider economic EEWS cost-effectiveness for an

active seismic region, since it allows the multi-decadal time-dependence of seismic hazard to be explicitly incorporated.

The most recent thirty year forecasts for California have been published under the acronym UCERF3 [10]. This third Uniform California Earthquake Rupture Forecast has been developed by the 2014 Working Group on California Earthquake Probabilities (WGCEP), and provides consensus estimates of the magnitude, location and likelihood of potentially damaging earthquake ruptures in the greater California region. Uncertainties in 30-year rupture likelihoods are quantified using an elaborate logic-tree of alternative model input values. The main active faults considered are mapped below.

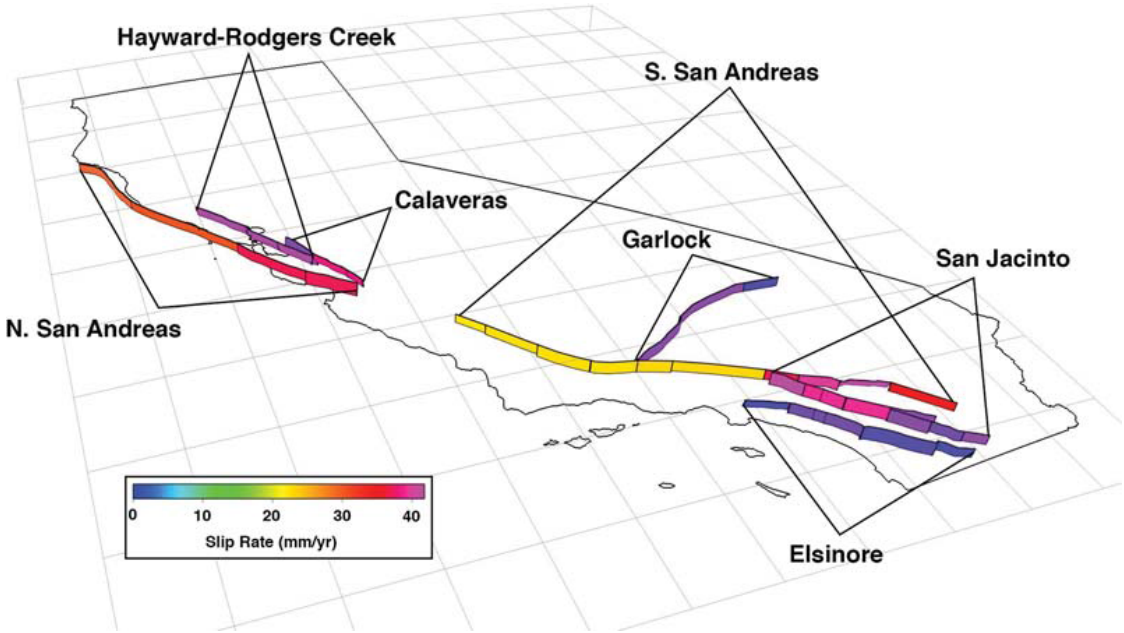

Figure 1: Main active faults in California [from [10], Field et al. (2015)]

Three key fault rupture scenarios for California casualty risk, which feature prominently in the annals of California earthquake history in the years 1857, 1906, 1868 are:

[A] M7.9 earthquake on the South San Andreas Fault
[B] M7.9 earthquake on the North San Andreas Fault
[C] M7.0 earthquake on the Hayward Fault

For each of these four generic scenarios, RMS has used an adapted form of its California earthquake casualty model to perform half a million random realizations of potential EEWS reductions in the number of fatalities and serious injuries. These simulations account for the progressively longer warning times at increasing epicentral distances, thus allowing proportionately more building occupants to find secure shelter to duck-cover-hold. In a building that has been damaged but has not collapsed, those with such secure shelter have a better chance of avoiding serious injury or death than those who fail to find such shelter.

For [A]: a repetition of the 1857 Fort Tejon earthquake at 8.20 am, EEWS might save the lives of about a hundred people indoors. For [B]: a repetition of the 1906 San Francisco earthquake at 5.12 am, EEWS might only save the lives of about twenty people indoors, because of the blind zone covering San Francisco, and the early hour. A rupture initiating far north of San Francisco would enhance the EEWS risk mitigation benefit. For [C]: a repetition of the 1868 Hayward earthquake at 7.53 am, but with a rupture initiating at the northern end, EEWS might save the lives of about eighty people indoors. This saving would be reduced if the rupture started further south.

A fourth significant fault rupture scenario for California casualty risk is [D]: a magnitude 7.5 earthquake on the San Jacinto Fault. At 2pm EEWS might save the lives of about a hundred people indoors. A fifth fault rupture scenario for California casualty risk is [E]: a magnitude 7.0 earthquake on the Calaveras Fault. At 2pm EEWS might save the lives of about ten people indoors.

Table 1: Summary of fatalities and serious injuries saved for five major earthquake scenarios

[A] M7.9 earthquake on the South San Andreas Fault	One hundred lives saved indoors at 8.20 am	Two hundred and forty serious injuries averted
[B] M7.9 earthquake on the North San Andreas Fault	Twenty lives saved indoors at 5.12 am	Seventy five serious injuries averted
[C] M7.0 earthquake on the Hayward Fault	Eighty lives saved indoors at 7.53am	One hundred and eighty serious injuries averted
[D] M7.5 earthquake on the San Jacinto Fault	One hundred lives saved indoors at 2pm	Two hundred and twenty serious injuries averted
[E] M7.0 earthquake on the Calaveras Fault	Ten lives saved indoors at 2pm	Sixty serious injuries averted

Taking a risk-averse stance on the uncertainties in the 30-year rupture hazard probabilities for the main faults and in their rupture locations, the expected number of lives saved in California through EEWS would be expected to exceed fifty over the next thirty years. The overall casualty risk mitigation, including the reduction of several hundred serious injuries inside buildings and some outside, and considering the demographics of an ageing and increasing population, would thus justify an investment of $500 million over thirty years, which would pay the annual EEWS operational costs.

As a historical benchmark, there have been just over two hundred earthquake deaths in California over the past 60 years. This is a comparatively modest figure for a seismic region, which reflects California's high professional stature in earthquake engineering, and the progressive drive towards enhancing seismic safety, which gains impetus with lessons learned from every major event. The proportion of these several hundred deaths that might have been avoided through EEWS is likely to have been under half. But note should be made of the dynamical seismological argument that the forthcoming half century in California may well be more active than the last.

Beyond California, the EEWS is scheduled also to cover the Pacific North West. The key disaster scenarios for Oregon and Washington are a M9 rupture of the whole

offshore Cascadia Subduction Zone, and smaller M8 ruptures of the southern section of this Zone. Based on these great earthquake scenarios, there is a clear justification for the Pacific North West EEWS. The regional quality of earthquake construction in the Pacific North West is generally lower, which amplifies the warning safety benefit, and the state capitals of Portland and Seattle could receive substantial warning of impending prolonged shaking from a great offshore earthquake. Sea-floor sensors near the Cascadia Subduction Zone would warn both of ground shaking as well as tsunamis. A Canadian offshore earthquake monitoring system is under development off British Columbia [11].

Fire following earthquake

Unlike seismic retrofit, EEWS would not reduce building damage from ground shaking. However EEWS does have some property protection capability: it can mitigate the loss from fire following earthquake. Scawthorn [12] has noted that the size of the fire following earthquake loss is difficult to accurately assess, but best estimates suggest a major earthquake in urban California will result in tens of billions of dollars in fire loss. Based on the latest UCERF3 forecasts, there is a very high likelihood of such a major urban Californian earthquake occurring during a thirty year time period.

One of the classic EEWS applications is for the automatic opening of fire station doors so that fire engines can respond to emergency calls without any delay from damaged door jamming. Apart from this benefit for fire suppression, the number of ignitions could be meaningfully reduced through EEWS. There are numerous types of ignition, ranging from overturned heat sources, to electrical short-circuits, to chemical spillage, and contact friction. In the Northridge earthquake, electrical short-circuits and sparking were the most common source of ignition. EEWS would have made no difference to these ignitions. However, about 20% of ignitions were attributable to a gas appliance flame, match/lighter, and other sources that potentially might have been amenable to manual control if there had been some warning time [13]. Prior earthquake preparedness in factories, offices and homes could include identifying and rehearsing rapid actions that could lower the risk of uncontrolled ignition.

Historical experience in California, such as from both the Loma Prieta and Northridge earthquakes, shows that many ignitions happen well outside the EEWS blind zone. For the M7.8 Southern California Shakeout scenario [14], approximately 1600 ignitions have been simulated, more than half of which are outside the EEWS blind zone, and a quarter are gas-related. For this scenario, the burnt area has value of $40 billion, so that the average fire loss per ignition is $25 million. If just 1% of the ignitions might be averted through EEWS ignition control, then the fire loss saving would be about $400 million. This scenario has about a 10% chance of occurrence in thirty years, so that the expected saving in fire loss from this single California disaster scenario alone is $40 million, which would pay for the EEWS installation costs.

EEWS stakeholder survey

Apart from its societal impact in reducing the toll of deaths and serious injuries, as well as fire following earthquake property loss, a public EEWS would have additional significant safety and commercial value for a diverse range of regional stakeholders.

For a number of stakeholders, advance warning of a possible power outage may enable a precautionary response to be initiated.

For most stakeholders, the expense of a private EEWS may not be commercially justifiable, given the many more common risks which need to be addressed. However, it would be cost-effective for these stakeholders to contribute collectively in keeping with their sense of corporate social responsibility to the community at large, including their own customers, staff and indeed families. Some of the major stakeholders in EEWS are listed below by industry.

Hospitals and Clinics

One of the significant EEWS benefits is heightened situation awareness. Even a few seconds of early warning should be of value to highly skilled professionals, such as surgeons, working with safety-critical precision instruments. Laser eye surgery is one of the most delicate and intricate surgical operations; the proportion of patients who experience a significant complication is about 1:100. Major earthquakes are infrequent, and the chance of a patient being unlucky enough to experience notable earthquake shaking during surgery is extremely small, about 1:100,000. This lies well within the error noise of surgical practice. Nevertheless, EEWS would enable surgeons to relieve patient anxiety over an earthquake occurring at a critical moment during an operation.

Retirement Communities and Nursing Homes

Each year, a typical U.S. nursing home with 100 residents reports 100 to 200 falls; many are unreported. Because of the frailty of the elderly, and their heightened vulnerability and propensity to decline in health sharply after falling, nursing homes and retirement communities should do whatever is possible to protect their residents from destabilizing sudden ground movement. Accordingly, they should especially value EEWS for providing crucial warning time for residents to find safe shelter. With entrance fees to some California retirement communities being as high as $1 million, due diligence over the safety of residents should extend to supporting the provision of hazard warning.

Hospitality Industry

Corporations that provide hospitality for their paying guests have an obligation to ensure safety and security. EEWS availability should be especially welcomed by high-end hotels, clubs and spas with an exclusive clientele, whose safety, comfort and convenience are paramount. Halting elevators to avoid guests being trapped between floors is a service that the larger hotels in California should provide. One of the celebrities shaken by the 1906 San Francisco earthquake whilst sleeping in a luxury city hotel was the Italian tenor, Enrico Caruso. The potential future liability costs of earthquake injuries to distinguished guests should encourage prestige Californian hotels to support a public EEWS.

Entertainment Industry

Amusement Parks

Fatal falls from Ferris wheels are very rare, but tragedies do happen: a girl fell to her death from a New Jersey Ferris wheel in 2011. Falls are possible because riders on Ferris wheels are rarely restrained with metal bars or seat belts. Unlike a roller

coaster, there are no designed physical forces that would throw a rider off. But every few decades, a large regional earthquake might turn a Ferris wheel trip into a dangerous thrill ride. However, a few seconds of earthquake warning would allow riders the opportunity to brace themselves for unexpected lateral movement. Safety is the first priority for the American amusement park industry, which has an annual revenue over $12 billion. Attendance is price-elastic, so business success depends on public confidence in safety, and it would be in their collective interest for California amusement parks to support a public EEWS.

Film Studios

The cost of injuries is especially high for film studios. Even a modest cosmetic injury could prevent a film star from appearing on screen for months. Body parts may be insured for tens of millions of dollars. Given that a large earthquake could shake all the stars in Hollywood, the aggregate risk would be hundreds of millions of dollars. It would thus be cost-effective for the film studios to contribute towards EEWS in California.

Casinos

Late night poker players at the Napa Valley Casino ran outside, leaving their chips behind, when a local M6.0 earthquake struck at 3.20am on August 24, 2015. In the event of a much larger earthquake occurring at a peak time in the late evening, it would be in the commercial self-interest of the casino management to provide the maximal warning possible for their customers. Not only would everyone be safer, both staff and customers, but this would also reduce the risk of acrimonious disputes over the ownership of chips left on the gambling tables, and winnings entitlements for disrupted games.

Construction Industry

Especially vulnerable outside are those who work above ground, e.g. construction workers and others who spend time on scaffolding and ladders. EEWS could provide time for workers above ground to find a safer position, and for loads on cranes to be stabilized. In the United States, there are about 50,000 injuries per year from occupational ladder accidents requiring treatment in emergency departments [15]. An additional several dozen injuries suffered in an earthquake during construction hours would not be a substantial risk, but an early earthquake warning would be a deserved additional tier of safety for those doing dangerous jobs on construction sites.

Manufacturing Industry

California has more manufacturing businesses than any other state. Computer and electronics comprise the state's largest industrial subsector. Although most of the chip manufacturing plants in Silicon Valley have long since moved to Asia, there remains a core of manufacturing plants left in California, which are vulnerable to sudden earthquake ground shaking. Some manufacturing plants could respond adaptively to sensing the initial ground motion, without the need for EEWS. However, other manufacturing plants would experience reduced damage and business interruption if there were a warning from a public EEWS.

Aviation Industry

Air travel is an important component of transport infrastructure. As with any natural hazard warning, both pilots and air passengers would benefit from a public EEWS.

During the Tohoku earthquake of March 11, 2011, one plane at Tokyo Narita airport veered off course as it taxied out to the runway, forcing the pilot to turn back to the terminal, suspecting a mechanical malfunction. Worse than such an episode, the contingency of an earthquake disrupting an airport traffic control system is one that airlines should wish to mitigate through early warning.

Automobile Industry
EEWS would be a desirable hi-tech safety feature enabling future autonomous vehicles in California to slow down automatically when an earthquake is detected. More conventionally, a public EEWS might reduce accidents from road, bridge or ramp failures. For example, an EEWS might cut the traffic load on an overpass by a few dozen vehicles. If one collapsed, as did the Cypress Freeway in the Loma Prieta earthquake, there might be up to a hundred fewer casualties. Traffic deceleration would also reduce the risk of road junction accidents where the traffic lights are out. It would also mitigate the risk of a car overturning after hitting a street break or obstruction, as happened with fatal consequences in the Northridge earthquake.

Wine Industry
The South Napa earthquake of August 24, 2014, fortunately occurred at night, so did not cause any injuries in the wine country. Although the M6.0 earthquake was not large enough for EEWS to have been effective, a future daytime M7 Northern California earthquake could demonstrate EEWS utility by mitigating serious injuries at wineries and wine stores from falling wine barrels and bottles. Given that the annual retail value of California wine sales in the U.S. exceeds $20 billion, some wine industry support for EEWS would be affordable and exhibit prudent risk management.

EEWS benefits for insurers

Increasingly, insurers worldwide are taking a pro-active stand encouraging and supporting risk mitigation. The historical origins of this interest dates back to the 17th century, when fire insurance was instigated after the destructive Great Fire of London. At this time, there was no London public fire service, so insurers paid for fire engines to attend to fires at their insured properties. California in the 21st century has a world class public fire service, for which fire insurers have provided guidance. Even if a home has no earthquake insurance, its fire policy will cover fire loss following an earthquake. So fire insurers have a significant financial interest in the establishment of EEWS. Beyond fire insurance, the operation of a West Coast EEWS would serve to reduce claims for a wide range of insurance products contingent on earthquake casualties. These are listed below:

Workers' compensation insurance. This is a mandatory coverage for employees. Relative to other states, California has one of the highest workers' compensation costs. Earthquakes can increase these further. In the Loma Prieta earthquake, most disabling work-related injuries would have been avoided if workers had managed to find shelter. About 30% of the occupational injuries incurred as a consequence of workers being struck by falling or overturning objects; about a quarter were fall related; and about 20% were due to workers being thrown or bumped into an object.

Event insurance. This cover is taken out by event organizers for specific occasions which may depend crucially on the fitness of key people, e.g. arts or sports

performers. Serious earthquake injury might force event cancellation. A variant of this is special project insurance, where a commercial project would have to be cancelled if key people were incapacitated. This cover is taken out by corporations as a protection against loss of certain crucial staff. Body part insurance covers a specific vital injury; the sum insured can be more than $100 million.

Health insurance. Some earthquake injuries may not be life-threatening, but nevertheless the cost of long-term disability care could be more expensive than a life insurance payout if the injured is young and requires lifelong assistance.

Liability insurance. An earthquake injury or fatality might be judged in court to be wrongful, leading to a punitive liability award, which might then involve a substantial liability insurance claim.

Summary

A West Coast EEWS could reduce significantly the earthquake toll of indoor serious injuries and fatalities, especially for the most dreaded large earthquakes. It would continue the quest to improve seismic safety in California [16]. The safety benefit, along with the fire loss reduction benefit, would warrant the EEWS investment not just for California, but for the West Coast. An investment in EEWS is different from other safety investments in having blanket geographic coverage on the West Coast, rather than enhancing safety in just a few counties. Indeed, for the same annual financial budget of $16 million, greater casualty risk mitigation could be achieved through funding a West Coast EEWS than by increasing the supply of backup emergency healthcare facilities, or through further seismic retrofit to reduce the post-earthquake healthcare demand. EEWS is thus cost-effective in a relative as well as absolute sense. Supplementary to improved emergency response and reduced building vulnerability, EEWS makes good economic safety sense. However, EEWS is not a substitute for such important measures.

Beyond life and fire safety, there are numerous regional stakeholders in the private sector who would stand to gain from EEWS operation. Their gain adds to the overall cost-effectiveness of EEWS. Quite apart from business continuity benefits and self-interest to protect key professionals, business leaders and executives, these stakeholders can also serve the broader public interest by contributing to EEWS funding. In the context of corporate social responsibility, support for EEWS would benefit all residents of California, as well as visitors from other states and abroad.

References

[1] Butry D.T., Brown M.H., Fuller S.K. (2007) Benefit-cost analysis of residential fire sprinkler systems. *NIST Office of Applied Economics Report 7451*.

[2] Stewart M.G., Ellingwood B.R., Mueller J. (2011) Homeland security: a case study in risk-aversion for public decision-making. *Int. J. Risk Assessment and Management*, **15**, 367-386.

[3] Durkin M.E. (1996) Casualty patterns in the 1994 Northridge, California, earthquake. *Proc. 11th WCEE*, Paper No. 979, Elsevier Science.

[4] Durkin M.E. (1992) Improving earthquake casualty and loss estimation. *Proc. 10th WCEE*, Balkama, Rotterdam.
[5] Mahue-Giangreco M., Mack W., Seligson H., Bourque L.B. (2001) Risk factors associated with moderate and serious injuries attributable to the 1994 Northridge earthquake, Los Angeles, California. *Annals of Epidemiology*, **26**, 806-813.
[6] CDC (2012) Costs of falls among older adults. www.cdc.gov/HomeandRecreationalSafety/Falls/fallcost.html
[7] Durkin M.E., Thiel Jr. C.C., Schneider J.E., DeVried T. (1991) Injuries and emergency medical response in the Loma Prieta earthquake. *Bull. Seism. Soc. Amer.*, **81**, 5, 2143-2166.
[8] Kuyuk H.S., Allen R.M. (2013) Optimal seismic network density for earthquake early warning: a case study from California. *Seism. Res. Lett.*, **84**, 6, 946-954.
[9] Shoaf K., Seligson H. (2011) Estimating casualties for the Southern California shakeout. *In: Human casualties in earthquakes (Eds. R. Spence, E. So, C. Scawthorn*), Springer Heidelberg.
[10] Field E.H. et al. (2015) Long-term time-dependent probabilities for the third uniform California earthquake rupture forecast (UCERF3). *Bull. Seism. Soc. Amer.*, **105**.
[11] Jones N. (2016) Canada builds quake warning system. *Nature*, **534**, 446-447.
[12] Scawthorn C. (2011) Water supply in regard to fire following earthquake. *PEER Research Center Report*: 2011/08.
[13] Scawthorn C., Cowell A.D., Borden F. (1997) Fire-related aspects of the Northridge earthquake. *Report prepared for the Building and Fire Research Laboratory*. NIST-GCR-98-743.
[14] Scawthorn C. (2011) Fire following earthquake aspects of the Southern California M_w7.8 earthquake scenario. *Earthquake Spectra*, **27**, 2, 419-441.
[15] CDC (2014) Occupational ladder fall injuries – United States, 2011 www.cdc.gov/mmwr/preview/mmwrhtml/mm6316a2.htm
[16] Alfred E. Alquist Seismic Safety Commission 2007-2011 (2007) *Earthquake loss reduction plan*. CSSC 2007-02.

Dynamic Behavior Analysis of Tigzirt Landslide

Melbouci Bachir

Laboratoire de Géomatériaux Environnement et Aménagement, Université Mouloud Mammeri, Tizi-Ouzou, Algérie, Email: melbouci_bachir@ummto.dz

Abstract

Landslides occur in unconsolidated formations at the interface with more rigid formations. Shaking at the basement impacts their dynamic evolution. This work is a contribution to the characterization and the numerical modeling of a landslide that affects the Tigzirt (Algeria) city center under the combined effect of water and seismic action.
The analysis is performed using the computer code Plaxis 2D. Both static and dynamic results of numerical calculations, confirm the precarious stability. The overburden and the depth of the water have a great influence on the dynamic response of the landslide. Dynamic stresses can increase the maximum displacement of about 90% compared to the static case.

Introduction

Kabylia has recently witnessed winters with particularly heavy rain. These storms are the cause of many cases of land instability especially in mountain regions which are sometimes very close to the densely populated coastline. These landslides are extensive and are likely to cause significant morphological changes. They result from two sets of factors: the natural conditions that control the stability of the slopes and climate and/or anthropogenic triggers (Dikau et al, 1996).

Tigzirt is located in Great Kabylia (Algeria) on the coast of the Mediterranean Sea, 40 km north of Tizi-Ouzou, 100 kilometers east of Algiers, the capital. Conducted studies have revealed the presence of a transformation zone at the interface between the substrate and the surface layers. Furthermore, the mechanical properties of surface geological formations in the area are altered with the presence of water. They foster the emergence of active and widespread landslides. The sliding surface was identified by observing samples from core drilling to relatively large depths of about 10 m at the foot of the hill and 30 meters halfway up the hillside.

Many previous earthquakes, originated on the active neotectonic sector (Boudiaf et al., 1999; Yelles-Chaouche et al., 2006) were able to weaken the slope by repeated loads (Duffaut, 2003). Seismic events produce horizontal forces in addition to the factors described above without changing the shear strength of the soil (Habib, 1997).
Due to the complexity of the problem at hand, we opted for the establishment of a multidisciplinary approach involving geomorphology, geology, hydrogeology and geotechnical engineering. This approach consists on an instability analysis phase followed by modelling.

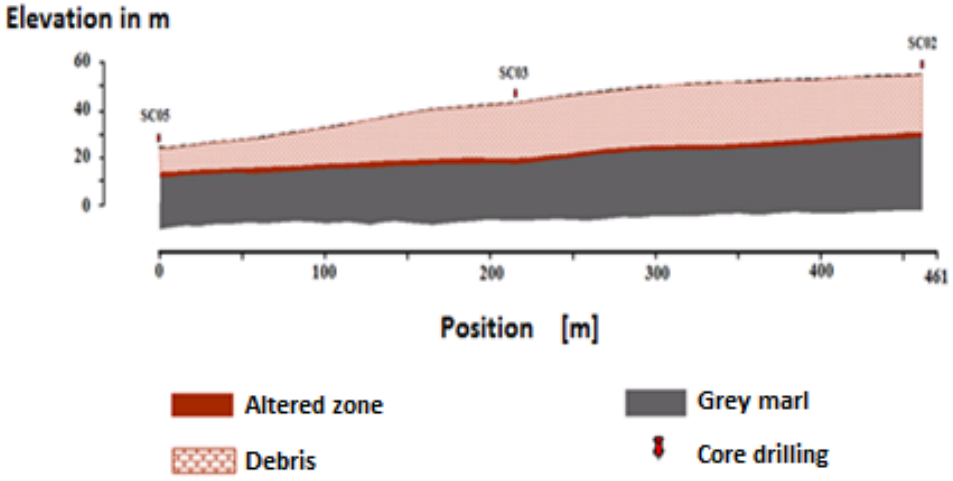

Figure 1: Geological profile produced according to the SC05-SC03-SC02 survey.

I – Description and characterization of Tigzirt sliding

The instability of the Tigzirt results from natural elements (geology, topography, the action of percolating water) and anthropic actions. Several destabilizing human activities were identified at Tigzirt city:

- the significant overload of the foot and the center of the unstable slopes and the uncontrolled cities development;
- the lack of drainage of superficial water and deep water at the unstable site and its surroundings (except of some natural gullies);
- deviation of several natural streams and clogging of water sources by development of urban spaces;
- abandoning the agricultural activities and deforestation of several slopes.

The transition from the state of stability to an unstable one (Dikau et al., 1996) has several reasons: external (erosion, earthquakes, building overburden); and internal (the increase in pore pressure, the alteration of the mechanical properties of geomaterials). The causes are generally combined.

I – 1 Morphology, hydrology and causes of slip

The urbanized site, object of this study, is located in the east of the city of Tigzirt. The slope at the site ranges from 13 ° and 15 °. The watershed of Tigzirt region stretches from the top of the mountain to the sea. The dip is to the north and in the same direction of the general slope of the landslide. This structure could be a favourable to the sliding of areas at higher elevation.

Rainfalls in the region are irregular and the climate has been described as quite cold in winter, hot and dry in summer. The highest rainfall are observed in November (109.8 mm) and maximum temperature (30.7 °) in August. The lowest moistures are 40.8% in July, the highest 94% in February.

The Tigzirt landslide grows along the interface between the substrate and the surface layer in a planar fracture form. The sliding surface is at the fringe of the altered marly substratum which has lower mechanical properties compared to healthy marl. The

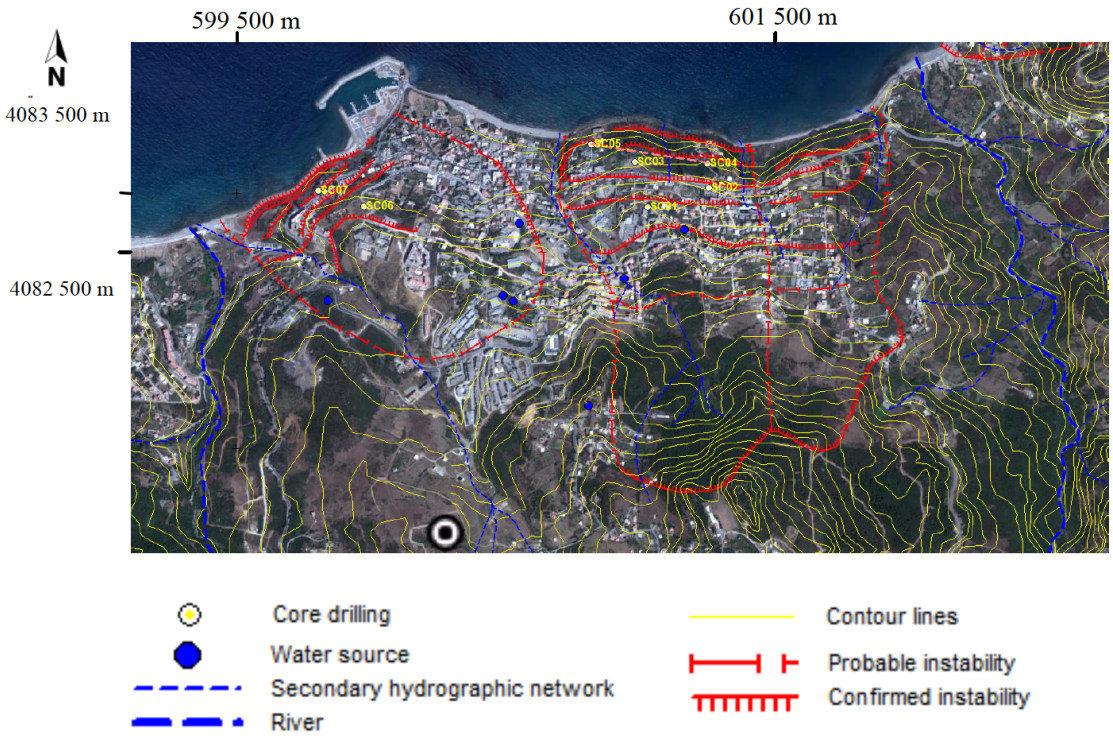

Figure 2: Map of mass gravitational mass movements mapped in the city of Tigzirt.

sliding layer is thicker than 30 m and has shown several sagging compartmentalized mechanisms. The fracture surface is plotted on a longitudinal section of the unstable slope (Figure 1). The geological section of the slope was defined by using the results of the SC01 survey and the cross sections made from the SC05- SC03- SC02 and SC05-SC04 survey (Figure 2).

The unstable slope has undergone several deformation processes that manifest on the surface by the appearance of longitudinal and transverse tear lines. In addition, these areas can be breakout areas of stagnation and infiltration of rainwater to the sliding surface which will contribute to the evolution and the reactivation of the landslide. In addition, a significant evolution of the coastline has been observed in recent years by comparing aerial images taken at different dates.

Given that the precarious stability of the Tigzirt site, any small change in hydrology or morphology can cause failure of the slope. In addition, the absence of drainage systems for surface water (gutters, drains ...) and the effect of accidental water infiltration into the unstable formations (which comes from broken water network) also contribute to the onset of instability. Failure to respect the environment and the unpredictable and varied developments (such as the clearing of forests carried out to develop Tassalast and Ferraoun beaches) are also amongst the main causes of landslides in this area. Furthermore, buildings are an aggravating factor for the stability of this area. Micro-destabilizing mechanisms are manifested by the gradual transformation of the marl materials into reworked materials under the action of water.The available records and morphological evidence observed at the surface reveal the existence of old movements, which, however, have not been listed before 1970. Since the winter of 1970, the activity of landslides and surface disturbances keep increasing.

I – 2 Geological and geotechnical data

To identify the different soil layers constituting the sliding region, a detailed analysis of boreholes drilled proves to be indispensable. The soil profile that slipped can be represented by two main formations: a first layer on the surface of Quaternary deposits consisting of scree clayey sandstone (debris) and a second deep layer of marl bedrock (Figure 1) with a disturbed zone with a thickness of about 2 m at the interface between these two formations. The minimum and maximum geotechnical properties of two marl layers are shown in Table 1.

Table 1: Range of values for the properties of the layers of Tigzirt site (Guirous et al, 2014).

Property Material	γ_d [KN/m^3]	Ip	φ' [°]	C' [KPa]	E [MPa]	υ
Clayey sandstone scree	17,3	38	30	0	800	0.33
Altered marl	14,8	28	26	0	200	0.3
Healthy marl	22,6	24	30	100	1700	0.3

I – 3 Specificity of the study area and seismicity

Coastal landslides significantly affect the ecosystem. The gravitational movement of the slope towards the sea causes an increase in sea level and so the flooding of certain areas of the catchment. This phenomenon is observed in the coastal town of Tigzirt. Using MapInfo mapping tool and exploiting aerial images of Tigzirt taken in 2006 and 2011, a significant evolution of the coastline at Tigzirt was observed (Figure 3).

Hydro-climatology conditions act negatively on the stability of slopes in different ways:

a) as a result of surface erosion due to runoff;
b) the effect of waves at the foot of the slope which removes major passive earth resistance;
c) the effect of water flow in the river: two types of flows are observed for this site (a flow in the direction of the river due to water infiltration and an upward flow of saline water under the influence of waves);
d) the effect of salt water on the marl bedrock (Tigzirt marl is very sensitive to climate and water).

Regional seismotectonics may cause sudden rupture of unstable Tigzirt slope (as this city is located in an active tectonic zone, Figure 4). The unstable Tigzirt site is bordered by several major active faults. They are located either on the mainland or offshore (Fig.4). Among the most important are: the Thenia fault with strike N120 ° E (Boudiaf et al., 1998), the reverse fault of Isser – Tizi-Ouzou and the reverse fault of Zemmouri that consists of a series of discontinuous fracture zones, located at sea. Stress induced by the Boumerdes earthquake (2003) to the landslide and probable uprising along the Thenia fault (causing the Boumerdes earthquake) may have increased the vulnerability of this precarious coastal slope already weakened by the significant development of urbanization; this led to the beginning of a field instability affecting about 136 Ha.

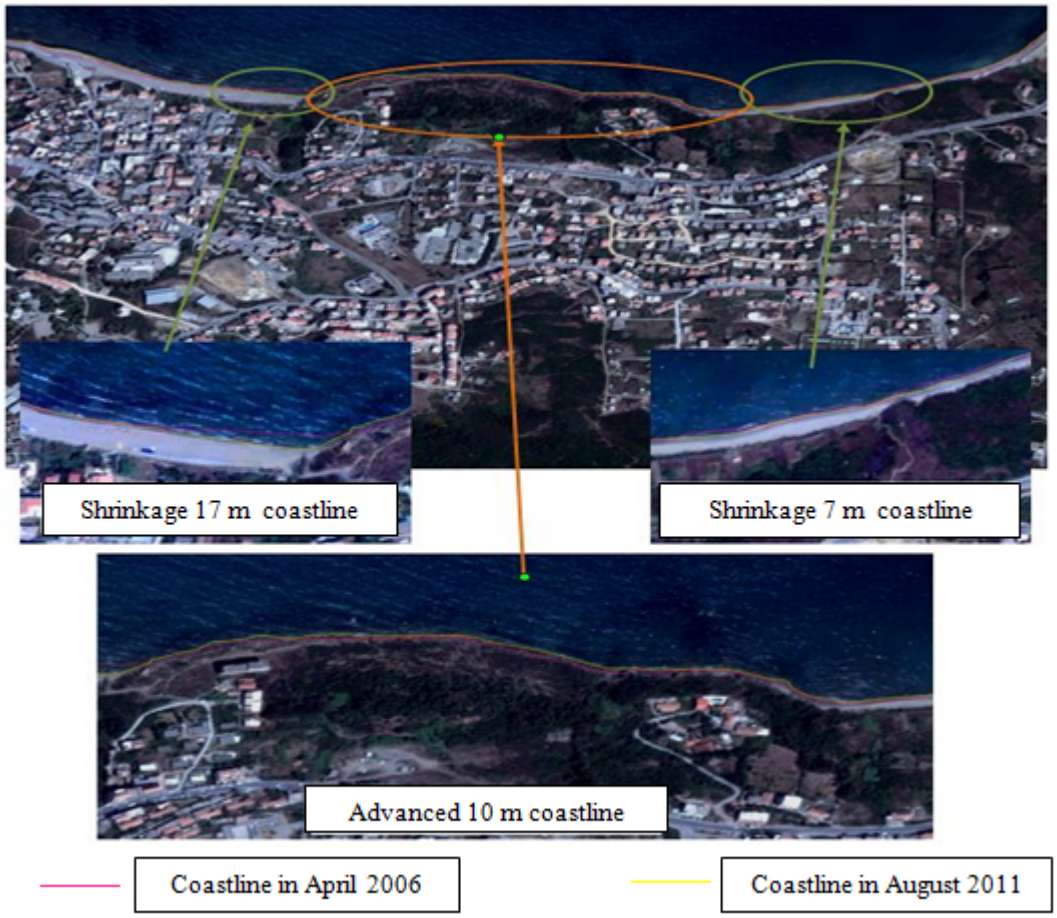

Figure 3: Evolution of the coastline at the instable zone between 2006 and 2011.

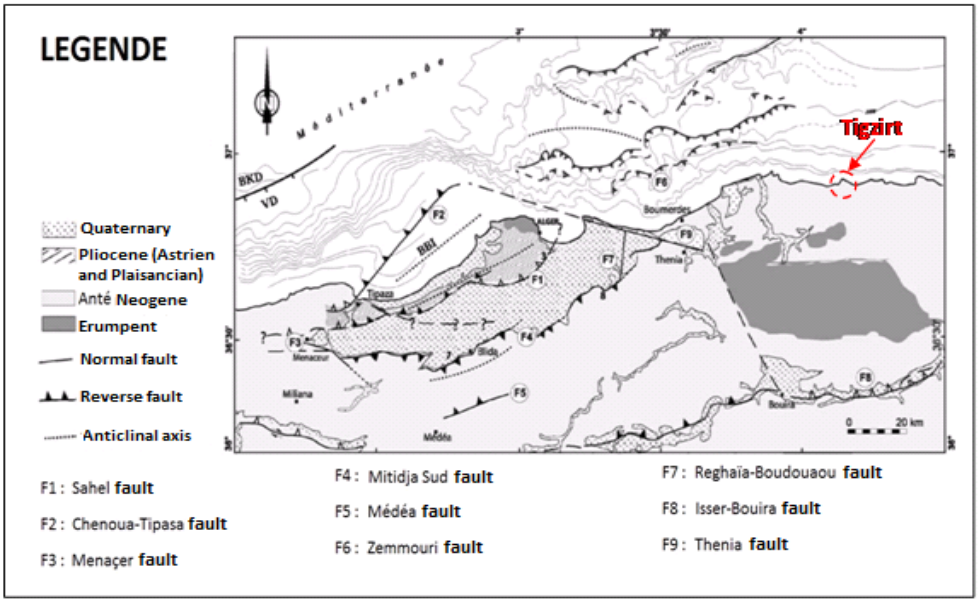

Figure 4: Structural Framework for the Algiers region (Yelles-Chaouche et al., 2006).

The activity of the landslide has not however been deeply influenced by the Boumerdes earthquake, which generated only light damage in the town. However, the hypothesis of a potential seismic site effect due to the topography and the presence of unstable formations into a thickness of 30 m, largely saturated with water and resting on a solid substratum (more strong seismic velocity), cannot be ruled out. This site effect significantly amplifies the horizontal components of vibration on the surface and thus would be extremely unfavorable for stability under dynamic stresses slope. However, this could be demonstrated only through seismic monitoring at the site missing to date.

II – Modelling of Tigzirt landslide

The finite element method was chosen for the numerical modeling of Tigzirt landslide with calculations using the code PLAXIS 2D Version 2011. This code provides the ability to manage large plain strain with the updating of the mesh after each iteration calculation. This method is inspired by classical stability analysis methods to limit equilibrium (Fellenius, Bishop, etc.), but without imposing a fracture surface beforehand.

The study of slope stability is based on the reduction of mechanical properties is an option available in PLAXIS (1999) called 'Phi-c reduction' and which calculates safety factors. In the approach "Phi-c reduction", the characteristic angles of friction ($tan\varphi$) and cohesion (C) of the ground are reduced progressively until rupture.

II – 1 Presentation of the model

The model is composed of three main layers: a surface cover composed of clayey sandstone's debris on compact marl bedrock topped with an altered fringe of a thickness of about 2 m. The Mohr-Coulomb law (elastic perfectly plastic) was chosen to simulate the long-term behavior of cohesive soils up the slope. It requires knowledge of six parameters: density, Young's modulus E, the Poisson coefficient ν, cohesion C, angle of friction φ and dilatancy angle ψ (considered to be zero for the soil at an angle of less than or equal to 30 ° friction).

The profile used is spread over a length of approximately 1330 m (Fig 5) and crosses all the unstable area from the main escarpment down to the sea. The maximum height of the profile is 270 m and the minimum is approximately - 60 m (under the sea level). The selected mesh consists of 2499 triangular elements at 15 knots with 12 integration points per element. The boundary conditions are defined as such (Fig 4):

- vertical geometric lines for which the abscissa (x) is equal to the smallest or the largest of the abscissa (x) of the model are locked horizontally ($U_x = 0$),
- the geometrical lines, for which the side (y) is equal to the smallest ordinate (y) of the model are fully blocked ($U_x = U_y = 0$).

II – 2 Presentation and interpretation of results

Four periods were considered in this study: a dry period when the clayey sandstone debris layer is not saturated and a wet period when this layer is considered saturated and an intermediate period when the water table depth fluctuates between 3 and 9 m.

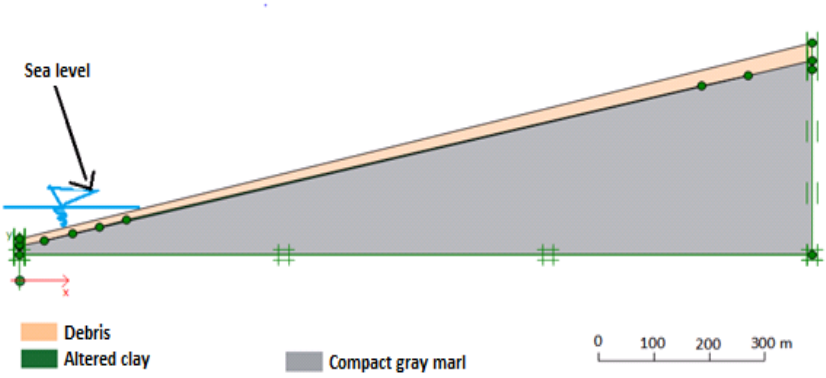

Figure 5: Tigzirt landslide model.

The wet period is normally characterized by the winter months and early spring, when heavy rains and melting snow have an effect on the supply of ground water. Thus four calculations are launched simultaneously taking into account the seismicity of the Tigzirt area, the overburdening effect due to urbanization varying the depth of the water table in increments of 3m depth to reach a depth of 12m.

Tigzirt is an average seismicity (zone II) from the Algerian earthquake regulation. Inspired by the accelerogram of Bourmedes of earthquake (2003), it is considered that the earthquake acts as a inertia force parallel to the slope.

Water table on the surface

This case is represented by the application of an overload of 10 KN/m on the slope of the foot and an excitation (seismic shear wave) of 0.34g at the base. This allows us to detect the most sensitive area in terms of instability.
The results obtained show that the maximum displacement obtained with this configuration is of the order of 12.92 m. (Fig.6). This displacement is six times higher than that found without application of the overload and without seismic excitation. Amplification of the seismic movement was observed at the altered clay layer with a response of the soil in peak acceleration of about 0.58 g. Plasticity zones generated by these three effects accentuated and aggravated movement and disturbed zone widens (Figure 7). The resulting safety factor which is of the order of 0.93 shows the instability of the slope. There has been a site effect that amplified seismic excitation to 0.58g.

Water table at 6m depth

In this case, a decrease in the rate of displacement was observed which is of the order of 95% (Fig. 8), relative to the previous case. The resulting safety coefficient is 1.12; this proves that the slope is in precarious stability condition. In addition, the displacement rate increased by 61% compared to the dynamic case without overload; which reflects the danger to the urbanized Tigzirt. The aquifer also plays an important role both in area and depth. Indeed, it weakens the weight of the slope by introducing a driving force.

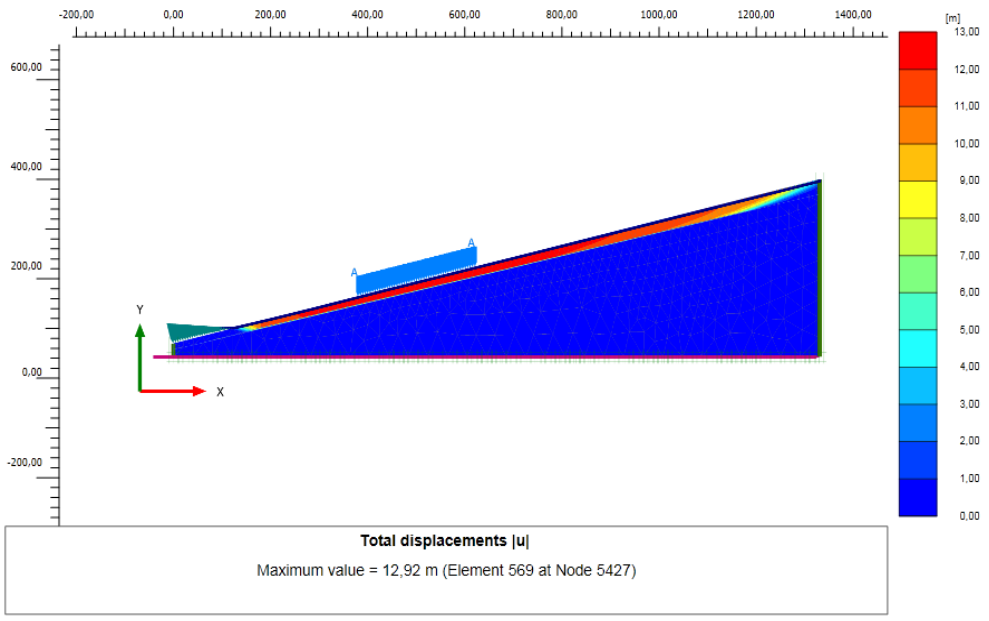

Figure 6: Displacements ||U||=12.92m as a result of the overload of urbanization and seismic excitation.

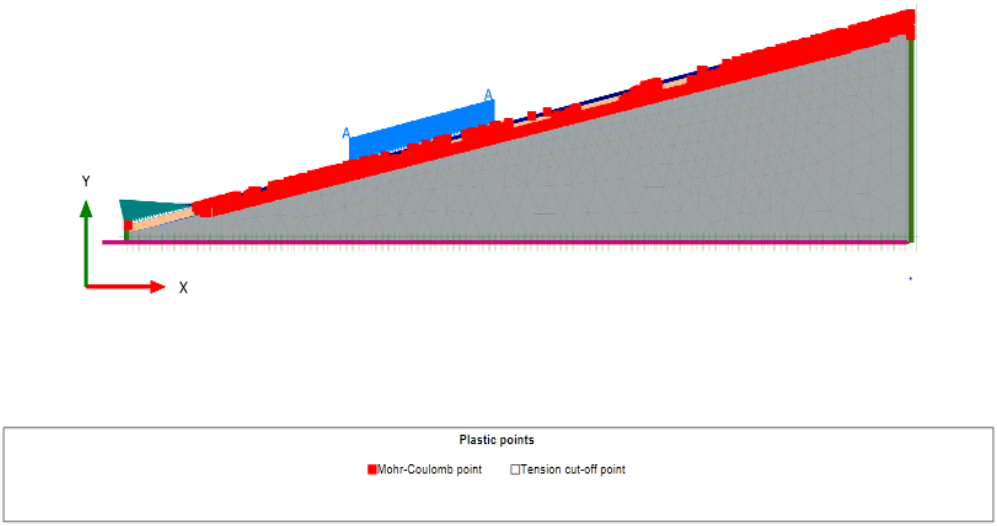

Figure 7: Map of the plasticized areas of slope for the case of the aquifer at the free surface under an overload and seismic excitation effect.

Water table at 9m depth

In this case, displacements decrease by 36% (Fig. 9), compared to the previous case (dynamic case with overload and 6m deep water table) and a slight increase of 4% in the dynamic case without overload. The deeper the water tables the lesser the impact of the overburden. In this case, the safety factor is unstable and varies $0{,}65 \leq Fs \leq 1.3$; which means that the side will not gain some stability than in the dynamic case without overload where Fs is 1.2. Plasticity zones generated widens (figure 10).

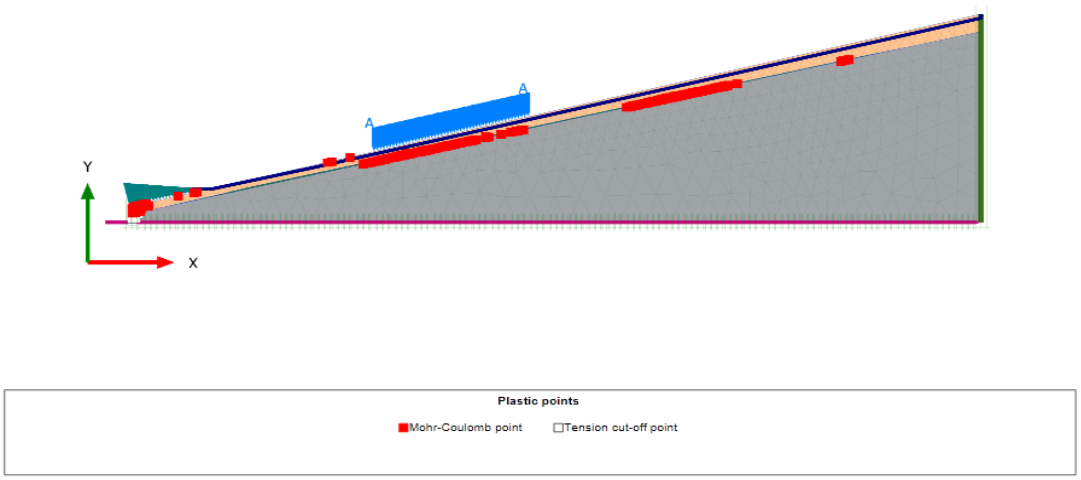

Figure 8: Map of the location of plasticity zones in the landslide for the case of aquifer at 6 m depth and under an overburden and a seismic excitation effect.

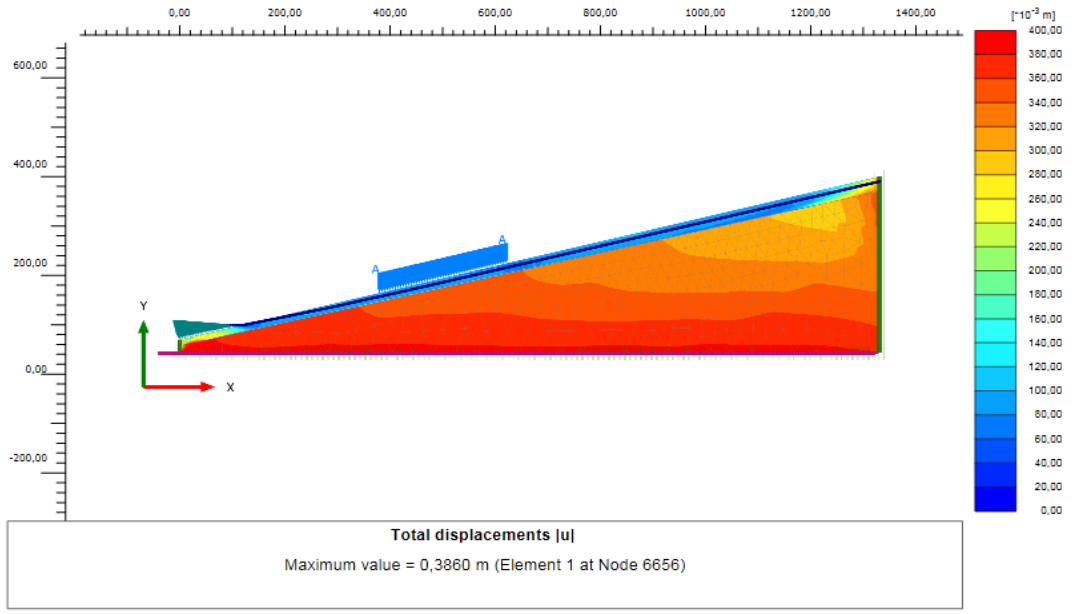

Figure 9: Displacements ||U|| = 0.386m watershed under the seismic excitation effect and aquifer 9 m deep.

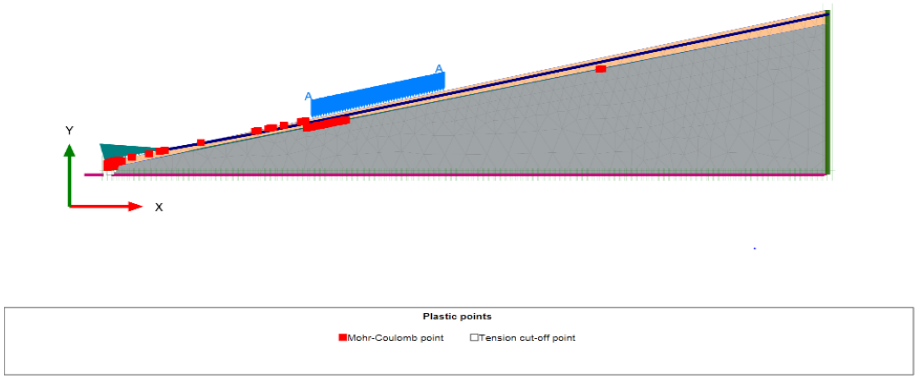

Figure 10: Map of the location of plasticity zones in the landslide for the case of aquifer at 9 m depth and under an overburden and a seismic excitation effect.

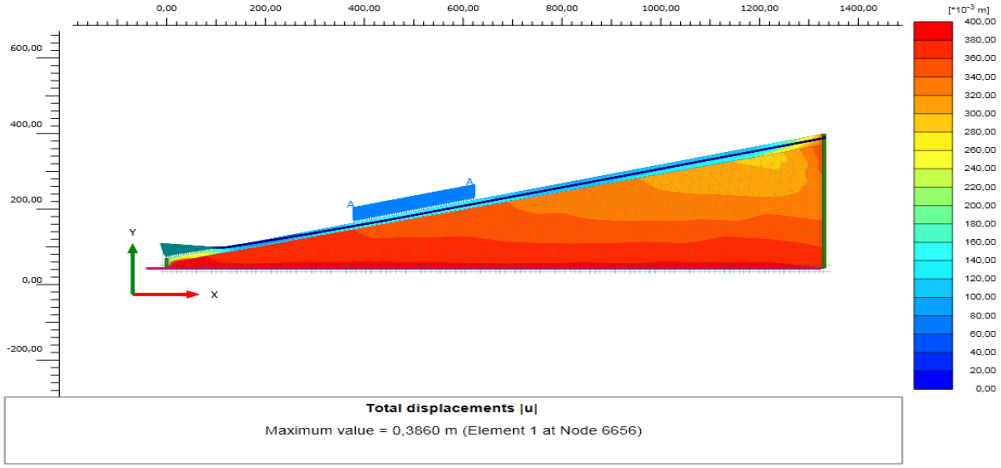

Figure 11: ||U|| = 0.386m watershed under the seismic excitation effect and water table at 12 m depth.

Water table at 12m depth

In this case, there will be no change (Fig. 11), compared to the previous calculation (depth 9m) as the rate of displacement is 0.386 m. So there has not been any influence on the rate of displacement when the water table depth exceeds 9m. The safety factor reached 1.3; which ensures the stability of the slope. Plasticity zones generated widens (Figure 12).

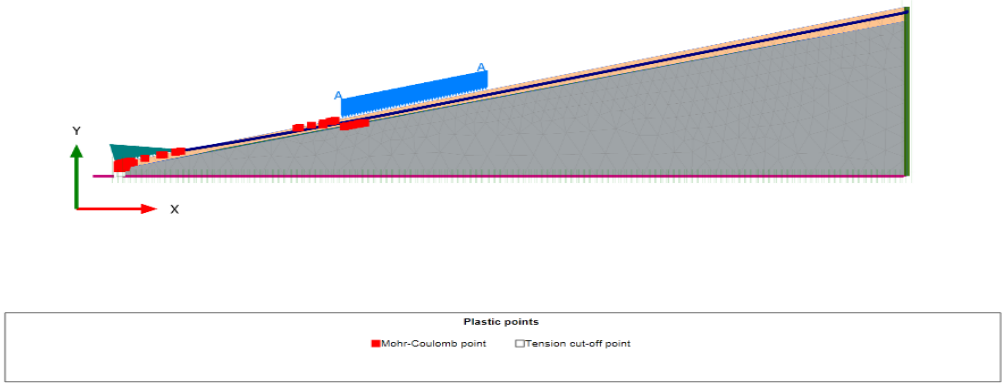

Figure 12: Map of the location of plasticity zones in the landslide for the case of aquifer at 12 m depth and under an overburden and a seismic excitation effect.

III – Conclusion

The results of the numerical analysis performed showed that the slope of the Tigzirt region is strongly influenced by the water table, urbanization and seismic activity. Indeed, for a slick surface, a significant amplification of the seismic signal is observed for the level of the disturbed zone of the slope. Thus, the plasticity zones generated by these three effects accentuated and aggravated the movement and the disturbed zone widened. Recorded displacements are maximum when the water table is on the surface. When the water level decreases, we observe a significant reduction in the rate of displacement which stabilizes when the water table reaches 9m.

References

BOUDIAF A., RITZ J.F. et PHILIP H. (1998), 'Drainage diversions as evidence of propagating active faults : example of the El Asnam and Thenia fault, Algeria'.Terra Nova, Vol. 10, pp. 236-244.

BOUDIAF A., PHILLIP H., COUTELLE A. et RITZ J.F. (1999), Découverte d'un chevauchement d'âge Quaternaire au sud de la Grande Kabylie (Algérie). *Geodinamica Acta*, vol. 12, n° 2, p. 71-80.

DIKAU R., BRUNSDEN D., SCHROTT L. AND IBSEN M.L. (1996), Landslide Recognition: Identification, Movement and Causes. John Wiley & Sons, England.

GUIROUS L., DUBOIS L. et MELBOUCI B.: Contribution à l'étude du mouvement de terrain de la ville de Tigzirt (Algérie). Bulletin of Engineering Geology and environment, Volume 73, Issue 4 (2014), pages 971-986.

HABIB P. (1997), *Génie géotechnique, application à la mécanique des sols et des roches*. Édit. Ellipses, Paris, 222 p.

L.N.H.C. (2002), 'Étude géotechnique de la zone de glissement 1ière tranche-Tigzirt', Internal report, file N° 6.0.120.2002.

YELLES-CHAOUCHE A., BOUDIAF A., DJELLIT H. ET BRACENE R. (2006), La tectonique active de la région Nord Algérienne – C.R géoscience, Vol.338, pp.126-139.

ROTHE, J. P. (1950), Les séismes de Kherrata et la sismicité de l'Algérie, Bull. Serv. Carte Geol. Algérie Geophys., 3, 3 –40.

MESLEM, A. F, YAMAZAKI, Y. MARUYAMA, D. BENOUAR, N. LAOUAMI N. (2008) 'Strong motion distribution and microtremor observation Following the 21 may 2003 boumerdes, algeria earthquake'. October 12-17, 2008 the 14th world conference on earthquake engineering, beijing, China.

Table of Contents

Déjà parus

Vol 1: Seismic Networks and Rapid Digital Data Transmission and Exchange (1990)
Vol 2: GPS for Geodesy and Geodynamics (1990)
Vol 3: Non Tidal Gravity Changes: Intercomparison between Absolute and Superconducting Gravimeters (1991)
Vol 4: Geodynamical Instrumentation Applied to Volcanic Areas (1991)
Vol 5: Local and National Seismic Networks: On Line Data Processing with Microcomputer Facilities (1992)
Vol 6: Application of Artificial Intelligence Techniques in Seismology and Engineering Seismology (1992)
Vol 7: European Macroseismic Scale 1992 (1993)
Vol 8: New Challenges for Geodesy in Volcanoes Monitoring (1995)
Vol 9: Dynamical Systems and Artificial Intelligence Applied to Data Banks in Geophysics (1995)
Vol 10: Accurate Orbit Determination and Observations of High Earth Satellites for Geodynamics (1995)
Vol 11: Non Tidal Gravity Changes: Intercomparison between Absolute and Superconducting Gravimeters (1995)
Vol 12: Application of Artificial Intelligence Techniques in Seismology and Engineering Seismology (1996)
Vol 13: Historical Seismic Instruments and Documents: a Heritage of Great Scientific and Cultural Value (1997)
Vol 14: Short Term Thermal and Hydrological Signatures Related to Tectonic Activities (1997)
Vol 15: European Macroseismic Scale (1998)
Vol 16: Geodynamical Hazards Associated with Large Dams (1998)
Vol 17: High Precision Gravity Measurements with Application to Geodynamics and Second GGP Workshop (2000)
Vol 18: Evaluation of the Potential For Large Earthquakes in Regions of Present Day Low Seismic Activity in Europe (2001)
Vol 19: L'Echelle Macrosismique Européenne 1998 New (version française) (2001)
Vol 20: Analytical Representation of Potential Field Anomalies for Europe (2003)
Vol 21: Escala Macrosismica Europea 1998 (spanish version) (2003)
Vol 22: IMG 2002- Instrumentation and Metrology in Gravimetry (2003)
Vol 23: The State of GPS Vertical Positioning Precision: Separation of Earth Processes by Space Geodesy (2004)
Vol 24: Forcing of Polar Motion in the Chandler Frequency Band: A Contribution to Understanding Interannual Climate Variations (2005)
Vol 25: GOCINA: Improving Modeling of Ocean Transport and Climate Prediction in the North Atlantic Region Using GOCE Gravimetry (2006)
Vol 26: International Comparison of Absolute Gravimeters in Walferdange (Luxembourg) of November 2003 (2006)
Vol 27: Escala Macrosismica Europea 1998 (updated spanish version) (2009)
Vol 28: Seismicity Patterns in the Euro-Med Region (2009)
Vol 29: Active Volcanism and Continental Rifting (2010)
Vol 30: Induced Seismicity (2010)